

博士論文

**Studies on the Evaluation of Vulnerability of Flood Disaster and on
the Detection of Flooded Areas Using Satellite Images**

(衛星データを用いた洪水脆弱性評価および洪水被害域の抽出に関する研究)

A. Besse Rimba

**System Design and Engineering
Graduate School of Science and Engineering**

Yamaguchi University

March 2017

SUMMARY

Floods are the third most damaging natural hazard globally. The vulnerability of human and financial capital across the globe to flood impacts are increasing. Changing demographics, rapid change in land use patterns and economic activities cause severe damage in floodplains. Besides, frequent occurrences of extreme precipitation are witnessed around the world due to anthropogenic climate change which further increases the magnitude of flood risk. In recent years, due to an increasing number in the frequency and intensity of extreme meteorological events potentially related to climate change, growing attention has been paid to emergency response and relief measures. Approximately 50% of total population in Japan and 75% of its assets are located in flood vulnerable areas. Since 2004, the number of flood in Japan has increased e.g. in recent years (3rd July 2006 in Kumamoto; 11-17 July 2007 in Kagoshima, Miyazaki, Kumamoto; 30th August 2008 in Aichi Prefecture and around Chubu region; 10th September 2015 in Ibaraki Prefecture and around Kanto region

Remote Sensing and Geographic Information System (GIS) are very helpful and effective tools in disaster management. Remote sensing and GIS can be applied in all phases of disaster management; disaster prevention, disaster preparedness, disaster relief, disaster rehabilitation and reconstruction. The remote sensing technology extracts the information from the satellite; GIS integrated the remote sensing data and others spatial data.

Remote sensing has two kinds of sensors, namely, a passive sensor (e.g., ALOS/AVNIR-2, Sentinel-2) and an active sensor (e.g., ALOS/PALSAR, ALOS-2/PALSAR-2). Passive sensors contain different types of spectrometers and radiometers. This sensor needs other source energy to record the information, such as solar energy. The active sensor is operated in the electromagnetic spectrum of the microwave fraction. Hence, the active sensor is possible to penetrate the atmosphere under most conditions weather because the wavelength of microwave is longer. This research utilized these data to conduct the flood analysis in Japan.

The aims of this research are to reduce the impact of flood by detecting the flood-vulnerable area. This research utilized the SAR images (i.e., ALOS/PALSAR, ALOS-2/PALSAR-2) because SAR sensor can penetrate the water vapor during the heavy rain. Nevertheless, its limitation, i.e. speckle, appears on the image as salt-and-pepper. Hence, this study introduced a new method to reduce the speckle noise on ALOS/PALSAR and ALOS-2/PALSAR-2 images and evaluated the best method to extract the flood area from ALOS-2/PALSAR-2 images.

This study is divided into 6 chapters. Chapters 1 and 2 explain about the background, problems, purposes, study area and supporting literatures, data, and tools.

Chapter 3 describes the method to estimate the flood vulnerability area by utilizing the rainfall, drainage density, slope, soil and land cover data. Two methods are conducted to estimate the flood vulnerability. The first method estimates the flood vulnerability by simply superimposed GIS method in Kumamoto City; and the second method integrates the Remote Sensing images, GIS and Analytical Hierarchy Process (AHP). By utilized the AHP process, the pair-wise parameters of flood are weighted: the research locations are in the Shirakawa watershed, Kumamoto Prefecture and Okazaki City, Aichi Prefecture.

Chapter 4 describes the best filter to reduce the speckle noise. During the flood periods, Synthetic Aperture Radar (SAR) is the best satellite image to derive information in the disaster area because SAR image can acquire the information in all weather conditions and can record the earth in day or night. Nevertheless, SAR image has speckle noise that appears as salts and peppers on the surface of the SAR image. However, this speckle noise contents the information. Removing the speckle by filtering is a common technique to acquire the clear image. The user can adjust the kernel size of the filter; small kernel size produces an unclear image and preserve the mean value of pixel, vice versa, big kernel size produces the clear image from speckle noise and over smoothed image that means some information disappeared. Hence, this chapter proposed a new method, i.e., Double filter, to remove the speckle without broadly loss information from ALOS/PALSAR and ALOS-2/PALSAR-2 images.

Chapter 5 describes three evaluation methods i.e., unsupervised classification, supervised classification and binarization method to extract flood area by using ALOS-2/PALSAR-2 image as a rapid response to flood disaster. The overestimate area due to the shadowing effect of SAR image is reduced by using DEM data. However, the limitation of SAR image (i.e., double bounce) can be solved in this study. The study area are in Joso City, Ibaraki Prefecture and Okazaki City, Aichi Prefecture. Furthermore, the best method was applied to detect flood in Okazaki City from ALOS/PALSAR images and compared to flood vulnerability of the result from Chapter 3.

Chapter 6 describes the conclusions and future works of this study.

The advantages of this study are;

1. This method could predict the flood-vulnerable area by integrating the remote sensing technology, GIS method and AHP procedure. It has a good accuracy, low cost, and it can be applied in another area even though with different characteristics.
2. The effective filter was introduced to make easier the flooded area extraction because detecting the edge of a flood was easier by the Double filter. The advantages of the proposed filter (i.e., double filter) were to reduce the speckle, to enhance the edge and detail object. Furthermore, the double filter increased the visual performance of the image.
3. The accurate flood extraction method was evaluated (i.e., binarization). The accuracy of the method was 94% by Kappa coefficient.

概要

洪水は、世界で被害額 3 番目の自然災害である。洪水による人的及び資産の脆弱性が増加している。人口増加、急速な土地開発、経済活動の拡大による洪水氾濫区域の増大がその理由である。さらには、人間の活動に起因する気候変動により世界中で強烈な台風、サイクロン、ハリケーン、前線に伴う豪雨が頻繁し、洪水のリスクが増加している。近年、気候変動に起因する極端な気象事象の回数と強度が増加することにより、緊急対応、あるいは長期にわたる対策のために多くのコストがかかっている。日本の全人口の約 50%とその資産の 75%が洪水氾濫危険区域にある。しかも特に 2004 年から日本における洪水発生件数は急増しており（例えば、熊本県：2006 年 7 月 3 日、鹿児島県・宮崎県・熊本県：2007 年 7 月 11 日、愛知県と中部地域：2008 年 8 月 30 日、茨城県と関東地域：2015 年 9 月 10 日）、これらの大量の降水量は大きな被害をもたらし、重大な経済的損失へとつながっている。

リモートセンシングと地理情報システム（Geographic Information System: GIS）は災害管理に非常に有益で効果的なツールである。リモートセンシングと GIS は、災害管理の全フェーズに応用できる。特に衛星リモートセンシング技術は衛星データとその他の空間データを統合した GIS から有効な情報を提供する。リモートセンシングには 2 種類のセンサがある。一つは受動センサ（例えば ALOS/AVNIR-2）、もう一つは能動センサ（例えば ALOS/PALSAR、ALOS-2/PALSAR-2）である。受動センサは分光計と放射計の異なるタイプがある。このセンサは情報を取得するために太陽光のようなエネルギー源を必要とする。一方の能動センサはマイクロ波領域の電磁波を自ら照射し、受信する。したがって、太陽光のようなエネルギー源を必要としない。しかもマイクロ波は波長が長いので、湿気が多い状態での大気（雲）を貫通することもできる。この能動センサは合成開口レーダー（Synthetic Aperture Rader: SAR）を用いることが多く、その場合には SAR センサとも呼ばれる。本研究では、日本の洪水解析を実施するためにこれらのデータを利用した。

本研究の目的は洪水氾濫区域を検出することにより、洪水の影響を低減することである。したがって、本研究では、大雨の中の水蒸気（雲）を貫通できる SAR 画像（ALOS/PALSAR、ALOS-2/PALSAR-2）を用いた。しかしながら SAR 画像にはスペckルと呼ばれる霜降りのような小さな斑点が必然的に現れる。そこで本研究では、ALOS/PALSAR と ALOS-2/PALSAR-2 画像におけるスペckルノイズを低減するための新しい方法、“二重フィルタ”を考案し、SAR 画像から洪水領域の情報を取得するための最善のフィルタを提案した。

本論文は 6 章から構成されており、1 章、2 章では、研究背景、課題と目的、研究範囲と先行文献について述べた。3 章から 6 章の内容は以下のとおりである。

3 章では、降水量、排水密度、土地の傾斜、土壌と土地被覆データをパラメータとして、洪水発生に対する脆弱な地域を推定する方法を示した。ここでは二つの方法を用いて洪水に対する脆弱性を検討している。一つ目は、上記パラメータを同じ重み付けで GIS 上に重ね合わせて評価する方法（Simply Superimposed Method）、熊本市を対象に洪水脆弱性を検討した。二つ目は、GIS と階層分

析法 (Analytical Hierarchy Process: AHP)を組み合わせた方法である。AHPでは一対比較によって上記パラメータの重みが決定される。この重みに基づいて GIS 上に上記パラメータを重ね合わせることで洪水脆弱性が評価される。対象場所は岡崎市とした。

4 章では、スペックルノイズを低減するための最適のフィルタについて検討した。フィルタによってスペックルノイズを除去することは明瞭な画像を作成するための一般的な方法である。その際、フィルタのカーネルサイズを自由に選ぶことができる。小さなカーネルサイズでは画素値は概して変化しないでスムーズでない画像を作り出す。一方、大きなカーネルサイズはスペックルノイズが消えた画像を作り出せるが、いくつかの情報がきえた過剰に平滑化したものとなる。以上のことを考えて、本章では、小さなカーネルサイズの異なるフィルタを 2 度使う方法、すなわち、“二重フィルタ”を考案し、ALOS/PALSAR と ALOS-2/PALSAR-2 を対象に、最適なフィルタリングを検討した。その結果から、できるだけ大切な情報を失うことなくスペックルノイズを除去する新しい方法を提案した。

5 章では、洪水災害発生に対して、行政ができるだけ早く対応するための情報を提供することを目的に、ALOS-2/PALSAR-2 画像を使うことで、洪水範囲を抽出する 3 つの方法（教師なし分類、教師あり分類、二値化）について検討した。SAR 画像の本質的特性に起因する“シャドウイング”という現象による過大な水域見積もりに対してはデジタル標高データ (Digital Elevation Model: DEM) を使うことで、その影響を減少することを試みた。しかしながら、この手法だけでは SAR 画像の他の本質的特色に起因する“二重反復”の問題は必ずしも解決できず、建物の密集する市街地の洪水被害の評価にはさらなる工夫が必要であることを明らかにした。ここでは、茨城県常総市と愛知県岡崎市を対象とした。

6 章では本研究の成果を取りまとめた。主な成果は以下のとおりである。

1. リモートセンシング技術と GIS 手法、AHP を統合することで、洪水に対して脆弱な地域の予測手法を提案した。この方法は、確度が高く、低コストで、本研究で対象とした地域と異なる特性をもつ地域であっても適用できる。
2. “二重フィルタ”という新しい効果的なフィルタを提案した。これは洪水領域を簡単に判読することができる。提案した二重フィルタの利点は、スペックルノイズの低減と明瞭なエッジと対象物の保存という、相反することを可能とするもので、画像の視認性を向上させる。
3. 教師なし分類、教師あり分類、二値化手法を用いて正確な洪水領域取得方法を評価した結果、二値化手法が最も良い結果であった。この方法による確度は κ 係数で 94%とであった。この方法では、処理時間、データに制約がある場合でも適用可能である。

LIST OF CONTENTS

Summary	i
Summary in Japanese	iv
List of contents	vi
List of figures	ix
List of tables	xii
CHAPTER 1 INTRODUCTION	1
1.1. Background	1
1.2. Research Scope and Objective	4
1.3. Research Outline	4
CHAPTER 2 METHODOLOGY, DATA AND STUDY AREA.....	7
2.1. Disaster Management and Vulnerability.....	7
2.1.1. Disaster Management	7
2.1.2. Vulnerability: A definition	9
2.1.3. Vulnerability: Conceptual framework.....	11
2.1.4. Vulnerability Mapping	13
2.2. Methodology.....	14
2.2.1. Remote Sensing.....	14
2.2.2. Geography Information System (GIS).....	23
2.2.3. Spatial Multi Criteria Analysis for Vulnerability Assessment	23
2.2.4. Accuracy Assessment.....	27
2.3. Data.....	29
2.3.1 Satellites data.....	30
2.3.2 Digital Elevation Model (DEM) data.....	30
2.3.3 Meteorological data	31
2.4. Overview of the study area	31
2.4.1. Okazaki City, Aichi Prefecture	32
2.4.2. Joso City, Ibaraki Prefecture	32
2.4.3. Shirakawa River, Kumamoto Prefecture	33
CHAPTER 3 INTEGRATED REMOTE SENSING DATA AND GIS METHOD TO FLOOD VULNERABILITY.....	34

3.1.	Introduction.....	34
3.2.	Flood problem in Kumamoto Prefecture and Okazaki City in Aichi Prefecture.....	36
3.2.1.	Shirakawa River in Kumamoto Prefecture and flood history	36
3.2.2.	Yahagi River in Okazaki City, Aichi Prefecture and flood history	37
3.3.	Material and Methods.....	40
3.3.1	Overview	40
3.3.2.	Flood vulnerability variable by simple superimposed method	43
3.3.3.	Flood vulnerability Variable by AHP	50
3.3.4.	Analytical Hierarchy Process (AHP)	58
3.4.	Result	60
3.4.1.	Flood-vulnerability Map by Simple Superimposed in Kumamoto City.....	60
3.4.2.	Flood-vulnerability Map by Simply Superimposed in Okazaki City	62
3.4.3.	Flood-vulnerability Map by AHP Process in Okazaki City	66
3.5.	Conclusion	72

CHAPTER 4 EVALUATION OF FILTERING PERFORMANCES TO REDUCE THE SPECKLE NOISE FOR DETECTING FLOOD INUNDATION AREAS FROM SAR IMAGES..... 74

4.1.	Introduction.....	74
4.2.	Methodology.....	77
4.2.1.	Overview	77
4.2.2.	Research location.....	79
4.2.3.	Dataset and Pre-processing	80
4.2.4.	Basic principle of SAR speckled image	81
4.2.5.	Filter types	81
4.2.6.	Performance Evaluation.....	83
4.2.7.	Assessment for Flooded Area	85
4.3.	Results	86
4.3.1.	Quantitative assessment.....	87
4.3.2.	Qualitative assessment	91
4.4.	Discussion	98
4.4.1.	Assessment for flooded area	100
4.4.2.	The strength of the proposed filter	102
4.5.	Conclusion	104

CHAPTER 5 EVALUATING THE EXTRACTION APPROACHES OF FLOOD EXTENDED AREA BY USING SAR IMAGES AS A RAPID RESPONSE TO FLOOD DISASTER	106
5.1. Introduction.....	106
5.2. Study area and data set.....	108
5.2.1. Study area	108
5.2.2. Dataset.....	111
5.3. Methodology.....	111
5.3.1. Flood extraction methods.....	111
5.3.2. Backscattering	114
5.3.3. Application Double filter	114
5.3.4. Image classification	114
5.3.5. Change detection by image differencing	116
5.3.6. Opening and closing.....	117
5.4. Result and Discussion	117
5.4.1. Accuracy assessment.....	119
5.4.2. The limitation of using SAR images	122
5.4.3. Flood extraction from ALOS/PALSAR in Okazaki City.....	123
5.4.4. Flood extraction from ALOS/PALSAR and flood vulnerable area by AHP method in Okazaki City	125
5.5. Conclusions.....	126
 CHAPTER 6 CONCLUSIONS.....	 128
 ACKNOWLEDGEMENT	 131
 REFERENCES.....	 132

LIST OF FIGURES

Figure 1. 1	Outline of the dissertation.....	5
Figure 2. 1	The “traditional” disaster cycle and the role of the risk assessment	8
Figure 2. 2	Vulnerability factors. Adapted from ISDR: Living with Risk.....	9
Figure 2. 3	Key Spheres of the Concept of Vulnerability	10
Figure 2. 4	Conceptual Flowchart of Hazard, Vulnerable, and Risk Assessment	11
Figure 2. 5	Conceptual model of vulnerability (BBC conceptual framework)	12
Figure 2. 6	Energy interaction in the atmosphere and at the earth’s surface	14
Figure 2. 7	Different portion of the spectrum are of different relevance to earth observation both in the type of information that we can gather and the volume of geospatial data acquisition	15
Figure 2. 8	A remote sensor measures reflected or emitted energy and an active sensor has its own source of energy	16
Figure 2. 9	The advanced Land Observing Satellite [JAXA, 2003]	18
Figure 2. 10	Sentinel-2 10 m spatial resolution bands: B2 (490 nm), B3 (560 nm), B4 (665 nm) and B8 (842 nm).....	21
Figure 2. 11	GIS for Disaster Management and Terrorism.....	23
Figure 2. 12	The continuous rating scale use for the pairwise comparison of factor multi-criteria analysis	25
Figure 2. 13	Hierarchical structure used to value product attributes and levels.	25
Figure 2. 14	Confusion matrix and common performance metrics calculated from it	29
Figure 2. 15	Overview of study areas.....	31
Figure 3. 1	Study location: Kumamoto City	37
Figure 3. 2	(a) Location of Aichi Prefecture in Japan; (b) Location of Okazaki City in Aichi Prefecture; (c) Research area in the lowland area of Okazaki City.....	38
Figure 3. 3	Proposed flowchart for simple superimposed method.....	41
Figure 3. 4	Proposed flowchart for AHP method.....	42
Figure 3. 5	Vegetation Index map of Shirakawa watershed.....	44
Figure 3. 6	Land cover map of Shirakawa watershed	45
Figure 3. 7	The Shirakawa watershed and research boundary map	46
Figure 3. 8	Slope map of Shirakawa watershed	47
Figure 3. 9	Rainfall map of Shirakawa watershed	49
Figure 3. 10	Rainfall distribution map of Okazaki City.....	51

Figure 3. 11	Drainage map of Okazaki City	53
Figure 3. 12	Slope map of Okazaki City	54
Figure 3. 13	Soil map of Okazaki City.....	56
Figure 3. 14	Land cover map of Okazaki City	58
Figure 3. 15	Flood vulnerability of Shirakawa watershed	61
Figure 3. 16	Flood vulnerability of Okazaki City according to the Simple Superimposed Method	63
Figure 3. 17	Relative operating characteristic curve for flood vulnerability in Okazaki City by using Simple superimposed method.....	65
Figure 3. 18	Vulnerable to flood area in the lowland of Okazaki City, the field survey of flood inundation in August 2008 and the sampling area for accuracy assessment.	69
Figure 3. 19	Relative operating characteristic curve for flood vulnerability in Okazaki City by using AHP procedure.	70
Figure 3. 20	Building on vulnerable to flooding area in Okazaki City	71
Figure 4. 1	Research flow chart.....	78
Figure 4. 2	Research location in Aichi Prefecture for ALOS/PALSAR and Ibaraki Prefecture for ALOS-2/PALSAR-2. Aichi Prefecture has 2 locations of flooded areas of which location 1 is shallow flood inundation (left), and location 2 is deep flood inundation (right).....	80
Figure 4. 3	Example of unclear delineation filter (a) Sobel filter 3x3, (b) Robert filter 3x3	87
Figure 4. 4	(a) Google Earth imagery, (b) Original image.....	92
Figure 4. 5	(a) Low Pass 3x3, (b) Low Pass 7x7, (c) Median 3x3, (d) Median 7x7, (e) Gamma 3x3, (f) Gamma 7x7 (g) Local Sigma 3x3, (h) Local Sigma 7x7	93
Figure 4. 6	Double filter performance from ALOS/PALSAR; (a) Median_Low Pass, (b) Local Sigma_Low Pass, (c) Local Sigma_Enhanced Lee, (d) Local Sigma_Enhanced Frost.....	94
Figure 4. 7	Single filter for ALOS-2/PALSAR-2 image (a) Google Earth image, (b) Original image (no filter), (c) Low Pass 3x3, (d) Gaussian Low Pass 3x3, (e) Gamma 3x3, (f) Local Sigma 3x3 (red circle: identified the speckle, red square: identified the edge and object).....	96
Figure 4. 8	Double Single Performance on ALOS-2/PALSAR-2 (a) Google Earth image (b) Original image (no filter) (c) Median_Low Pass, (d) Median_Enhanced Frost, (e) Local Sigma_Low Pass, (f) Local Sigma_Enhanced Frost.....	97

Figure 4. 9	Detected flooded area by using No-filter, Single filter and Double filter for shallow inundation area (a, b and c) and deep inundation area (d, e and f). Shadow area is accumulated inundation area during the flood period.....	101
Figure 4. 10	Single filter (left) and Double filter (right) visual performance comparing to the no-filter image and Google Earth image	103
Figure 5. 1	Study area.....	110
Figure 5. 2	Flowchart of proposed methods.....	113
Figure 5. 3	(a) Kinugawa River condition before collapse (May 6th, 2008) and (b) after collapse (September 11th, 2015). The image was orthorectified by Geospatial Information Authority of Japan (GSI). (c) Google Earth image (October 9th, 2015).....	118
Figure 5. 4	(a) Aerial photography by GSI; (b) Pre-and post-disaster RGB (before-after-after)	119
Figure 5. 5	Estimation of flooded area by using methods; (a) Unsupervised classification, (b) Supervised classification and (c) Binary/Backscattering threshold.	121
Figure 5. 6	(a) Slope map, (b) Land use classification of pre-disaster image by supervised classification, (c) Building area in Pre-and post-disaster RGB (before-after-after), (d) Building area in Aerial photography	123
Figure 5. 7	Building histogram of building from Pre- and Post-disaster images.....	124
Figure 5. 8	Flood extraction by binarization method from ALOS/PALSAR image in Okazaki City.....	124
Figure 5. 9	Flood vulnerable area by AHP method and flood extraction method from ALOS/PALSAR during flood in 2008 in Okazaki Prefecture.	125

LIST OF TABLES

Table 2. 1	ALOS main characteristics [JAXA, 2003]	17
Table 2. 2	AVNIR-2 Characteristics [JAXA, 2003]	19
Table 2. 3	PALSAR Specification [JAXA, 2003].....	19
Table 2. 4	ALOS-2 main SpecificationALOS-2 main Specification [JAXA, 2003]	20
Table 2. 5	Value of CF and A for ALOS/PALSAR (JAXA, 2003)	22
Table 2. 6	List of satellite images.....	30
Table 2. 7	The extremes meteorological of Okazaki City [Weblio, 2016]	32
Table 3. 1	Flood event related to the weather (Okazaki, 2015).....	39
Table 3. 2	Total Area of vegetation index in Shirakawa watershed	43
Table 3. 3	Land-use/land-cover classification scheme by land-use cover types stratified according to the U.S. Geological Survey’s land use and land cover classification system for use with remote sensor data (Anderson, et al., 1976)	44
Table 3. 4	Total area of land cover in Shirakawa watershed.....	45
Table 3. 5	Drainage density of Shirakawa subwatershed	46
Table 3. 6	Total of slope degree in Shirakawa watershed	47
Table 3. 7	Total area of rainfall distribution in Shirakawa watershed	48
Table 3. 8	Watershed characteristic as flood/run-off parameters (Ven T. Chow, with modification)	49
Table 3. 9	Rainfall classification Japan Meteorology Agency (JMA)	51
Table 3. 10	Slope classification [Haynes, 1998].	53
Table 3. 11	Japanese system of soil groups (Amano, 1985)	55
Table 3. 12	Soil infiltration rate based on % Slope (USDA, 1990)	57
Table 3. 13	Nine-point pairwise comparison scale (Saaty, 1987; Saaty, 2008).....	59
Table 3. 14	Total area of flood vulnerability in Shirakawa watershed.....	61
Table 3. 15	Flood parameters for simple superimposed in Okazaki City	62
Table 3. 16	The contingency table.....	64
Table 3. 17	Ranking of flood vulnerability parameters	67
Table 3. 18	Weighted comparison table	67
Table 3. 19	Consistency of pair comparison	67
Table 3. 20	Weighted flood hazard ranking	68
Table 4. 1	List of the filtered image	79
Table 4. 2	List of data used for filtering analysis	80

Table 4.3	Signal performance of filtered images	88
Table 4.4	Enhancing performance (edge preserving) of filtered images	89
Table 4.5	Enhancing performance (detail preserving) of filtered images	90
Table 4.6	The summary of the best quantitative performance	91
Table 5.1	Specification ALOS/PALSAR and ALOS-2/PALSAR-2 images for this study	111
Table 5.2	Value of CF and A for ALOS-2/PALSAR-2	114
Table 5.3	Accuracy assessment of flood extraction approaches	121

CHAPTER 1

INTRODUCTION

1.1. Background

A disaster occurs when a significant number of vulnerable people experience a hazard and suffer severe damage and disruption of their livelihood system in such a way that recovery is unlikely without external aid (Wisner, et al., 2003). One of frequently occurring disaster is flood. The majority (90%) of disasters between the periods of 1995-2015 are weather-related, wherein 47% are associated with flooding. Disasters have become intense and frequent affecting 2.3 billion people wherein 95% resides in Asia (Guha-Sapir & Wahlstrom, 2015).

Normal floods are presumed and occurred in many places in the world as they present rich soil, water and transportation method. However, flash flooding at unpredictable scale (damaging scale) and with extreme frequency effects loss to life, livelihoods, and the environment damage. Over the past decades, the pattern of floods beyond all continents has been increasing, becoming more regular, strong and unpredictable for local societies, especially as issues of development and poverty have pointed more people to live in the area of vulnerable to flooding. The Fourth Assessment Report (2007) of the Intergovernmental Panel on Climate Change (IPCC) predicts that 'heavy precipitation phenomenon, which is very likely to increase in frequency, will augment flood risk' [IPCC, 2007]. These floods will influence life and livelihoods in human settlements in all regions, e.g., coastal zones, river deltas, and mountains. Usually, flooding is also rising in urban areas, generating severe dilemmas for the low level of economic communities. Floods due to nature are complicated issues caused by a range of community's vulnerabilities, improper development planning, and climate variability. Floods can be forecasted to a reasonable coverage, with the elimination of flash floods, whose scale and nature are often less certain [ADPC & UNDP, 2005]. The causes of the hazard require being understood for it to be properly addressed [IPCC, 2007]. It is the result of interactions between natural processes as well as human activity as mentioned below:

- a. Meteorological: most flood losses are the result of extreme, intense and long-term floods due to the meteorological phenomena for example prolonged and intense rainfall, cyclones, typhoons, storms and tidal surges, hydrological. Flooding can also be affected by increased run-off. The ice or snow melt, impermeable surfaces, saturated land, poor infiltration rates, land erosion, anthropogenic can increase the run-off.

- b.** Floods are also impacted by both natural and human activities such as: increasing the population, land-use, land deforestation, intensive agriculture, unplanned flood control measures, socio-economic development activities, urbanization and climate change.

Japan is particularly vulnerable to flooding since its steep geography and a humid climate characterized by torrential rains and typhoons (Kazama , et al., 2009). Approximately 50 % of the total population in Japan and approximately 75% of its assets are located in flood vulnerable areas (ICHARM, 2005). The vulnerable area dominated in the alluvial plains (Tockner, et al., 2008). The number of floods, enhanced the damage due to flooding, have increased since 2004 (Kazama , et al., 2009). Several local heavy rainfalls in Japan have been documented by Japan Meteorological Agency (JMA) [JMA, 2016] e.g. in recent year (3rd July 2006 in Kumamoto; 11-17 July 2007 in Kagoshima, Miyazaki, Kumamoto; 30th August 2008 in Aichi Prefecture and around Chubu region; 10th September 2015 in Ibaraki Prefecture and around Kanto region). All of these heavy rainfalls created local floods and damage, leading to significant economic losses (Tezuka, et al., 2013).

Vulnerability maps are most frequently designed with the support of computer technology as known as Geographic Information Systems (GIS), and digital land survey devices designed for use in the field. However, vulnerability maps can also be generated manually by a background of printed maps, for example, satellite imagery, land use maps, road maps, river map or topographic maps.

Vulnerability maps can utilize in all phases of disaster management: prevention, mitigation, preparedness, operations, relief, and reconstruction and lessons-learned. In the prevention plane, planners can apply vulnerability maps to avoid high-risk zones when expanding areas for residence, commercial or industrial park. Technical experts can warn on areas where the infrastructure can be influenced in the case of a disaster.

In the field of disaster mitigation, in particular, remote sensing can help to analyse areas that are prone to natural and man-made hazards and potential damages. Risk and vulnerability assessments are important parts of disaster management and can be supported by remote sensing for pre-disaster analyses. Regarding to flood risk and vulnerability assessment and modelling, remote sensing techniques have been used in damage assessment and rapid mapping to support the emergency response phase immediately after a disaster has occurred. Remote sensing also gives contributions to vulnerability and risk assessment in the pre-disaster phase by deriving relevant information such as land use, settlement areas and buildings, elevation, etc. and monitoring of reconstruction and rebuilding in the post-disaster phase. In general, there are two main goals using

remote sensing data for analysing damage: rapid mapping assessment (Belward, et al., 2007) and mapping the affected hazard impact zone (McAdoo, et al., 2007) .

Sentinel Asia is international collaboration in Asia Pacific region to respond the natural disasters. Sentinel Asia provides the satellite images and it is available to access the disaster information after disaster occurring immediately. Occurrences of such extreme flood events necessitate rapid response to evaluate disaster impacts, plan of relief and rescue efforts as part of disaster management practices. The rapid response mapping using satellite remote sensing technology is widely used, increasingly preferred an alternative option for emergency assessment and operation of flood disaster management efforts. Flood maps derived from remote sensing observation platforms play central role in aiding rapid response emergency operations and long-term flood hazard assessment (Brivio, et al., 2002). Hence, the rapid mapping assessment is important related to the flood extended mapping.

By analysing the difference image before and after disaster the flooded can be detected. Remote sensing is a helpful tool to detect change because of the satellite repeatedly visiting the same area after short intervals of time and with consistent spatial resolution while utilizing the same sensor (Singh, 1989). Some studies have been done using remote sensing to detect the land change [Rawat & Kumar, 2015; Hegazy & Kaloop, 2015; Butt, et al., 2015; Alqurashi & Kumar, 2013]. The application of remote sensing in disaster management is widespread (Martino, et al., 2009; Schumann, 2015; Wiesmann, et al., 2001).

Synthetic Aperture Radar (SAR) image is powerful to observe the flood area during flood occurring because during the rainy season the panchromatic wavelength is difficult to obtain the clear images. Nevertheless, SAR images have some limitations for example speckle. Speckle has a big impact and leads to misclassification when classification depends on the pixel-based classification. The previous researchers have generally found that when pixel-based methods are applied to high-resolution images the speckles noise produces that contributes to the inaccuracy of the classification. [Campagnolo & Cerdeira, 2007]; [De Jong, et al., 2001]; [Van de Voorde, et al., 2004]. Speckle refers to a noise-like characteristic produced by coherent systems such as SAR and Laser systems (note: Sun's radiation is not coherent). It is evident as a random structure of picture elements (pixels) caused by the interference of electromagnetic waves scattered from surfaces or objects. When illuminated by SAR, each target contributes backscatter energy which, along with phase and power changes, is then coherently summed for all scatters, so called random-walk. This summation can be either high or low, depending on constructive or destructive interference. This statistical fluctuation (variance), or uncertainty, is associated with the brightness of each pixel in

SAR imagery. Filtering is one method to reduce the speckle. A speckle filtering is, therefore, a compromise between speckle removal (radiometric resolution) and thin details preservation (spatial resolution) (SARMap, 2009)

According to recent condition on flood study by using satellite data to extract the flood area and predicting vulnerable area to be flooded, some problems were found as follows:

1. The number of floods, enhanced the damage due to flooding, have increased since 2004. Thus, the flood-vulnerable area and its impact to human and financial condition increased.
2. The speckle noise appears as salts and papers on a surface of SAR image that leads the miss classification and difficult to detect flood in shallow inundation area. Thus, we need to reduce the speckle noise to improve the edge detection of flood, especially in the shallow area.
3. It was possible to obtain the satellite images from ALOS-2/PALSAR-2 immediately after the flood occurring. Hence, we need the rapid response to extract the flood inundation area by utilizing the ALOS-2/PALSAR-2.

1.2. Research Scope and Objective

This research was conducted to use ALOS/PALSAR and ALOS-2/PALSAR-2 data to detect and identify the flood area. SAR images that have L band with ~23 cm wavelength possible to penetrate the cloud and water vapour [JAXA, 2016].

The objectives of this research are:

1. To reduce the impact of flood by identifying the area of vulnerable to flood in Kumamoto City, Kumamoto Prefecture and Okazaki City, Aichi Prefecture.
2. To propose a new method to reduce the speckle noise on ALOS/PALSAR and ALOS-2/PALSAR-2 images by Double filter method which is a new method the author proposed. Hence, the flood edge detection will be easier.
3. To evaluate the methods of extracting the flash flood area by utilizing ALOS-2/PALSAR-2 images as a rapid response to the disaster.
4. To evaluate the model of flood vulnerability by multi-parameters and flood detection from ALOS/PALSAR in Okazaki City, Ibaraki Prefecture.

1.3. Research Outline

This research theme is divided into three sub-themes. The first part is predicting the vulnerable area to flood by utilizing the satellite data and GIS method. The second part is processing data to

reduce the noise on SAR images and explained the flood extraction method by using SAR image. The third part is combining the first and second part and evaluating the model. Fig. 1.1 describes the outline of the dissertation. The dissertation is constructed by six chapters, as follows:

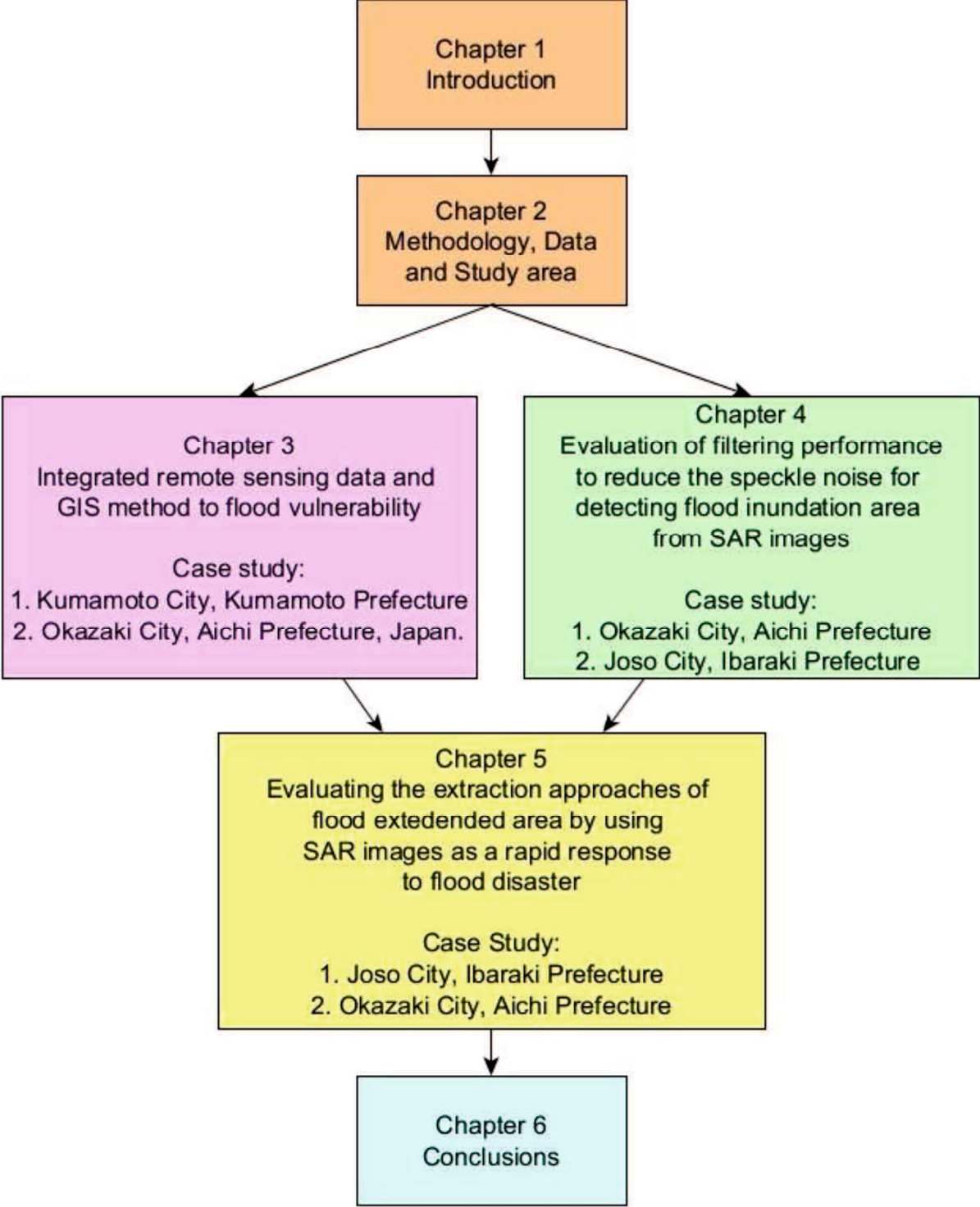


Figure 1. 1 Outline of the dissertation

Chapter 1

This chapter phrases the introduction of the research. The chapter discusses the general introduction and basic motivation of this study. The research problem and research scope are listed, and research objectives are given.

Chapter 2

This chapter discusses the disaster management and vulnerability, data that used in this research and research methodology. The technical procedures are explained in this section.

Chapter 3

Chapter 3 describes the method to reduce the impact of flood by predicting the flood-vulnerable area. The result displayed the vulnerable to flood area by utilizing two methods, i.e., simply superimposed method and Analytical Hierarchy Process (AHP). The research areas were in Shirakawa watershed in Kumamoto Prefecture and Okazaki City in Aichi Prefecture.

Chapter 4

Chapter 4 describes the best filter to reduce the speckle noise from SAR images. The result of this chapter shows the effectiveness of the Single filter and Double filter on ALOS/PALSAR and ALOS-2/PALSAR-2 image to reduce the speckle noise and to detect edge of flood in the shallow and deep inundation areas. The research locations are in Okazaki City, Aichi Prefecture and Joso City, Ibaraki Prefecture.

Chapter 5

Chapter 5 describes the effective method to extract the flood from SAR images. This chapter compared three methods i.e., unsupervised classification, supervised classification and binarization method to extract the flood by utilized SAR images. The research location is in Joso City in Ibaraki Prefecture and utilizes ALOS-2/PALSAR-2 images. The best method is applied to ALOS/PALSAR images in Okazaki City, Aichi Prefecture. Chapter 5 also superimpose the method from Chapter 3 to predict the flood vulnerability by AHP and extract flood extraction from ALOS/PALSAR images to evaluate the effectivity of predicting and extracting method.

Chapter 6

Chapter 6 presents the conclusions and the future works of the research.

CHAPTER 2

METHODOLOGY, DATA AND STUDY AREA

This chapter explains about Disaster management and vulnerability, supporting methodology and satellite data, and study areas.

2.1. Disaster Management and Vulnerability

2.1.1. Disaster Management

Disaster management should consist of an organized effort to mitigate against, prepare forecast, respond to, and recover from a disaster [UN-ISDR, 2004].

1. *Mitigation* relates to pre-activities that actually eliminate or reduce the chance or the effects of a disaster. Mitigation activities involve assessing the risk and reducing the potential effects of disasters, as well as post-disaster activities to reduce the potential damage of future disasters. Examples of mitigation mechanisms include land-use regulations, engineering works, building codes and insurance programs.
2. *Preparedness* consists of planning how to respond in case an emergency or disaster occurs and working to increase the resources available to respond effectively. Preparedness covers contingency planning, resource management, mutual aid and cooperative agreements with other jurisdictions and response agencies, public information, and the training of response personnel.
3. *Response* refers to activities that occur during and immediately following a disaster. They are designed to provide emergency assistance to victims of the event and reduce the likelihood of secondary damage. Response activities include search and rescue, evacuation, emergency medical services and fire-fighting, as well as reducing the likelihood of secondary effects, for example to the contents of damaged buildings. Local government officials, as well as the community itself, constitute the "first responders" and therefore have to handle disasters for hours or even days before state and foreign resources arrive on the scene.
4. *Recovery* constitutes the final phase of the disaster management cycle. Recovery continues until all systems return to normal or near normal. Long-term recovery from a disaster may go on for years until the entire disaster area is either completely restored or redeveloped for entirely new purposes that are less disaster-prone. Recovery activities encompass temporary

housing, restoration of basic services (e.g. water, electricity), food and clothing, debris clearance, psychological counselling, job assistance, and loans to restart small businesses.

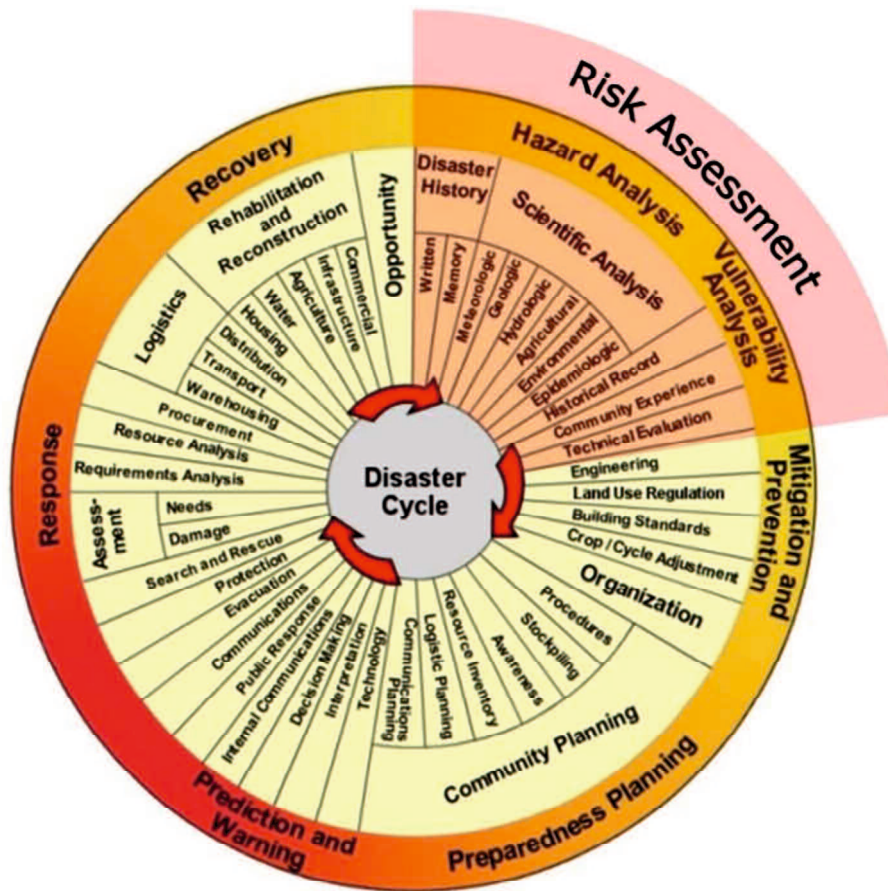


Figure 2. 1 The “traditional” disaster cycle and the role of the risk assessment [UN-ISDR, 2005]

A general strategy for disaster risk reduction must firstly establish the risk management context and criteria, and characterize the potential threats to a community and its environment (hazard); secondly it should analyse the social and physical vulnerability and determine the potential risks from several hazardous scenarios in order to, finally, implement measures to reduce them (see Fig. 2.1). The final goal, reduction of disaster risk in the present and control of future disaster risk, should be achieved by combining structural and non-structural measures that foster risk management as an integrating concept and practice which are relevant and implemented during all stages of a community’s development process and not just as a post-disaster response. Disaster risk management requires deep understanding of the root causes and underlying factors that lead to disasters in order to arrive at solutions that are practical, appropriate and sustainable for the community at risk [UN-ISDR, 2005].

2.1.2. Vulnerability: A definition

The vulnerability is defined as the set of conditions and processes resulting from physical, social, economic, and environmental factors, which increase the susceptibility of a community to the impact of hazards as shown in Fig. 2.2. The physical factors encompass susceptibilities of the built environment. The social factors are related to social issues such as levels of literacy, educations, the existence of peace and security, access to human rights, social equity, traditional values, beliefs, and organizational systems. In contrast, economic factors are related to issues of poverty, gender, level of debt and access to credits. Finally, environmental factors include natural resource depletion and degradation. In addition, it is important to recognize the existence of a “natural” vulnerability towards climate change; coastal zones, e.g., are generally highly vulnerable against sea-level rise or storm surges because of their exposure. In relation to coping capacity, the disaster community introduces this concept as part of the measures included within disaster-risk reduction. Coping capacity is conceived as the means by which people or organizations use available resources and abilities to face adverse consequences that could lead to a disaster [UN-ISDR, 2004]. In general, this involves managing resources, both in normal times as well as during crises or adverse conditions. The strengthening of coping capacities usually builds resilience to withstand the effects of natural and human-induced hazards.

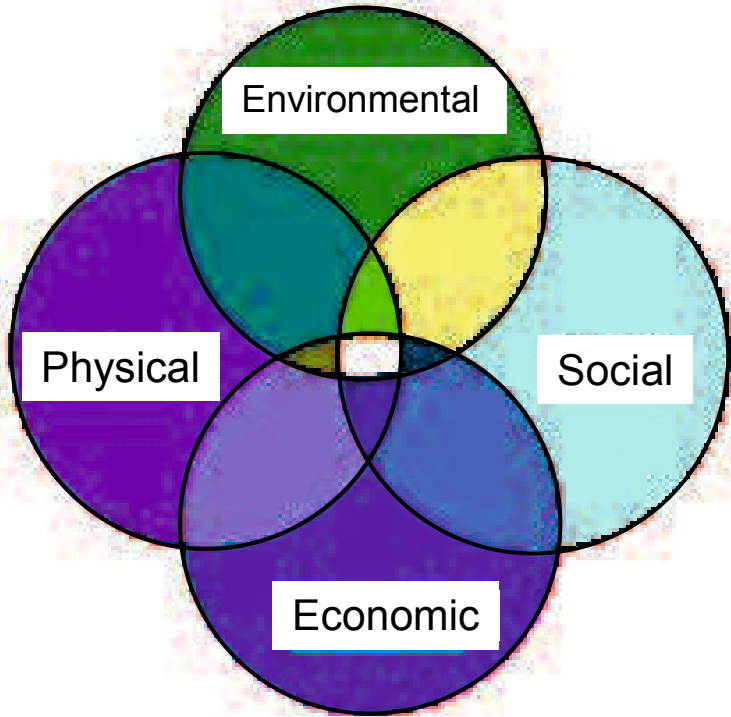


Figure 2. 2 Vulnerability factors. Adapted from ISDR: Living with Risk. [UN-ISDR, 2004]

Multiple definitions and different conceptual frameworks of vulnerability exist, because several distinct groups have different views on vulnerability as shown in Fig. 2.3. Academic staff from different disciplines, Disaster management agencies, development corporations, climatic change organization etc. The first definition is still related only to physical vulnerability while in the other definitions we find that vulnerability is influenced by several factors, mostly mentioned are physical, economic, social and environmental factors [UN-ISDR, 2004].

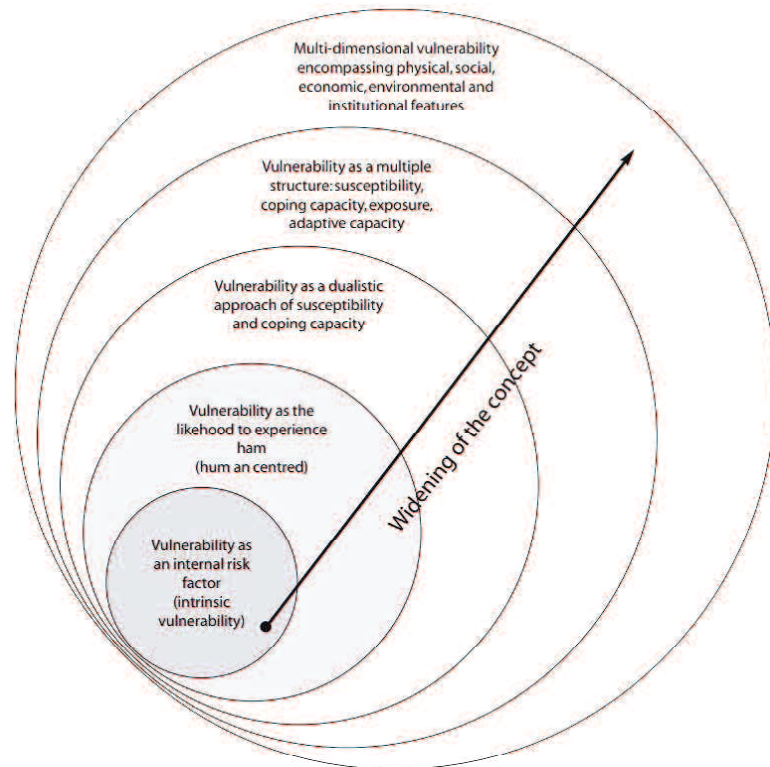


Figure 2.3 Key Spheres of the Concept of Vulnerability [Birkmann & Wisner, 2006]

Some definitions of vulnerability:

1. “The degree of loss to a given element at risk or set of elements at risk resulting from the occurrence of a natural phenomenon of a given magnitude and expressed on a scale from 0 (no damage) to 1 (total damage)” [UNDRO, 1991].
2. “The conditions determined by physical, social, economic and environmental factors or processes, which increase the susceptibility of a community to the impact of hazards (UN/ISDR, 1994).
3. “The characteristics of a person or group in terms of their capacity to anticipate, cope with, resist and recover from impacts of a hazard” [Wisner, et al., 2003]

4. “A human condition or process resulting from physical, social, economic and environmental factors, which determine the likelihood and scale of damage from the impact of a given hazard” [UNDP, 2004].
5. “The intrinsic and dynamic feature of an element at risk that determines the expected damage/harm resulting from a given hazardous event and is often even affected by the harmful event itself. Vulnerability changes continuously over time and is driven by physical, social, economic and environmental factors” [Villagrán De León, 2006].
6. “Vulnerability is the degree to which a system is susceptible to, and unable to cope with, adverse effects of climate change, including climate variability and extremes. The vulnerability is a function of the character, magnitude, and rate of climate change and variation to which a system is exposed, its sensitivity, and its adaptive capacity” [IPCC, 2007].

2.1.3. Vulnerability: Conceptual framework

The following United Nations definitions are provided and a summary is made regarding the disciplines concerned as displays in Fig. 2.4. [UNDRO, 1991]

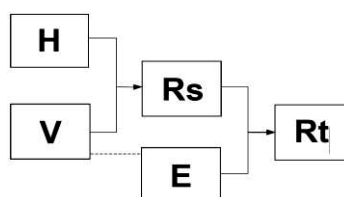


Figure 2. 4 Conceptual Flowchart of Hazard, Vulnerable, and Risk Assessment [UNDRO, 1991]

- *Natural hazard (H)* determination involves the estimation of the probability of occurrence (within a specific period of time in a given area) of a potentially damaging natural phenomenon. The disciplines concerned are earth and atmospheric sciences.
- *Vulnerability (V)* determination involves the estimation of the degree of loss suffered by a given element at risk or a set of such elements, resulting from the occurrence of a natural phenomenon of a given magnitude and expressed on a scale from 0 (no damage) to 1 (total damage). The disciplines concerned are human geography, construction engineering, etc.
- *Specific risk (Rs)* determination involves the estimation of the expected degree of loss due to a particular natural phenomenon and as a function of both natural hazard and vulnerability ($R_s=H*V$). The disciplines concerned are human geography, construction engineering, etc.

- *The elements at risk (E)* include the population, buildings, civil engineering works, economic activities, public services, utilities and infrastructure, etc., at risk in a given area.
- *Risk (Rt)* determination involves the estimation of the expected damage or loss of property and human lives and the disruption of economic activity due to a particular natural phenomenon ($R_t = R_s * E$). The disciplines concerned are urban planning, urban and human geography, and economy.

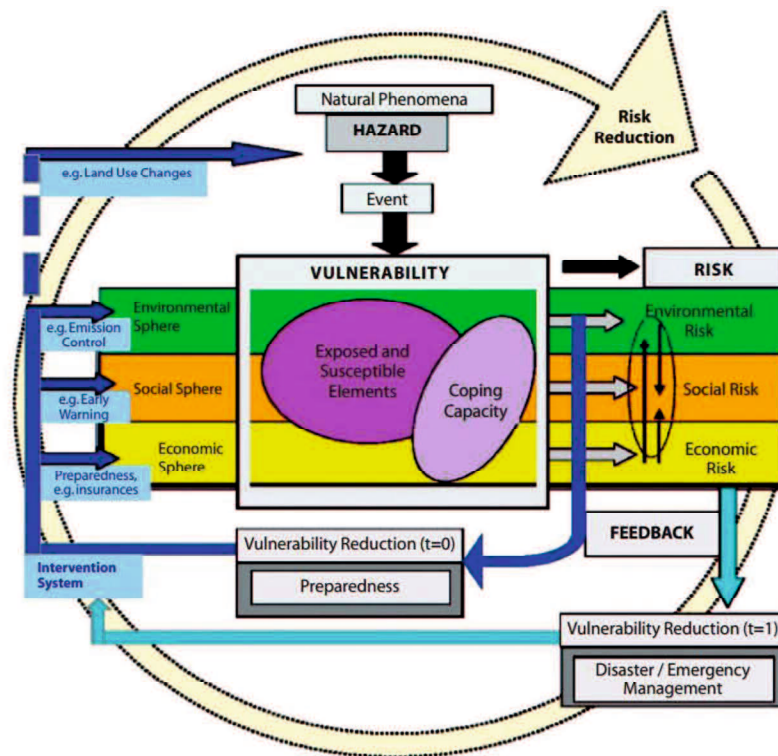


Figure 2. 5 Conceptual model of vulnerability (BBC conceptual framework) [Birkmann, 2005].

Another model regarding risks and vulnerabilities has been developed by [Birkmann, 2005] at The United Nations University-Institute for Environment and Human Security (UNU-EHS). The three types of vulnerabilities presented in the model: economic, social, and environmental, are influenced by both exposure and coping capacities, as can be seen in Fig. 2.5. The primary focus on social, economic and environmental issues represents the close link of the model to the debate of sustainable development. This BBC model views vulnerability within a feedback loop system and by that stressing the fact that vulnerability analysis goes beyond the estimation of deficiencies and the probability of loss. It shows the need to focus simultaneously on vulnerabilities, existing coping capacities as well as on potential actuation tools to reduce the vulnerabilities related to the three key thematic areas, the social, the economic and the environmental sphere. In this context the model promotes a proactive understanding of vulnerability, that means it underlines the

necessity to set up activities to reduce vulnerabilities before an event strikes the society, the economy or the environment ($t=0$). The primary focus on social, economic and environmental issues represents the close link to the debate of sustainable development. The underlying understanding of the vulnerability of the socio-economic system (anthroposphere) on the one hand and the environmental vulnerabilities on the other hand as well as assessing them simultaneously shows a close link to the debate of vulnerability within the climate change community. The environmental change and the sustainable development community stressing the fact that human interactions have to be viewed within the environmental context that means a key focus of these schools are human-environmental interactions.

2.1.4. Vulnerability Mapping

A vulnerability map gives the precise location of sites where people, the natural environment or property are at risk due to a potentially catastrophic event that could result in death, injury, pollution or other destruction. Such maps are made in conjunction with information about different types of risks, for example, a vulnerability map can show the housing areas that are vulnerable to a chemical spill at a nearby factory. But it just as likely, could delineate the commercial, tourist, and residential zones that would be damaged in case of a 100-year flood or, more devastation, a tsunami

Vulnerability maps are most often created with the assistance of computer technology called GIS and digital land survey equipment designed for use in the field. However, vulnerability maps can also be created manually using background maps such as satellite imagery, property boundaries, road maps, or topographic maps. In such cases the municipality's planning office should be involved in order to take advantage of the base maps that have already been made for other purposes.

Vulnerability maps can be of use in all phases of disaster management: prevention, preparedness, mitigation, operations, relief, recovery and lessons-learned. In the prevention stage planners can use vulnerability maps to avoid high-risk zones when developing areas for housing, commercial or industrial use. Technical experts can alert about places where the infrastructure can be affected in case of a disaster. Fire departments can plan for rescues before a potentially dangerous event is at hand. During an exercise where a predetermined scenario takes place, the rescue crews may use the map to determine where to respond first to save human lives, the environment or property. They can also be used to evacuation routes to test the effectiveness of these routes for saving large numbers of residents and tourists and moving special groups such as

senior citizens, children and those with handicaps. The operation officers can update about the disaster situation and the need for and the location of sensitive areas.

2.2. Methodology

Remote sensing and Geography Information Systems (GIS) are broadly developed in order to environmental analysis.

2.2.1. Remote Sensing

"Remote sensing is the science or art of obtaining information about the Earth's surface without directly being in contact with it. This is accomplished by sensing and recording reflected or emitted energy and processing, analysing, and applying that information." (Canada Center for Remote Sensing, 2016). The energy interaction in the atmosphere is explained in Fig. 2.6.

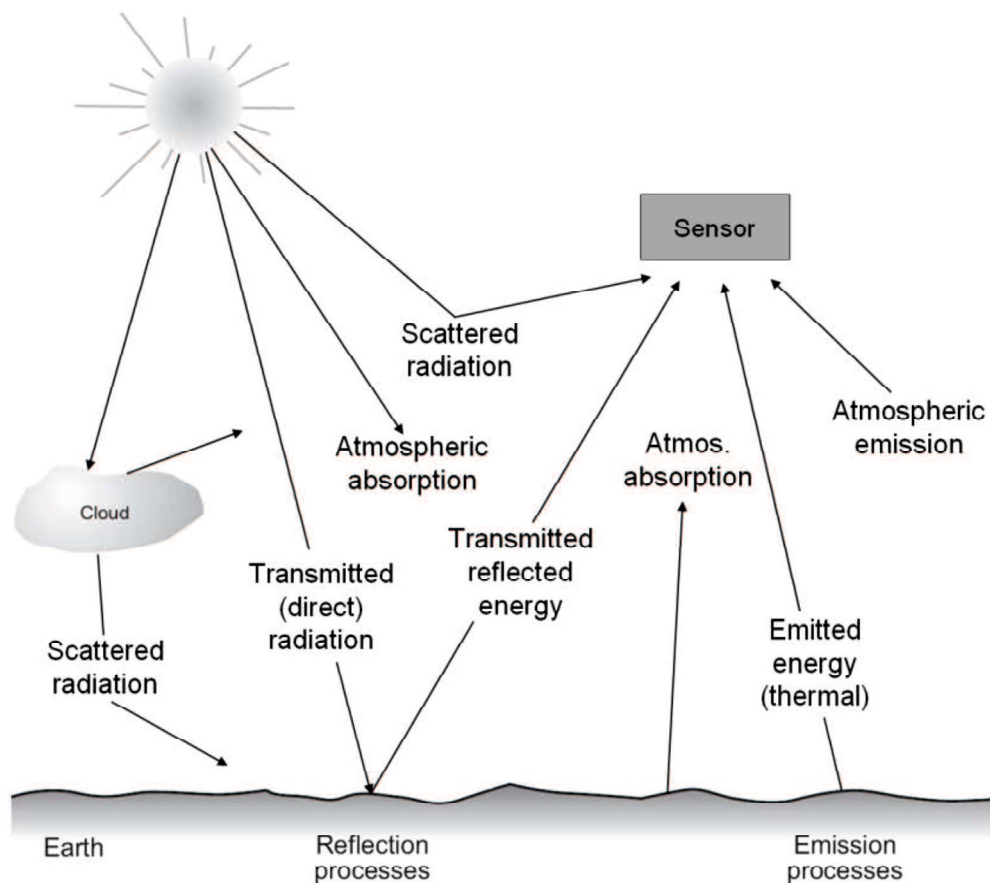


Figure 2. 6 Energy interaction in the atmosphere and at the earth's surface [Tempfli, et al., 2009]

Remote sensing is the science to get the information about the Earth's feature using instruments which are remote to the Earth's surface [Joseph, 2005]. To denote identification of earth features, the characteristic of electromagnetic radiation, which is reflected/emitted by the earth system is distinguished. A device to detect the electromagnetic radiation reflected or emitted from an object is called a sensor which is located on the platform (e.g., satellite, aircraft, etc.).

Before the sun's energy reaches the Earth's surface, three remote sensing relevant interaction in the atmosphere occur, i.e., absorption, transmission and scattering. The energy transmitted is then either absorbed by the surface material or reflected. The reflected energy also suffers from scattering and absorption in the atmosphere before reaching the remote sensor. (Tempfli, et al., 2009)

The electromagnetic spectrum (EM) ranges from the shorter wavelengths (including gamma and x-rays) to the longer wavelengths (including microwaves and broadcast radio waves) (Canada Center for Remote Sensing, 2016). The total range of wavelengths of the electromagnetic spectrum radiation is as known as EM spectrum. Fig. 2.7 illustrates the total spectrum of EM radiation. Gamma rays, X-rays, UV radiation, visible radiation (light), infrared (IR) radiation, microwaves and radio waves are the different portion of the spectrum. Each of these named portions denotes a range of wavelengths, no one specific wavelength. The EM spectrum is continuous and does not have any clear-cut class boundaries.

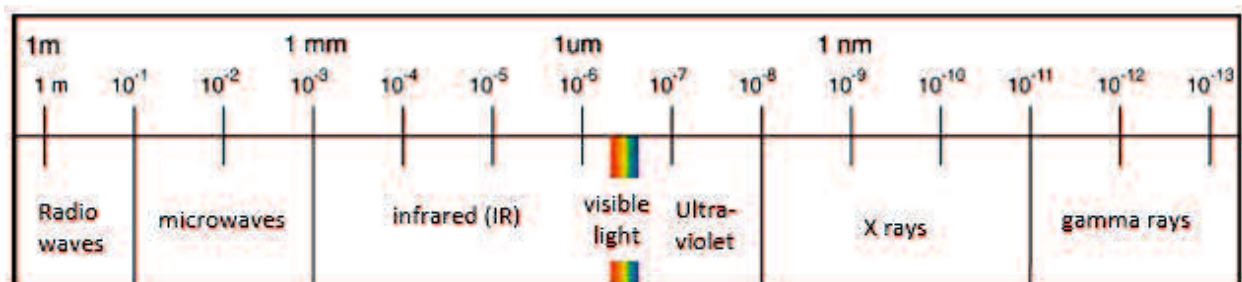


Figure 2. 7 Different portion of the spectrum are of different relevance to earth observation both in the type of information that we can gather and the volume of geospatial data acquisition [Tempfli, et al., 2009].

The sun contributes a very useful source of energy for remote sensing. The visible wavelengths of the sun energy are reflected, absorbed and re-emitted as same as thermal infrared wavelengths. Remote sensing systems which measure the energy that is commonly known as passive sensors. Passive sensors can be applied to detect energy when the naturally occurring

energy is possible. For all reflected energy, this can only occur when at time when the sun is lighting the Earth. There is no reflected energy possible from the sun at night. The energy that is originally emitted from the earth (such as thermal infrared) can be recognized day or night, as long as the quantity of energy is large adequate to be recorded.

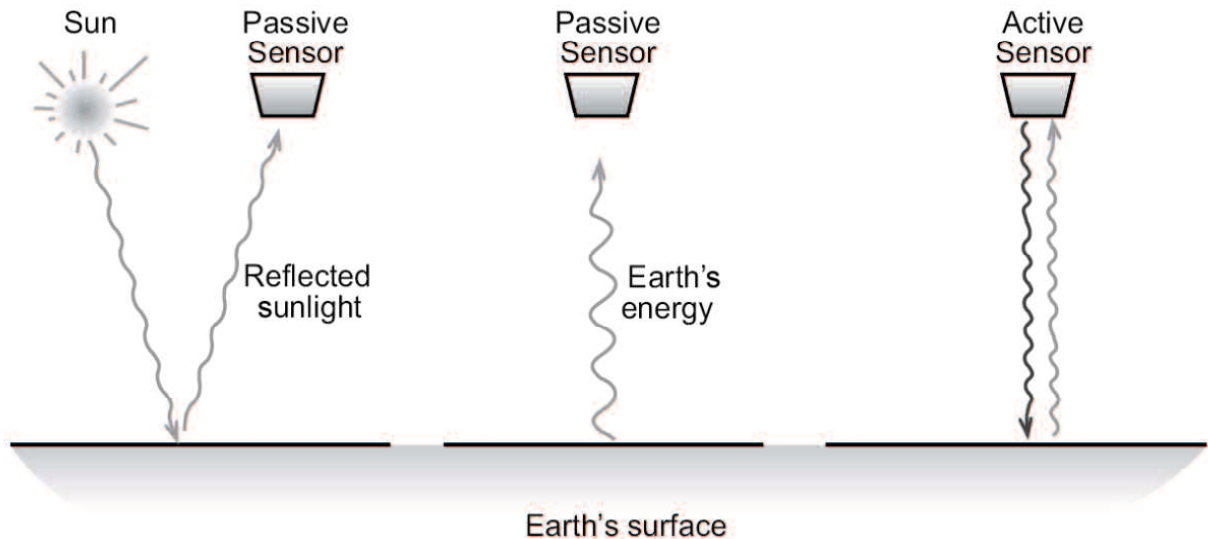


Figure 2. 8 A remote sensor measures reflected or emitted energy and an active sensor has its own source of energy [Tempfli, et al., 2009]

Active sensors provide their energy source for illumination. The active sensor emits radiation which is directed to the object to be examined. The radiation reflected from that object is detected and measured by the sensor. Advantages of active sensors are the capacity to obtain measurements anytime, despite the night time or bad weather. Active sensors can be employed for analysing wavelengths that are not adequately equipped by the sunlight, such as microwaves. However, active systems expect the generation of an equitably large of energy to sufficiently illuminate the object. [Canada Center for Remote Sensing, 2016]. The passive and active sensor can be seen as illustrate in Fig. 2.8.

The output of this technique can be an image/binary data which displays in the digital format. For some remote sensing apparatuses, the length between the target being captured and the platform, represents a substantial task in defining the detail of information obtained and the total area imaged by the sensor. The detail information of an image depends on the spatial resolution of the sensor and relates to the size of the smallest feasible feature that can be detected. Also, the

temporal resolution is also important for the satellite remote sensing system, which refers to the temporal of the satellite passes on the same territory.

Remote sensing advances the ability to observe and collect data for wide areas relatively quickly and is an important source of improving natural resources management, land use and protection of the environment.

2.2.1.1. Advanced Land Observing Satellite (ALOS)

Advanced Land Observing Satellite (ALOS) was utilized in this research. The ALOS system was launched by Japan Aerospace Exploration Agency (JAXA) on January 24th, 2006 (see Table 2.1).

Table 2. 1 ALOS main characteristics [JAXA, 2003]

Item		Specifications
Launch	Vehicle	H-IIA
	Date	January 24 th , 2006
	Site	Tanegashima Space Center
Orbit	Type	Sun-Synchronous Sub recurrent
	Local Time at DN	10:30 AM \pm 15min.
	Altitude	691.65km (above equator)
	Inclination	98.16 degree
	Orbital Period	98.7 min.
	Revolutions per day	14+27/46 rev./day
	Recurrent Period	46 days
Mission Instruments	Earth Observation	Panchromatic Remote-sensing Instrument for Stereo Mapping (PRISM) Advanced Visible and Near Infrared Radiometer type 2 (AVNIR-2) Phased Array type L-band Synthetic Aperture Radar (PALSAR)
	Other	Technical Data Acquisition Equipment (TEDA)
Mission Data Handling System	Data Compression	PRISM : 1/4.5, 1/9 (Non-Reversible compression) AVNIR-2 : 3/4 (Reversible compression)
	Multiplex Method	CCSDS Multiplex
	Data Recording and Reproducing	High Speed Solid State Recorder (HSSR) 1 set - Recording capacity: over 96GB -Recording speed: 360/240/120Mbps (selectable) -Reproducing speed: 240/120Mbps (selectable) Low Speed Solid State Recorder (LSSR) 1 set -Recording capacity: 1GB (0.5GB x 2 partitions) -Recording speed: 40kbps -Reproducing speed: 16Mbps

IOCS System	Ka band	Transmission: 26.1GHz Receiving: 23.540GHz Transmission rate (symbol rate / data rate): For DRTS 277.52Mpsps / 240Mbps
	S band	Transmission: 2220.00MHz Receiving: 2044.25MHz
Direct Transmission	X band	Frequency: 8105MHz Transmission rate (symbol rate / data rate): 138.76Mpsps / 120Mbps
	USB	Transmission: 2220.00MHz Receiving: 2044.25MHz

The ALOS has three remote sensed instruments the Panchromatic Remote-sensing instrument for Stereo Mapping (PRISM) for digital elevation mapping. Fig. 2.9 shows the ALOS components. PRISM is a panchromatic radiometer with 2.5m spatial resolution at nadir which has three independent optical system for viewing nadir, forward and backward producing a stereoscopic image along the satellite's track. Each telescope consists of three mirrors and several CCD detectors for push-broom scanning. The nadir-viewing telescope covers a width of 70km; forward and backward telescope cover 35 km each.

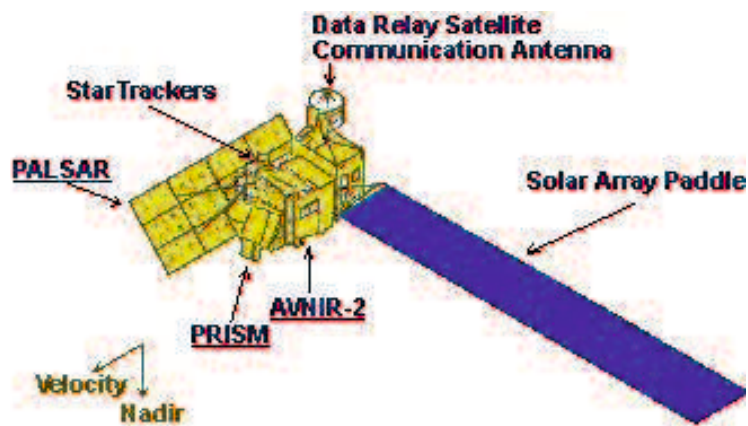


Figure 2. 9 The advanced Land Observing Satellite [JAXA, 2003]

AVNIR-2 (Table 2.2) is a visible and near infrared radiometer for monitoring land and coastal zones and provides better spatial land coverage maps and land-uses classification maps for monitoring the regional environment. The AVNIR-2 provides 10-meter spatial resolution images. The high resolution was realized by improving the CCD detectors.

Table 2. 2 AVNIR-2 Characteristics [JAXA, 2003]

Number of bands	4
Wavelength	Band 1 : 0.42 to 0.50 micrometers Band 2 : 0.52 to 0.60 micrometers Band 3 : 0.61 to 0.69 micrometers Band 4 : 0.76 to 0.89 micrometers
Spatial resolution	10 m (at nadir)
Swath width	70km (at Nadir)
S/N	>200
MTF	Band 1-3 : >0.25 and Band 4 : >0.20
Number of detectors	7000/band
Pointing Angle	-44 to + 44 degree
Bit length	8 bits

Note: AVNIR-2 cannot observe the areas beyond 88.4 degree north latitude and 88.5 degree south latitude.

The ALOS/PALSAR has 10m resolution (See Table 2.3). These satellite has L-band wavelength. It can be easy to detect a water surface because of its wavelength is L-band which can penetrate the canopy of vegetation (JAXA, 2016). To utilize fully the data obtained by these sensors, the ALOS was created with two advanced technology: the former is the high speed, and large ability mission data handling technology and the latter is the accuracy spacecraft position and attitude determination capability. They will be essential to high-resolution remote sensing satellites in next decade. AVNIR-2 is used for providing the input parameters in the multi-criteria analysis; land cover mapping, and the calculation of normalized difference vegetation, soil and water index, while PRISM is used in the pan-sharpening process.

Table 2. 3 PALSAR Specification [JAXA, 2003]

Item	Specifications
Centre frequency	1270 MHz / 23.6 cm
Chirp band width	28 MHz (single polarisation) 14 MHz (dual, quad-pol., ScanSAR)
Transmission power	2 kW (peak power)
Pulse Repetition Frequency	1500 – 2500 Hz (discrete stepping)
Image modes	Single polarization (HH or VV) Dual pol. (HH+HV or VV+VH) Quad-pol. (HH+HV+VH+VV) ScanSAR (HH or VV; 3/4/5-beam)
Bit quantisation	3 or 5 bits (5 bits standard)
Off-nadir angle	Variable: 9.9 – 50.8 deg. (inc. angle range: 7.9 - 60.0) ScanSAR: 20.1-36.5 (inc. 18.0-43.3)
Look direction	Right
Yaw steering	ON

Swath width	70 km (single/dual pol.@41.5°) 30 km (quad-pol.@21.5°) 350 km (ScanSAR 5-beam)
Ground resolution Rg (1 look) x Az (2 looks)	~ 9 m x 10 m (single pol.@41.5°) ~ 19 m x 10 m (dual pol.@41.5°) ~ 30 x 10 m (quad-pol.@21.5°) ~ 71-157m (4 look) x 100m (2 look) (ScanSAR 5-beam)
Data rates	240 Mbps (single/dual/quad-pol) 120 or 240 Mbps (ScanSAR)

2.2.1.2. Advanced Land Observing Satellite (ALOS-2/PALSAR-2) images

The ALOS-2 is the replacement of the ALOS, but the structure of the new satellite is quite different from its predecessor ALOS. By concentrating on one particular instrument, it can maximize its achievement to be greatly proper for its main mission of monitoring disasters regardless of day or night and weather situations. The potential of the radar, the PALSAR-2 of the ALOS-2, has been significantly enhanced from the ALOS's PALSAR in all features including resolution, observation band, and time lag for data provision. Besides, the satellite's fundamental capacity has been improved for carrying the radar achievement such as data transmission speed and high precision position retention with new technology. While the ALOS-2 is presented with the necessary capacity for speedy disaster monitoring, its improvement has also generated a quality of new technologies that can be applied for future satellite development. Detail information about ALOS-2/PALSAR-2 is listed in Table 2.4. (JAXA, 2016). It should be suitable for flood inundation areas detection in urban and rural area [Natsuaki, et al., 2016; Rosenqvist, et al., 2014]. In addition, PALSAR-2 also provides a number of data observation angles which can enhance the number of prospects and accuracy for flood observations [Honda, et al., 2016].

Table 2. 4 ALOS-2 main Specification ALOS-2 main Specification [JAXA, 2003]

Life	Designed life : 5 years, Target : 7 years
Launch date	May 24 th , 2014
Launch vehicle	H-II A24
Launch site	Tegnagashima Space Center, Japan
Altitude	628 km
Lap time	About 100 min
Revisit time	14 days
Spacecraft mass	Under 2,100 kg (including propellant)
Mission data transmission	Direct transmission and via data relay orbit
PALSAR-2 (frequenchy)	L band (1.2GHz)

2.2.1.3. Sentinel-2 image

The Sentinel-2 is a wide-swath, high-resolution, multi-spectral imaging mission, supporting Copernicus Land Monitoring studies, including the monitoring of vegetation, soil and water cover, as well as observation of inland waterways and coastal areas. The Sentinel-2 Multispectral Instrument (MSI) will sample 13 spectral bands; four bands at 10 meters, six bands at 20 meters and three bands at 60 meters spatial resolution [ESA, 2000] as shown in Fig. 2.10.

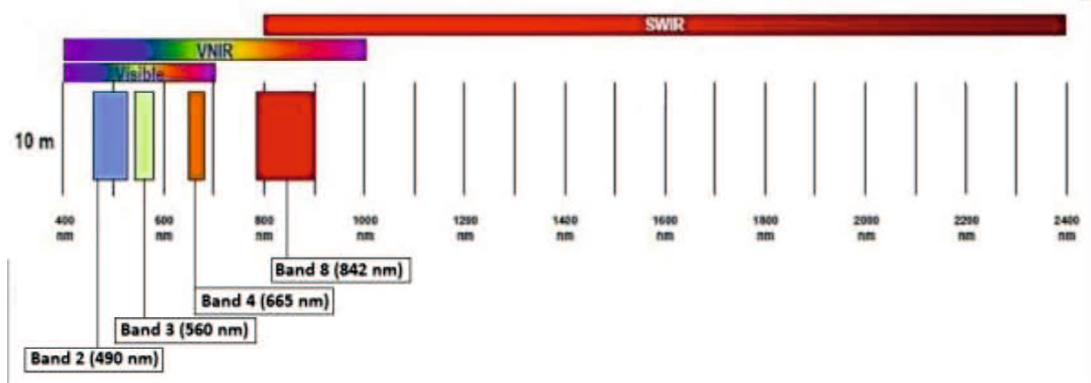


Figure 2. 10 Sentinel-2 10 m spatial resolution bands: B2 (490 nm), B3 (560 nm), B4 (665 nm) and B8 (842 nm) [ESA, 2000]

2.2.1.4. Pre-processing of ALOS/PALSAR and ALOS-2/PALSAR-2

Pixel values represent the radiance of the surface in the type of digital numbers (DNs), which are calibrated to adequate a convinced range of values. Sometimes the DNs are denoted as the brightness values. Transformation of DN values to absolute radiance values is an essential process for qualified analysis of several images acquired by diverse sensors. Because each sensor has its calibration parameters used in noting the DN values, the same DN values in two images recorded by two different sensors may denote two different radiance values [Chander, et al., 2009].

The first step of processing the ALOS/PALSAR data is converting from the DN to the backscattering coefficient (sigma-naught) σ^0 denote as dB; it can be done by the following equations (JAXA, 2016).

$$\sigma^0 = 10 \log_{10}(DN^2) + CF \quad (2.1)$$

where: σ^0 is backscattering coefficient; DN is a digital number; CF for ALOS/PALSAR and ALOS-2/PALSAR-2 are -83 as listed in Table 2.5 (JAXA, 2003). CF can be calculated by following Eq.2.2; where A_x is area of the compound and C_x is concentration of the compound.

$$CF = A_x / C_x \quad (2.2)$$

Table 2. 5 Value of CF and A for ALOS/PALSAR and ALOS-2/PALSAR-2 (JAXA, 2003)

CF	mean (dB)	std (dB)
CF ₁	-83.0	0.406
A	32.0	-

2.2.1.5. Image Classification in Remote Sensing

There are three famous methods to classify the image in remote sensing as explained below;

- *Unsupervised classification*: Pixels are classified based on the reflectance properties of pixels (as known as clusters). The user recognizes the number of groups to create and which bands to be applied. With this information, the image analysis software produces groups. There are several images classifying algorithms, for example, K-means (vector quantization) and the Iterative Self-Organizing Data Analysis Technique (ISODATA). The user manually distinguishes each group with land cover classifications. It's usually the case that double interprets for a single land cover classification. The user blends clusters into a land cover type. The unsupervised classification image classification method is used when no sample sites exist. Unsupervised step generates clusters and assigns classes (GISGeography, 2016).
- *Supervised classification*: The user decides representative training area for each land cover type in the digital image. The image analysis software utilizes the training sites to classify the land cover categories in the whole image. The analysis of land cover is according to the spectral value determined in the training area. The digital image analysis software defines each class on what it resembles most in the training area. The frequently used supervised classification algorithms are maximum likelihood and minimum distance classification. Supervised classification steps: select training areas, generate a signature file and classify (GISGeography, 2016; Eastman, 2001).
- *Object-based (object-oriented) image analysis classification*: This method is named multi-resolution segmentation. Multiresolution segmentation provides homogenous image objects by clustering pixels. Objects are produced with different scales in an image simultaneously. These objects are more meaningful than the traditional pixel-based segmentation since they can be ordered according to texture, context, and geometry. Object-based image method recommends the use of multiple wavelengths for multiresolution segmentation and class. For case, infrared, elevation or existing shape files can concurrently be utilized to analyze image objects. Multiple bands can have context with each other. This context comes in the form of neighborhood relationships, proximity and distance between layers (GISGeography, 2016; Eastman, 2001).

2.2.2. Geography Information System (GIS)

GIS is a computer-based system that presents the following four sets of capabilities to handle georeferenced data: data capture and preparation, data management, including storage and maintenance, data manipulation and analysis and presentation (Huisman & de By, 2001). GIS technology predicts disaster areas which are vulnerable and most probable to occur (Bahuguna, et al., 2013). GIS has role in disaster as shown in Fig. 2.11

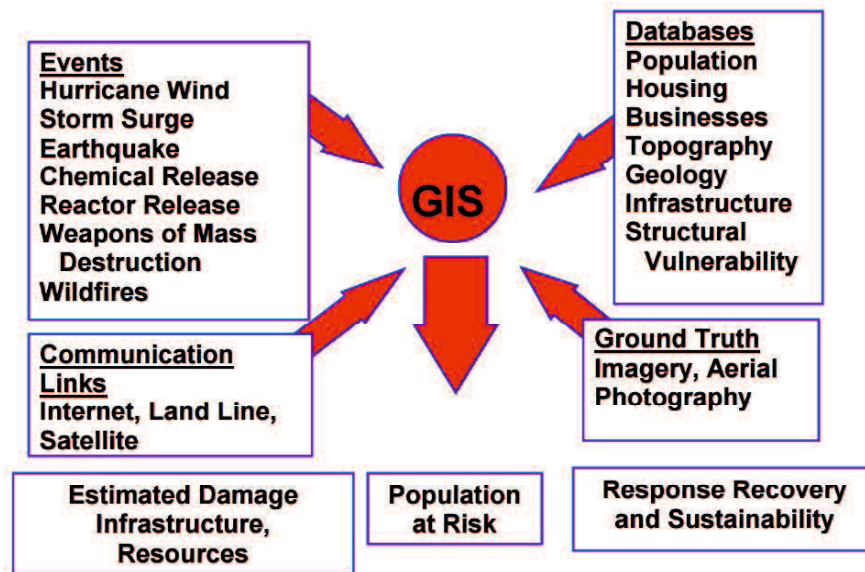


Figure 2. 11 GIS for Disaster Management and Terrorism (Johnson , 2000)

2.2.3. Spatial Multi Criteria Analysis for Vulnerability Assessment

GIS provides the decision-maker with a powerful set of tools for the manipulation and analysis of spatial information. The idea of GIS as a box of tools for handling geographical data is useful. Items from the toolbox of GIS can, in various combinations, be used to solve a multitude of problems involving spatial data. To meet a specific objective, it is frequently the case that several criteria will need to be evaluated (Eastman, 2001). Such a procedure is called Multi-Criteria Evaluation (MCE) (Voogd, 1983; Carver, 1991). Another term that is sometimes encountered for this is modelling. However, this term is avoided here since the manner in which the criteria are combined is very much influenced by the objective of the decision. MCE techniques (often referred to as multi-criteria analysis or MCA) began to emerge during the early 1970s from a critique of traditional neoclassical environmental economics. A number of workers, particularly in the

regional economic planning and decision-making research fields (Voogd, 1983; Carver, 1991; Eastman, 2001)

Multi-dimensional decision and evaluation models (of which MCE is a part) provide tools for analysing the complex trade-offs between choice alternatives (e.g. sites, plans) with different environmental and socio-economic impacts. The formal mathematical framework used to describe multi-dimensional decision-making is based on multi-objective optimization theory in which both conflicting and complementary objectives are described as a decision problem with multiple objectives. In multidimensional models, appropriate units of measurement are applied to each factor in the problem rather than trying to impose artificial 'shadow' prices, as in many classical models (e.g. cost-benefit analysis).

Simple superimposed and Analytical Hierarchical Process (AHP) are example methods for decision making. The primary issue in Simple Multi-Criteria Evaluation or Simple superimposed method is concerned with how to combine the information from several criteria to form a single index of evaluation. In the case of Boolean criteria (constraints), the solution usually lies in the union (logical OR) or intersection (logical AND) of conditions (Eastman, 2001). Because of the different scales upon which criteria are measured, it is necessary that factors be standardized before combining the parameters with the equal weight of each parameter (Eastman, 2001). It becomes the limitation of this method. Thus, we proposed another method which is called as the Analytical Hierarchical Process (AHP). For the multi-criteria evaluation is based on AHP developed by Saaty [Saaty, 1980]. The AHP has been extensively applied on decision-making problems [Saaty, 2008], and extensive research has been carried out to apply AHP to risk assessment. The input of spatial multi-criteria analysis is a set of maps that are the spatial representation of the criteria, which are grouped, standardized and weighted in a 'criteria tree.' The output is one or more 'composite index maps,' which indicates the realization of the model implemented.

The AHP is essentially an interactive one where a decision-maker or group of decision-makers relay their preferences to the analyst and can debate or discuss opinions and outcomes [Proctor, 2000]. The AHP is based upon the construction of a series of Pair-Wise Comparison Matrices (PCMs), which compare all the criteria to one another.

Although a variety of techniques exist for the development of weight, one of the most promising would appear to be that of pairwise comparison developed by Saaty [Saaty, 1977] in the context of a decision-making process known as AHP. In the procedure for multi-criteria analysis using the weighted linear combination, it is necessary that the weight sum to be 1. In Saaty's technique, weight of nature can be derived by taking the principal eigenvector of a square reciprocal matrix of pairwise comparisons between the criteria. The comparison concern the

relative importance of the two criteria involved in determining suitability for the state objective. Ratings are provided on a nine-point continuous scale (see Fig. 2.12).

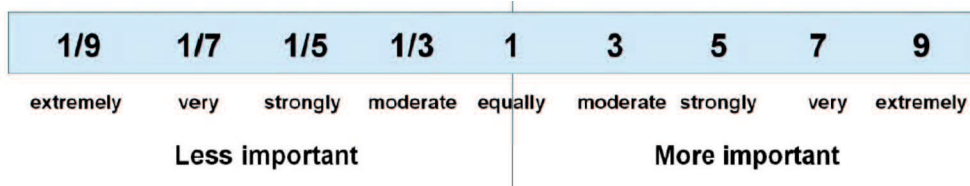


Figure 2. 12 The continuous rating scale use for the pairwise comparison of factor multi-criteria analysis

AHP allows eliciting weights for each parameter and levels taking them into consideration to explain individuals' behaviour in choosing their preferred product. In order to implement the AHP, one needs to carry out a survey where individuals are asked to value different parameter that follow a hierarchical structure (Fig. 2.13). In our case each attributes in the tree is divided into three different levels to be also valued.

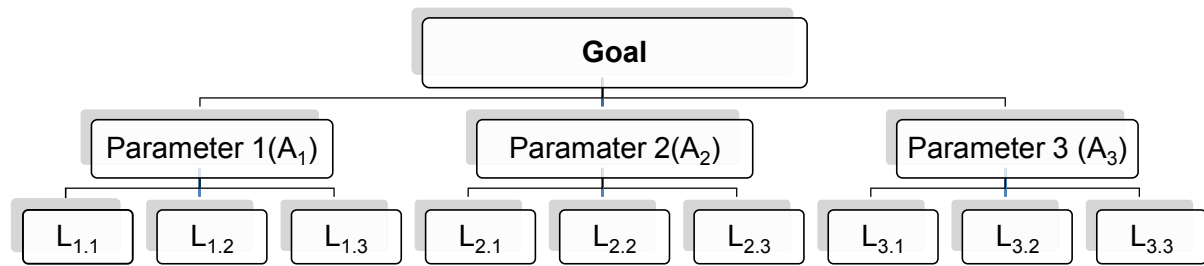


Figure 2. 13 Hierarchical structure used to value product attributes and levels.

The relative importance or weights (w) for Parameter (A_n) and levels ($L_{n,p}$), where; $n (1, \dots, N)$ is the number of attributes and $p (=1, \dots, P)$ is the number of levels, are obtained from pairwise comparisons. In order to make these comparisons and determine the intensity of preferences for each option, [Saaty, 1987] proposed and justified the use of 9 points scale (Fig. 2.11). The relative importance of each attributes is obtained by comparing this attribute with all other attributes. From the answers provided, a matrix with the following structure is generated for each individual $k (1, \dots, K)$ known as Saaty matrix:

$$S_k = \begin{bmatrix} a_{11k} & a_{12k} & \dots & a_{1jk} \\ a_{21k} & a_{22k} & \dots & a_{2jk} \\ \dots & \dots & a_{ijk} & \dots \\ a_{i1k} & a_{i2k} & \dots & a_{NNk} \end{bmatrix} \quad (2.3)$$

where a_{ijk} represents the value obtained from the comparison between parameter/level i ($i \in N / i \in P$) and parameter/level j ; ($j \in N / j \in P$) for each individual k . This square matrix has two fundamental properties: (a) all elements of its main diagonal take a value of one ($a_{iik}=1 \forall i$), and (b) all other elements maintain that pair-wise comparisons are reciprocal (if $a_{ijk}=x$ then $a_{jik}=1/x$). If perfect consistency in preferences holds for each decision-maker, it should also hold that $a_{ihk} \times a_{hjk} = a_{ijk}$ for all i, j and h ($h \in N / h \in P$). This condition implies that values given for pair-wise comparisons represent weights given to each objective by a perfectly rational decision-maker $a_{ijk} = w_{ik}/w_{jk}$ for all i and j . Therefore, the Saaty matrix can also be expressed as follows:

$$S_k = \begin{bmatrix} \frac{w_{1k}}{w_{1k}} & \frac{w_{1k}}{w_{2k}} & \dots & \frac{w_{1k}}{w_{Nk}} \\ \frac{w_{2k}}{w_{1k}} & \frac{w_{2k}}{w_{2k}} & \dots & \frac{w_{2k}}{w_{Nk}} \\ \dots & \dots & \dots & \dots \\ \frac{w_{Nk}}{w_{1k}} & \frac{w_{Nk}}{w_{2k}} & \dots & \frac{w_{Nk}}{w_{Nk}} \end{bmatrix} \quad (2.4)$$

Under such circumstances, K weights (w_{Nk}) for each parameter and K weights (w_{Pk}) for each level can be easily determined from the $N(N-1)/2$ values and $P(P-1)/2$ values for a_{ijk} respectively. However, perfect consistency is seldom present in reality, where personal subjectivity plays an important role in doing the pair-wise comparison. In Saaty matrixes ($S_k=a_{ijk}$) in which some degree of inconsistency is present, alternative approaches have been proposed to estimate the weight vector that better is able to represent the decision maker's real weight vector. Saaty [1980; 2003] proposed two options as the best estimate of real weights: the geometric mean and the main eigenvector. Other authors have proposed alternatives based on regression analysis [Laininen & Hämäläinen, 2003] or goal programming [Bryson, 1995]. No consensus has been reached regarding what alternative outperforms the others [Fichtner, 1986]. As all criteria meet the requirements to estimate the above-mentioned weights, we choose the geometric mean [Aguarón & Moreno-Jiménez, 2000]. Using this approach, weights assigned by subject to each attribute and level are obtained using the following expression:

$$w_{ik} = \sqrt[N, P]{\prod_{i=1}^{i=N, P} a_{ijk}} \quad \forall i, k \quad (2.5)$$

AHP was originally conceived for individual decision-making, but it was rapidly extended as a valid technique for the analysis of group decisions [Easley, et al., 2000]. Thus, in order to compare

attributes weights between AHP and CE results, group preferences must be considered. Therefore, we need to aggregate the corresponding individual weights (w_{ik}) across subjects to obtain a synthesis of weights for each attribute and level (w_i). The aggregation process should be carried out following Forman and Peniwati, [1998], who consider that the most suitable method for aggregating individual weights (w_{ik}) in a social collective decision-making context is that of the geometric mean:

$$w_i = \sqrt[K]{\prod_{k=1}^{k=K} w_{ik}} \quad \forall i \quad (2.6)$$

In the same context, with the aim to obtain weights' order for levels of each attributes we need to calculate a global weight for each levels ($w_{G_Ln,p}$). This global levels' weight is obtained by multiplying aggregated levels' weights (w_i for each level $L_{n,p}$) by its corresponding weight (w_i) of parameter (A_n) as mentioned by Malvinas, et al., [2005].

$$w_{G_Ln,p} = w_{A_n} \times w_{Ln,p} \quad (2.7)$$

Where, $\sum w_{G_Ln,p} = 1$, for all levels.

2.2.4. Accuracy Assessment

The accuracy of a classification is usually assessed by comparing the classification with some reference data that is believed to accurately reflect the true land-cover. Sources of reference data include among other things ground truth, higher resolution satellite images, and maps derived from aerial photo interpretation. The result of an accuracy assessment typically provides us with an overall accuracy of the map and the accuracy for each class in the map. For example, in a land cover map, the water class could be very accurate but some of the vegetation classes might be less accurate. This can have a significant effect on the utility of the map and in some cases may indicate that some classes should be merged.

2.2.4.1. Overall accuracy

The *overall accuracy* is calculated by summing the number of correctly classified values and dividing by the total number of values. The correctly classified values are located along the upper-left to lower-right diagonal of the confusion matrix. The total number of values is the number of values in either the truth or the predicted-value arrays following Eq. 2.8.

$$\text{Correctly classified values} = \frac{\text{correctly classified}}{\text{Total number of value}} \quad (2.8)$$

2.2.4.2. Kappa Coefficient

The results of an accuracy assessment are usually summarized in a confusion matrix. Kappa can be used as a measure of agreement between model predictions and reality [Congalton, 1991] or to determine if the values contained in an error matrix represent a result significantly better than random [Jensen, 2000; Danoedoro, 2012] Kappa is computed using Eq. 2.9.

$$K = \frac{M \sum_{i=j=1}^r n_{ij} \sum_{i=j=1}^r n_i n_j}{M^2 - \sum_{i=j=1}^r n_i n_j} \quad (2.9)$$

Where, r is the rows in the error matrix; n_{ij} is the number of observation in row, column j ; n_i is the total number of observation in row i ; n_j is the total number of observation in column j ; M is the number of observation in matrix. Kappa Coefficient measures of agreement between the predicting map and the reference data (Lillisand, et al., 2004; Danoedoro, 2012).

2.2.4.3. A Receiver Operating Characteristics (ROC)

A receiver operating characteristics (ROC) graph is a technique for visualizing, organizing and selecting classifiers based on their performance. ROC graphs have long been used in signal detection theory to depict the trade-off between hit rates and false alarm rates of classifiers [Egan, 1975] and [Swets, et al., 2000]. ROC analysis has been extended for use in visualizing and analysing the behaviour of diagnostic systems [Swets, 1988].

Formally, each instance is mapped to one element of the set $\{p,n\}$ of positive and negative class labels. A classification model (or classifier) is a mapping from instances to predicted classes. Some classification models produce a continuous output (e.g., an estimate of an instances class membership probability) to which different thresholds may be applied to predict class membership. Other models produce a discrete class label indicating only the predicted class of the instance. To distinguish between the actual class and the predicted class we use the labels $\{Y,N\}$ for the class predictions produced by a model.

Given a classifier and an instance, there are four possible outcomes. If the instance is positive and it is classified as positive, it is counted as a true positive; if it is classified as negative,

it is counted as a false negative. If the instance is negative and it is classified as negative, it is counted as a true negative; if it is classified as positive, it is counted as a false positive. Given a classifier and a set of instances (the test set), a two-by-two confusion matrix (also called a contingency table) can be constructed representing the dispositions of the set of instances. This matrix forms the basis for many common metrics.

Figure 2.14 shows a confusion matrix and equations of several common metrics that can be calculated from it. The numbers along the major diagonal represent the correct decisions made, and the numbers of this diagonal represent the errors—the confusion—between the various classes. The true positive rate¹ (also called hit rate and recall) of a classifier is estimated as Eq.2.10.

$$\text{tp rate} \approx \frac{\text{Positives correctly classified}}{\text{Total positives}} \quad (2.10)$$

The false positive rate (also called false alarm rate) of the classifier is estimated as Eq. 2.11.

$$\text{fp rate} \approx \frac{\text{Negatives incorrectly classified}}{\text{Total negatives}} \quad (2.11)$$

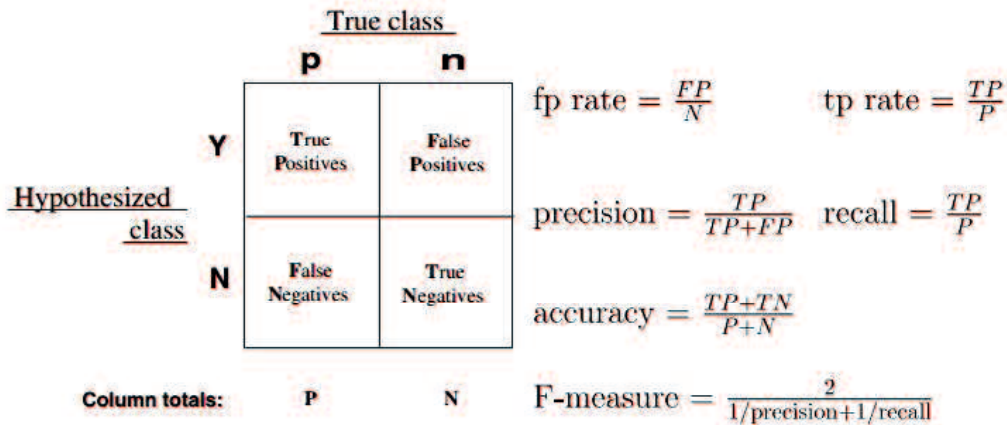


Figure 2. 14 Confusion matrix and common performance metrics calculated from it
[Fawcett, 2006]

2.3. Data

Several datasets are required for the studies on the detection of flooded areas and the evaluation of the vulnerability of flood disaster using the satellite images. The data are raster data from Japan Aerospace Exploration Agency (JAXA), i.e., ALOS (AVNIR-2 and PALSAR) and ALOS-

2/PALSAR-2 imageries, Sentinel-2 imagery for the European Space Agency (ESA), Digital Elevation Model (DEM) from The Geospatial Authority of Japan (GSI), and meteorology data from the Automated Meteorological Data Acquisition System (AMeDAS) from Japan Meteorology Agency (JMA).

2.3.1. Satellites data

Table 2.6 lists the satellite images utilized in this study.

Table 2. 6 List of satellite images

Satellite imagery	Sensor	Date	Related Chapter
ALOS/AVNIR-2	Passive	2012/5/12	Ch.3
ALOS/PALSAR	Active	2007/8/21	Ch.5
		2008/8/31	Ch.4 and Ch.5
ALOS-2/PALSAR-2	Active	2015/7/31	Ch.5
		2015/9/10	Ch.4 and Ch.5
Sentinel-2	Passive	2016/11/22	Ch.3

2.3.2. Digital Elevation Model (DEM) data

As topography is one of the major parts in most types of hazard study, the generation of a Digital Elevation Model (DEM) represents a major task. DEMs can be obtained from a variety of methods, such as digitizing contours of existing topographic maps, topographic levelling, EDM (Electronic Distance Measurement), differential Global Positioning System (GPS) measurements, (digital) photogrammetry, Interferometric Synthetic Aperture Radar (InSAR), and Light Detection and Ranging (LiDAR). Many products of maps can be produced from DEMs using fairly simple GIS operations. A wide range of data sources can be selected for the generation of DEMs these days. The selection depends on the data availability for a specific area, the price and the application.

The Geospatial Information Authority of Japan (GSI) provides a high spatial resolution of DEM. Based on surveying methods, 5m mesh of elevation data is divided into two types. First was created based on the airborne laser, which is the center point grid of mesh by data equivalent to those published (digital elevation map of 5meter) and longitude difference at the surface and separated by interval of 0.2 seconds latitude difference. This method has been applied for the target of metropolitan areas.

The second one is based on the photogrammetric. In this method, the mesh of 0.2 seconds difference in latitude (approximately 5m) interval, the data of the ground surface is created by removing bridge and houses, trees, etc., the target of this method is urban areas and used for the application of city planning.

2.3.3. Meteorological data

Precipitation was appropriated in this research, the data derived from JMA by AMeDAS. AMeDAS provides precipitation data by using radar/rain gauge-analyzed. Precipitation data represents precipitation with high dimensional accuracy and is published every thirty minutes with a spatial resolution of 1 km. For forecast, AMeDAS issues every thirty minutes to provide estimates of hourly precipitation values for the following six hours with a spatial resolution of 1 km [Japan Meteorology Agency, 2008].

2.4. Overview of the study area

The research was conducted in three study areas; Okazaki City in Aichi Prefecture, Joso City in Ibaraki Prefecture and Kumamoto Prefecture as shown in Fig. 2.15. These areas have experienced flood.

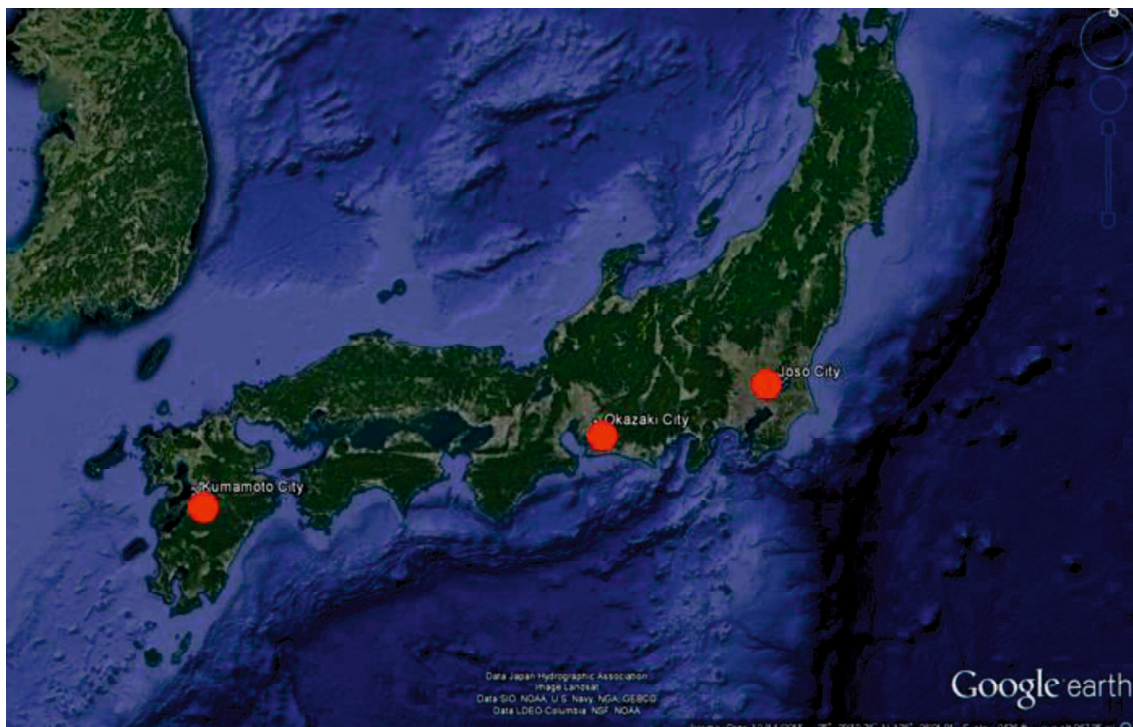


Figure 2. 15 Overview of study areas

2.4.1. Okazaki City, Aichi Prefecture

Okazaki City is located in the middle part of Aichi Prefecture, Japan the north latitude is 34°57'15.6" and the east longitude 137°10'27.7". According to the census data on 1st June 2016, the population number is 382.846 [Okazaki City, 2016] and total area 387.20 km² [Weblio, 2016]. Okazaki City is the third biggest City after Nagoya City and Toyota City in Aichi Prefecture [Weblio, 2016].

Table 2. 7 The extremes meteorological of Okazaki City [Weblio, 2016]

Phenomena	Observation value	Observation date
Highest temperature	38.8°C	1 st August 2011
Lowest Temperature	-7.6°C	4 th April 1999
Daily precipitation	263.5 mm	29 th August 2008
Hour precipitation	146.5 mm	29 th August 2008

The average annual temperature of Okazaki City is 17.0 °C, the average highest temperature is 36 °C, and the average minimum temperature -1 °C, annual rainfall is about 1200mm. The extremes meteorological data of Okazaki City are listed in Table 2.7 [Weblio, 2016].

2.4.2. Joso City, Ibaraki Prefecture

The Joso City is positioned in the southwestern part of Ibaraki prefecture. The distance from Tokyo is approximately 55 km. Its width is about 20 km in north-south, and 10 km in east-west axis and its total area is 123.52 km². The relief of the city has flat land with some low hills of soft shapes. The altitude is 5-24 m. Its moderate climate for four seasons is a typical one of the Pacific Ocean temperate zone.

Kinugawa River is passing almost centre part of the city starting from north to south. The east side of the river has become a widespread area of rice field because of the lowland. The west region of the river has low hills and spread farms, villages, cultivated fields, widespread woods-plains-, and is being developed, with the development of industrial places, residential plazas, golf course activity, etc., as one of the strategic areas of Tokyo Metropolitan Region, strengthening urban structure roles. According to the statistics data on 1st January 2015, Joso City has the population of 65,370 and the total area is 123.52 km² [JosoCity, 2016].

2.4.3. Shirakawa River, Kumamoto Prefecture

Shirakawa River originates from Mt. Aso caldera and flows down to Kumamoto City. It runs from Takamori Nakodake Aso (altitude 1,433m) to lowland area and accumulates to the Ariake Sea. Shirakawa River is located in Kumamoto Prefecture. According to Ministry of Land, Infrastructure, Transport and Tourism (MLIT) Shirakawa River has 74 km length and 480 km² of the basin area.

Upstream of Aso region is one of the highest rainy areas in Japan; it is twice from the average annual rainfall in Japan. When the upstream has ceiling water, it will expand the damage in the Kumamoto City such as the flood. Besides that Upstream has a large amount of volcanic ash, as well as expanding the damage flows down during the flood [MLIT, 2016].

CHAPTER 3

INTEGRATED REMOTE SENSING DATA AND GIS METHOD TO FLOOD VULNERABILITY

3.1. Introduction

The population growth, especially in urban areas, has been increasing to utilize the flood-prone areas [Larsen, 2009]. Furthermore, the United Nations defined flooding as the most frequent and greatest hazard [Nations, 2012] and high population areas are relatively high-risk for natural disaster [Rufat, et al., 2015; Nations, 2012; Wilby & Keenan, 2012]. That condition triggers the rapid accumulation of runoff waters which causes flooding. In addition, the potential for flood casualties and damages is also increasing in many regions due to social and economic development, such as urbanization which put pressure on land use change (Ouma & Ryutaro , 2014; Rufat, et al., 2015). Refer to the most severe scenario of the Representative Concentration Pathways (RCP) 8.5 in East Asia, the extreme rainfall increased by 25-35% in 2071-2100 (Hong & Bae-Ahn, 2015). In Kumamoto Prefecture and Aichi Prefecture, the number of heavy rainfall days, such as days with hourly precipitation of ≥ 50 mm/hour and ≥ 100 mm/ hour has been increasing as 60% and 110% since 1979 (JMA, 2016). Thus, we chose the urban area as a case study in Kumamoto Prefecture and Aichi Prefecture.

Flood risk management is commonly divided into flood risk assessment and flood risk mitigation (Schanze, et al., 2006). One of the strategies of flood risk management against flood impact in region scale is the identification of vulnerable areas to provide early warning, facilitate quick response and decrease the impact of possible flood events. Recently, the integration of remote sensing technology (i.e., a method to extract the up to date information from satellites [Panagiota, et al., 2011; Ebert & Kerle, 2008]), GIS (i.e., data integration [Ebert & Kerle, 2008]) and field surveys has been conducted to assess the impact of flood damage by vulnerability mapping.

Multi-criteria evaluation (MCE) is the common approach in determining the areas vulnerable to flood disaster. The basic aim of MCE analysis techniques is 'to investigate a number of choice possibilities in the light of multiple criteria and conflicting objectives' (Voogd, 1983). Two type MCE was applied in this study i.e. Simple superimposed method and Analytical Hierarchy Process (AHP). Simple superimposed is overlaid multi-parameters with equal weight;

there is not dominant parameters nor ranking of each parameter. The procedure of simply superimposed method follows; define the problem, break a problem into submodels, determine significant layers, reclassify or transform the data within a layer, combine the layers and analyze (ArcGIS, 2016). The limitation of Simple superimposed method is all parameters have the same weight. However, this method has the advantage due to easy to be applied. The expert's judgment is not necessary for this method.

AHP method is the vice versa from the Simply superimposed method. AHP introduced by Saaty; this method selects the required criteria by ranking the parameters and combines the qualitative and quantitative factors [Saaty, 1987; Saaty, 2008; Saaty, 1977; Saaty, 1980]. The AHP method is applied to the decision-making process. Some studies employed AHP for hazard assessment such as, floods [Ouma & Ryutaro, 2014; Siddayao, et al., 2014; Kazakis, et al., 2015; Bathrellos, et al., 2016; Bathrellos, et al., 2017], tsunamis [Sambah & Miura, 2014; Sambah & Miura, 2014; Poursaber & Ariki, 2016], landslides [Bathrellos, et al., 2017; Kayasthaa, et al., 2013; Hasekioğulları & Ercanoglu, 2012; Shahabi & Hashim, 2015; Ahmed, 2015; Rozos, et al., 2011; Ahmed, 2015], droughts [Ekrami, et al., 2016] and seismic hazards [Bathrellos, et al., 2016]. In flood hazard assessment, Ouma and Tateishi (2014) integrated AHP and GIS to predict flood vulnerability by using six parameters; rainfall, drainage, elevation, slope, soil and land use. According to their AHP calculation, the soil was the weightiest parameter. In addition, the consistent ratio (CR) of their study was 9%. CR is used to conclude whether the evaluation is sufficiently consistent i.e., the rational value of CR is $\leq 10\%$ or ≤ 0.1 (Saaty, 1977). Siddayao *et al.* (2014) investigated population density, distance from the river bank and site elevation as AHP parameters for flood vulnerability. Distance from the river bank was the highest contributing factor to floods in AHP calculation, and CR was 3.34%. Kazakis *et al.* (2015) calculated the flood hazard using the AHP approach and utilizing seven parameters including rainfall intensity, slope, flow accumulation, elevation, distance from drainage network, land use and geology. The flow accumulation was the highest influencing parameter to floods, and CR was 8% (Kazakis, et al., 2015). Bathrellos et al. (2016) investigated urban hazard assessment with the AHP procedure and utilized six parameters (i.e., slope, elevation, distance from channel stream, distance from totally covered streams, hydro-lithological formation and land cover); the highest parameter was land cover and CR was 4%. The advantage of AHP is that it is designed to solve complex problems involving multiple criteria. In addition, it is also designed to handle situations in which the subjective judgments of individuals constitute an important part of the decision process. However, the limitation of AHP is insufficient ability to define the uncertainty because the model predicts

the estimates only without estimation error of each output level (Bathrellos, et al., 2017; Bathrellos, et al., 2013).

This study deals with the first element of flood risk management, i.e. the definition of flood hazard areas in a specific region. The objective is to identify flood hazard zones, where mitigation assessment should be undertaken for urban development. Flood hazard assessment can support decision-makers and government for urban developing. Bathrellos *et al.* (2012), studied hazard assessment (i.e., flood, landslide, and seismic hazard assessment) as a component to measure suitability for urban development and proposed natural hazard assessment as a method for determining the suitability of urban growth and light industry development. Additionally, some researchers studied flood-risk assessment as a prominent component of urban planning [Ran & Nedovic-Budic, 2016; van Herk, et al., 2011; Plate, 2002]. Thus, a spatial, multi-criteria index has been proposed to characterize such areas by integrating the technology of the remote sensing and GIS method to measure the physical parameters of flood vulnerability. The physical parameters of flood vulnerability were rainfall, drainage density, slope, soil and land cover. The rainfall, drainage density, slope, land cover data were generated from satellite images; the soil was digitalized using GIS method. All the parameters were combined by GIS method by simply superimposed method and pair-wise using AHP procedure. All data were downloaded from public open access data. The study areas are located in Shirakawa watershed in Kumamoto Prefecture and in Okazaki City, Aichi Prefecture in Japan. Even though the index is tailored to the specific geography and land cover characteristics of the study area, it can be modified and applied in other areas.

3.2. Flood problem in Kumamoto Prefecture and Okazaki City in Aichi Prefecture

3.2.1. Shirakawa River in Kumamoto Prefecture and flood history

The length of the Shirakawa River is approximately 78 km, with the headwaters at Mt. Aso and the downstream in Kumamoto City. The topography of the Shirakawa River is mountainous near the headwaters and flat in the middle and downstream. Because of this topography, even when no rain falls in the middle and downstream parts of the river, flood is possible from rain on Mt. Aso. The water flows from Mt. Aso to Kumamoto City in approximately 2 hours. Figure 3.1 shows the research area.

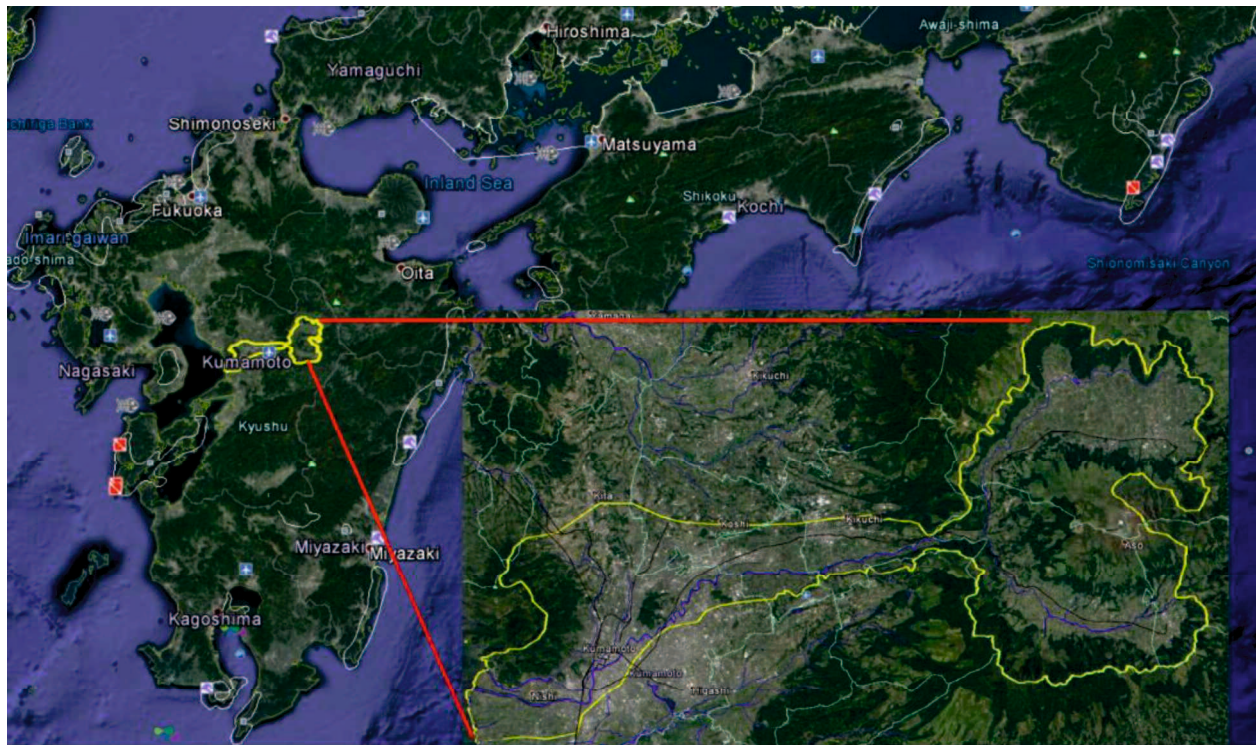


Figure 3. 1 Study location: Kumamoto City

According to the flood history of the study area, Kumamoto City has experienced floods on August 30, 1980, July 2, 1990 and July 12, 2012, with the water level reaching an estimated 2,300 m³/s in each flood.

3.2.2. Yahagi River in Okazaki City, Aichi Prefecture and flood history

The study area is located in the middle part of Aichi Prefecture and has an area 387.20 km² (Weblio, 2016) from Latitude 34°53'30"N to 35°2'30"N and Longitude 137°7'0"E to 137°25'0"E. Okazaki City is the third biggest city in Aichi Prefecture (Weblio, 2016) with a population of 382,846 people (OkazakiCity, 2016). It has a humid subtropical climate and an elevation ranging from 0 m to 789 m above the sea level (OkazakiCity, 2016). Center of the city consists of alluvial plains. The eastern part of the city is a mountainous area which has an altitude of 789 m (i.e., Mt. Hongu) and the rest is lowland area which has an altitude ranging between 0-300 m (OkazakiCity, 2016).

We selected the lowland area as the study area as shown in Fig. 3.2. The study area is passed by big rivers, namely the Yahagi River which flows from North to South. Thus, the land use within this area is dominated by agriculture, particularly paddy field. Precipitation occurs

throughout the year with the heaviest in the summer season (i.e., June to September) and during typhoon phenomena. The temperature range is from -1 °C to 36 °C with an average annual temperature of 17.0 °C, and the annual rainfall is about 1200mm/year.

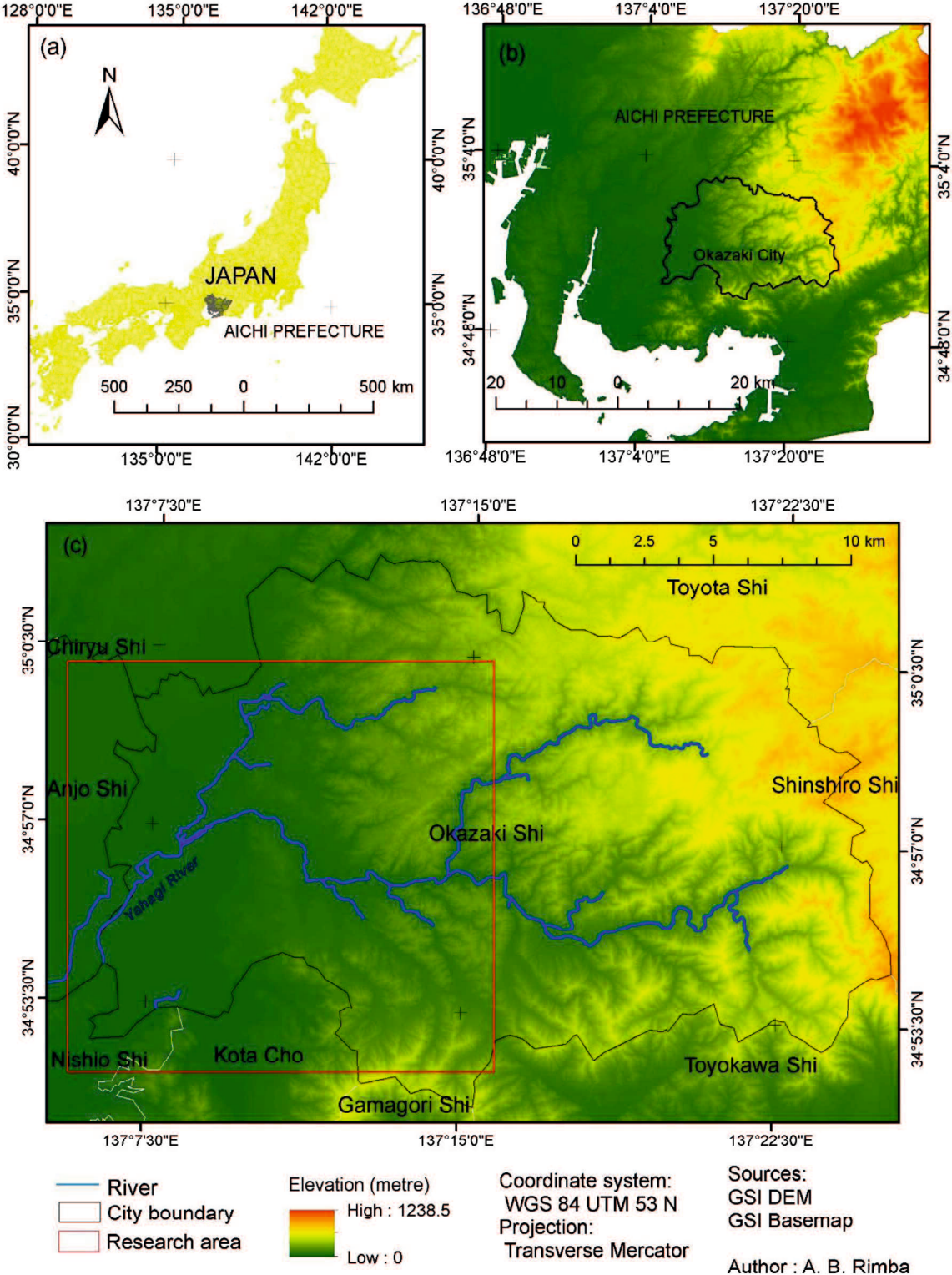


Figure 3. 2 (a) Location of Aichi Prefecture in Japan; (b) Location of Okazaki City in Aichi Prefecture; (c) Research area in the lowland area of Okazaki City.

From 1996 to 2008, severe heavy rains and flooding due to typhoons occurred 18 times as listed in Table 3.1. Large flood impacts occurred on 11-13th September 2000 and 30th August 2008. However, the flood in 2008 was the most severe; the rainfall intensity was about 146 mm/hour at 2:00 am in the morning [JMA, 2016]. Around 1,110 houses were flooded above floor level, and 2,255 houses were flooded below floor level [Adachi, 2009; Okazaki, 2015]. In addition, some areas of the neighboring city (i.e. Anjo City) were also flooded. The flood survey was conducted during the flood by the local government of Okazaki City and Ministry of Land, Infrastructure, Transportation and Tourism (MLIT) [OkazakiCity, 2013]. This survey was used to verify the results of this study.

Table 3. 1 Flood events related to the weather (Okazaki City, 2015)

Year	Month/ day	Disaster type	Affected by flood			
			Flooding up the floor (Building)	Flooding under the floor (Building)	Non- resident (Building)	Road flooding (Place)
1996	8/29	Heavy rain	2	30		
1997	7/10	Heavy rain and flood warning		1		1
	7/11	Heavy rain and flood warning				6
	7/28	Heavy rain				3
	7/15	Typhoon no 19	5	103		18
1998	8/29	Heavy rain and flood warning				4
	9/15-16	Typhoon no.5				1
	10/1	Heavy rain and flood warning				1
1999	6/29-30	Heavy rain and flood warning				11
	9/14-15	Typhoon no.16		5		6
2000	9/11-13	Heavy rain and flood warning	414	1193		45
2001	8/21-22	Typhoon no 1	3	55		3
	9/10-11	Typhoon no 15		5		
2003	8/8-9	Typhoon no 10		1		
2004	6/21	Typhoon no 6			1	
	10/8-9	Typhoon no 22		38		4
	10/20-21	Typhoon no 23			3	
2008	8/28-30	Heavy rain	1110	2255		

3.3. Materials and Methods

3.3.1. Overview

Vulnerability maps can be utilized in all steps of disaster management: Prevention, preparedness, mitigation, operations, relief, recovery and lessons learned (Edwards, et al., 2007). In recent years, urban areas have faced increased risk of disasters and the potential of economic and human losses from natural hazards. To build sustainable communities in the urban area, integration between urban planning and hazard mitigation effort is necessary (Bathrellos, et al., 2017; Bathrellos, et al., 2012). Thus, the vulnerability map can be used as one of the strategies for scenario modeling for urban planning. The vulnerable mapping related to the distribution of level risk-flood occurring; Vulnerability maps can be utilized in all steps of disaster management as mentioned above (Edwards, et al., 2007).

Two methods were applied to this study i.e., Simply superimposed method and Analytical Hierarchy Process (AHP) method. Simply superimposed method for Shirakawa watershed area was conducted by following Fig. 3.3. We used three types of satellite data in this research: ALOS/AVNIR-2 imagery to derive the Normalized Difference Vegetation Index (NDVI) and land cover, DEM from the Geospatial Information Authority of Japan (GSI) and rainfall data derived from AMeDAS and downloaded from the JMA website. The DEM was derived to get slope data and the river pattern. Rainfall data were rainfall averages in the rainy season (July 2012) in Kumamoto Prefecture. The reason of using the GSI Map and Google Earth in this research is verification of the parameters of this research. In this case, the land cover and the NDVI are verified by these data.

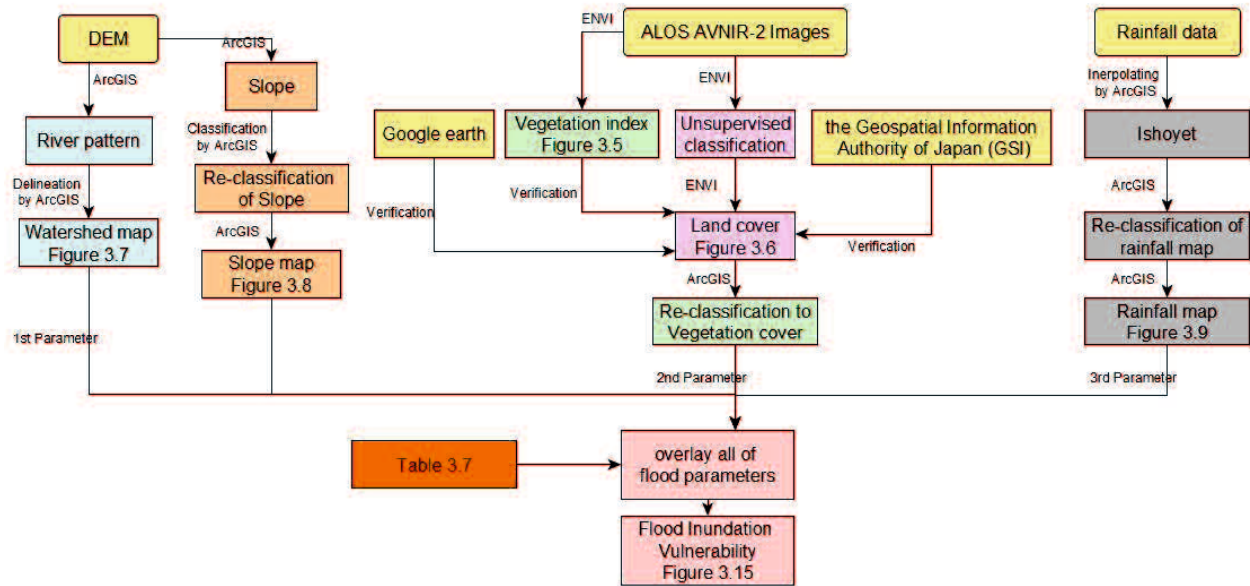


Figure 3. 3 Proposed flowchart for Simply superimposed method

Integrating the remote sensing data, GIS and AHP are quite effective tools to generate flood vulnerability data for urban areas. The overall method description for flood vulnerability was explained in Fig. 3.4. There are five physical parameters for flood vulnerability utilized in this study, namely, rainfall, drainage density, slope, soil and land cover. We generated the slope map and drainage density from DEM data from GSI. Soil map distribution was generated from MLIT. The rainfall spatial distribution was generated from AMeDAS data from JMA. The land cover was generated from Sentinel-2 imagery of the European Space Agency (ESA) product which was verified by Google Earth image. Then, by integrating all of those components, the flood-vulnerable area was assessed by AHP method. Finally, the flood-vulnerable area was verified by using field survey data taken during the flood event in Okazaki City that was conducted by the local government of Okazaki City and MLIT. We utilized three software systems to process the data; The European Space Agency-the Sentinel Application Platform (ESA SNAP) software and ENVI 4.8 by Harris Geospatial Solution software for processing land cover and ArcGIS 10.2.2 by ESRI software for processing hydrological parameter and vulnerability index. Integrating the AHP procedure, GIS and remote sensing could preserve the up to date information, with low cost, good visualization.

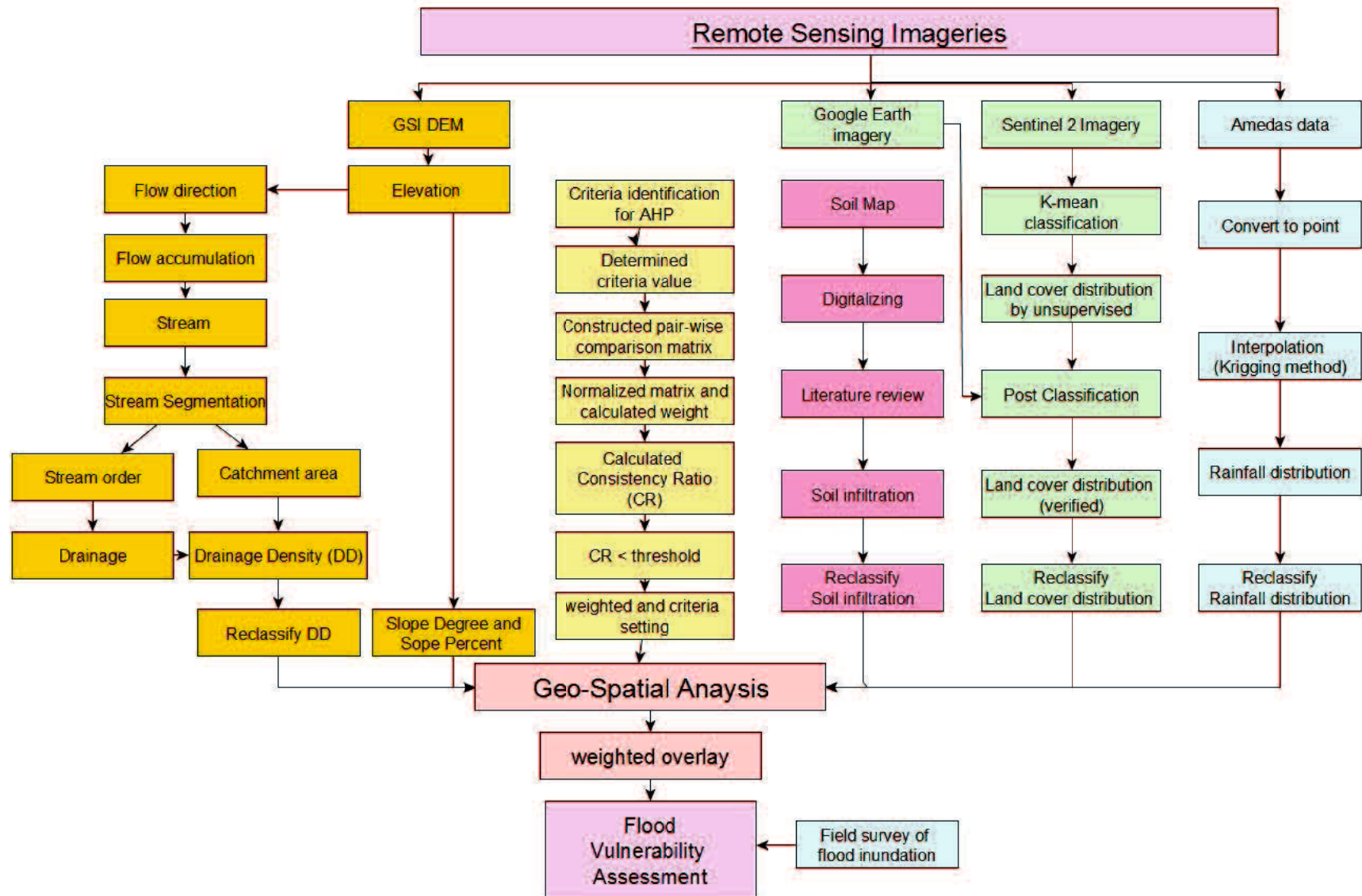


Figure 3. 4 Proposed flowchart for AHP method

3.3.2. Flood vulnerability variable by Simply superimposed method

3.3.2.1. Vegetation and Land cover classification

Vegetation Index: The NDVI is a calculation that impress into the amount of infrared radiation reflected by vegetation. Live green vegetation engages solar radiation, which they use as a source of energy for photosynthesis. The NDVI is frequently used to observe drought, to observe and forecast agricultural production, to aid in forecasting hazardous fire areas and to represent desert encroachment. The NDVI is desired for global vegetation observing because it can recompense for changing enlightenment conditions, surface slope, aspect and other extraneous factors [Lillisand, et al., 2004]. The idea that the NDVI is useful for sensing vegetation is that fit vegetation reflects excellently in the near-infrared band of the electromagnetic spectrum. Green leaves have a reflectance of 20% or less in the 0.5- to 0.7-micron range (green to red) and approximately 60% in the 0.7- to 1.3-micron range (near-infrared). These spectral reflections are ratios of the reflected over the received radiation in all spectral bands individually; hence, they take on values between 0.0 and 1.0. Thus, the NDVI itself varies between -1.0 and +1.0 that expressed as follows Equation 3.1 [ArcGIS, 2016].

$$NDVI = \frac{IR - R}{IR + R} \quad (3.1)$$

where: IR = Pixel values from the infrared ban, R = Pixel values from the red band.

Table 3. 2 Total Area of NDVI in the Shirakawa watershed

NDVI	Area (km ²)
(-0.75-0.1)	213.40
(0.1-0.3)	110.92
(0.3-0.58)	235.36
Total	559.68

Figure 3.5 and Table 3.2 describe the condition of vegetation index of the Shirakawa River in spatial and tabular. It was generated from ALOS/AVNIR-2.

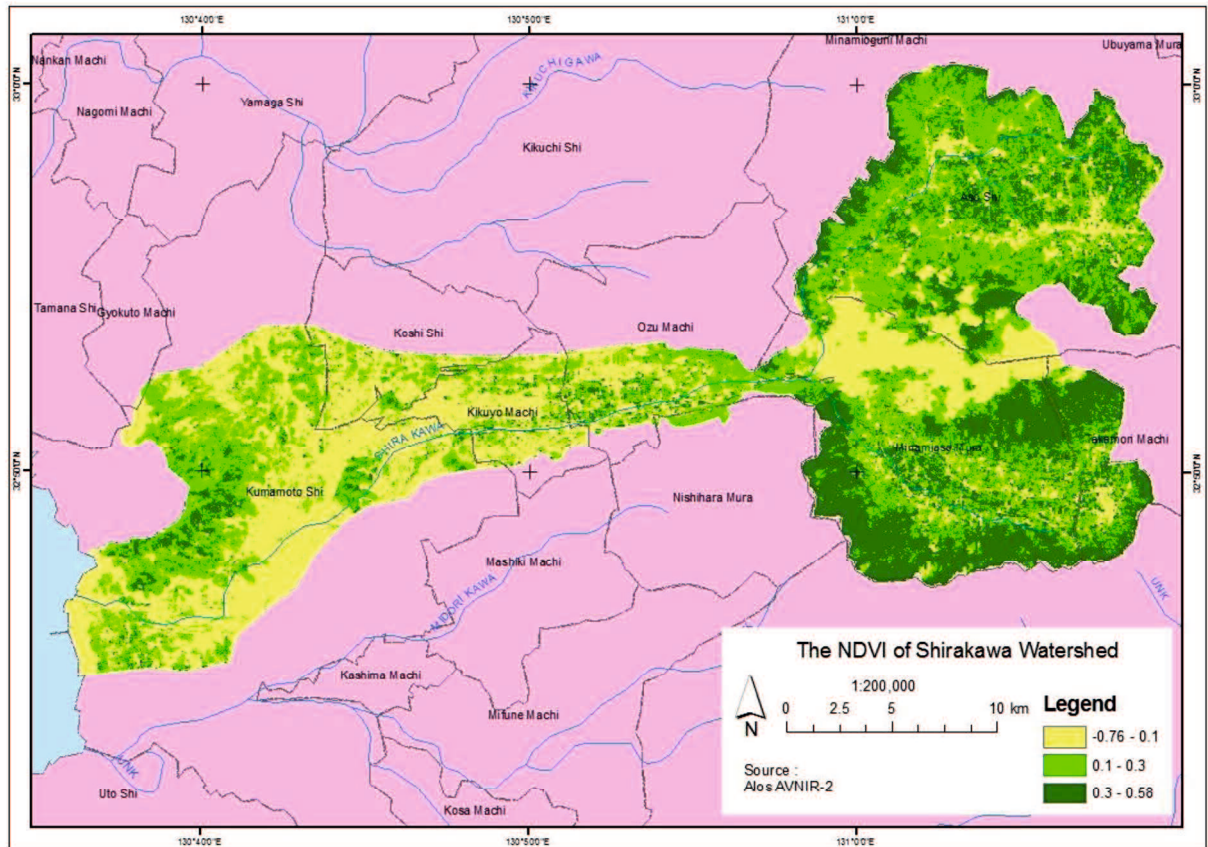


Figure 3. 5 Vegetation Index map of the Shirakawa watershed

Land Cover: Land-cover assessment is one of the highly important parameters inland-resources management. Land use control (LUC) inventories are supposedly increasing prominence in various resource sectors, such as agricultural planning, settlement surveys, environmental analyses and operational planning based on agroclimatic zones. Spatial land-cover information is necessary for proper management, planning and monitoring of natural resources [Zhu, 1997]. Satellite remote-sensing imagery is a viable source for assembly quality land-cover information at the local, regional and global scales [Csaplovics, 1998] as is shown in Table 3.3.

Table 3. 3 Land-use/land-cover classification scheme by land-use cover types stratified according to the U.S. Geological Survey's land use and land cover classification system for use with remote sensor data (Anderson, et al., 1976)

Item	Description
Build-up land	Area that have been populated with residential, commercial, industrial, transportation and facilities.
Forest of rangeland	Area covered with mature trees, shrubby plants and other plants growing close together.

Water	Area covered with water such as river and lakes
Agricultural land	Rain fed cropping, planted and irrigated cropping areas, areas covered mainly with herbaceous vegetation with shrubs
Barren land	Mountainous or hill areas, areas with no vegetation cover, degraded land and all unused area.

Figure 3.6 shows the distribution of land cover map and Table 3.4 shows its total area in km². It was derived from ALOS/AVNIR-2.

Table 3. 4 Total area of land cover in the Shirakawa watershed

land cover	Area (km ²)
forest	235.36
hard surface	50.24
bare land	80.56
mixing farm	110.92
water body	42.49
cloud	40.11
Total	559.68

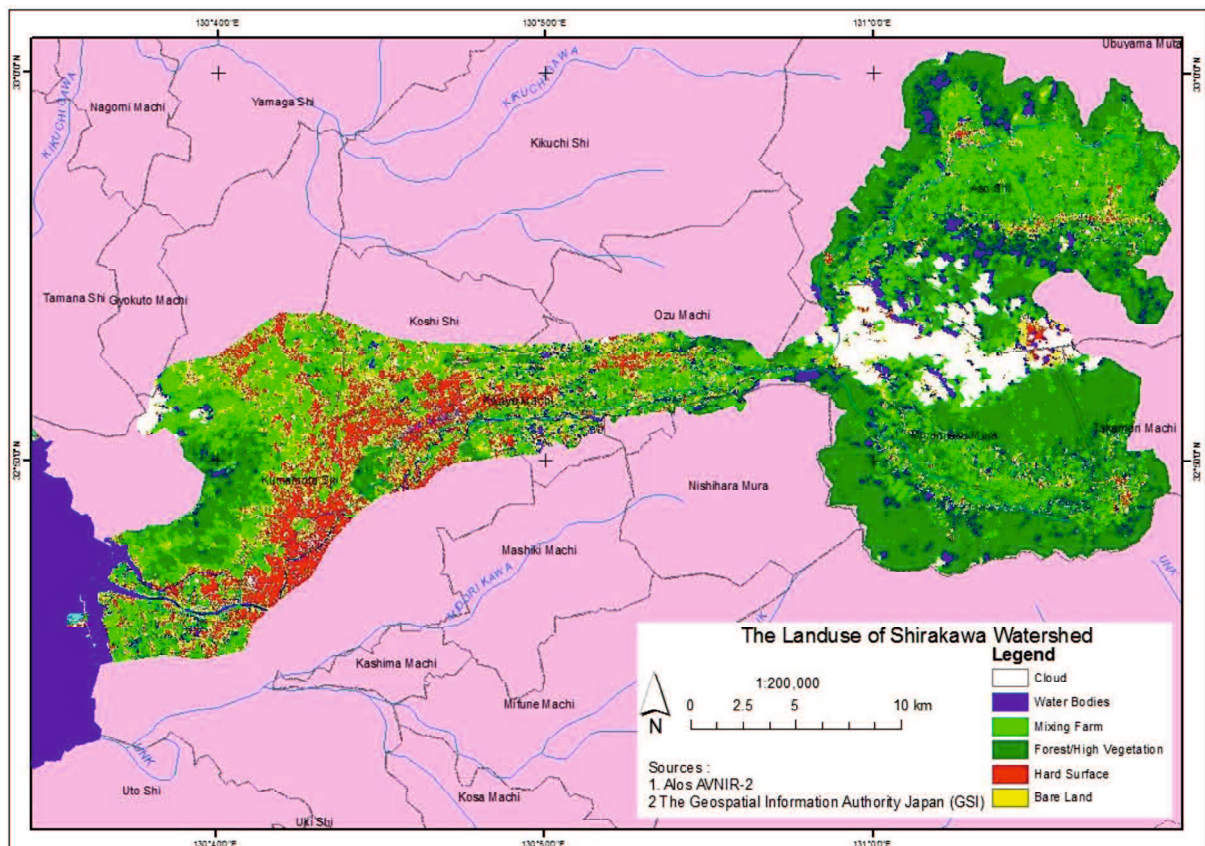


Figure 3. 6 Land cover map of Shirakawa watershed

3.3.2.2. Digital Elevation Model (DEM)

A DEM contains terrain elevations for ground location at frequently spread out horizontal intervals. DEMs can be expanded for the generation of three-dimensional visuals that display topography slope, aspect and topography profiles amongst selected points. DEMs have developed an important source of geographical data for many scientific and engineering uses, for example, hydrological and geological analyses, infrastructure planning and environmental uses. If topographical data are unobtainable, DEMs from remotely sensed data can be used instead. DEM generation method and DEM quality measurement apply in disaster studies, such as pre- or post-earthquake events and volcanoes [d'Ozouville, et al., 2008] .

Figure 3.7 and Fig. 3.8 were derived from DEM data form GSI. The watershed of Shirakawa River was shown in Table 3.5. It list the drainage density of the Shirakawa sub-watershed.

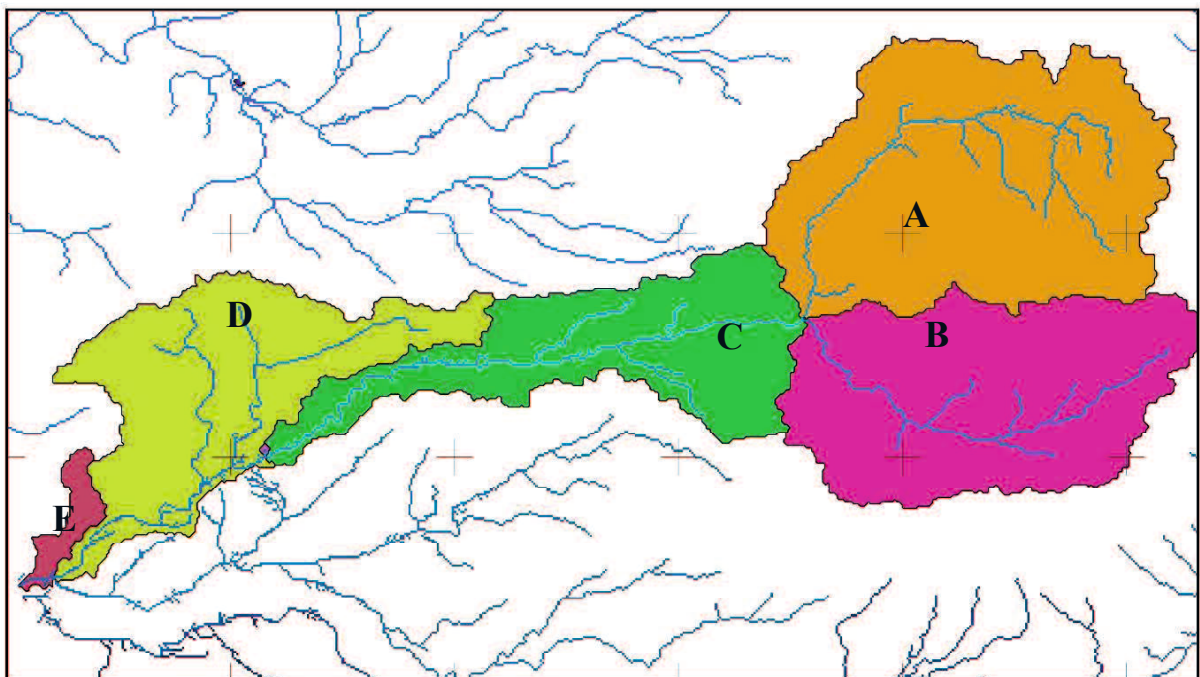


Figure 3. 7 The Shirakawa watershed and research boundary map

Table 3. 5. Drainage density of Shirakawa sub-watershed

Sub watershed	Area (m ²)	Stream length (m)	Drainage Density (m ² /m)
A	210663206	51969	0.00024669
B	117200174	37970	0.00032398
C	131220350	44731	0.00034088
D	169217372	45184	0.00026702
E	9904323	1747	0.00017639

Slope distribution was shown in Table 3.6 and Fig. 3.8. list the total distribution of each slope category.

Table 3. 6 Total of slope degree in Shirakawa watershed

slope	Area (km ²)
>30 %	0.39
10 – 30 %	55.73
5 – 10 %	91.91
0 – 5 %	411.64
Total	559.68

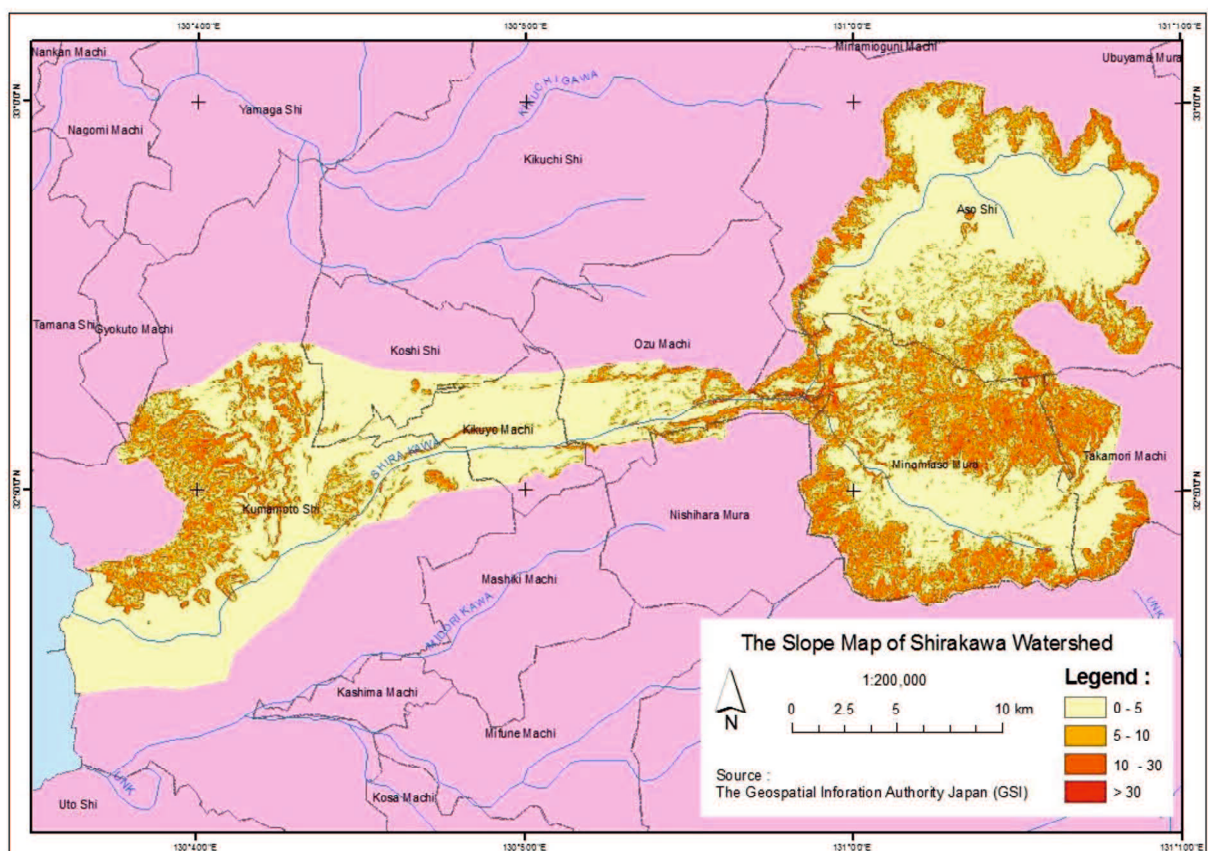


Figure 3. 8 Slope map of the Shirakawa watershed

3.3.2.3. The Isohyet

An Isohyet is an imaginary line on a weather map that connects points which have equal amounts of precipitation during one period of time. An isohyet map is a map that displays precipitation data. The contoured lines connect areas of equal rainfall and a colour scale is often used to differentiate

between areas. Isohyet maps are prepared by interpolating rainfall data recorded at gauged points [Chow, et al., 1964].

The method to draw the isohyet map: (1) arithmetic mean method; the simplest method by which average rainfall is recorded at a number of rain gauges. It is reasonable if the rain gauges are homogeneously distributed over the study area and the individual gage measurements do not diverge, (2) relative weight, if some rain gauges are considered more representative of the study area than others, (3) the Thiessen method: all points in the watershed catchment are the same as that at the nearest rain gauge, thus the depth recorded at a given gauge is applied out to a distance halfway to the next station in any direction. The relative weight for each gauge is determined from the corresponding areas of application in a Thiessen polygon network. The boundaries of the polygons are formed by the perpendicular bisectors of lines joining adjacent gauges. The Thiessen method is more accurate than the arithmetic-mean method, but it is in flexible because a new Thiessen network must be constructed each time a change is made in the gauge network, such as when data are missing from one of the gauges. Moreover, the Thiessen method does not directly account from orographic influences on rainfall. Some of these difficulties are overcome by the construction of isohyets using observed depths at rain gauges and interpolation between adjacent gauges. Other methods of weighting rain-gauge records have been offered, such as the reciprocal distance squared method in which the effect of rainfall at a gauged point on the computation of rainfall at an un-gauged point is contrariwise proportional to the distance between the two points [Wei & McGuinness, 1973]. Singh and Chowdhury (1986) studied the several methods for computing areal average precipitation, including those explained above and concluded that all the methods give a comparable result, especially when the time period is long [Singh, & Chowdhury, 1986].

Figure 3.9 shows the distribution of the Shirakawa watershed's rainfall intensity in July 2012 and Table 3.7 list its distribution. It was derived from AMeDAS data.

Table 3. 7 Total area of rainfall distribution in the Shirakawa watershed

Rain	km²
<20 mm/day	13.90
21 – 30 mm/day	487.60
41 – 50 mm/day	58.18
Total	559.68

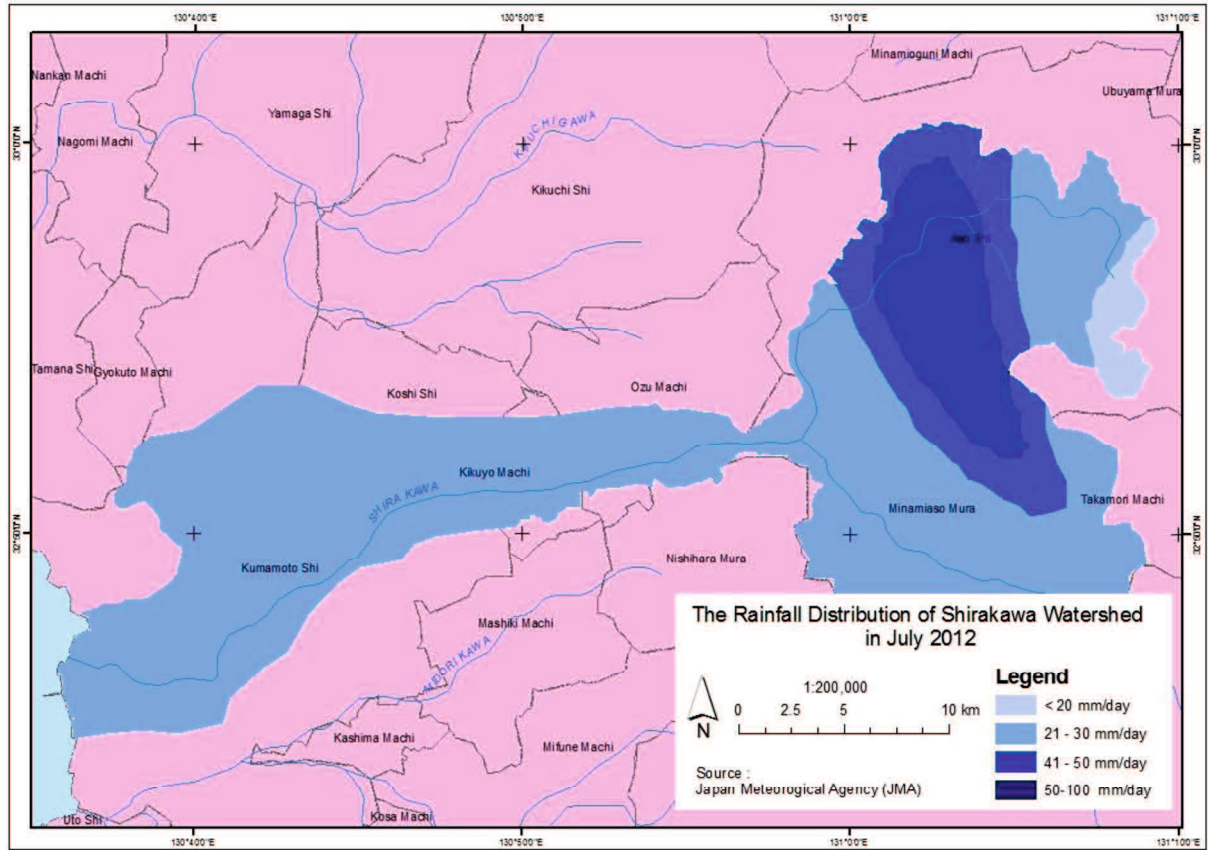


Figure 3. 9 Rainfall map of the Shirakawa watershed

3.3.2.4. Flood parameter

Parameters of the flood in this research follow the Table 3.8 below.

Table 3. 8 Watershed characteristic as flood/run-off parameters (Ven T. Chow, with modification)

Parameters	Units	Category	Score	Data source	Description
Slope	30%	steep	20	Topography map DEM	Topography map GSIdem
	10 – 30%	mountainous	15		
	5 – 10%	surge	10		
	0 – 5%	relatively flat	5		
Vegetation cover	Vegetation high density	low	5	Satellite interpretation	Satellite imagery
	Vegetation medium density	moderate	10		
	Vegetation low density	high	15		
	Settlement hardened surface	high	20		
Rainfall	<20 mm/ 24 hours	low	5	AMeDAS	Satellite imagery
	21-50 mm/hours	moderate	10		
	51-100 mm/hours	high	15		
	>100 mm/hours	extreme	20		

The Equal-interval Classification (constant class intervals): The total score from Table 3.8 can be classified by use of the equal-interval classification. In this classification method, each class consists of an equal-data interval along the dispersion graph shown in the equation. To determine the class interval total score, divide the range of all data (highest data value minus lowest data value) by the number of classes.

$$\text{Class interval} = \frac{\text{range of data}}{\text{number of classes}} \quad (3.2)$$

After determining the class interval, add the result to the lowest value of the dataset, which gives the first class interval. Then add this interval as many times as necessary to reveal the number of predefined classes. The values of the classifications are shown below:

Class 1 (very low) : 15 – 24

Class 2 (low) : 25 – 33

Class 3 (medium) : 34 – 42

Class 4 (high) : 43 – 51

Class 5 (very high) : 52 – 60

3.3.3. Flood vulnerability Variable by AHP

The flood vulnerability variables were determined by literature review; rainfall (Kazama , et al., 2009; Ouma & Ryutaro , 2014; Kazakis, et al., 2015; Greenbaum, et al., 1998; Setiawati, et al., 2016; Rimba & Miura, 2016; Setiawati & Miura, 2016; Horton, 1945); drainage density [Ouma & Ryutaro , 2014; Pallard, et al., 2009; Merz & Bloschl, 2008; Lazzaro, et al., 2014; Anwar, 2011; Moglen, 1998]; Slope [Ouma & Ryutaro , 2014; Kazakis, et al., 2015; Rimba & Miura, 2016]; Soil [Ouma & Ryutaro , 2014; Bateman, et al., 2010; Ghazavi, et al., 2010]; and Land cover (Rimba & Miura, 2016; Zope, et al., 2016; Al-Khudhairy & Shepherd, 1997; Halounova & Holubec, n.d.).

3.3.3.1. Rainfall

Floods are related to extremes in precipitation (from tropical storms, thunderstorms, orographic rainfall, widespread extratropical cyclones, etc.) (Trenberth, 2005). A combination of precipitation characteristic (e.g., the amount of rainfall, intensity, duration and spatial distribution) influences the flood events (Setiawati, et al., 2016; Horton, 1945). Flash floods due to relatively small cells of conventional activity have received much attention and are deemed characteristics of small to medium basins (Bracken, et al., 2007). The rainfall cannot immediately infiltrate as ground water

i.e. runoff. It converges to the catchment area. The heavy rainfall rises the amount of discharge from rivers and causes overflowing. According to the flood record by MLIT, this case often occurs in Japan. Table 3.9 lists the rainfall intensity classification by JMA (JMA, 2016).

Table 3. 9 Rainfall classification Japan Meteorology Agency (JMA)

Rainfall intensity	Description
10-20 mm/hours	Slightly strong rain
20-30 mm/hours	Strong rain
30-50 mm/hours	Heavy rain
50-80 mm/hours	Very hard rain
>80 mm/hours	Raging rain

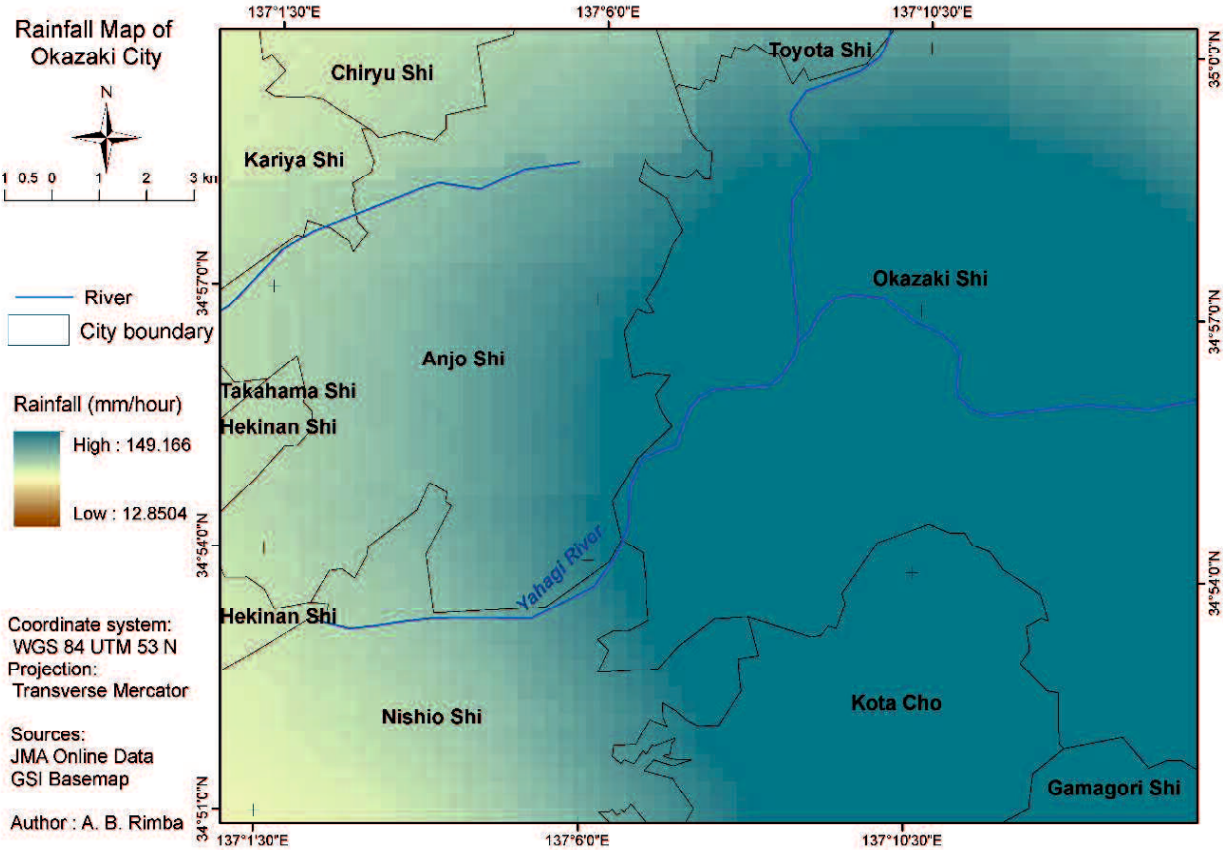


Figure 3. 10 Rainfall distribution map of Okazaki City

Figure 3.10 was generated from JMA data. It was interpolated by the Kriging Method [Rimba & Miura, 2016] from 20 observation points in Aichi Prefecture during extreme rainfall (i.e., the rainfall intensity was 146 mm/hour or 263.5 mm in two hours on August 29th, 2008).

Flooding could occur when the amount of rainfall was 199 mm to 435 mm for five hours or 406 mm to 608 mm for one week [Setiawati, et al., 2016].

3.3.3.2. Drainage density

Drainage density (DD) is the ratio of the sum length of streams in the watershed over its contributing area (Horton, 1945) as shown in Eq.3.3

$$DD = \frac{\sum L}{A} \quad (3.3)$$

where $\sum L$ is the total length of streams and A is the area. $\sum L$ and A must be measured in the same units. In this study, the unit was m/m².

Drainage density influences the water output and sediment from the system (Gregory & Walling, 1968). Low drainage density area is commonly found in high permeable soil and high-density vegetation; high drainage density area is commonly found in the impermeable surface material (e.g., rocky hill slopes), arid area and areas with sparse vegetation cover (Pallard, et al., 2009; Moglen, 1998). Integration of drainage density and rainfall were considered by many researchers as a parameter of flooding (Lazzaro, et al., 2014; Anwar, 2011; Ogden, et al., 2011).

Drainage density has two influences regarding peak of the flood (Pallard, et al., 2009) i.e., direct (e.g., the length of stream network and hillslope paths) and indirect (e.g., geomorphology) (Merz & Blöschl, 2008).

Figure 3.11 displays the drainage density, it was generated from GSI DEM. We extracted the elevation from the DEM data and created the stream from the elevation map. We generated the stream order and calculated the catchment area. Rationing the stream total length and catchment area followed Eq. 3.3 to generate the drainage density.

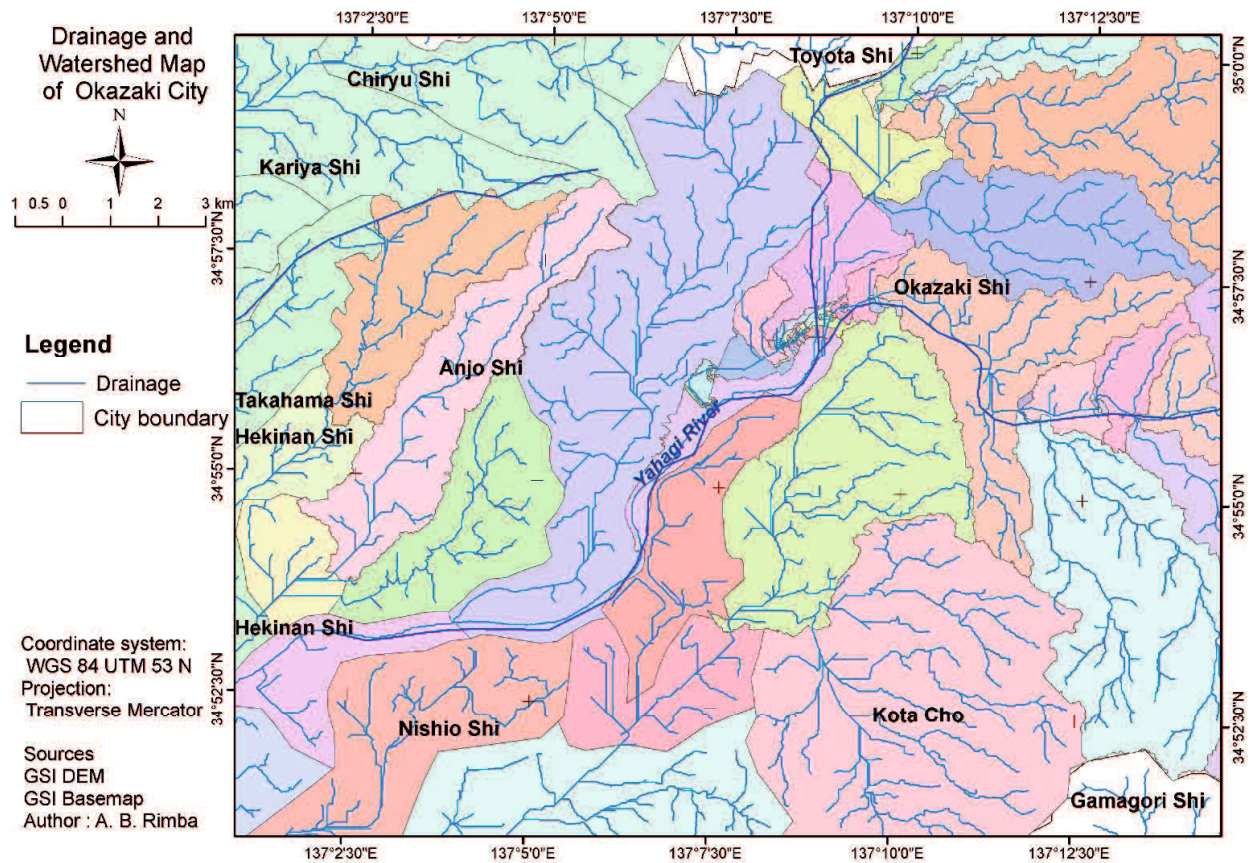


Figure 3. 11 Drainage map of Okazaki City

3.3.3.3.Slope

The slope is the ratio of steepness or the degree of inclination of a feature relative to the horizontal plane. Gradient, grade, incline and pitch are also used interchangeable with slope [Geokov, 2012]. The slope is typically denoted as a percentage, an angle, or a ratio. The average slope of a topo feature can be measured from contour lines on a topo map or by DEM. The slope is achieved by dividing the rise over run. Multiply this ratio by 100 to expose slope as a percentage. The slope angle represented in degrees is obtained by taking the arctangent of the ratio between rise and run [Geokov, 2012]. Table 3.10 lists the slope classification in Okazaki City.

Table 3. 10 Slope classification [Haynes, 1998].

Slope Class	Slope (%)	Slope (Degree)	Terminology
1	0 - 0.5	0	Level
2	> 0.5 - 2	0.3 – 1.1	Near level
3	> 2 – 5	>1.1 – 3	Very gently slopes
4	> 5 – 10	>3 – 5	Gently slopes
5	> 10 – 15	> 5 – 8.5	Moderate slopes

6	> 15 – 30	> 8.5 – 16.5	Strong slopes
7	> 30 – 45	> 16.5 – 24	Very strong slopes
8	> 45 – 70	> 24 – 35	Extreme slopes
9	> 70 – 100	> 35 – 45	Steep slopes
10	> 100	> 45	Very steep slopes

Figure 3.12 shows the distribution of slope in Okazaki City. It was generated from the elevation map extracted from GSI DEM data.

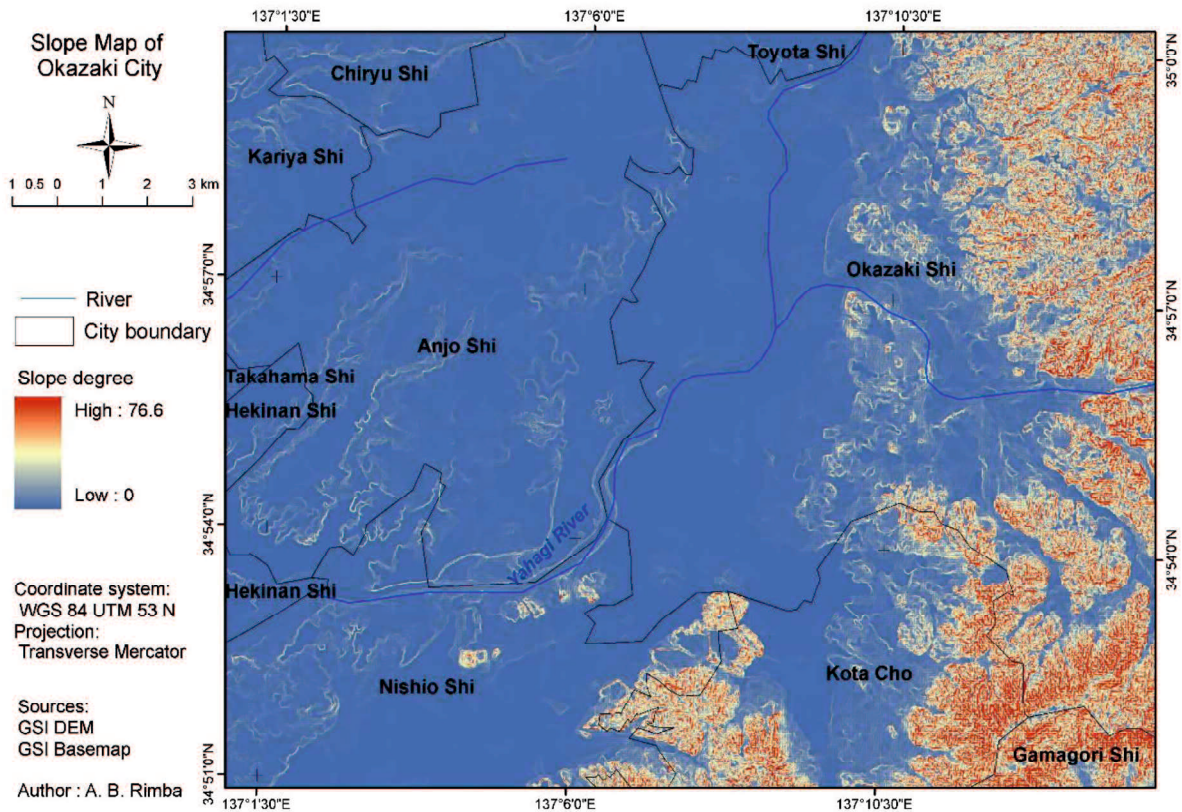


Figure 3. 12 Slope map of Okazaki City

3.3.3.4. Soil

Soils in Japan are grouped into soil groups as the higher class, soil series groups as the medium class and soil series as the lower classification [Amano, 1985]. Soil groups were divided according to their morphology and parent material; soil series groups were divided according to the variation of the thickness of humus layer, freckling and texture; soil series is basic unit classification (grouped according to parent material, morphology and process) [Amano, 1985; Obara, et al., 2014]. Table 3.11 lists the soils group in Okazaki City.

Table 3. 11 Japanese system of soil groups (Amano, 1985)

Soils group	Description
Ando soils	Ando soils are from volcano parent material and unconsolidated soils. Their colors are dark rich from organic matter and have well-drained conditions. At an altitude of 3300m, their textures are sandy-silt regosoils [Perrin, et al., 2001; Amano, 1985]
Ando soils (wet)	Ando soils wet have the same parent material as the Ando soils but poorly-drained conditions and have freckle due to groundwater or irrigation water. Their colors are dark and rich from organics. They distribute in alluvial bottom land and are utilized as a paddy field. [Amano, 1985]
Brown forest soils	Brown Forest soils are composed by various parent material. Their colors are yellow-brown, and they are well-drained and spread in a mountainous area as upland crops, tree crops and pasture. Small parts of these soils are utilized for cultivating [Amano, 1985].
Gley soils	Gley soils are poorly drained alluvial plains and high ground-water tables. These soils are broadly used for paddy rice cultivation [Amano, 1985].
Gray lowland soils	Gray Lowland soils are from Holocene alluvial plains or polders under well- to imperfectly drained conditions. These soils are the most productive for paddy cultivated soil in Japan [Amano, 1985]
Muck soils	Muck soils decompose more than 20% of organic matter from back marshes, the margin of peat moor, etc. Compared to Ando soils, they have low phosphate retention and widely utilized as a paddy field [Amano, 1985].
Red soils	Red soils are decomposed from various parent materials. These soils decompose due to humid conditions, and the warm to the temperate climate in West Japan. Red soils are spreadly in terraces and hills of low altitude near seacoasts and are suitable for upland crops, tree crops and grasses [Amano, 1985].
Yellow soils	Yellow soils decompose due to humid warm and humid temperate climates. Their characteristics are similar to Red soils except for their yellow color. Some of them are poorly drained and have freckles [Amano, 1985].
Man-made soils (artificially flattened areas)	Man-made soils are emplaced soil at least to a depth of 35 cm from the surface. These soils are deeply disturbed or reshaped by humans. There are two types of man-made soils according to their altitude, i.e. Man-made Upland soils and Man-made Lowland soils [Amano, 1985].

Figure 3.13 displays the distribution of soil groups in Okazaki City. It was generated by manual digitalizing by using ArcGIS 10.2.2. This soil map was produced by the National Land Agency (a.k.a MLIT) on July 7th, 1975.

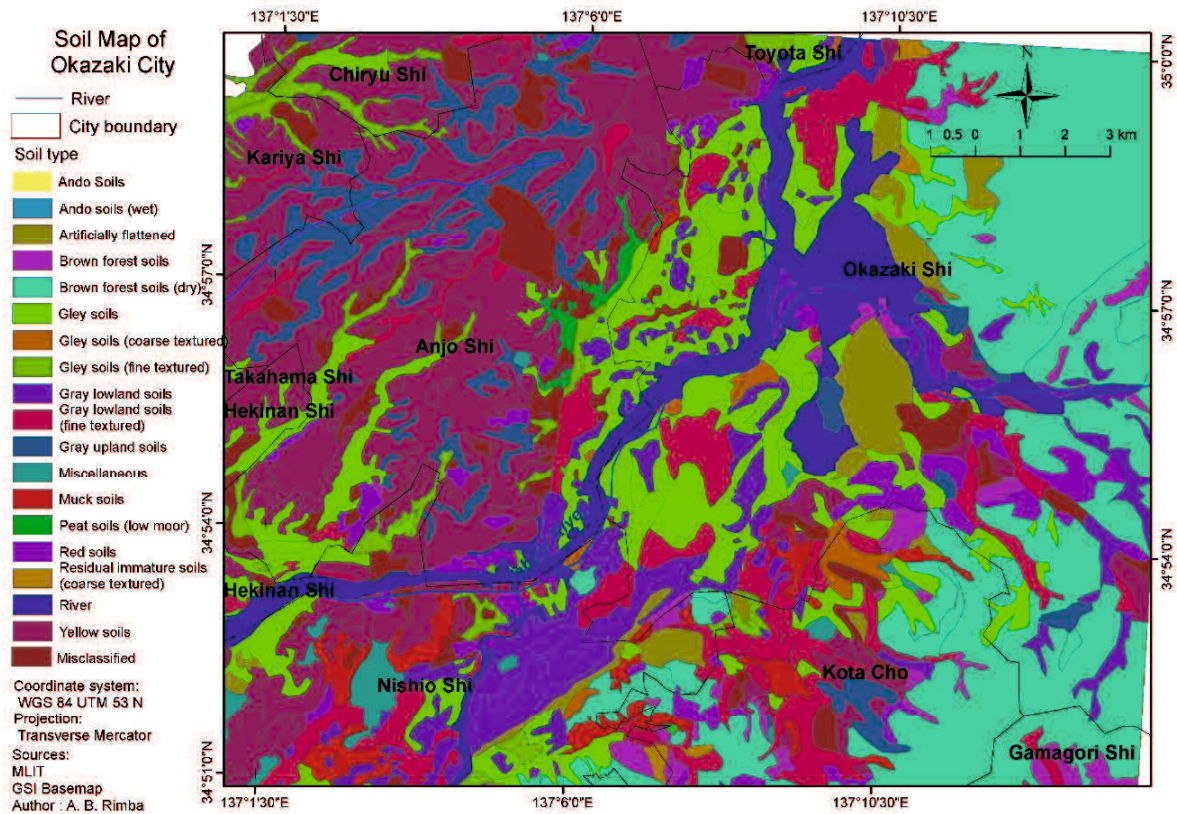


Figure 3. 13 Soil map of Okazaki City

Soil water infiltration is used as a flood parameter. It influences the runoff, soil loss, aquifer recharge, irrigation management and plant water availability. The rate of water infiltration depends on external factors and soil properties, which vary based on the type of soil [Tejedor, et al., 2013]. Thus, a literature review was done to investigate the characteristic of the soil type [Amano, 1985; Kyuma & Kawaguchi, 1966; Institute of Soil Science, 1981; Kern, 2010; Tejedor, et al., 2013; Doerr, et al., 2000]. Soil water infiltration is a parameter that needs to be known to explain many processes such as runoff, soil loss, and aquifer recharge, as well as for irrigation management and plant water availability [Tejedor, et al., 2013].

The water levels in the level area are very low (Brouwer, 1990). This condition becomes worse during the rainy season. The infiltrating process from the previous rainy day is still continuing when the new rainy day comes, or the rainfall intensity is larger than the infiltration rate, and this condition could lead to flooding. Soil rate infiltration according to the slope is listed in Table 3.12.

Table 3. 12 Soil infiltration rate based on % Slope (USDA, 1990) (Kern, 2010; Johnson, 1991)

Soil Texture, Type	Infiltration Rate (IR) mm/hour				
	0-4%	5-8%	8-12%	12-16%	> 16%
Coarse Sand	31.75	25.40	19.05	12.70	7.87
Medium Sand	26.92	21.59	16.26	10.66	6.86
Fine Sand	23.88	19.05	14.22	9.65	6.10
Loamy Sand	22.35	17.78	13.46	8.89	5.59
Sandy Loam	19.05	15.24	11.43	7.62	4.83
Fine Sandy Loam	16.00	12.7	9.65	6.35	4.06
Very Fine Sandy Loam	14.99	11.94	8.89	6.10	3.81
Loam	13.72	10.92	8.38	5.59	3.56
Silt Loam	12.70	10.16	7.62	5.08	3.30
Silt	11.18	8.89	6.60	4.57	2.79
Sandy Clay	7.87	6.35	4.83	3.05	2.03
Clay Loam	6.35	5.08	3.81	2.54	1.52
Silty Clay	4.83	3.81	2.79	2.03	1.27

3.3.3.5. Land-cover

Land use is the surface cover of the earth in a specific location (e.g., vegetation type, a man-made structure, etc.) [Sohl & Benjamin , 2012]. It can be derived directly from remote sensing data and it needs to be verified by survey [Sohl & Benjamin , 2012; Ahmed & Ahmed, 2012; Ahmed, et al., 2013]. Furthermore, the land use can represent the socio-economic condition in the certain area (Ouma & Ryutaro , 2014; Ahmed & Ahmed, 2012). The classification of land-use is listed in Table 3.3.

Figure 3.14 shows the distribution of Land cover map that was generated with Sentinel-2 imagery. We downloaded the Level-2A (Bottom-of-atmosphere reflectance in cartographic geometry, prototype product). It was recorded on November 22, 2016. It is a panchromatic image with 10 m for visible and VNIR band (Band 2, 3, 4 and 8) [ESA, 2000].

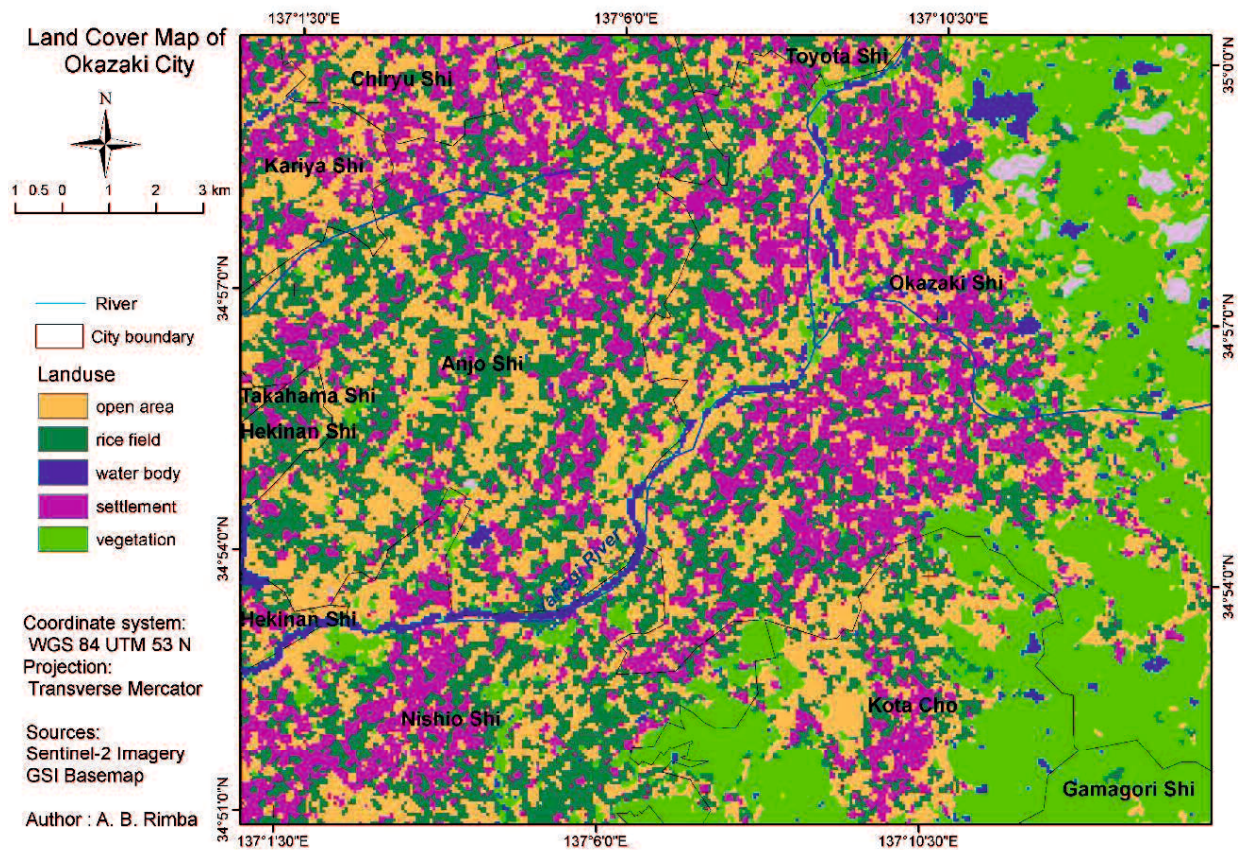


Figure 3. 14 Land cover map of Okazaki City

3.3.4. Analytical Hierarchy Process (AHP)

AHP is a decision-making technique utilized for solving complex problems, with many parameters of interrelated objectives or concerned criteria. The level of each parameter is not equal; some parameters are dominant to others. Different weights can generate the difference in the level of susceptibility [Ahmed, 2015]. It is based on ranking from the experts, literature reviews and previous study. The AHP pair-wise have to be consistent to all pair-wise comparisons. The AHP parameters for flooding were adopted from Ouma and Tateishi (2014) (Ouma & Ryutaro , 2014), and we modified by interviewing two hydrologists. Ouma *et al.* formulated the parameter with 16 experts (4 hydrologists, four engineers and eight end-users). They selected six high influence parameters (rainfall, drainage density, elevation, slope, soil and land use). We modified the parameter by literature review and evaluation from experts to decide the influencing parameter for flooding. Thus, we utilized rainfall, drainage density, slope, soil and land cover as the parameters.

3.3.4.1. Relative weight of parameters

The ranking is related to their relative importance as listed in Table 3.13. The relative importance has a range from 1 to 9; 1 means an equal contribution of the pair-wise parameter and 9 means very important parameter [Saaty, 1987; Saaty, 2008].

Table 3. 13 Nine-point pairwise comparison scale (Saaty, 1987; Saaty, 2008)

Intensity of importance	Definition	Explanation
1	Equal importance	Two elements contribute equally to the objective
3	Moderate importance	Experience and judgment slightly favor one parameter superior another
5	Strong Importance	Experience and judgment strongly favor one parameter superior another
7	Very strong importance	One parameter is favored very strongly superior another; its dominance is demonstrated in practice
9	Extreme importance	The evidence favoring one parameter superior another is of the highest possible order of affirmation
2,4,6,8 can be used to express intermediate values, 1.1, 1.2, etc. for parameters that are very close in importance		

The number of parameter influences the matrix; 3x3 for three parameters, 4x4 for four parameters, 5x5 for five parameters and so on. The proposed method used a 5x5 matrix. The comparisons of parameters were generated from the expert judgment, literature review and the previous study. The weighting calculation follows Eq.3.4.

$$A = \begin{bmatrix} a_{11} & a_{12} & a_{13} & a_{14} & a_{15} \\ a_{21} & a_{22} & a_{23} & a_{24} & a_{25} \\ a_{31} & a_{33} & a_{34} & a_{35} & a_{35} \\ a_{41} & a_{42} & a_{43} & a_{44} & a_{45} \\ a_{51} & a_{52} & a_{53} & a_{54} & a_{55} \end{bmatrix}, a_{kk}=1, a_{lk}=\frac{1}{a_{kl}}, a_{kl} \neq 0 \quad (3.4)$$

where A is weight of the parameter, a_{kl} (kl = 11, 12, ... 54,55)

The right eigenvalue (ν) corresponding to the maximum eigenvalue (λ_{\max}) is calculated to normalize and find the relative weight (A_ν) of the matrix by following Eq. 3.5

$$A_\nu = \lambda_{\max} \nu \quad (3.5)$$

3.3.4.2. Consistency Index (CI) and Consistency Ratio (CR)

The output of AHP has to be consistent for all the pairwise comparisons which measured by Consistency Index (CI) and Consistency Ratio (CR) (Saaty, 1977). The consistency index (CI) is obtained by Eq.3.6; where n is a number of parameters.

$$CI = \frac{\lambda_{max} - n}{n - 1} \quad (3.6)$$

The final calculation is consistency ratio; it is a ration of the CI and random index (RI), RI value for five parameters is 1.12 (Saaty, 1987). The maximum threshold of CI is ≤ 0.1 and $CR \leq 10\%$ (Saaty, 1977); the rational value is when the CI and CR fulfilled the maximum threshold value. The consistency ratio (CR) is obtained Eq. 3.7.

$$CR = \frac{CI}{RI} \quad (3.7)$$

3.4. Result

3.4.1. Flood-vulnerability Map by Simple Superimposed in Kumamoto City

The flood-vulnerability map is the final map for this research. It was created by combining three parameters: the slope map, the land-cover map and the rainfall map. The weighting method for determining the class value, in which each feature on the map has a value, was used. This value was determined by use of the Ven T. Chow method [Chow, et al., 1964], with modification and has equal weight. The level of vulnerability was categorized into five classes: very low, low, medium, high and very high. The classes were determined by use of the equal-interval method, which is the maximum range value subtracted by the minimum range value and then divided by number of classes. By applying Equation 3.2, the interval class of classification is 8. By use of this method and the pattern of parameters, the highest vulnerable area is determined to be in the middle of Shirakawa watershed. The cloud is still covering the information because this research used only image data as the primary data and all the image data were processed from satellite data. The total area of the flood vulnerable area can be seen in Table 3.14. The distribution of flood-vulnerable areas can be seen in Fig. 3.15.

The vulnerability map shows that the lower area has high flood vulnerability. For example, the rainfall becomes surface runoff in the settlement areas because of the hard road surfaces and less vegetation density. The headwater Shirakawa watershed has low flood vulnerability, because this area has high vegetation density and it was covered by forest. On the other hand, this area has a steep and mountainous slope. Therefore, slope failure can occur in this area.

Table 3. 14 Total area of flood vulnerability in Shirakawa watershed

Vulnerability	km ²
Very Low	17.47
Low	242.12
Medium	184.56
High	114.32
Very High	1.21
Total	559.68

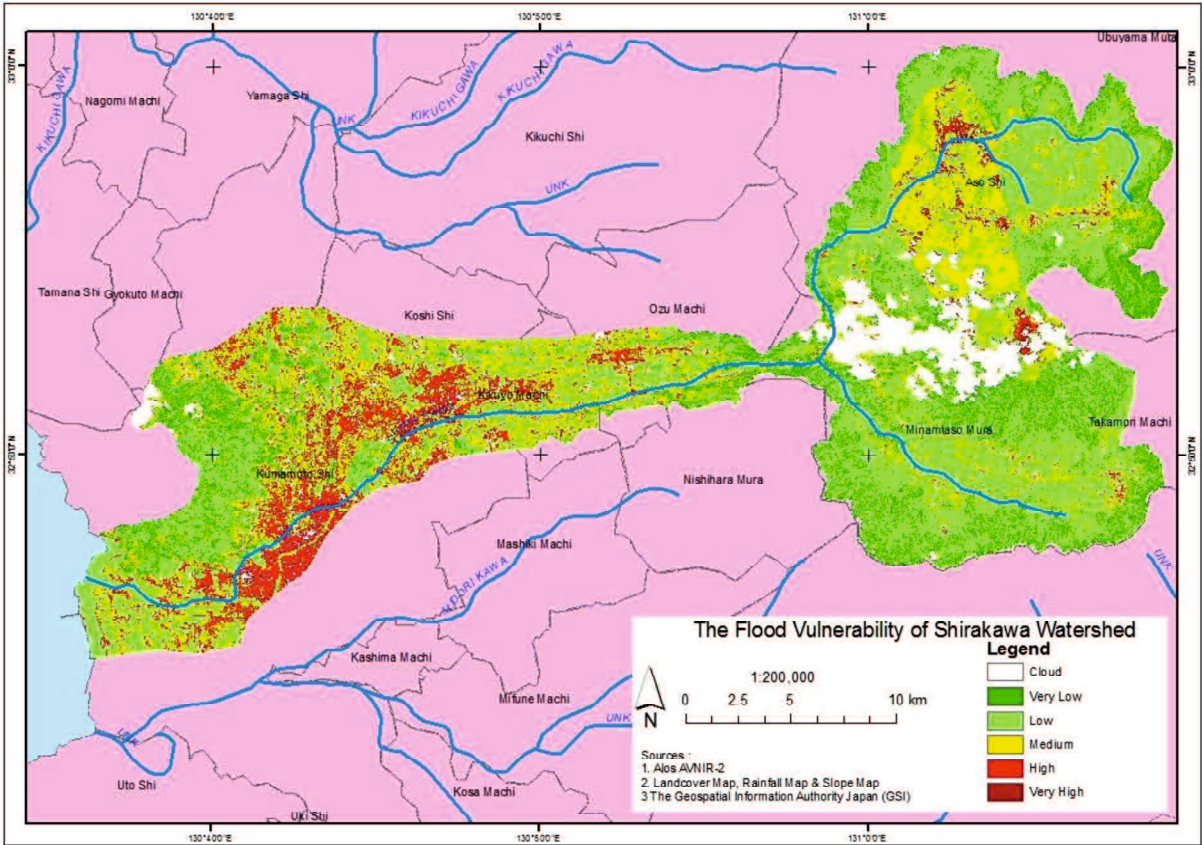


Figure 3. 15 Flood vulnerability of the Shirakawa watershed

To determine the flood-vulnerability area, these parameters should be of use. In this case, vegetation cover should protect this watershed. However, this area is always flooded, even though it is covered by vegetation. The most vulnerable area is approximately 115.59 km², out of the total area of 559 km². This research is only one way to produce the vulnerability map. The vulnerability area in this paper was produced on the basis of satellite imagery only. This result needed to be verified by field survey and historical flood data.

The limitations of this method were; all parameters have the same weight, only three parameters influenced the flood vulnerability, no verification data. Thus, the same procedure was done and applied to Okazaki City as explained in Section 3.4.2.

3.4.2. Flood-vulnerability Map by Simply Superimposed in Okazaki City

By applying Simply superimposed method following from Shirakwa watershed, this method was applied to Okazaki City. There was five parameter which have same weight as listed in Table 3.15. This table was generated from re-classification of Table 3.3, Table 3.9, Table 3.10 and Table 3.12 according to the literature review.

Table 3. 15 Flood parameters for simple superimposed in Okazaki City

Parameters	Re-classify the parameter	Ranking
Rainfall intensity (JMA, 2016)	10-20 mm/hours	1
	20-30 mm/hours	2
	30-50 mm/hours	3
	50-80 mm/hours	4
	>80 mm/hours	5
Drainage density (DD) [ESRI, 2001]	< 0.001434 m/m ²	1
	0.001435-0.00287 m/m ²	2
	0.00288-0.004305 m/m ²	3
	0.004306- 0.00574 m/m ²	4
	>0. 00574 m/m ²	5
Slope [Demek, 1972]	Very strong, Extreme, steep and very steep slope	1
	Strong slope	2

	Gentle slope to Moderate slope	3
	very gentle slope	4
	Level to Near level	5
Soil [Brouwer, 1990] (Basic infiltration rates by FAO)	Less 30 mm/hour (sand)	1
	20-30 mm/hour (sandy loam)	2
	20-10 mm/hour (loam)	3
	5-10 mm/hour (clay loam)	4
	1-5 mm/hour (clay)	5
Land cover [Rimba & Miura, 2016]	Vegetation (forest)	1
	Vegetation (crops tree)	2
	Barren land	3
	Build up land	4
	Rice field and open area	5

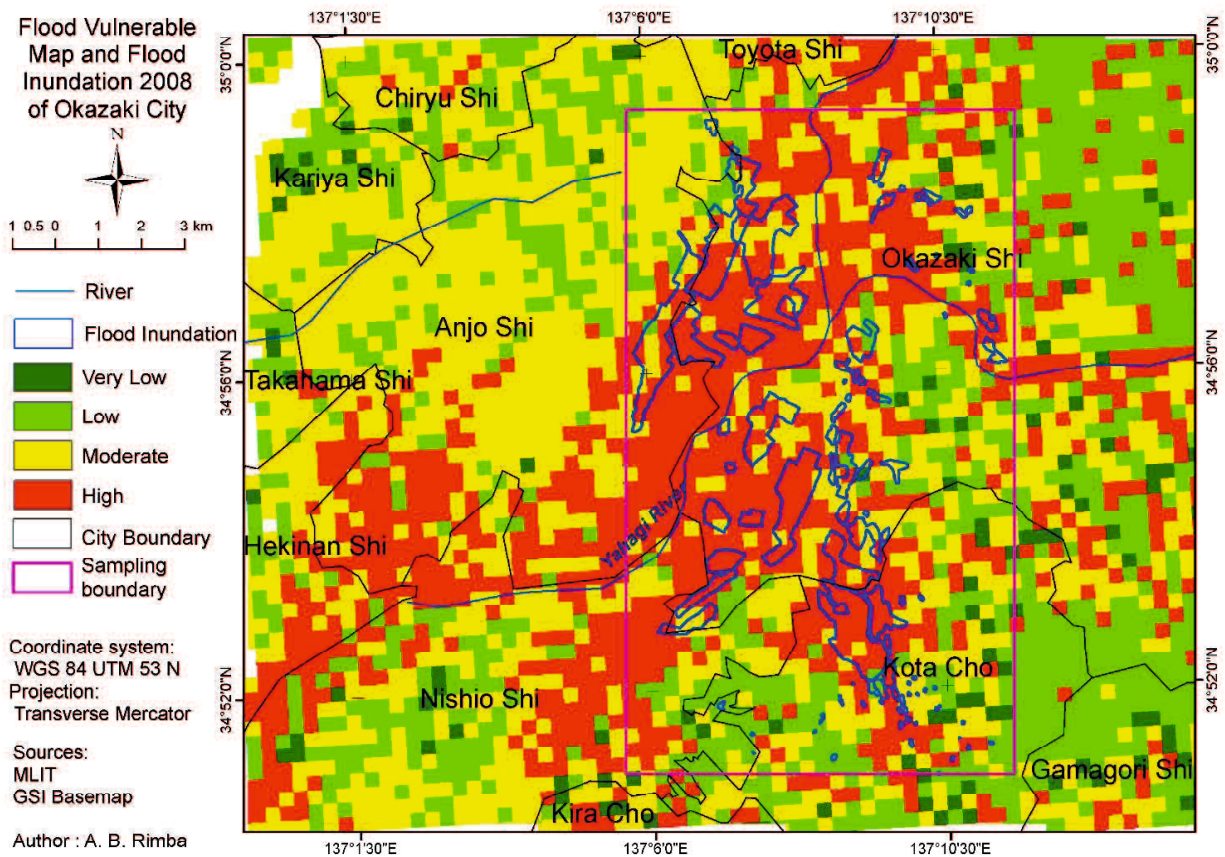


Figure 3. 16 Flood vulnerability of Okazaki City according to the Simple Superimposed Method

The flood distribution can be seen in Fig. 3.16. The vulnerability interval class was grouped according to Eq. 3.2. The level of vulnerable intensity “very low”, “low”, “moderate” and “high” based on the experts knowledge following AHP vulnerable level. The weakness of this method is the same weight for all parameters. In the real condition, the level of flood parameters must be different depend on their influence to the flood characteristic. Hence, this method was improved by using AHP. We used the same parameters and area to show how much the improvement of the accuracy of Simple Superimposed Method.

3.4.2.1. Flood Validation for Simple Superimposed Method

In order to validate our assessment, a quantitative method was applied. This method is based on the contingency table which was shown in Table 3.16. The flood threshold used for flood discrimination is high vulnerability area (red color) and non-flood discrimination is others (very low to moderate). In Table 3.16, a, b, c, and d stand for “hit”, “false alarm”, “miss” and “correct negative”. The “Hit” represents correctly estimated flood area, “miss” represent when flooding is not estimated but actual flooding occurs, “false alarm” represents when flooding is estimated but actually flooding does not occur, and “correct negative” describes correctly estimated non-flooded.

Table 3. 16 The contingency table

Model	Survey		Total
	Flood	Non-Flood	
Flood	a	b	a+b
Non-Flood	c	d	c+d
Total	a+c	b+d	a+b+c+d

Using the result shown in Table 3.16, we calculated the Probability of Detection (POD), Probability of False Detection (POFD), Critical Success Index (CSI), Bias and Relative Operating Characteristic (ROC) [Mason, 1982; Brooks, 2004; Brooks, et al., 2011] as determined in Eq. 3.8-3.11.

$$POD = \frac{a}{(a + c)} \quad (3.8)$$

$$POFD = \frac{b}{(b + d)} \quad (3.9)$$

$$CSI = \frac{a}{(a + c)} \quad (3.10)$$

$$Bias = \frac{(a+b)}{(a+c)} \quad (3.11)$$

POD explained how good the model estimates are in detecting flooding area; the range is 0 (false prediction) to 1 (perfect prediction). POFD shows false alarm of flood; its range 0 (no false prediction) to 1 (perfectly false prediction). Bias measures the similarity of “yes” model and “yes” survey. A perfect score is 1, <1 means under forecast and >1 over forecast. CSI means how well the “yes” model correspond to “yes” survey; 0 indicates no correspondence and 1 indicates perfect.

ROC curves represent excellent, good, and worthless for an accuracy assessment. The accuracy is measured by the area under the ROC curve which was called Area Under Curve (AUC). An area of 1 represents a perfect test; an area of 0.5 represents a worthless test. The accuracy classification of AUC was explained as follows: 0.9-1 excellent (A), 0.80-0.90 = good, 0.70-0.80 = fair, 0.60-0.70 = poor, 0.50-0.60 = fail. Referring to Fig. 3.16, our model produced flood vulnerability area with the AUC 89%. It means that our model would be considered good at separating flooded and non-flooded area. The AUC can be calculated by following Eq.3.12.

$$AUC = \sum_{i=1}^n [x_{i+1} - x_i] \left[y_i + y_{i+1} - \frac{y_i}{2} \right] \quad (3.12)$$

Where x is the rate of POD for scenario i ; y is the rate of POFD for the scenario i ; and n is the number of suitability group.

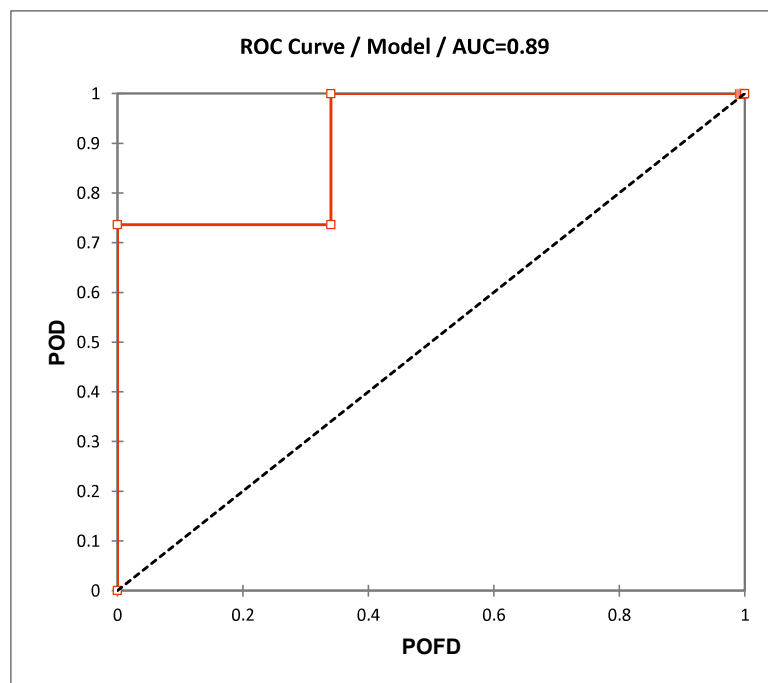


Figure 3. 17. Relative operating characteristic curve for flood vulnerability in Okazaki City by using Simple superimposed method.

We generated accurate results; POD (0.73) means the high accuracy of flood event which occurred in predicted flood area, POFD (0.34) means that low probability of false alarm of the flood, CSI 0.3 means normal correspondent and Bias (2.2) means over prediction of flooded area. The ROC can be seen in Fig. 3.16 and the Area Under Curve (AUC) was 0.89.

3.4.3. Flood-vulnerability Map by AHP Process in Okazaki City

3.4.3.1. Ranking of the map criteria by AHP

The main use of AHP is the ranking and prioritization of multi-criteria parameter. Priority framework quality affects the effectiveness of available sources which are the essential judgment from the decision maker. Furthermore, the experts usually use their experiential judgment when making the decision. Each of the expert participants determined the weight to the design factors with the following procedures (Saaty, 2008):

1. Determine each factor percentage to distinguish the weight.
2. Assign the least important factor from step 1 and assume the importance scale among the objective is linear.
3. The importance of factor should be ranked from 1 to 5, where 1 represents least important factor and 5 is the most important one.

The calculation of the ranking of each factor was conducted by using pairwise comparison which can be seen in Eq. 3.4. The results are shown in Table 3.16. There are five factors which were considered in this process namely, rainfall, drainage density, slope, soil and land cover. Then, we normalized the converted matrix which can be shown in Table 3.17. A more detailed calculation was described in Equation 3.5. The priority (Table 3.18) is also called normalized principal eigenvector, and it is used to weight the standardized raster layer. From Table 3.18, the consistency check CI was calculated referring to Eq.3.6 and it is shown in Table 3.19. Then, we computed CR as also shown in Table 3.17. This step is necessary to determine if our comparisons are consistent. The CR is designed in such a way that if $CR < 10\%$, the ratio indicates a reasonable level of consistency in the pairwise comparison. As shown in Table 3.19, since the CR is less than 10%, the ratio indicates a reasonable consistency in this analysis, and it implies that the determined weights are acceptable. In addition, the calculation of the eigenvector is used as a coefficient for the respective factor maps which combined in the weighted overlay.

Table 3. 17 Ranking of flood vulnerability parameters

Criteria	Rainfall	Drainage density	Slope	Soil	Land cover
Rainfall	1	1	1/3	2	2
Drainage density	1	1	1/2	2	2
Slope	3	2	1	4	4
Soil	1/2	1/2	1/2	1	1
Land cover	1/2	1/2	1/4	1	1
Summary	6	5	2 $\frac{1}{3}$	10	10

Table 3. 18 Weighted comparison table

	Rainfall	Drainage	Slope	Soil	Land cover	Priority	Percent
Rainfall	0.167	0.200	0.143	0.200	0.200	0.174	17%
Drainage	0.167	0.200	0.214	0.200	0.200	0.196	20%
Slope	0.500	0.400	0.429	0.400	0.400	0.434	43%
Soil	0.083	0.100	0.107	0.100	0.100	0.098	10%
Land cover	0.083	0.100	0.107	0.100	0.100	0.098	10%
Total	1	1	1	1	1		100%

Table 3. 19 Consistency of pair comparison

	Rainfall	Drainage density	Slope	Soil	Land cover
Lambda	1.0189	1.0024	1.0016	1.0024	1.0024
Note; n=5, CI=0.007, CR=0.6 %					

To calculate the weight and ranking in each factor, the pairwise comparison matrix and factor map are employed. The weight value provided the prioritize factor which expressed as a percentage value between 0 to 100 %. Using linear weighted combination, the sum of weight was expressed as 100%. A summary of targeted factors, their weights and rankings are listed in Table 3.20. We applied the information in this table to generate the distribution of vulnerable area to flooding. The ranking of each reclassified factor is based on literature review. We reclassified the Table 3.3, Table 3.9, Table 3.10 and 3.12 as the same as Table 3.15. The range of ranking was 1 to 5; highest influence factor was rank 5 and lowest influence factor was 1. The order of normalized weight was Slope parameter (43%), Drainage density (DD) parameter (20%), Rainfall intensity (17%) then infiltration rate (10%) and land cover (10%). Looking at the weight of each factor one can see that slope has the highest weight. It implies that slope has more contribution to flooding than other factors. Slope influences the direction of the runoff or subsurface drainage. Furthermore,

the slope has dominant control of the rainfall of stream flow, duration of flow and duration of infiltration process.

Table 3. 20 Weighted flood hazard ranking

Parameters	Relative weight	Re-classify the parameter	Ranking
Rainfall intensity (JMA, 2016)	17%	10-20 mm/hours	1
		20-30 mm/hours	2
		30-50 mm/hours	3
		50-80 mm/hours	4
		>80 mm/hours	5
Drainage density (DD) [ESRI, 2001]	20%	< 0.001434 m/m ²	1
		0.001435-0.00287 m/m ²	2
		0.00288-0.004305 m/m ²	3
		0.004306- 0.00574 m/m ²	4
		>0. 00574 m/m ²	5
Slope [Demek, 1972]	43%	Very strong, Extreme, steep and very steep slope	1
		Strong slope	2
		Gentle slope to Moderate slope	3
		very gentle slope	4
		Level to Near level	5
Soil [Brouwer, 1990] (Basic infiltration rates by FAO)	10%	Less 30 mm/hour (sand)	1
		20-30 mm/hour (sandy loam)	2
		20-10 mm/hour (loam)	3
		5-10 mm/hour (clay loam)	4
		1-5 mm/hour (clay)	5
Land cover [Rimba & Miura, 2016]	10%	Vegetation (forest)	1
		Vegetation (crops tree)	2
		Barren land	3
		Build up land	4
		Rice field and open area	5

Once the weight in each factor was determined, the multi-criteria analysis was performed to produce flood-vulnerable area by using the GIS approach. To compute the vulnerable area, a weight linear combination was applied as shown in Eq.3.13.

$$Vulnerable\ Index = 0.17 * R + 0.2 * DD + 0.43 * S + 0.1 * So + 0.1 * LC \quad (3.13)$$

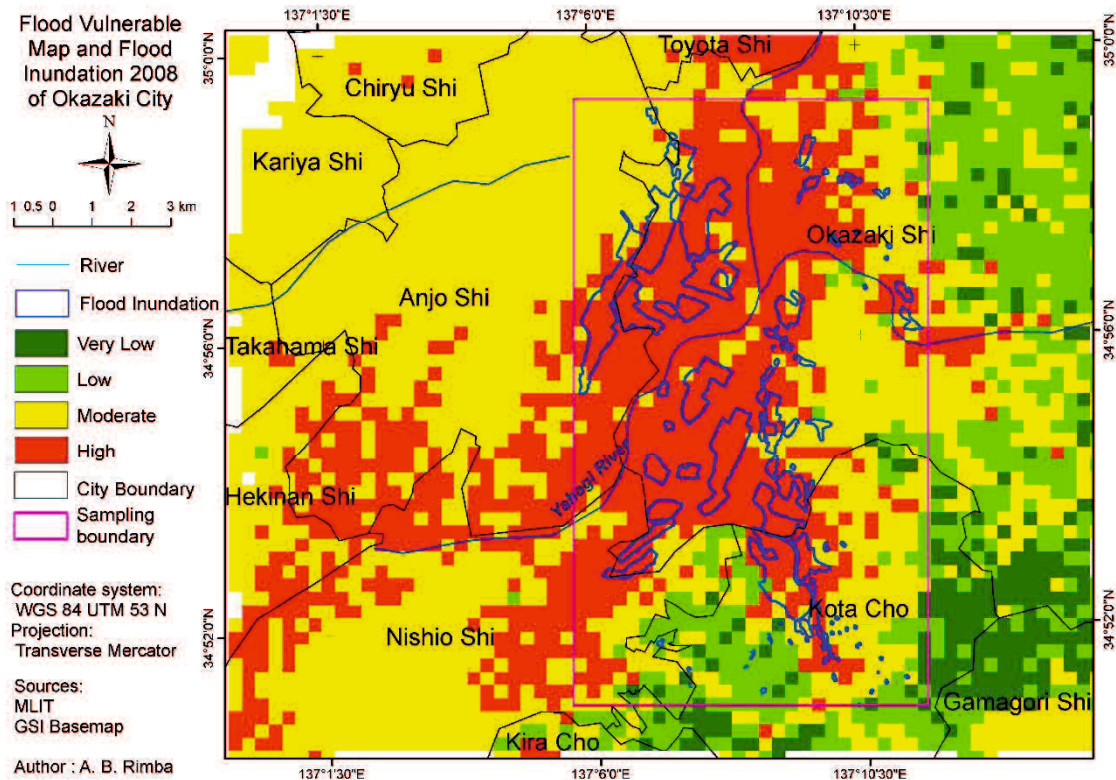


Figure 3. 18 Vulnerable to flood area in the lowland of Okazaki City, the field survey of flood inundation in August 2008 and the sampling area for accuracy assessment.

The result is the flood-vulnerable area in the lowland of Okazaki City. It is shown in Fig. 3.18 and Fig. 3.20. It was categorized into four vulnerable classes, e.g., “very low”, “low”, “moderate” and “high” according to the expert's knowledge-based classification. The result described that 28% area was classified as a high hazard zone. This area was close to the big river and in lowland area; 5 % of lowland area of Okazaki City was categorized as a moderate level of vulnerability to flooding in the lowland area. The difference of infiltration rate categorized the lowland area into high and moderate flood-vulnerable levels. In contrast, 67% of the Okazaki City was categorized as very low to low level of flood hazard. Most of the area was located in higher elevation and far from DD area as shown in Fig. 3.18 and Fig. 3.20, the main city of Okazaki is prone to high vulnerability. It was due to very slow infiltration rates and near level slope. Finally, a single map from a combination of multi-parameter and multi-criteria analysis was shown in Fig. 3.18, as the representation of flood prediction map for the study.

3.4.3.2. Flood Validation for AHP method

The flood-vulnerable area was distributed in the level to near level slope of 0-2%, drainage density more than 0.00574 m/m², rainfall over 80 mm/hour, very slow infiltration rate (1-5 mm/hour) and land surface covered by rice field and open area (Table 3.20). In addition, to perform the validation, flooding based field verification which was conducted by the local government of Okazaki City and MLIT was used. The survey data of flood extent was employed for verification. Figure 3.18 shows the flood vulnerability map, survey data of flood extent in 2008 and sample area for accuracy assessment.

We generated accurate results; POD (0.88) means the high accuracy of flood event which occurred in predicted flood area, POFD (0.28) means that low probability of false alarm of the flood, CSI 0.44 means normal correspondent and Bias (1.9) means over prediction of flooded area. The ROC can be seen in Fig. 3.19 and the Area Under Curve (AUC) was 0.95.

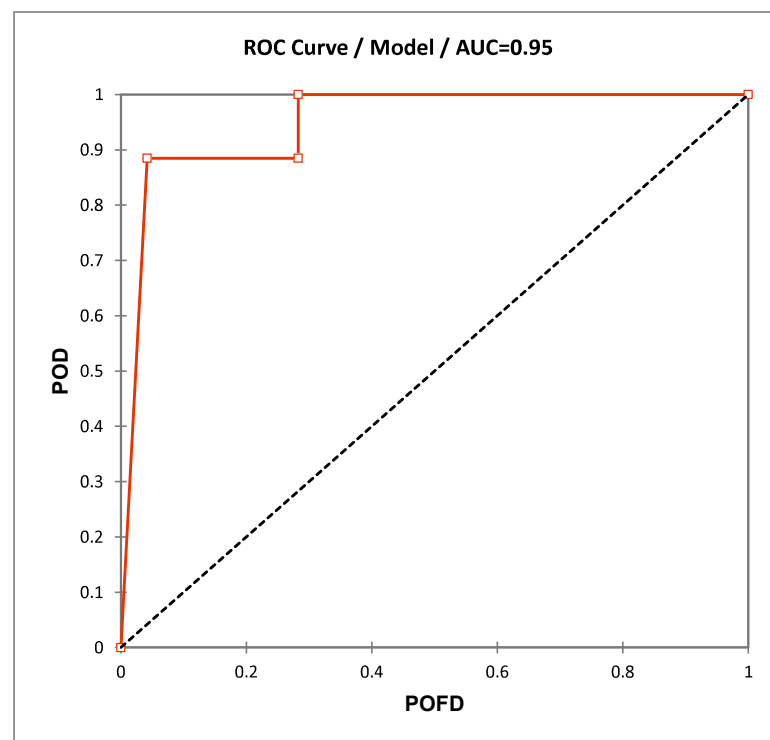


Figure 3.19 Relative operating characteristic curve for flood vulnerability in Okazaki City by using AHP procedure.

3.4.3.3. Urban Flood Risk Area

The assessment of flood risk area was accomplished by using land cover type. We evaluated the risk of flooding based on land cover type by using cluster analysis. Approximately 10,612.07 ha was vulnerable to flood in the lowland area of Okazaki City. The result stated that agriculture and

residential areas were 49.5 % and 29.6% respectively of the total flood-vulnerable area, while the lowest percentage of the vulnerable area was located in the open area (17.5%) and the vegetation e.g. forest (3.4%). It occurred due to land cover influence on filtration rate.

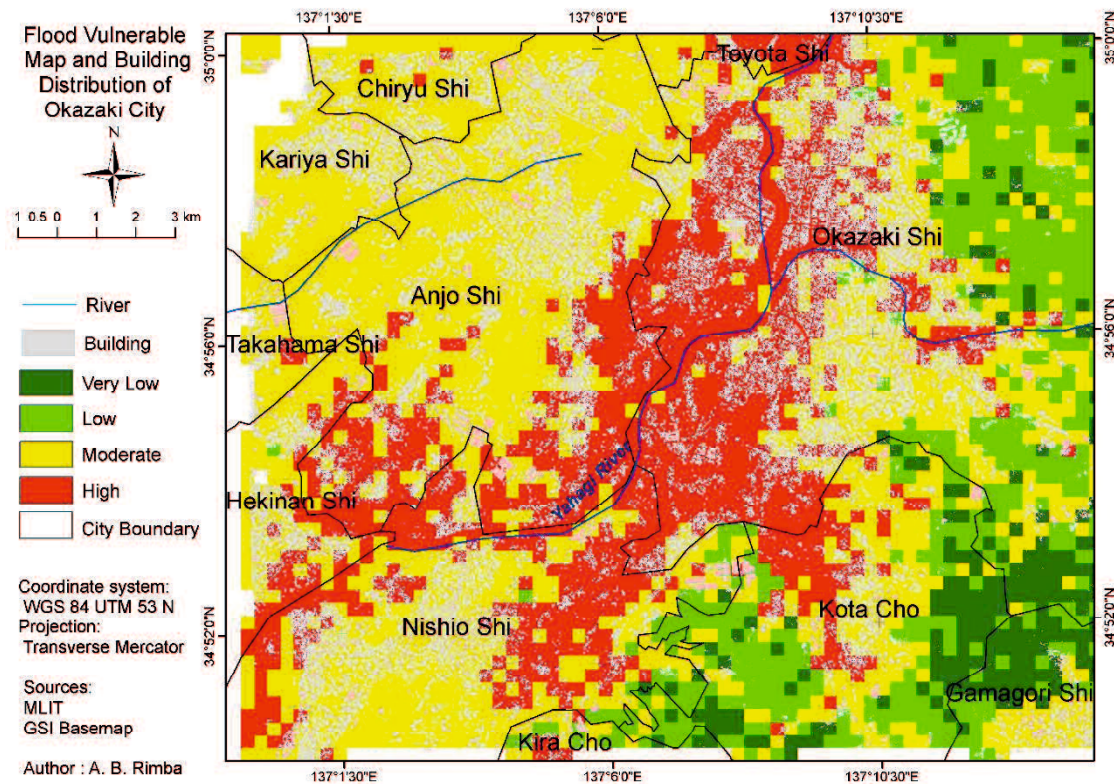


Figure 3. 20 Building on vulnerable to flooding area in Okazaki City

Regarding the flood simulation with the building data from GSI (all permanent buildings; offices, schools, hospitals, houses, etc), flooding affected approximately 1136.66 Ha total of building area as shown in Fig. 3.20 with gray color indicating the building area. According to the building distribution, more than half of the population in the lowland area of Okazaki City lived in flood-prone areas. Moreover, Okazaki City was also covered by agricultural land which consisted of paddy (1,400 ha), wheat (560 ha), soy (505 ha), and vegetable and fruits (i.e., eggplant, strawberry, grape (48.9 ha)) (Okazaki, 2013). Most of the agricultural sector was located around the Yahagi River which was also categorized as a flood-prone area. This condition caused major economic loss, in particular in infrastructure, agriculture and suspension of business activity. Flood inundation caused not only economic loss but also caused various diseases such as waterborne disease, vector-borne disease, etc.

Urban sustainability can be influenced by economic development, socioeconomic policy, population growth, physical environment, and natural hazards [Rozos, et al., 2011; Xiao, et al., 2007]. However, in the interim of planning, development, and management of an urban area, only the economic and social variables are usually considered. As a result, in vulnerable sites, such as areas with steep slopes, natural hazards often occur, in particular floods which can cause a huge destruction of the social and economic network and lead to the loss of human lives and property. In order to avoid the aforementioned outcome, during the planning and growth of an urban area, it is necessary for the decision makers, engineers, planners, and managers to consider the physical variables of the urban area, in particular the susceptibility to natural hazards.

Multi-criteria analysis such as AHP is an effective decision support tool for dealing with complex decision constellations where technological, economical, ecological, and social aspects have to be covered. The AHP method was applied and combined with GIS and Remote Sensing for assessing the level of flood vulnerability of areas. Furthermore, this method was relatively inexpensive, easy to use and more importantly, allows the combination of many parameters, statistical analysis and physical properties which can derive from satellite or survey data. However, AHP has its problems and challenges. AHP relies on input from the experts, and it is sometimes difficult to find experts

3.5. Conclusion

It is difficult to reduce the occurrence of natural disasters, including floods. What we can do is minimize the impact of natural disasters. Assessing the vulnerable area to flooding disasters is one of the parameters in creating a flood risk map for disaster mitigation and urban planning.

This study tried to determine the area that was vulnerable to flooding using integrated approaches of remote sensing, GIS, to simply a superimposed method and spatial multi-criteria evaluation through AHP approach. The simply superimposed method was refined by AHP procedures and enhanced the accuracy from 0.89 AUC to 0.95 AUC. The limitation of the Simply superimposed method in this study was the equal weight of all parameters of flood vulnerability. Two locations were applied to flood vulnerability mapping, i.e., Shirakawa watershed in Kumamoto Prefecture and Okazaki City in Aichi Prefecture. Due to the lack of verification data in Kumamoto Prefecture, we deeply analyzed data for Okazaki Prefecture.

The parameters of the slope, drainage density, rainfall intensity, infiltration rate, and land cover were applied to predict the affected area of flooding. The AHP calculation shows that slope

was the highest weight (43%) in determining vulnerability to flooding through the spatial-weighted overlay, followed by drainage density (20%), rainfall intensity (17%), infiltration rate (10%) and land cover (10%). This calculation resulted in a 0.6% for consistency ratio. The slope parameter was the most important parameter because the slope influences the flow direction, runoff and soil infiltration. There are several measurement methods for urban planning in Japan, which are applied to each area by the local government varying by local circumstances under the City Planning Law [MLIT, 2013]. According to the structure of City Planning System from MLIT, there are three components i.e., Land Use Regulation, Urban Facilities and Urban Development Projects; one component of Urban Development Projects is promotion district for reconstruction of the disaster-stricken urban area. We proposed the result of this study as a consideration for urban planning in Okazaki City. The result of the flood-vulnerable areas shows excellent accuracy; POD (0.88), POFD (0.28), CSI (0.44), Bias (1.9) and AUC (0.95) from the ROC graph. This method can be utilized to complement the hazard map of MLIT.

The total area of Okazaki City is approximately 95,679.2 ha, and 10,612.07 ha or 11.1% of total area is highly vulnerable to flooding. The land cover with the highest risk to the flood was a resident area (29.6%) and agriculture area (49.5%) from the total area of the flood-vulnerable area in the lowland area. Those areas were close to the big river and had slow infiltration rate, and level to near level slope. This condition influences the economic condition. By analysis of the building distribution and the flood risk area, it is clear that approximately 1,366.66 ha total of construction area (i.e., offices, schools, hospitals, houses, etc) is in the flood-prone area.

This method can be applied in other areas, even with different geographical characteristics from this study area. The use of other parameters, including river proximity and a comparison study using other sources of elevation data will be analyzed for future work. This study aimed to evaluate the physical parameter of flood vulnerability. For future work, we will consider the social, economic, ecological, culture and institutional. This study contributes to an important approach for the effectiveness of disaster mitigation and urban planning.

CHAPTER 4

EVALUATION OF FILTERING PERFORMANCES TO REDUCE THE SPECKLE NOISE FOR DETECTING FLOOD INUNDATION AREAS FROM SAR IMAGES

4.1. Introduction

Remote sensing is a useful tool to investigate the natural hazards and disasters such as flood, typhoon, landslide, land subsidence, tsunami, forest fire and others [Schumann, 2015; Martino, et al., 2009; Wiesmann, et al., 2001]. Recent researches have identified the potential of remotely sensed data to improve our understanding of hydrological hazards, especially surface phenomena such as flooding [Yan, et al., 2015; Bates, 2012; Joyce, et al., 2009; Gillespie, et al., 2007; Sanyal & Lu, 2004; Adam, et al., 2014; Smith, 1997]. They concluded that the use of satellite imagery in natural hazards damage assessment and prediction could be very cost and time effective, and the use of synthetic aperture radar (SAR) data is strongly recommended for flood inundation mapping because of their all-weather and day–night capability and the sensitivity of microwaves to liquid water.

Flooding is a major hazard in both rural and urban areas worldwide, but it is in urban areas that the risks to people and the economic impacts are most severe [Mason, et al., 2012; Ouma & Ryutaro, 2014]. Rapid flood mapping, together with uncertainty assessment and delivery of flood maps, are of considerable importance for response activity planning during emergencies and as a support for long-term risk management [Giustarini, et al., 2014]. Floods are one of the most important natural disasters as they inundate large areas causing damage to agricultural crops and property, road and rail links, and the loss of human lives [Brivio, et al., 2002; Babcock & Mitchell, 1980; Son, et al., 2013]. In Japan, several catastrophic flood events have caused extensive damage to property and the national economy due to its topography, geography, and climate [Assteerawatt, et al., 2016; Kazama, et al., 2009; ICHARM, 2005]. The SAR imagery has considerable advantage over other sensors operating at visible or infrared wavelengths of the electromagnetic spectrum. The limitation of visible and infrared wavelengths are cannot penetrate the cloud cover often associated with flood events due to their day–night and all-weather capability, fine spatial resolution, and ability to yield synoptic images of inundation extent (Nascetti, et al., 2014; Horritt, et al., 2001; Hunter, et al., 2007). However, SAR imagery application in flood hazard mapping is still severely limited such as by the discontinuous availability of images, the relatively short length of data sets, and weaknesses in detecting flooding due to the speckle noise [Alfieri, et al., 2014; García-Pintado, et al., 2013; Pulvirenti, et al., 2011; Mascarenhas, 1996].

The Advanced Land Observing Satellite-2 (ALOS-2) Phased Array L-band Synthetic Aperture Radar-2 (PALSAR-2) should be suitable for flood inundation areas detection because of its high resolution and suitable for observing natural land surfaces [Natsuaki, et al., 2016; Rosenqvist, et al., 2014]. In addition, PALSAR-2 also offers a number of data observation angles which can increase the number of opportunities for flood observations [Honda, et al., 2016]. The Japanese 3rd generation L-band SAR satellite, ALOS-2/PALSAR-2, uses almost the whole bandwidth allocated for L-band active sensor of Earth Exploration Satellites Service specified by the Radio Regulation in order to realize the high-resolution observation [Kankaku, et al., 2016]. The first and second generation of Japanese L-band SAR satellite (Japanese Earth Resources Satellite-1 (JERS-1) and ALOS/PALSAR, respectively, were successfully used to identify inundation flooded areas [Chapman, et al., 2015; Ramsey III, et al., 2013; Van De Giesen, 2001; Townsend & Walsh, 1998; Rimba, et al., 2016]. Moreover, ALOS-2/PALSAR-2 also has been used for monitoring and extraction flooded areas [Honda, et al., 2016; Ariei, et al., 2016; Yamazaki & Liu, 2016]. In most case examples, however, the analyses were carried out using only a single type of filter to reduce speckle-noise which affects the less accuracy of the extraction results of flooded areas. Furthermore, the number of studies that used a combination of multiple type filters to detecting flooded inundation regions is limited.

Speckle noise is one important factor that can impact on the accuracy of flood mapping from SAR imagery [Adam, et al., 2014; Giustarini, et al., 2014; Gan, et al., 2012; Senthilnath, et al., 2013]. Speckle is noise on a radar image due to the phase fluctuations of the electromagnetic return signals (Argenti, et al., 2013; Foucher & Lopez-Martinez, 2014; Sumantyo & Amini, 2008). Speckle noise can make the detection and interpretation to be difficult for automated as well as human observers. (Bazi, et al., 2005; Inglada & Mercier, 2007; Niu & Ban, 2013; Xi, et al., 2015; Patel, et al., 2010). Speckle leads to a grain-like appearance of SAR images decreasing their contrast and radiometric quality [Barber, et al., 2012]. Meanwhile, speckle noise also changes the spatial statistics of the underlying scene backscatter which in turn makes the classification of imageries a difficult task [Durand, et al., 1987]. Reduction of speckle noise is one of the most important processes to increase the quality of coherent radar images [Mansourpour, et al., 2006]. Speckle noise is often an undesirable effect, thus speckle filtering turns out to be a critical pre-processing step for detection/classification optimization [Gagnon & Jauan, 1997].

There were two types of techniques to reduce speckle (Pohl & Genderen, 2016; Qiu, et al., 2004). The first technique which is called multi-look processing (each look has beam/ray value) averages the beam/ray of several images or “looks” of different portions of available azimuth spectral bandwidth (synthetic aperture), or other polarization states of the same location (Lillisand,

et al., 2004). However, as is well known, the resulting images suffer from a degradation of spatial resolution [Nyoungui, et al., 2002]. The second technique involves the use of image processing to smoothen the image which is divided into two approaches. The first approach is digital filtering which is achieved in the frequency domain by wavelet transformation (Gagnon & Jauan, 1997; Qiu, et al., 2004). The second approach is accomplished in the spatial domain, where the noise is reduced by averaging or statistically manipulating the values of neighboring pixels (Qiu, et al., 2004). Generally, flood maps derived from SAR observations are the result of image processing procedures [Mason, et al., 2010; Matgen, et al., 2007; Martinis, et al., 2015; Yulianto, et al., 2015; Pradhan, et al., 2016]. However, given the lack of perfect procedure and no best practice on selecting one over another, the chosen mapping procedure may introduce errors or uncertainties in the retrieved flood map [Giustarini, et al., 2014].

In recent years, several studies have evaluated speckle filtering methods to increase the accuracy level of object classification in the earth's surface from SAR images. For example, Meer *et al.* (1993) and Argenti *et al.* (2013) developed filter by developing algorithm multiresolution adaptive least squares smoothing (MAS). Huang and Genderen (1996) compared eight ready-made speckle filters for ERS-1&2 Imagery by quantitative and qualitative evaluation. Sheng and Xia (1996) evaluated seven speckle filters in the Radar Module of Erdas/Imagine(R) [Sheng & Xia, 1996]. Nyoungui *et al.* (2002) evaluated ten speckle filtering algorithms for land cover classification from SAR images. Qiu et al. (2004) developed median filter by using local statistic to detect and replace the speckle. Deledalle *et al.* (2009) developed a new filter namely the probabilistic patch-based (PPB) filter; it extends the Non-Local Mean (NLM) filter to the domain of SAR images by exploiting its connections to the weighted maximum likelihood estimator (WMLE) [Argenti, et al., 2013; Deledalle, et al., 2009]. Li *et al.* (2010) investigated the new filter, namely a Level set filter, this filter developed from Lee filter theory to reduce the speckle. Dellepiane and Angiati (2014) measured the quality of filtered de-speckled SAR Images and introduced a new method to determine the filter performance. Maity *et al.* (2015) reviewed various speckle filtering techniques to remove the speckle noise from various images in case of medical images, active Radar images and SAR images. Furthermore, Senthilnath *et al.* (2013) investigated Lee, Frost and Gamma MAP using kernel sizes 3x3, 5x5 and 7x7 on C band of RADARSAT-2 image (medium spatial resolution). They found that Gamma MAP is the best filter for flood extent extraction analysis and proposed Mean Shift Segmentation (MSS) for detecting inundated flood area. However, no studies have evaluated speckle filtering algorithms for monitoring and extraction flooded inundation regions from SAR images, especially from ALOS/PALSAR (medium spatial resolution) and ALOS-2/PALSAR-2 (high spatial resolution) data.

This study evaluated the best filter for detecting flood from ALOS/PALSAR image and ALOS-2/PALSAR-2 image. The Double filter method is proposed in this research as one method to reduce the speckle and preserve the information. This method do not widely change the pixel value. By applying the Double filter, a small kernel size can be used to prevent losing information due to over smooth impact, and it produces a clear image without a significant loss of information because the Double filter prevents the degrading of pixel intensively and preserves the edges by combining the advantages of the two filters.

4.2. Methodology

4.2.1. Overview

The goal of this chapter is selecting the best filters to make easier detecting flood inundation from ALOS/PALSAR and ALOS-2/PALSAR-2 images by utilizing broadly used image processing software, e.g., Research Systems ENVI or ERDAS imagine software. This research follows the method shown in Fig. 4.1. Overall, there are three main processes namely, Digital Number (DN) conversion, filtering, evaluation and application of flood detection. The Digital Number values are converted to backscattering coefficients; then the image is filtered one time or two times. Quick visual performance selected the filtered images, if the image can delineate the object clearly, the quantitative and qualitative assessment are performed. Finally, the selected images are applied to show the effectivity of the filter in distinguishing the inundated and non-inundated area. The filters are (1) Low Pass, (2) Gaussian Low Pass, (3) Median, (4) Sobel, (5) Roberts, (6) User-defined convolution, (7) Lee filter, (8) Enhanced Lee filter, (9) Frost filter, (10) Enhanced Frost filter, (11) Gamma filter, (12) Kuan filter, (13) Local Sigma filter and (14) Bit Error filter. Each filter has advantages and disadvantages, however, by combining the advantages of two filters, a better filter can be achieved. The purpose of filtering SAR images is to evaluate the best filter performance to reduce the speckle and preserve the edges and object detail.

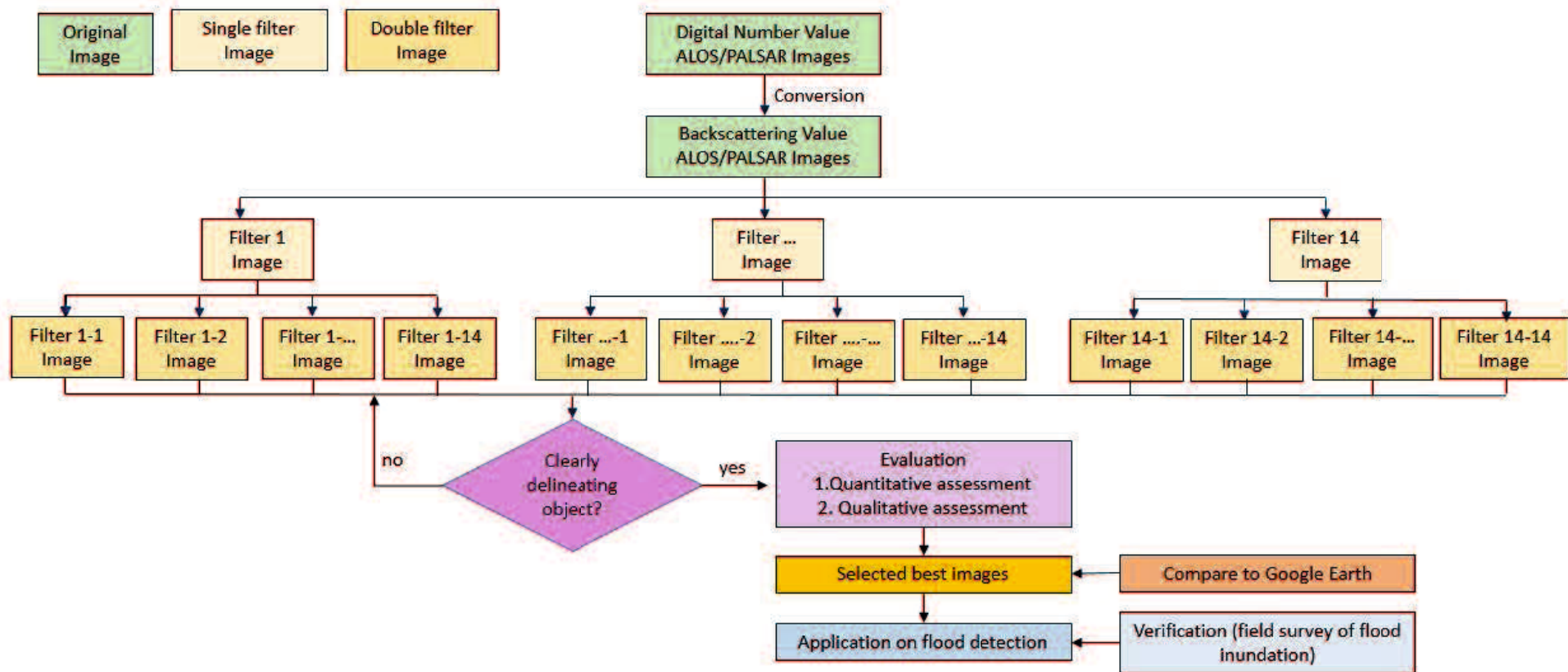


Figure 4. 1 Research flow chart

The converted images from DN to backscattering coefficient are filtered by the 14 filters using kernel size 3x3 and 7x7. The images filtered with kernel size 3x3 are filtered for a second time by applying 14 filters. Thus, this study generated 224 filtered images from ALOS/PALSAR images and 18 images from ALOS-2/PALSAR-2 as listed in Table 4.1.

Table 4. 1 List of the filtered image

Number of Images	Processing	Image Type
14	Single filter (3x3 kernel size)	ALOS/PALSAR
14	Single filter (7x7 kernel size)	ALOS/PALSAR
196	Double filter	ALOS/PALSAR
9	Single filter (3x3 kernel size)	ALOS-2/PALSAR-2
9	Double filter	ALOS-2/PALSAR-2

The quantitative and qualitative assessment evaluate the filtered images. After we had determined the best filter from ALOS/PALSAR, we applied it to the ALOS-2/PALSAR-2 image. All processes in this filtering method were conducted by ENVI 5.3 software using default system parameters.

4.2.2. Research location

Flooded areas were recorded by Google Earth on March 28th, 2014 (before the flood event). We applied the filters to Aichi Prefecture for the ALOS/PALSAR image and Ibaraki Prefecture for the ALOS-2/PALSAR-2 image. On August 30th, 2008, the heavy rainfall occurred in Chubu Area and the highest rainfall intensity was 146 mm/hour at 2:00 am in the morning in Okazaki City, Aichi Prefecture [JMA, 2016]. 1,110 flooded houses above floor level were flooded and 2,255 houses below floor level [Adachi, 2009; Okazaki, 2015]. On September 9th to 11th, 2015, the heavy rainfall occurred in Tohoku and Kanto area that led the flood in Joso City, Ibaraki Prefecture, Japan. 12,088 homes were flooded (Council, 2016; JosoCity, 2016). Figure 4.2 shows the research locations.

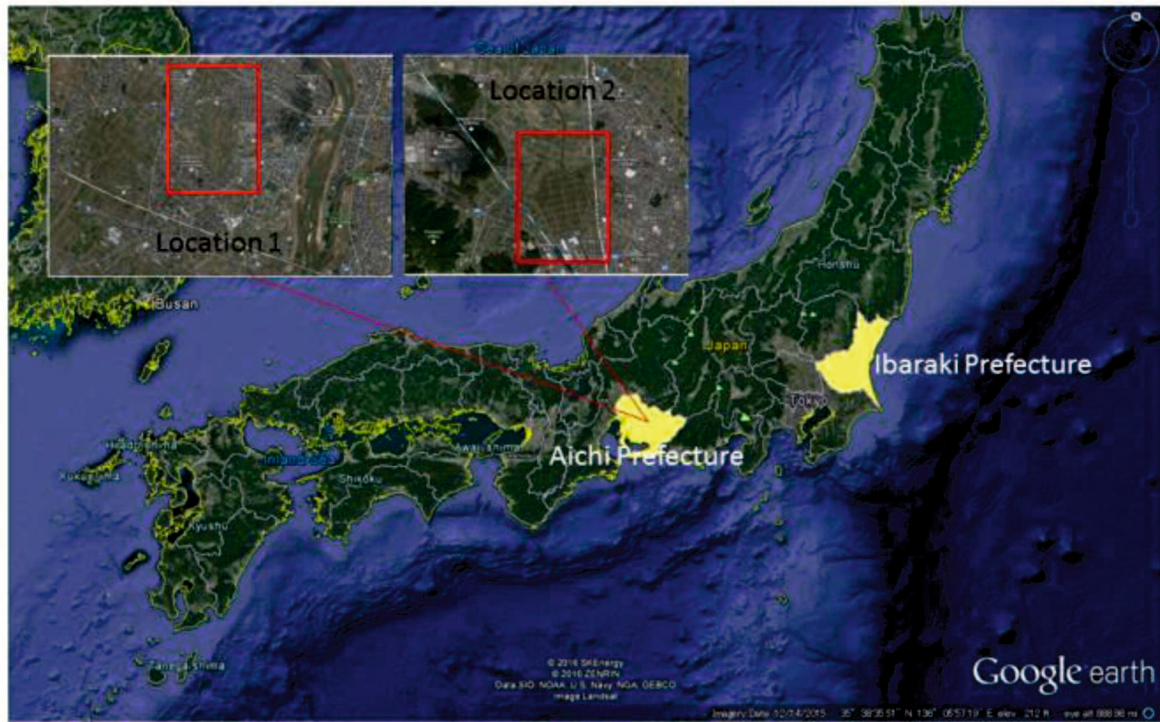


Figure 4. 2 Research locations in Aichi Prefecture for ALOS/PALSAR and Ibaraki Prefecture for ALOS-2/PALSAR-2. Aichi Prefecture has 2 locations of flooded areas of which location 1 is shallow flood inundation (left), and location 2 is deep flood inundation (right)

4.2.3. Dataset and Pre-processing

Table 4.2 lists the images in this research; Level 1.5 and HH polarization was useful in flood study comparing to VV, VH and HV polarization. For the ALOS-2/PALSAR-2 image, the selected filters were applied from ALOS/PALSAR images.

Table 4. 2 List of data used for filtering analysis

Image	Date	Resolution	Off-nadir	Polarization	Location
ALOS/PALSAR	2008/8/31	6.25 m	34.3°	HH	Aichi Prefecture
ALOS-2/PALSAR-2	2015/9/10	3 m	35.8°	HH	Ibaraki Prefecture

The starting point for processing the level 1.5, Digital Numbers (DN) of the image were transformation to Backscattering Coefficient (σ^0) as explained in Eq. 4.1.

$$\sigma^0 = 10 \log_{10}(DN^2) + CF \quad (4.1)$$

where: σ^0 is backscattering coefficient (dB); DN is a digital number; CF for ALOS/PALSAR and ALOS-2/PALSAR-2 are -83 (JAXA, 2003).

4.2.4. Basic principle of SAR speckled image

Speckle or fading displays as a salt and pepper granular form due to the constructively or destructively wave to generate stronger or weaker signals; thus, a pixel to pixel has intensity variation (Goodman, 1976; Lee, et al., 1994). Speckle appears when the examination point is moved, the path length traveled by the scattered component changes, a new and independent value of intensity may result from interference process (Qiu, et al., 2004; Goodman, 1976). This speckle pattern contains a multitude of a bright spot where the interference has been highly constructive, a dark spot where the interference has been highly destructive, and irradiance levels between these extremes [Joso City, 2016; Panchagnula, 2012]. The speckle noise has a standard deviation linearly to the mean and modeled as a multiplicative process (Qiu, et al., 2004). Hence, more speckle noise appears in brighter pixel areas (North & Wu, 2001). In a SAR image, the speckle can be bright or dark pixel and inconstant of mean radiometric for homogenous areas (Bruniquel & Lopes, 1997). A homogeneous area in SAR images can be formulated as Eq. 4.2;

$$I(x, y) = R(x, y) \times S_n(x, y) \quad (4.2)$$

Where (x, y) are the spatial scale and azimuth coordinates of the resolution cell center. $I(x, y)$ is the strength of SAR images. $R(x, y)$ is a random rule of radar reflectivity (unspeckled radiance). $S_n(x, y)$ is a form of speckle noise having a stationary random method with unit mean and variance proportional to an effective number of looks N and is statistically independent of $R(x, y)$ (Gir, et al., 2015; Huang & Genderen, 1996).

4.2.5. Filter types

Convolution filters and adaptive filters were applied in this study. Convolution filters created a blur effect on the image. The speckle noise usually appears in or near to the brighter pixel area because the higher signal strength means higher speckle noise appearing (North & Wu, 2001). Convolution filters (ENVI, 2004) are Low Pas, Gaussian Low Pas, Median, Sobel, Roberts and User-defined convolution. Adaptive filters aim to effectively reduce speckle in radar images without eliminating the object details (Jensen, 2004). The mean and variance of pixel interest of adaptive filters are equal to the local mean and variance off all pixels within the user-selected

moving window (Lee, 1980; Qiu, et al., 2004). Adaptive filters are Lee (Lee, 1980), Enhanced Lee (Lopez, et al., 1990), Frost (Zhenghao & Fung, 1994), Enhanced Frost (Lopez, et al., 1990), Gamma (Lopez, et al., 1993), Kuan (Kuan, et al., 1987), Local Sigma (Eliason & McEwen, 1990) and Bit Error (Eliason & McEwen, 1990).

4.2.5.1. Single filter

A single filter is applying one filter to an image by using kernel size 3x3, 5x5, 7x7, 9x9, and so on. The applied filter can be convolution filter or an adaptive filter. This study applied 14 kinds of the Single filter with 3x3 and 7x7 kernel size. Applying a small kernel size enable to remove the speckle noise. However, applying the big kernel size smoothed the images.

4.2.5.2. Double filter

In purpose to classify the flooded and non-flooded areas, a new method to reduce speckle by filtering was introduced, i.e. the Double filter method. Double filtering is a method that filtered twice by using a combination of different filters. Commonly, during filtering processing, the user decides the kernel size of the filter, such as 3x3, 5x5, 7x7, and 9x9 (Sinha & Dougherty, 1998). The kernel size has an important role in preserving the information. Using a big kernel size, for example, kernel size 7x7 or 9x9, the user obtains an image clean from speckle but may lose some information because the speckle contains the information. The most common problem when reducing speckle is degradation of pixel image depending on the level of smoothing filter (Sheng & Xia, 1996). Lee *et al.* (1994) confirmed that, in general, applying small kernel size (such as 3×3) can preserve better information (Lee, et al., 1994). However, when a small kernel size is used, the speckle remains. Hence, the Double filter method was proposed in this research as one method to reduce the speckle and preserve the information. This method did not widely change the pixel value. By applying the Double filter, a small kernel size can be used, and it produces a clear image without a significant loss of information because the Double filter prevents the degrading of pixel intensively and preserves the edges by combining the advantages of the filters.

In this study, the Double filter is applying two combinations of Single filter with 3x3 kernel size to prevent the lost information due to the smoothing effect during filtering processing. The combination of A and B is different with the combination of B and A. The 3x3 filter size was applied to generate the Double filter image. This filtered image by Double filter supposed to reduce the speckle, enhance the edge and detail of the object.

4.2.6. Performance Evaluation

4.2.6.1. Quantitative assessment

The quantitative assessment was applied by using the statistical analysis. The quantitative assessments were categorized into two groups. The first group was Signal performance to measure the ability of the filter to reduce the speckle by metric parameter (SSI and MPI). The second group was the Enhancing performance of filtered image to measure the ability of filter in preserving the edge (EEI and MAE), preserving the feature line (FPI) and fine detail (IDPC).

1. Signal performance of the filtered image

a. Speckle Suppression Index (SSI)

Speckle Suppression Index (SSI) is one of the common techniques to measure the speckle strength [Lee, et al., 1994]. The SSI given by Eq. 4.3 corresponds to the ratio between normalized standard deviations of the pixel value of an original image and a filtered image (Sheng & Xia, 1996; Dellepiane & Angiati, 2014). It is a vestige of constant at homogeneous areas determined by the amount of speckle [Qiu, et al., 2004; Hagg & Sties, 1996].

$$SSI = \frac{\left(\frac{std S_o}{mean S_o}\right)}{\left(\frac{std S_i}{mean S_i}\right)} \quad (4.3)$$

In addition, the filtered image has less variance due to the speckle suppression. Thus, a value of SSI is smaller than 1.0 and the larger SSI value, the greater SSI speckle suppression (Sheng & Xia, 1996). However, SSI is not reliable when overestimated

b. Mean Preservation Index (MPI)

The SSI is not reliable when the filters overestimate the mean value. Thus the *Mean Preservation Index* (MPI) is necessary. The MPI has a good ability to represent the mean preservation capability of a filter and it allows a filter comparison to be made with various homogeneous regions (Dellepiane & Angiati, 2014). The MPI calculation was explained in Eq.4.4 (Dellepiane & Angiati, 2014). The MPI utilizes the sample mean due to computing from a homogeneous region (Dellepiane & Angiati, 2014). A low value indicates better performance of the filters.

$$MPI = \left| 1 - \frac{S_i}{S_o} \right| \quad (4.4)$$

2. Enhancing performance of filtered image

a. Edge Enhancing Index (EEI)

The Edge Enhancing Index (EEI) is one of the techniques to measure the ability of filter in persevering the edge [Sheng & Xia, 1996], such as the boundary between the land and water body. The equation of this index is given by Eq. 4.5.

$$EEI = \frac{\sum |S_{o1} - S_{o2}|}{\sum |S_{i1} - S_{i2}|} \quad (4.5)$$

Where S_{i1} and S_{i2} are the original values of the pixel on other sides of the edge; and S_{o1} and S_{o2} are the pixel values from the filtered image. The both sides of water body and land were selected to execute this parameter. Its value is usually less than 1.0 [Qiu, et al., 2004]. Higher value of EEI indicates a better ability of edge preservation [Sheng & Xia, 1996].

b. Mean Absolute Error (MAE)

Mean Absolute Error (MAE) given by Eq.4.6 helps to measure edge sharpness (Dellepiane & Angiati, 2014; Willmott & Matsuura, 2005). It measures the extent of difference from the output image to the input image.

$$MAE = \frac{1}{K} \sum_{i=1}^K |S_i - S_o| \quad (4.6)$$

Where S_i is value of the pixel value in the original image; and S_o is the pixel value of the filtered output image, and K is the number of pixels (i.e., size of the image). A lower value of MAE shows good performance.

c. Feature-Preserving Index (FPI)

Feature-Preserving Index (FPI) is one of the techniques to measure the speckle ability for preserving the feature [Sheng & Xia, 1996]. *FPI* given by Eq.4.7 corresponds to calculate the feature line and subtle structure.

$$FPI = \frac{\sum_1^n (2 \cdot S_o - S_{o1} - S_{o2})}{\sum_1^n (2 \cdot S_i - S_{i1} - S_{i2})} \quad (4.7)$$

where S_i is the pixel value of the original image on the linear feature, S_{i1} and S_{i2} are the neighboring pixels on both sides of feature, whereas S_o , S_{o1} and S_{o2} are the filtered values of the corresponding pixel. FPI value are also lower than 1.0. The greater the FPI value, the better the linear feature being preserved.

d. Image Detail-Preserving Coefficient (IDPC)

Image Detail-Preserving Coefficient (IDPC) is a correlation coefficient between the original pixel value and the filtered pixel value [Sheng & Xia, 1996]. IDPC indicates the filter ability to preserve the fine detail and subtle structure, i.e., point feature [Qiu, et al., 2004]. A higher value of IDPC indicates more detail in preservation capability [Sheng & Xia, 1996].

4.2.6.2. Qualitative assessment

Visual assessment or *Visual performance evaluation* is selecting the filtered image by visual interpretation. The visual assessment is the easy and effective way to investigate the capability of the filter to suppress speckle and to preserve the detail (Dellepiane & Angiati, 2014; Raouf & Lichtenegger, 1997). Good performance is when the image enhances the edge, object details and is easy to interpret. Thus, this evaluation consisted of three criteria: speckle reduction, preserving the edges and object detail.

Visual performance evaluation was conducted two times; the first visual performance evaluation was conducted by selecting the filters that could preserve the edges or could delineate the object (i.e. clearly delineation and unclearly delineation filter image). We called as a quick visual analysis. The second visual performance evaluation was assessed after statistics performance evaluation. From the statistic performance evaluation, we selected the best filter combinations by comparing the statistic values of images. The selected combination images were compared with the original image to show the difference of pixels' numbers. Because the speckle noise appears on the surface of the image, thus, visual performance evaluation was the first parameter and statistical performance evaluation was the second parameter to select the best filter.

4.2.7. Assessment for Flooded Area

For detecting the flooded area, the Iterative Self-Organizing Data Analysis Technique (ISODATA) classification was conducted to measure the efficiency of the selected filter in delineating the flood inundated area. ISODATA is an unsupervised classification calculated by the variation in the minimum distance of distribution pixel (ENVI, 2004). ISODATA evaluates the selected data to cluster in multidimensional data space. Each cluster has a centroid; all the unallocated pixels are allocated to the nearest centroid. The allocation process of the pixel is repeated until there is no change or a small change of pixel in class centroid; this is called iteration. The steps of ISODATA are as follows: 1) selecting the class mean data, 2) re-computing the class mean to reallocate the pixel, 3) repeating step 2 if any changes of the class exist. This classification does not require

information on feature classification. Feature classification must have the information to discriminate amongst categories (Kumar & Bhatia, 2014). However, the essential factor in ISODATA is only the distance; if the distance for the class mean is less than the minimum value, it can be merged to be one class (ENVI, 2004). By using ISODATA classification, we assumed that classification factor was only by a distance of pixel. When the image had a lot of speckle noise, the distance of the same backscattering value was great. This leads to a large number of class centroids. Hence, by applying ISODATA classification to a selected filter, the ability of the filter to reduce speckle noise can be determined by its number of the class centroid.

ALOS/PALSAR images were used to observe the flood inundation areas. Flood extent mapping using SAR images was widely applied because water appears dark with very low backscattering compared to other objects (Smith, 1997). This study applied to the pilot area in Aichi Prefecture, Japan for ALOS/PALSAR images and in Ibaraki Prefecture, Japan for ALOS-2/PALSAR-2 (Fig. 4.2).

4.3. Results

Unable to preserve the edges and object detail were removed. The best filter is usually selected based on qualitative evaluations performed through visual analysis (Dellepiane & Angiati, 2014). We reduced some filtered images by a quick visual performance to minimize the number of images. By using a visual performance, 14 Single filter images and 196 Double filter images have been classified into two categories, i.e. unclear delineation filters and clear delineation filters. Nine Single filter images and 98 Double filter images were selected as clear delineation images. All these images were evaluated by quantitative and qualitative performance. The unclear delineation filters for Single filter were Sobel filter, Robert filter and Kuan filter (see Fig. 4.3). User defined filter changed the pixel value. Thus, we did not utilize these filters for the next analysis. Figure 4.3 shows an example of unclear delineation images. Both Sobel and Robert showed bad performance; Sobel showed an over bright image and many speckles as shown in the red circle (i.e., the red circle was the homogenous image). In addition, the red box showed a black block object due to the high intensity of the signal. Robert filter showed more speckles than Sobel filter that covered the information of the image, as shown in the red circle. Much information was lost when applied these filters due to its speckle contents.

These filters continued the process to the next performance evaluation Single filter images with kernel size 7x7 image showed low performance on the visual performance evaluation. Hence,

it was not analyzed for statistical performance. The clear delineation filters were Low Pass, Gaussian Low Pass, Median, Lee, Enhanced Lee, Frost, Enhanced Frost, Gamma and Local Sigma filters.

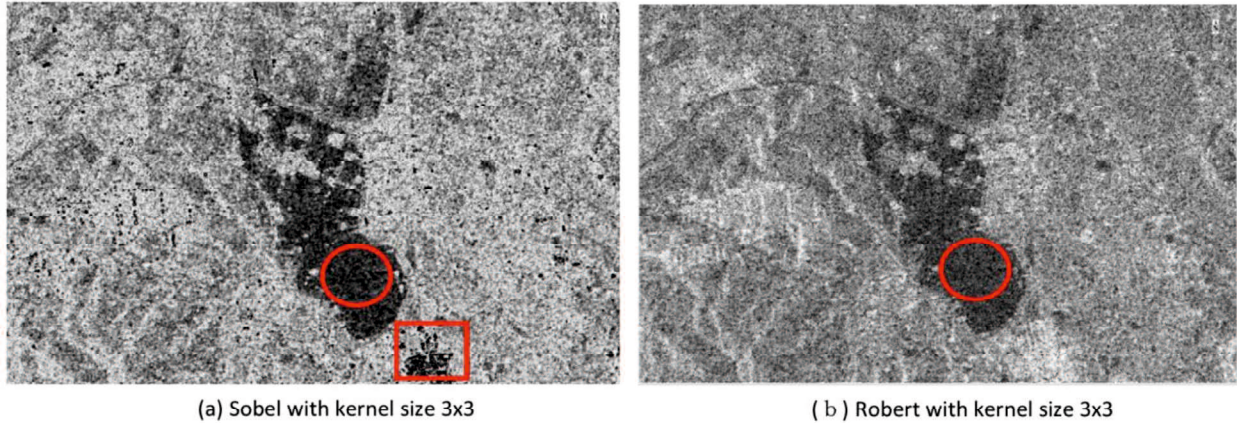


Figure 4. 3 Example of unclear delineation filter (a) Sobel filter 3x3, (b) Robert filter 3x3

4.3.1. Quantitative assessment

Six of quantitative performance measures, including SSI, MPI, EEI, MAE, FPI and IDPC were calculated for each filtered image. For the Single filter, we listed 9 filters; and for the Double filter, we only listed the filter which has strength in quantitative parameters.

4.3.1.1. Signal performance of the filtered images

Table 4.3 lists the signal performance evaluation of filters. The low value of SSI and MPI indicated as better performance. The SSI of the original image was 1; the SSI of filtered image near to 1 means less speckle suppressed. The MPI of the original image was 0; the MPI of filtered image near to 0 means well-preserved the mean value. For the Single filter, Low Pass and Local Sigma show better performance for both ALOS/PALSAR and ALOS-2/PALSAR-2 image. For the Double filter from the ALOS/PALSAR image the combination of Median with Low Pass, Enhanced Lee and Enhanced Frost were better in SSI; combination of Local sigma with Low Pass, Enhanced Lee and Enhanced Frost were better in MPI. And the Double filter from ALOS-2/PALSAR-2 image, the combination of Median with Enhanced Frost and combination of Local Sigma and Low Pass were better in SSI; Combination of Median and Local Sigma with Low Pass, Enhanced Lee and Enhanced Frost were better in MPI. According to Table 4.3, Signal performance of Double filter showed better performance comparing to Single filter. The Double filter was able to suppress the speckle noise and to preserve the mean value of the image.

Table 4. 3 Signal performance of filtered images

Type	Pair Order	Filter Name	ALOS PALSAR		ALOS-2/PALSAR-2	
			SSI	MPI	SSI	MPI
		Original image	1	0	1	0
Single filter	1	Low Pass	*0.666	0.017	*0.800	0.009
	2	Gaussian Low Pass	0.945	0.010	0.965	0.003
	3	Median	0.720	0.004	0.825	0.010
	7	Lee	0.835	0.008	0.807	0.009
	8	Enhanced Lee	0.691	0.017	0.807	0.009
	9	Frost	0.723	0.017	0.814	0.009
	10	Enhanced Frost	0.691	0.047	0.806	0.009
	11	Gamma	0.727	0.017	0.838	0.009
	13	Local Sigma	0.951	*0.003	0.955	*0.001
Double filter	2-9	Gaussian Low Pass_Frost	0.691	0.004	0.807	0.010
	3-1	Median_Low Pass	**0.626	0.006	0.780	**0.006
	3-8	Median_Enhanced Lee	**0.626	0.006	0.782	**0.006
	3-10	Median_Enhanced Frost	**0.626	0.006	**0.782	**0.006
	13-1	Local Sigma_Low Pass	0.662	**0.001	**0.782	**0.006
	13-8	Local Sigma_Enhanced Lee	0.675	**0.001	0.801	**0.006
	13-10	Local Sigma_Enhanced Frost	0.675	**0.001	0.800	**0.006

*best performance for Single filter; **best performance for Double filter

4.3.1.2. Enhanced performance of filtered image

This group has categorized the parameters according to their ability in preserving the edge, line and fine detail of the image. EEI and MAE measured the ability of the filter to emphasize the boundary of the homogeneous object. FPI measured the ability to preserve the line object and IDPC measured the fine object detail (i.e. point object).

1. Edge preserving

Table 4.4 lists the filter performance from ALOS/PALSAR and ALOS-2/PALSAR-2 by EEI and MAE. Good performance of edge preserving was indicated by the higher value of EEI and lower value of MAE. For the Single filter from ALOS/PALSAR image, Local Sigma and Gamma were the best filters to preserve the boundary of the homogenous object (i.e., water body); for the ALOS-2/PALSAR-2 image, Low Pass and Gaussian Low Pas filter were the best filter to preserve the edge in enhancing of the homogeneous object.

For the Double filter from the ALOS/PALSAR image, the combination of Local Sigma with Low Pass, Enhanced Lee and Enhanced frost generated better value in preserving the edge; For

the ALOS-2/PALSAR-2 image, the combination of Local Sigma with Low Pass generated better performance in preserving the edge.

Table 4. 4 Enhancing performance (edge preserving) of filtered images

Type	Pair Order	Filter Name	ALOS PALSAR		ALOS-2/PALSAR-2	
			EEI	MAE	EEI	MAE
		Original image	1	0	1	0
Single filter	1	Low Pass	0.663	0.103	0.417	*0.010
	2	Gaussian Low Pass	0.958	0.008	*0.731	*0.010
	3	Median	0.675	0.125	0.397	0.211
	7	Lee	0.674	0.014	0.703	0.020
	8	Enhanced Lee	0.663	0.070	0.417	0.020
	9	Frost	0.674	0.012	0.437	0.027
	10	Enhanced Frost	0.663	0.070	0.417	0.019
	11	Gamma	0.663	*0.004	0.492	0.094
	13	Local Sigma	*0.972	*0.004	1.004	0.030
Double filter	2-9	Gaussian Low Pass_Frost	0.674	0.045	0.431	0.010
	3-1	Median_Low Pass	0.608	0.046	**0.703	0.020
	3-8	Median_Enhanced Lee	0.608	0.046	0.417	0.020
	3-10	Median_Enhanced Frost	0.608	0.046	0.437	0.027
	13-1	Local Sigma_Low Pass	**0.675	**0.004	0.417	**0.009
	13-8	Local Sigma_Enhanced Lee	**0.675	0.021	0.492	0.094
	13-10	Local Sigma_Enhanced Frost	**0.675	0.021	1.004	0.030

*best performance for Single filter; **best performance for Double filter

2. Detail-preserving

Detail-preserving measured by using FPI for a line object and IDPC for a point object were shown in Table 4.5; the high value of FPI and IDPC denoted a good performance. For Single filter, Low Pass and Gaussian Low Pass were the best to preserve the line object for ALOS/PALSAR; Gaussian Low Pass and Local Sigma were better to preserve the point for ALOS/PALSAR image. For Single filter from the ALOS-2/PALSAR-2 image, Gaussian Low Pass and Local Sigma were good in preserving the fine detail of the object. In additional, some values of FPI were overestimated in this study. The FPI value should be less than 1.

For Double filter from ALOS/PALSAR image, a combination of Local Sigma with Low Pass and Enhanced Frost generated value better in preserving the line object; and the combination of Gaussian Low Pass with Frost showed better performance in fine-detailed the object. For Double filter from the ALOS-2/PALSAR-2 image, FPI overestimated in calculating the value except for

combination of Local Sigma with Enhanced Frost. Nevertheless, the combination of Local Sigma and Low Pass generated an image better in preserving the fine detail.

Table 4. 5 Enhancing performance (detail preserving) of filtered images

Type	Pair Order	Filter Name	ALOS PALSAR		ALOS-2/PALSAR-2	
			FPI	IDPC	FPI	IDPC
		Original image	1	1	1	1
Single filter	1	Low Pass	*0.891	0.860	1.009	0.878
	2	Gaussian Low Pass	*0.891	*0.989	1.001	*0.989
	3	Median	1.016	0.833	0.928	0.864
	7	Lee	0.861	1.060	1.007	0.986
	8	Enhanced Lee	0.807	0.860	1.009	0.878
	9	Frost	0.871	0.881	1.009	0.895
	10	Enhanced Frost	0.807	0.860	1.009	0.878
	11	Gamma	0.801	0.860	1.009	0.807
	13	Local Sigma	0.876	*0.989	0.929	*0.989
Double filter	2-9	Gaussian Low Pass_Frost	0.843	**0.869	1.001	**0.989
	3-1	Median_Low Pass	0.852	0.782	1.007	0.986
	3-8	Median_Enhanced Lee	0.852	0.782	1.009	0.878
	3-10	Median_Enhanced Frost	0.852	0.782	1.009	0.895
	13-1	Local Sigma_Low Pass	**0.891	0.843	1.009	**0.989
	13-8	Local Sigma_Enhanced Lee	0.876	0.843	1.009	0.807
	13-10	Local Sigma_Enhanced Frost	**0.891	0.843	**0.929	**0.989

*best performance for Single filter; **best performance for Double filter

Considering the quantitative performance of filtered image from ALOS/PALSAR and ALOS-2/PALSAR-2, we summarized the best quantitative performance (i.e. Table 4.3 to 4.5) in Table 4.6.

According to Table 4.6, the Single filter (Low Pass, Gaussian Low Pass, Gamma and Local Sigma) shows the best performance in quantitative. And for the double filter, all the combination of selected filter have a strong performance. However, the combination of Local Sigma and Low Pass showed 4 from 6 strength of quantitative performance, i.e., MPI, EEI, MAE, and FPI for ALOS PALSAR and SSI, MPI, MAE and IDPC for ALOS-2 PALSAR-2. All the best filters in Table 4.6 were considered and evaluated their performance in qualitative performance.

Table 4. 6 The summary of the best quantitative performance

Type	Pair Order	Filtered image	Statistical Indicator	
			ALOS PALSAR	ALOS-2/PALSAR-2
Single filter	1	Low Pass	SSI, FPI	SSI, MAE
	2	Gaussian Low Pass	FPI, IDPC	EEl, MAE, IDPC
	3	Median	-	-
	7	Lee	-	-
	8	Enhanced Lee	-	-
	9	Frost	-	-
	10	Enhanced Frost	-	-
	11	Gamma	MAE	-
	13	Local Sigma	MPI, EEI, MAE, IDPC	MPI, IDPC
Double filter	2-9	Gaussian Low Pass_Frost	IDPC	IDPC
	3-1	Median_Low Pass	SSI	MPI, EEI
	3-8	Median_Enhanced Lee	SSI	MPI
	3-10	Median_Enhanced Frost	SSI	SSI, MPI
	13-1	Local Sigma_Low Pass	MPI, EEI, MAE, FPI	SSI, MPI, MAE, IDPC
	13-8	Local Sigma_Enhanced Lee	MPI, EEI	MPI
	13-10	Local Sigma_Enhanced Frost	MPI, EEI, FPI	MPI, FPI, IDPC

4.3.2. Qualitative assessment

The qualitative assessment was conducted by evaluating the visual performance of selected image from Table 4.6.

4.3.2.1. ALOS/PALSAR image

Figure 4.4 displays the condition of the area in Google Earth and the original image (i.e. no filter). It was compared to Fig. 4.5 and Fig. 4.6 to show the visual performance of Single filter and Double filter from ALOS/PALSAR.

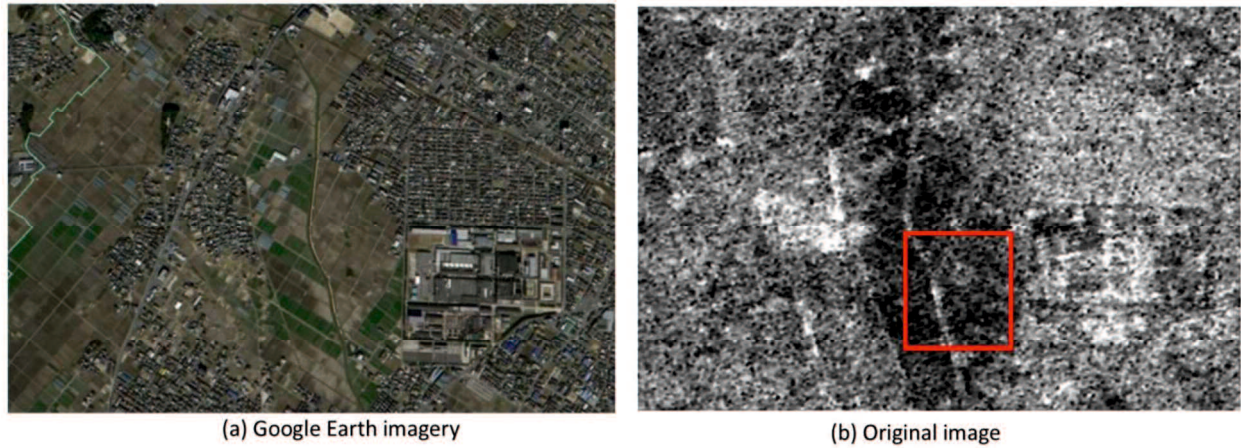


Figure 4. 4 (a) *Google Earth imagery*, (b) *Original image*

Figure 4.5 shows the visual performance of Single filter performance with kernel size 3×3 and 7×7 for ALOS/PALSAR image. Images with kernel size 3×3 show some speckle on all images in Fig. 4.5, and those with kernel size 7×7 show over smoothing. The difference between each filter can be seen in the red box. It showed the same object but with a different shape due to a different kind of filter. The visual performance was evaluated by three criteria: speckle reduction, preservation of edges and object detail. The Low Pass (Fig. 4.5a) shows the blurred image for 3×3 . The Gaussian Low Pass (Fig. 4.5c) and Local Sigma (Fig. 4.5g) showed low performance and similar to original image (Fig. 4.5b); the feature was a homogenous object (i.e., water). Nonetheless we could not distinguish the object due to the speckle. Compared to all Single filters, Gamma showed the best performance in visual performance evaluation for 3×3 kernel size even though some speckles appeared (Fig. 4.5e) the filter was able to distinguish the object and preserve the edges. For 7×7 kernel size (Fig. 4.5b and 4.5f) as shown in the red box, it showed an over smoothed object. We were unable to clearly see the white line in the red box that is shown in other filters. Hence, we lost much information.

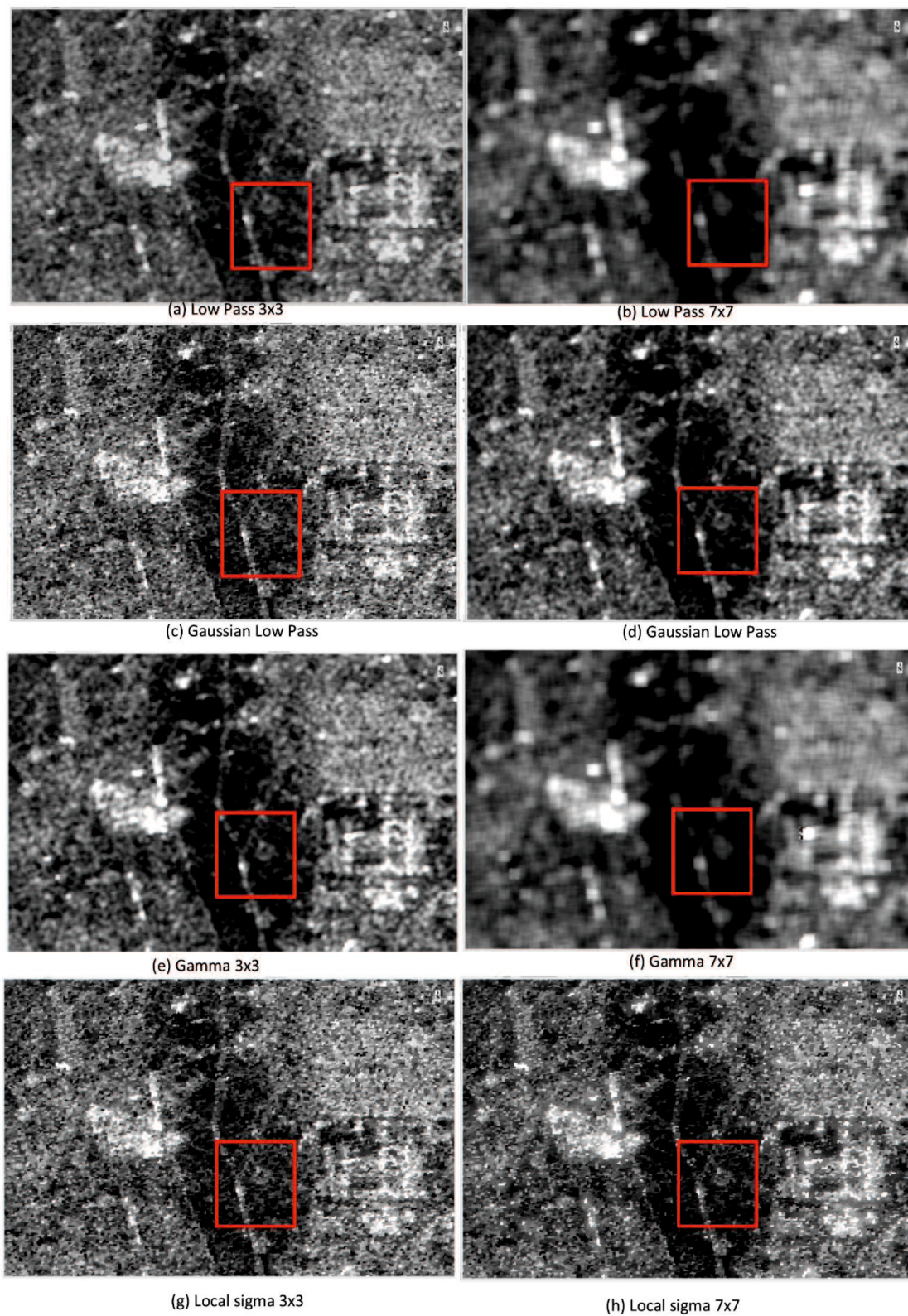


Figure 4. 5 (a) Low Pass 3x3, (b) Low Pass 7x7, (c) Median 3x3, (d) Median 7x7, (e) Gamma 3x3, (f) Gamma 7x7 (g) Local Sigma 3x3, (h) Local Sigma 7x7

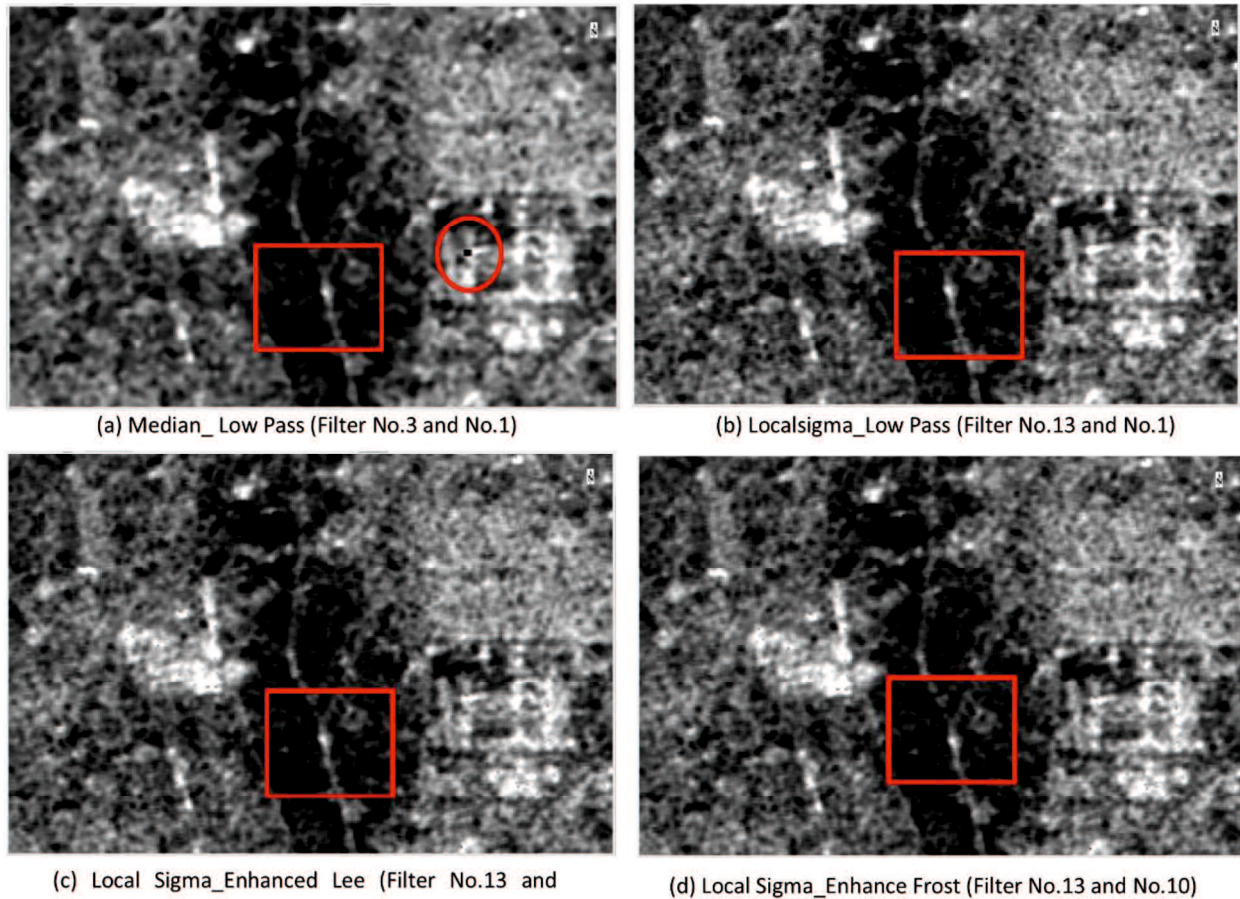


Figure 4. 6 Double filter performance from ALOS/PALSAR; (a) Median Low Pass, (b) Local Sigma Low Pass, (c) Local Sigma Enhanced Lee, (d) Local Sigma Enhanced Frost

Figure 4.6 shows the performance of Double filter on the ALOS/PALSAR image. The combination of Median and Low Pass (Fig. 4.6a) showed low performance because of a black block as shown in the red circle and over smoothing as shown in the red box. Figure 4.6a was not listed in Table 4.6, nevertheless, we display to show the example of low performance in quantitative and its impact on qualitative performance; we could see the black pixel due to the high-intensity signal in the red circle. Median filter conserved edges, linear features, and object details, even in low-contrast areas because the edge of an object can clearly be seen even though for the dark object (low backscattering value). Hence in this study, Median showed a strong edge and block in each pixel. Lee et al. (1994) declared that the 3×3 Median filter preserves the texture information very clearly but does not retain the mean value at an acceptable level [Lee, et al., 1994]. The Median was a convolution filter where reduced some bright areas due to high signal intensity. Thus, the combination of Median and Low Pass shows low performance in visual due to combining their weakness. Local Sigma filter as the first filter showed high visual performance because it could preserve edges and the details of objects as shown in Fig 4.6b, 4.6c and 4.6d.

Thus, we could distinguish objects such as roads, water, and others. Local Sigma combinations with Low Pass, Enhanced Frost and Enhanced Lee showed good performance as shown in Fig. 4.6b, 4.6c and 4.6d by visual performance evaluation; all combinations show less speckle noise.

The best filter from ALOS/PALSAR image for Single filter was Gamma filter because it showed better visual performance than others and powerful in MAE. The combination of Local Sigma and Low Pass was the best for the Double filter because it was better performance in statistical parameters (MPI, EEI, MAE, FPI) and showed better performance in visual.

4.3.2.2. ALOS-2/PALSAR-2 image

Figure 4.7 shows filtered images for ALOS-2/PALSAR-2. It is located in the area of Ibaraki Prefecture which flooded on September 10th, 2015. Figure 4.7a is Google Earth image and Fig. 4.7b is the original image without filtering. Figure 4.7b has similar performance with Gaussian Low Pass (Fig. 4.7d) and Local Sigma (Fig. 4.7e). We can focus on the red circle which shows the homogeneous object in Fig. 4.7b, 4.7d and 4.7e; from these images, we could find speckle noise on the surface of the images. The speckle noise can be detected easily in the homogeneous object (e.g., water surface) as shown in the red circle in Fig. 4.7. The red box in Fig. 4.7 shows the heterogeneous object; we could detect the edge and object detail easily by examining the heterogeneous object. Low Pass (Fig. 4.7c) produced a higher contrast image than the others where we can see the edges of each object and also object detail as shown in the red box.



(a) Google earth images



(b) Original Image (no filter)



(c) Low Pass (Filter No.1)



(d) Gaussian Low Pass (Filter No.2)



(e) Local Sigma (Filter No.13)

Figure 4. 7 Single filter for ALOS-2/PALSAR-2 image (a) Google Earth image, (b) Original image (no filter), (c) Low Pass 3x3, (d) Gaussian Low Pass 3x3, (e) Gamma 3x3, (f) Local Sigma 3x3 (red circle: identified the speckle, red square: identified the edge and object)

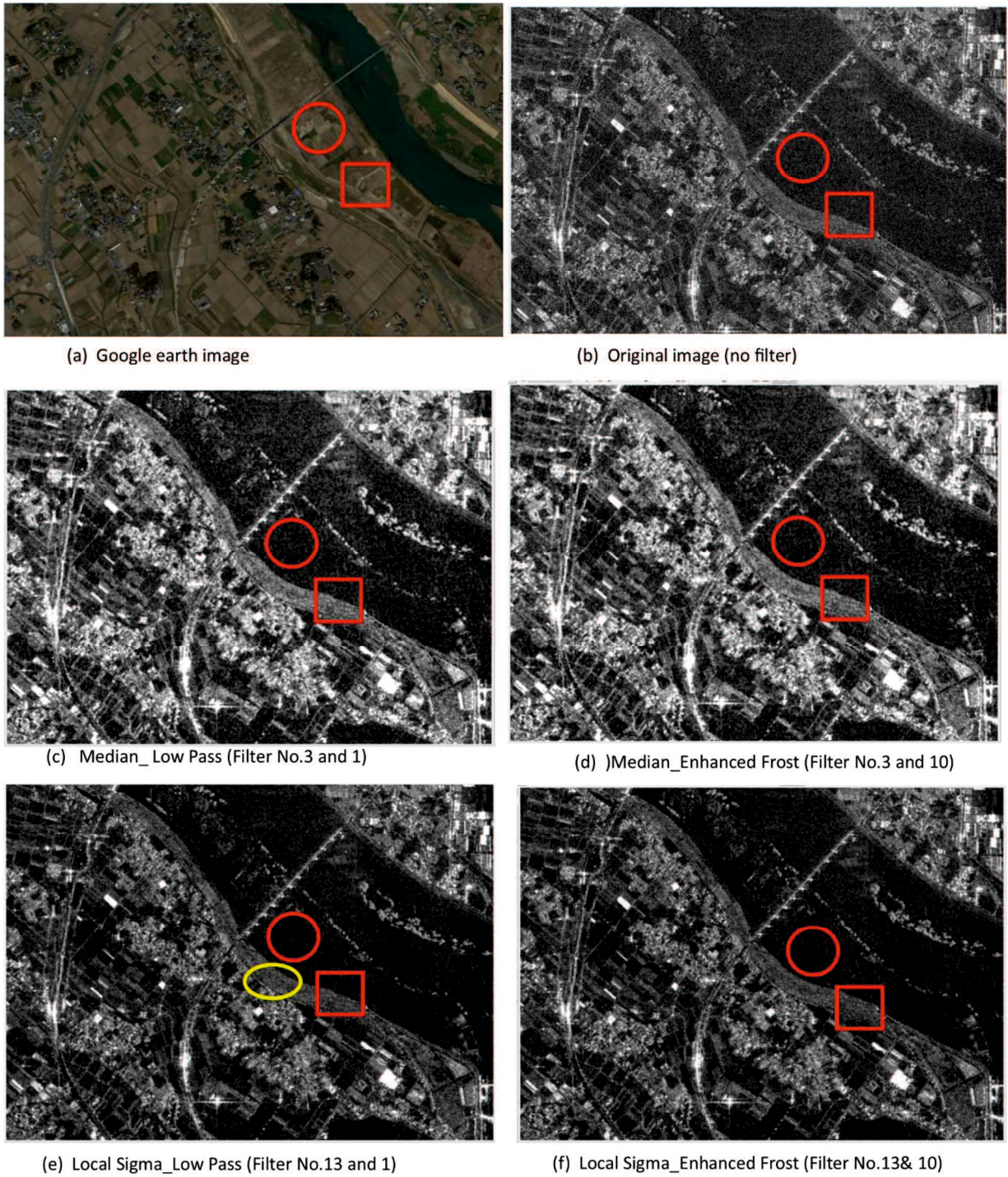


Figure 4. 8 Double Single Performance on ALOS-2/PALSAR-2 (a) Google Earth image (b) Original image (no filter) (c) Median Low Pass, (d) Median Enhanced Frost, (e) Local Sigma Low Pass, (f) Local Sigma Enhanced Frost. (Red circle shows the speckle, red box shows the edge and object detail, yellow ellipse: used in Fig .4.9)

Figure 4.8 shows the Double filter performance comparing to Google Earth image and the original image. The red box shows the preservation of edge and object detail. The red box shows the water and non-water, and the red circle shows the speckle noise in the homogeneous object.

The red circle showed that Fig. 4.8c and 4.8d had more speckle noise on the surface of the image compared to the others. Their images are brighter than others. Figure 4.8e showed the clear river line during flooding and homogeneous object clear from speckle. Figure 4.8e was the combination of Local Sigma and Low Pass; Local Sigma preserved the object detail and Low Pass removed the speckle by smoothing and reduced the intensity of the signal. Thus, this combination did well in visual performance. Hence, the best Double filter for ALOS-2/PALSAR-2 was a combination of Local Sigma and Low Pass.

By evaluating quantitatively and qualitatively of the filtered image from ALOS-2/PALSAR-2, the best filter was Low Pass for Single filter and combination of Local Sigma with Low Pass for the Double filter.

4.4. Discussion

According to the analysis of ALOS/PALSAR images, the best filter for Single filter with kernel 3x3 is Gamma filter. The strength of Gamma filter is to distinguish the homogenous object (e.g., flood inundation area or water body). The principle of Gamma filter is that the pixel being filtered is replaced with a value calculated based on the local statistics (Saad, et al., 1996) where the local statistic is offering better performance within the homogeneous area. The Low Pass needs to be considered for the best filter from ALOS/PALSAR because it shows a good performance in Speckle Suppression Index (SSI) meaning good performance at removing speckle in the homogenous area.

Low Pass filter is excellent for smoothing because it is average the pixel value in moving window. Thus, it replaces the significant difference of the pixel value (i.e. the low or the high values). Thus, using big kernel sizes should be avoided when applying this filter. The user loses information due to over-smoothing on the ALOS/PALSAR image for Single filter. In contrary, Low Pass filter shows the best performance on the ALOS-2/PALSAR-2 image for Single filter because this image has a good spatial resolution. Therefore, Low Pass could preserve the detail even though smoothing filter was applied. It preserves the shape of the object clearly. ALOS-2/PALSAR-2 has spatial resolution 3 meters, and ALOS/PALSAR has approximately 10 meters spatial resolution; this is a significant difference that causes many differences in image processing results. ALOS-2/PALSAR-2 has a high signal intensity that causes the object to looks bright (North & Wu, 2001). Low Pass removes the over brightness of the image due to the signal intensity. According to this study, Low Pas filter enhanced its performance when the image has a

good spatial resolution. It could remove the brightness intensity due to the type of convolution filter.

For the Double filter on ALOS/PALSAR and ALOS-2/PALSAR-2, the combinations of Local Sigma with Low Pass shows the best performance among Double filter images. Local Sigma is strong in MAE. Hence, it could preserve the edges better than other filters. The local sigma only calculated the standard deviation in moving window and replaced the center pixel by averaging the neighboring pixel. Hence, Local Sigma was good in some statistic parameter. The algorithm of local sigma is given by, Eq. 4.8 to 4.11. We assumed that $W_{(i,j)}$ is a moving window with pixel $w_{(i,j)}$ as its center. The window size is $2k + 1$ (i.e. k is integer) and must be odd numbers (e.g., 3, 5, 7, 9, 11, etc.)

$$T_{(i,j)} = \sum_{m=i-k}^{i+k} \sum_{n=i-k}^{j+k} w(m,n) \quad (4.8)$$

$$N_{(i,j)} = (2k + 1)^2 \quad (4.9)$$

$$\mu_{(i,j)} = \frac{T_{(i,j)}}{N_{(i,j)}} \quad (4.10)$$

where $T_{(i,j)}$ is summarize of the pixel value; $N_{(i,j)}$ is the number of the pixel and $\mu_{(i,j)}$ is the local mean in moving window. To obtain the local sigma, we substituted the Eq. 4.8, 4.9, and 4.10 to Eq. 4.11.

$$\sigma_{(i,j)} = \sqrt{\frac{\sum_{m=i-k}^{i+k} \sum_{n=i-k}^{j+k} W_{(i,j)} - \mu_{(i,j)}^2}{N_{(i,j)}}} \quad (4.11)$$

Even though the Local Sigma was strong in preserving the mean value of pixel (MPI), enhancing the edge (EEI and MAE) and fine detail (IDPC) due to only calculating the standard deviation in moving window, however, it was low in visual performance because some speckles appear on the filtered images. The Local Sigma filter is adaptive to local variance, not the variance of the whole image. It is a reason why Local Sigma filter has a good statistical performance but low in visual. Saad et al. (Saad, et al., 1996) stated that Local Sigma filter does not exclude heterogeneous pixels in a homogenous region, we also found the heterogeneous pixels in the homogenous region that showed as bright pixels in the dark area. It makes the Local Sigma have low performance in visual performance. Even though the Local Sigma filter has a disadvantage as

a Single filter, its limitation became an advantage when combining with another filter because Local Sigma does not change the pixel value, but it enhances the edges and contrast of the object. Low Pass can cover the limitation of local Sigma because it removes the speckle by smoothing.

4.4.1. Assessment for flooded area

In August 2008, heavy rain occurred in Japan. The most impacted area was Aichi Prefecture. The rains caused floods in Okazaki City and Anjo City, and the depth of the flood inundation reached 1.05m from 28th to 31st August (Japan Meteorology Agency, 2008). ALOS/PALSAR images were used to detect the flood inundation areas. Figure 4.2 shows the flood location on Google Earth before flooding in Aichi Prefecture. There are two locations; Location 1 had shallow flood inundation (Fig. 4.9a, 4.9b and 4.9c) and Location 2 had deep flood inundation (Fig. 4.9d, 4.9e and 4.9f). Deep flood inundation means that the area was flooded over 0.5m (Japan Meteorology Agency, 2008). The inundation field survey conducted by the local government was accumulated of inundation area during flood period; the satellite images was recorded on August 31st,2008.

Figure 4.9 displays the detected flooded areas by using No-filter, Single filters and Double filters. They are representative images of selected filters; the images were applied to ISODATA classification. In the case of deep inundation area, it was easy to detect the edge of flooded area by using both of Single filter or Double filter. The effectivity of Double filter for detecting flood can be seen in Fig. 4.9c. However, the reflectance of water was weak in the shallow inundation area. In this area, the detected object by the satellite is not only water but also other objects, e.g., soil and grasses. Removing speckle in the homogenous object was easier comparing to the heterogeneous objects.

The unsupervised classification (ISODATA classification) was chosen in this study; it was classified based exclusively on the image statistics without obtainability of a training area or prior knowledge of the area (ENVI, 2004). The ISODATA classification was applied to the original image and to selected filter images. We applied 15-20 of classes by using ENVI 5.3 software: the classification of the original image (no filter) produced many classes but only a small number of pixels in one group of class. Hence, we got many classes centroid. It was unable to generate a good classification because the area of one class was narrow. To display Fig. 4.9a and 4.9d, we displayed uncountable class centroid. Whereas for Fig. 4.9b and 4.9e, we displayed some class centroid and we applied a few class centroid for Fig. 4.9c and 4.9f. No filter and Single filter image represented the separated flood area; we could see white areas (non-flood) in the red area. The flooded area in this pilot area should be merged as one polygon, but due to a large amount of speckle noise, this

flood area contents many polygons due to many numbers of the class centroid. By double filter we could easily to detect the edge of flood area. Hence, this filter will be useful to automated extraction of inundation area by utilizing SAR images.

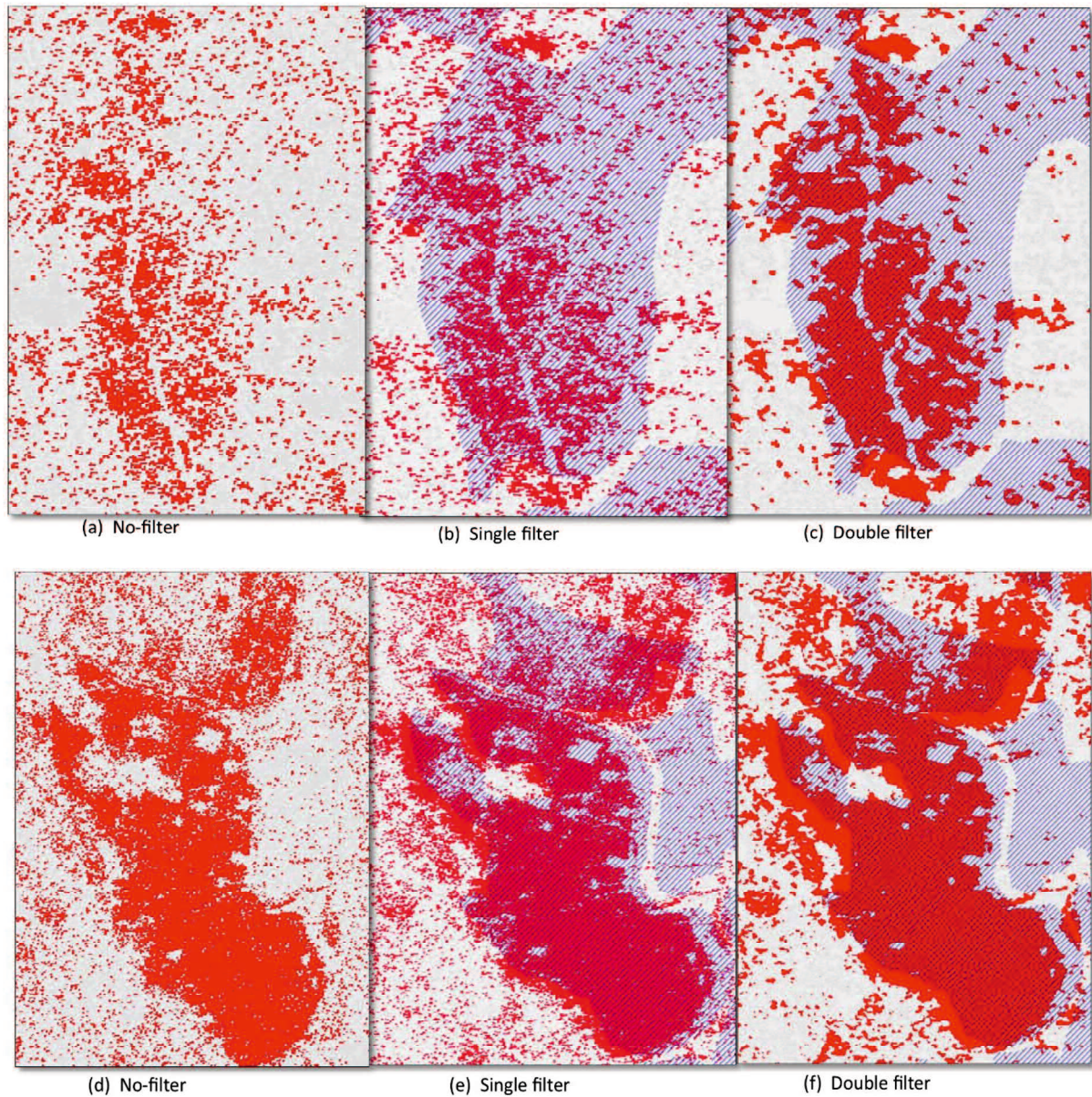


Figure 4. 9 Detected flooded area by using No-filter, Single filter and Double filter for shallow inundation area (a, b and c) and deep inundation area (d, e and f). Shadow area is accumulated inundation area during the flood period

Visual performance for the Single filter as shown in Fig. 4.9b and Fig. 4.9e described that Single filter showed low performance comparing to Double filter images. For the deep inundation area, both Single filter and Double filter were able to distinguish the unflooded and flooded area.

However, for the shallowly inundated area, Single filter enabled merging of the area which had the same backscattering value. Hence, the flooded area is shown by many of tidy polygons. This result means that filter type influences the classification result. According to the ISO classification results, the Double filter image could distinguish the object with more detail than Single filter images.

Although radar does not penetrate inundated water, it can reflect the surface action of oceans, lakes, and other bodies of water and sometimes provide information about the bottom features of the water body (Jensen, 2000). Thus, we could apply the ALOS/PALSAR image with HH polarization to detect the flood inundated area. HH polarization has better performance comparing to others polarization for detecting the flood [Manjusree, et al., 2012]. It is quite easy to reduce speckle in the homogenous area such as water compared to the heterogeneous area. The filter removes the speckle on the homogeneous object (Jensen, 2004). The shallowly inundated area is an example of the heterogeneous area during the flood. It is difficult to be detected by the satellite images, especially in SAR images because the image reflection is mixed. However, when applied to the flood, we required that the filter is able not only to reduce the speckle in water bodies but also able to preserve edges and object detail. These are fundamental requirements. According to Fig. 4.9, extracting the flood in deep inundation area was easy by Single filter or Double filter. However, for the shallow inundation area, it was easier to extract the flood area by using the Double filter.

Because floods are temporary phenomena, we need to know the inundation edge of the flooded area and the area around the flooded area should be informative. Especially in the case of Aichi Prefecture, where the flood occurred in Okazaki City and Anjo City, precise information about flooded area in related to evacuation the flood victims were required. Hence, by filtering images with the proper filter, we could detect flooded area easily.

4.4.2. The strength of the proposed filter

Dong et al. and Gonzalez et al. have already pointed out that speckle filtering can effectively reduce the speckle level. However, it can filter more or less, smear edges and blur images. In this study, we found that the size of the kernel, type of filter and combination of filters played an important role in reducing speckle noise, preserving the information and classifying objects in SAR images. We utilized adaptive filters and convolution filters to reduce the speckle on an ALOS/PALSAR image and ALOS-2/PALSAR-2 image. We proposed to filter two times, known as the Double filtering method; this method was not over smooth the image because we combined

the advantage of different filters. Thus, by Double filter we can achieve the purposes of filtering; to reduce the speckle noise, preserve the edges, and preserve the object detail; flooded and non-flooded area can be easily distinguished, and this filter can be applied by using commercial and freeware software.

Generally, by the quantitative assessment, the Double filter showed better performance in suppressing the speckle and preserving the mean value of the filtered image. It was emphasized by the lower value of the SSI and MPI. The additional figure to emphasize the advantage of the Double filter can be seen in Fig. 4.10.

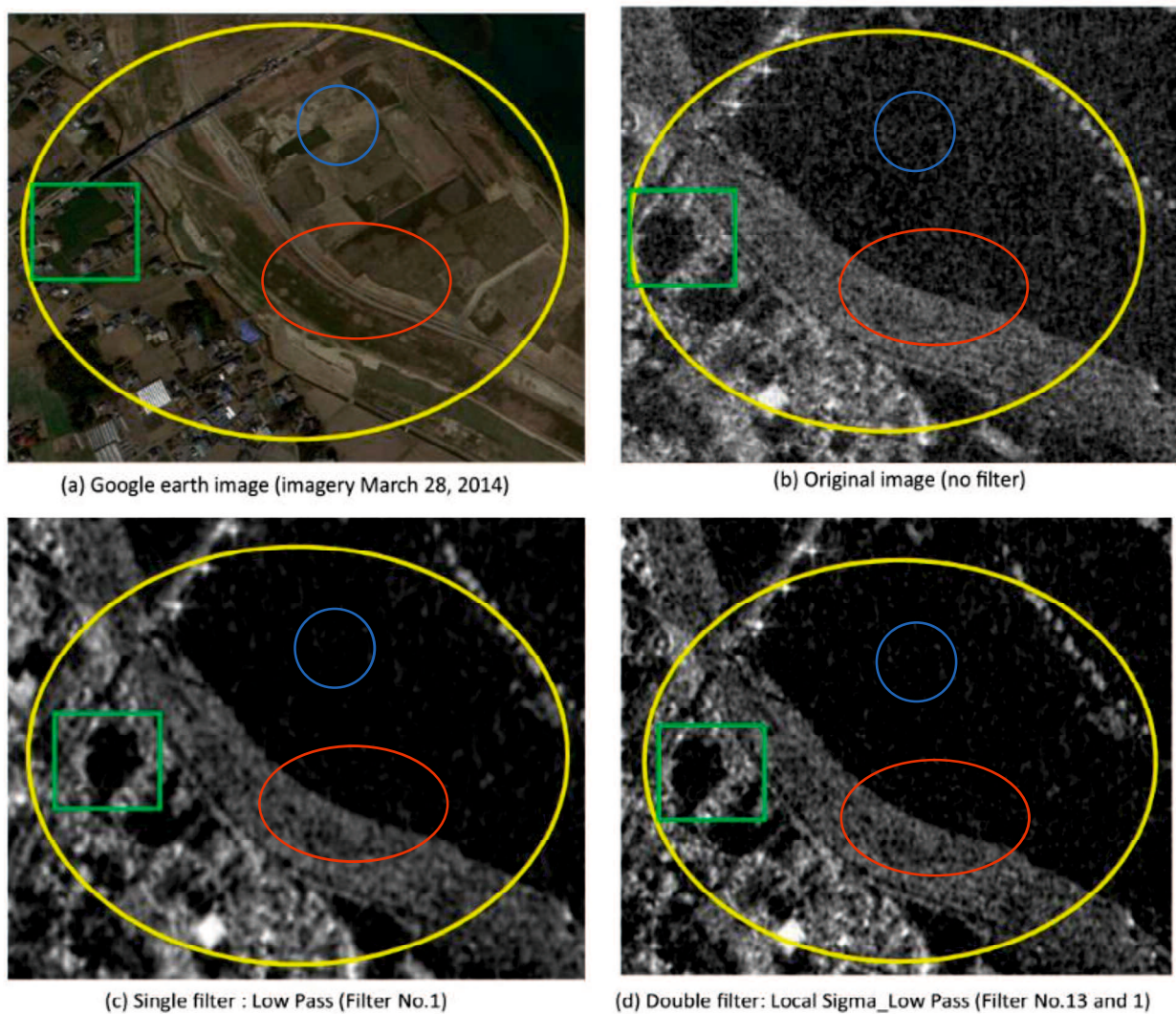


Figure 4. 10 Single filter (left) and Double filter (right) visual performance comparing to the no-filter image and Google Earth image. Green box: vegetation, blue circle: water, red ellipse: bare/soil.

Figure 4.10 shows the visual performance of the best Single filter (c) and the best Double filter (d) that we extracted from Fig. 4.7 and Fig. 4.8. Figure 4.10 shows that Double filter (d) had better contrast image than a Single filter and it could preserve more edge and object detail comparing to the Single filter image. We could easily recognize the object due to its strong edge pattern for example vegetation (green box); its shape was similar to the Google Earth image. The blue circle shows the water object, white part in this circle means speckle. Red ellipse shows the detail of object, Single filter shows more over-smoothed compare to the Double filter. Double filter generated less speckle image comparing to the no-filter image and Single filter image. According to Fig. 4.10, the spatial resolution was improved by the Double filter.

Improvement of resolution can be achieved by adding the comb filter (Kulpa, et al., 2004). A comb filter inserts a delayed type of a signal to itself, affecting constructive and destructive interference (Smith, 2010). Improved resolution can be expressed by following Eq. 4.12.

$$\delta = \frac{1}{2k} \sqrt{R\lambda} \quad (4.12)$$

Where R is distance between the radar and the range, λ is wavelength of the transmitted signal, and k is coefficient depending on the length of the impulse response. The Low Pass filter increased the length of impuls response. The precise determination of coefficient k is difficult because the real and imagery parts of the impuls response have different lengths (Kulpa, et al., 2004). Hence, by added the comb filter, in this case is Local sigma filter, the coefficient k is increased what improves achieved resolution.

4.5. Conclusion

This study proposed the Double filter method to reduce speckle noise and preserve the edge and object detail on ALOS/PALSAR images and ALOS-2/PALSAR-2 images. Kernel size and type of filter have an important role in the classification process.

According to the quantitative assessment (i.e. statistic parameters; SSI, MPI, EEI, MAE, FPI and IDPC) and qualitative assessment (i.e. visual performance) to measure the speckle reduction, edge and fine object detail, we recommended the combination of Local Sigma with Low Pass filter for application in flood detection.

Double filtered images show better performance than Single filter images. The Double filtered images combined the advantage of the different filters. Hence, we could get the best combination of the filter that can reduce the speckle noise and preserve the edge and object detail. Double filter improved the spatial resolution because the length of impulse response increased by

combination Local Sigma filter with Low Pass filter. Applying the Double filter on flooded area has advantages in that it is easy to recognize the flooded area in the shallowly inundated area.

Finally, the future tasks are evaluating the Double filter for automated extraction of inundated area from SAR images. And also, applying the Double filter method to other SAR images, different level of SAR images and different polarization are challenging. Furthermore, we will apply this double filter to other applications, e.g., land classification and other natural disasters.

CHAPTER 5

EVALUATING THE EXTRACTION APPROACHES OF FLOOD EXTENDED AREA BY USING SAR IMAGES AS A RAPID RESPONSE TO FLOOD DISASTER

5.1. Introduction

Flash flood is defined as a quick onset of a flood with a short-term duration and a moderately high peak outflow (Zhang, et al., 2015). It happens quickly, commonly within six hours of rainfall, and is sometimes followed by debris flows, mudflows, bridge and river bank collapse, and damage to infrastructures and houses (Hapuarachchi, et al., 2011). The height of flash floods can exceed 10 m (~30 ft) [Davis, 2001]. Remote sensing has been applied to flash flood studies, including flash flood monitoring by the near-infrared Lidar (Tamari & Guerrero-Meza, 2016), flash flood prediction by remotely-sensed precipitation (Yucel, 2015), and flash flood damage mapping (Singh, et al., 1993).

Some studies have been done by previous researchers to detect flash floods. Kuldeep and Garg (2016) investigated floods by using image fusion of Cartosat-1 and Resourcesat-1. By using object-based classification, they categorized the land cover into nine classes with segmentation scale 80. They utilized the panchromatic image to extract the flood. It can be possible to utilize the panchromatic data once the rain has finished and the water has inundated for a few days. Hence, the panchromatic image is powerless to apply to extracting the flood immediately during torrential rains (Nascetti, et al., 2014). During a flood event, radar sensors are the best sensors to detect the inundation area; radar measures the returned signal, i.e. backscatter, and can measure the terrain regardless of the weather and time [Campbell & Wynne, 2011; Dellepiane, et al., 2000; Horritt, et al., 2001; Wiesmann, et al., 2001]. Water has low backscattering in SAR images [Baldassarre, et al., 2011] because water has a smooth surface (Richards, 2009). The water area is shown as a dark area in SAR images because the signal directly reflects like a mirror reflection on smooth surfaces. Manjustree *et al.* investigated the best polarization to extract the flood by using RADARSAT-2. They concluded that transmitted Horizontal and received Horizontal (HH) polarization was better than transmitted Horizontal and received Vertical (HV) polarization, transmitted Vertical and received Horizontal (VH) polarization, and transmitted Vertical and received Vertical (VV) polarization (Manjusree, et al., 2012). Pierdicca *et al.* (2008) investigated the flood inundation area by integrating ERS-1 imagery, land cover map and DEM data. Mason *et al.* (2010) detected flooding in an urban area by applying TerraSAR-X and Lidar data to eliminated effects of shadow

and layover.

Typhoon 18 passed through Japan and caused torrential rain from West Japan to Northern Japan in 2015. The typhoon brought heavy rainfall to Tohoku and Kanto area. From 7th-11th September the rainfall intensity exceeded 500mm for the Tohoku region and 600mm for the Kanto region. Especially in Tochigi Prefecture, the rainfall intensity was observed by 16 observation points that reached 550mm during the 24 hours from September 10th to 11th. As a result, the heavy rain occurred during the evening [Central Disaster Prevention Council, 2016; Joso City, 2016] and caused the river bank collapse in the middle of the night. The Japanese government's Fire and Disaster Management Agency and other national and local governments reported 12,088 flooded homes [Central Disaster Prevention Council, 2016; Joso City, 2016].

ALOS-2/PALSAR-2 as the first satellite to record the flooded area in Joso City has a major role in a rapid flood response. This satellite was designated to visit the disaster-prone area around Sentinal Asia member (Asia Pacific) immediately after the disaster occurring. ALOS-2/PALSAR-2 image also has been utilized for monitoring and extraction flooded areas [Honda, et al., 2016; Arii, et al., 2016; Yamazaki & Liu , 2016]. In the case of the flood in Joso City, the ALOS-2/PALSAR-2 recorded the flood area at 2:43 am, a few hours after the flood occurrence. This means that rapid data from this satellite is available when a disaster occurs. The aim of this study is to evaluate the extraction methods of the flooded area by a quick method using satellite images, because rapid flood inundation extraction and delivery of flood inundation maps during a flood period can support crucial information for government and decision makers to highlight relief and rescue processes.

Hence, this study compared methods to extract the flood data for a rapid response to the flash flood. The extraction of flood data used three methods; unsupervised classification (Vassileva, et al., 2015), supervised classification [Yamazaki & Liu , 2016] and binarization or thresholding of backscattering value (Hong, et al., 2015). Some researchers investigated these methods to flood. Vassileva *et al.* (2015) investigated flooding in Ljubljana (Slovenia) by extracting the shadow using unsupervised classification and utilizing RADARSAT-2 images combining with Shuttle Radar Topography Mission (SRTM) images with 90m of spatial resolution. The advantage of this research was an application in a wide area without training area. Yamasaki and Liu (2015) had analyzed Joso City by using ALOS-2/PALSAR-2 that recorded September 10th, 11th, 13th and October 10th 2015 by classifying the land cover. They also extracted the water body by using 5m DEM data. According to their study, the peak of the flood was on 11th September 2015. As known,

the flood in Joso City occurred due to the bank collapse. Their result was unable to show the bank collapse by using their flood extraction method. Yamasaki and Liu (2016) applied some data to monitoring the distribution of the flood inundation. Hong *et al.* (2015) studied the water area extraction by thresholding and integrating the RADARSAT SAR imagery, Landsat imagery and DEM data. They utilized LANDSAT 5 TM to extract the land use by unsupervised classification, extract water from RADARSAT SAR imagery by thresholding the backscattering of water and topography correction by applying DEM data. All the studies offered method using SAR images (medium and high-resolution data) for detecting the flood. However, no study have compared the effective method and high accuracy using ALOS-2/PALSAR-2 (high-resolution data) for flood detection.

This study intended to extract the flash flood as a rapid response. This study evaluated three methods to extract the flooded area in Joso City during the flood on 10th September 2015. Two of the approaches used are land cover classification and one method uses binarization or threshold of backscattering value. A straightforward and informative method was required to fulfil flash flood extraction as a rapid response. The method should trim the long processing time. All the methods were verified by using the aerial photo as a field survey. ALOS-2/PALSAR-2 as SAR image has a disturbance, e.g., speckle and shadowing that caused the overestimating the inundated area. The speckle noise was removed by applying double filter (Rimba, et al., 2016) and shadowed area was removed by slope map (Mason, et al., 2010).

The selected method from this chapter was applied to ALOS/PALSAR image to detect and extract flood in Okazaki City where was studied in Chapter 3. Furthermore, the result of flood extraction from ALOS/PALSAR was superimposed to flood vulnerability prediction and field survey of flood in 2008 by Okazaki Government.

5.2. Study area and data set

5.2.1. Study area

Joso City is positioned in the southwestern part of Ibaraki prefecture and approximately 55 km from Tokyo. Its width is approximately 20 km north-south and 10 km east-west with a total area of 123.52 km². The relief of the city has flat land with some low hills with altitude of 5-24 meters above sea level. Joso City has four seasons as a typical example of the Pacific Ocean temperate zone (JosoCity, 2016).

Kinugawa River passes almost through the central part of Joso City running from north to south. The east side of the river has become a broad area of rice because of the lowland. The west region of the river has low hills and spread farms, villages, cultivated fields, widespread wood-plains; and is being developed with the development of industrial places, residential plazas, golf courses, and so on, as one of the strategic areas of Tokyo Metropolitan Region, strengthening urban structure roles. According to the Statistics data as of 1st January 2015, Joso City has population 65,370 people [JosoCity, 2016]. Fig. 5.1 displays the study area.

Before the flood control dam was constructed in the upstream of Kinugawa River, flood used to occur due to heavy rain (e.g., September 1935, September 1938, September 1947, August 1949, September 1982 and July 2002) (MLIT, 2017). However, the heavy rainfall occurred in September 2015 and caused flash flood in east part of Joso City due to the river bank collapse. Flood inundated for a few days in Joso City (JosoCity, 2016) and caused two people die, more than 40 injured people and more than 5,000 extremely destroyed houses (JosoCity, 2016). The number of loss of life and material lead the rapid response to the flood. Thus, this study was applied in Joso City as the study case for rapid response to the flood.

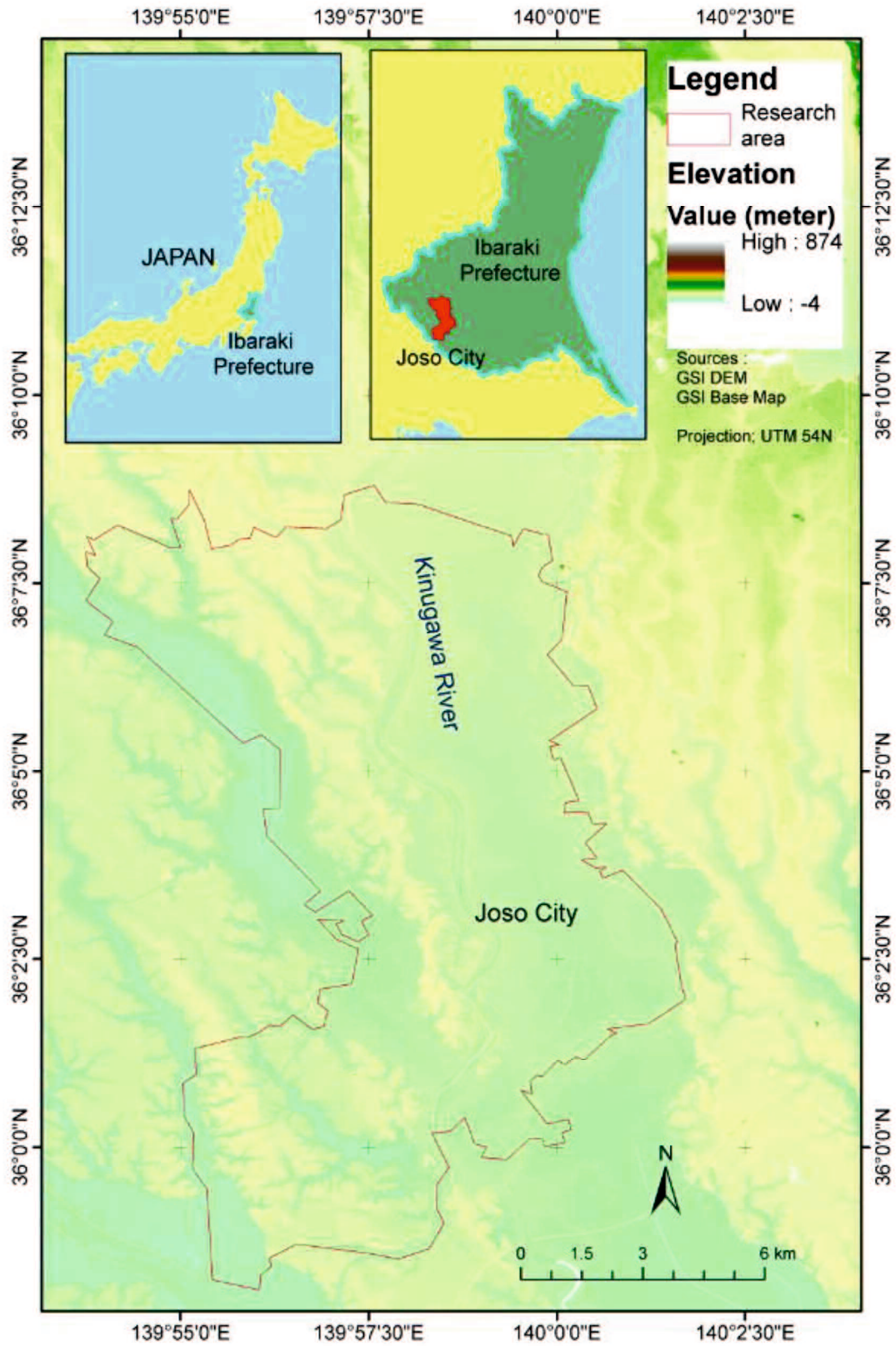


Figure 5. 1 Study area (source; Google Earth)

5.2.2. Dataset

This study utilized three kinds of data. Digital Elevation Model (DEM), 5 meter accuracy, was provided by The Geospatial Information Authority of Japan (GSI) with Geography Markup Language (GML) format. We utilized this data to generate the slope map; Aerial photo (recorded September 9th, 2015) during flooding in Joso City; it was provided from GSI in order to verify the extraction methods. ALOS-2/PALSAR-2 images provided by JAXA as listed in Table 5.1.

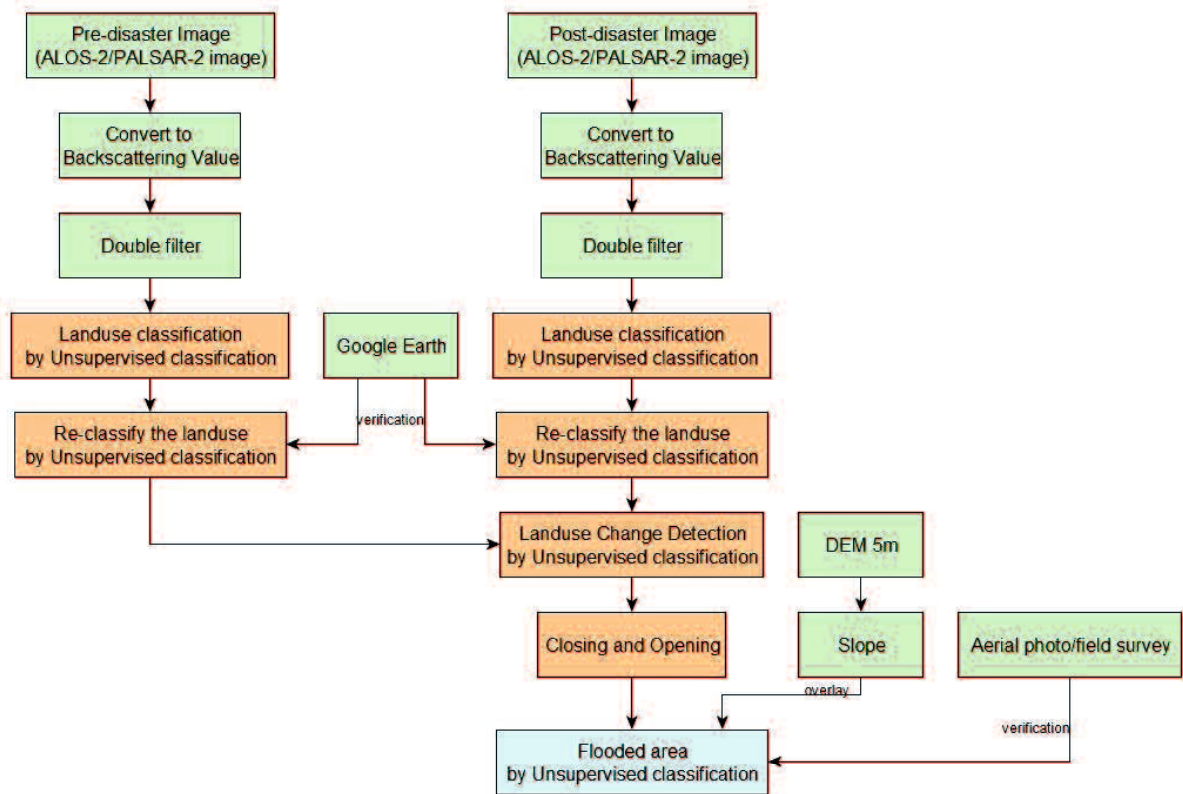
Table 5. 1 Specification ALOS/PALSAR and ALOS-2/PALSAR-2 images for this study

Satellite	Date	Image	Observation direction	Off-nadir	Polarization	Res.
ALOS-/PALSAR-2 (Joso City)	2015/9/10	Post- disaster	Descending	35.8°	HH	3m
	2015/7/31	Pre-disaster	Descending	35.8°	HH	3m
ALOS/PALSAR (Okazaki City)	2008/8/31	Post- disaster	Descending	34.3°	HH	6.25 m
	2007/8/21	Pre-disaster	Descending	21.5°	HH	6.25 m

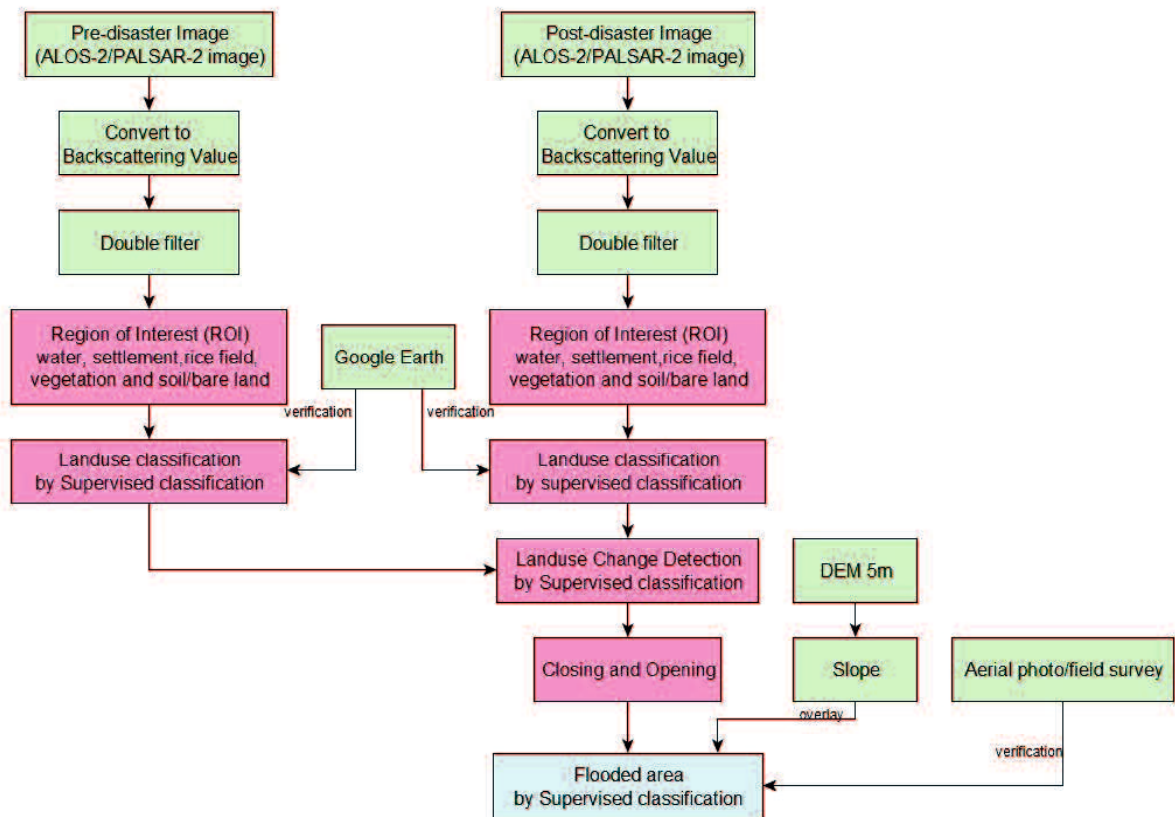
5.3. Methodology

5.3.1. Flood extraction methods

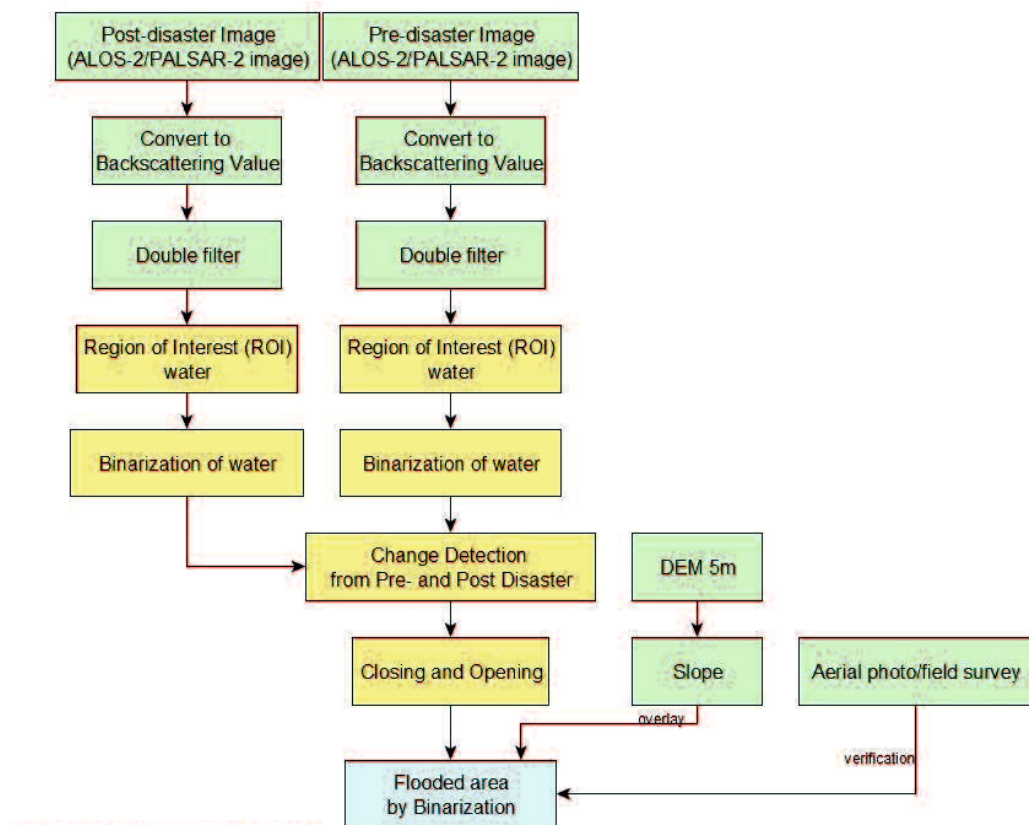
In this study, unsupervised classification and supervised classification which classified the land use and detected the land use change. Binarization method extracted the backscattering of water. We used only SAR images (pre- and post-disaster) to extract the land cover and flood inundation. Field survey verified the extraction flood; the distribution which has similar distribution with the field survey was selected as the recommended method. Overestimation of the flood area by using SAR image could be reduced by superimposing to slope data. We decided the margin of slope data according to the flood distribution of field survey. Otherwise, the limitation of SAR image in settlement area (e.g., double bounce) was not included in this study. The flowchart of proposed methods is displayed in Fig. 5.2.



(a) Unsupervised classification method



(b) Supervised classification method



(c) Binarization/thresholding method

Figure 5. 2 Flowchart of proposed methods

Three methods were applied to extract the flood inundation in Joso City when the flood was occurring in September 2015 by utilizing the ALOS-2/PALSAR-2 images. All these methods utilized pre- and post-flood of SAR images. Post-disaster image refers to an image recorded during the flood. We applied unsupervised classification as the first method and supervised classification as the second method to classify the land use pre- and post-disaster. Land use classification of pre- and post-disaster image were superimposed to find the land use change. The third method was extracting the water backscattering from pre- and post-disaster and deciding the threshold of the flood inundation, i.e., binary/backscattering threshold method. The change area from pre- and post-disaster image is identified as the inundation of flood. The best method was applied to ALOS/PALSAR image for Okazaki City.

5.3.2. Backscattering

The first step of processing the ALOS-2/PALSAR-2 data was converting from the digital number (DN) to the backscattering coefficient (sigma-naught) in order to generate the value of backscattering of the object. It denotes as dB and obtained by the following Eq. 5.1 (JAXA, 2016).

$$\sigma^0 = 10 \log_{10}(DN^2) + CF \quad (5.1)$$

where: σ^0 is backscattering coefficient; DN is a digital number; CF for ALOS-2/PALSAR-2 are 83 (JAXA, 2003) as listed in Table 5.2. CF can be calculated by following Eq.5.2; where A_x is area of the compound and C_x is concentration of the compound.

$$CF=A_x/C_x \quad (5.2)$$

Table 5. 2 Value of CF and A for ALOS-2/PALSAR-2

CF	mean (dB)	std (dB)
CF ₁	-83.0	0.406
A	32.0	-

5.3.3. Application Double filter

The Double filter is applied to all data in this chapter. The Double filter is a new method to reduce the speckle by filtering an image two times using a different type of filter as explained in Chapter 4. By applying the Double filter, the classification of flooded and non-flooded area is more accurate compared to the Single filter. The recommended combination of filters was the combination of Local Sigma filter as the first filter and then Low Pass filter as the second filter.

5.3.4. Image classification

5.3.4.1. Unsupervised classification

Unsupervised classification: Pixels are classified based on the reflectance properties of pixels (i.e. clusters or group). The unsupervised classification method of image classification is used when no sample sites exist (GISGeography, 2016; Eastman, 2001). It is a grouping algorithm that customs an iterative procedure to discrete image pixels into a spectrally similar group according to their position in spectral space (Enderle & WeihJr, 2005). There are several unsupervised classifying algorithms for images, for example, K-means (vector quantization) and the Iterative Self-

Organizing Data Analysis Technique (ISODATA). ISODATA was applied in this study by utilizing the software ENVI 5.3. The process of unsupervised classification starts by initiating the cluster of the pixel and calculating the mean of the cluster. During the iteration process, the similar characteristics of the pixel and closer distance is grouped into one class. The process is repeated until all the pixel are classified. By applying this method, we recognized the number of groups to create and which bands to apply and manually distinguish each group into new classifications. In Remote sensing application, unsupervised classification is broadly used for land cover and land use classification (Hegazy & Kaloop, 2015; Abdullahi, et al., 2017; Movia, et al., 2016), and coral habitat mapping (Li, et al., 2017). The land cover was divided into 5 classes i.e. rice field, water, vegetation, building and soil or bare/open land area. We did the re-classify to the classified image from the software and then verified using Google Earth images.

5.3.4.2. Supervised classification

Supervised classification: The user selects a representative training area for the digital image classification. Supervised classification in remote sensing field is broadly utilized to classify the land cover and land use (Rawat & Kumar, 2015; Hegazy & Kaloop, 2015; Butt, et al., 2015). The image analysis software utilizes the training sites to classify the land cover categories in the whole image. The analysis of land cover is performed according to the spectral value determined in the training area. The frequently used supervised classification algorithms are maximum likelihood and minimum distance classification. Supervised classification steps are: select training areas, i.e. Region of Interest (ROI), generate the signature file and classify (GISGeography, 2016). The clustering process of the supervised classification follows the same procedure as unsupervised classification. Supervised classification repeats the calculation of unclassified pixels to the same characteristics of the training area.

By following the training area of supervised classification, the software calculated pixels similar to the training area. In this study, the land use were classified into five classes; rice field, water, vegetation, building and soil or bare/open land area. The difference of unsupervised and supervised method is how to making the classification of land use. In unsupervised classification, we allowed the software ENVI 5.3 to classify the image. In supervised classification, we selected the ROI and asked the software to classify the pixels by their similarity or by distance.

5.3.4.3. Binarization

Image binarization is one of the fundamental techniques of image processing. Image binarization is a method that separates the pixel values into two groups, namely white as the background and

black as foreground [Si Qi & Lei, 2002]. Thresholding has an important role in the binarization process, because the suitable threshold value is the beginning of the next process operation, e.g., feature extraction, segmentation, target recognition and so on [Zhang & Dou, 2014].

The threshold method proposed by Otsu is a global adaptive binarization technique, which is the best representative of global adaptive thresholding and tries to find a single threshold value for the whole image [Otsu, 1979]. Image thresholding is a simple arrangement of image segmentation. It is a way to create a binary image from a grayscale or full-color image (ENVI, 2004).

Given an image $I(x, y)$ containing light object (change) on a dark background (no-change), the object may be extracted by a simple thresholding.

$$I(x, y) = \begin{cases} 1 & I(x, y) > T \\ 0 & I(x, y) \leq T \end{cases} \quad (5.3)$$

Where; T is the threshold value given empirically or statistically by the researcher. All the pixels which are part of the object (change) are denoted 1, and the background (no change) are denoted 0 [Singh, 1989]. The local knowledge or visual interpretation about the scene or the area is meaningful in the thresholding method [Schowengerdt, 1983]. In this study, we only extracted the water for pre- and post-disaster images. When selecting the sample area of water by using ROI, we have to know the area very well. We can utilize the google earth data or other satellite images to verify the sample area, when we don't have local knowledge about the study area. After we found the difference of pre- and post-disaster image, i.e., change detection, we decided the threshold of the flood area by utilizing the mean value of the change detection histogram.

5.3.5. Change detection by image differencing

Change detection is a method of recognizing differences in the condition of an object or phenomenon by detecting it at different times. The conditions for using an image for change detection are fulfilled when having the images have the same area and are obtained at different times (t_1 and t_2) [İlsever & Unsalan, 2012]. The formula of image differencing follows Eq. 5.4.

$$I_d(x, y) = I_1(x, y) - I_2(x, y) \quad (5.4)$$

Where I_1 and I_2 are the images generated from t_1 and t_2 , and (x, y) are positions of the pixels. The resulting image, I_d , denotes the intensity change of I_1 from I_2 . This technique works only if images are orthorectified/georeferenced.

The basic principle of change detection by applying remote sensing technology is that changes in land cover are seen according to the variation of radiance values; and the difference in radiance due to land cover change must be significant due to the other factors, e.g., atmospheric condition, difference sun angle and difference soil moisture [Singh, 1989].

In this study, the change detection approach was utilized to show the different of pre- and post-disaster images. It was applied after classification process of pre- and post-disaster images. The difference of classified object was identified as the flooded inundation area.

5.3.6. Opening and closing

Opening and closing are two significant operators from mathematical morphology. Both of them derived from the fundamental operations of erosion and dilation. Opening and Closing were applied to binary images, although there are also gray level versions. The primary effect of an opening is somewhat like erosion in that it tends to remove some of the bright pixels (foreground) from the boundaries of regions of foreground pixels. However, it is less destructive than erosion in general. The impact of the operator is to preserve *foreground* regions for the opening process and background regions for the closing process that have a similar shape to this structuring element, or that can completely contain the structuring element while removing all other regions of foreground pixels for opening and background pixels for closing (HIPR2, 2004). The purpose of this process was to generate a smooth classification result. This process required two classes of images. Thus, the classification image grouped into flooded area and non-flooded area.

5.4. Result and Discussion

The flood in Joso City occurred due to typhoon no.18 that caused torrential rains in the Kanto area and Tohoku area. The Kinugawa river discharge rate increased and caused the river bank to collapse.

Figure 5.3 shows the condition of the Kinugawa river; before the bank collapsed (recorded on May 6th, 2008 by GSI using the aerial photo) in Fig. 5.3(a), during the river bank collapse (recorded on September 11th, 2015 by GSI using the aerial photo) in Fig. 5.3(b) and one month after the damage (recorded on October 9th, 2015 by Google Earth) in Fig. 5.3(c). The water of the Kinugawa River flowed to Joso City through this point. The river bank was repaired a few days after the flood.

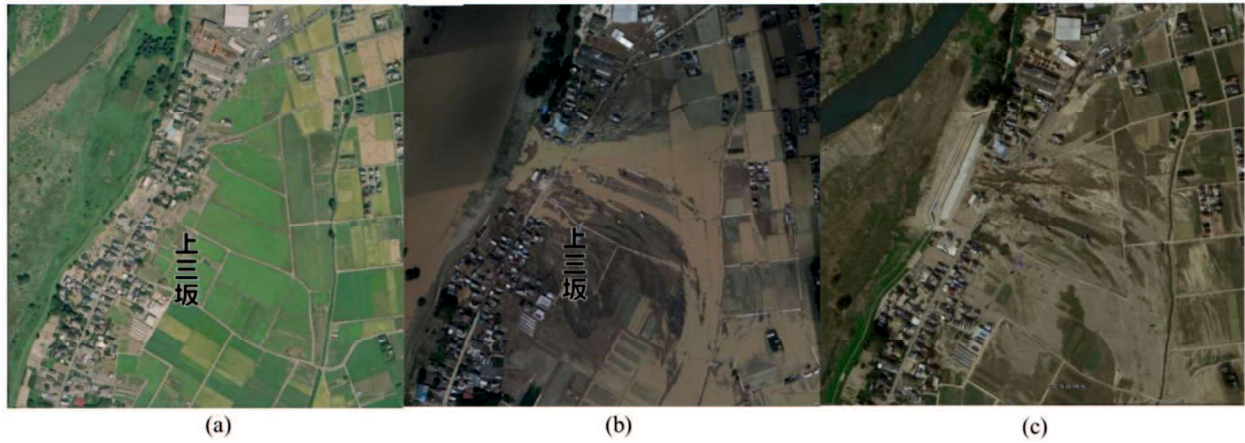


Figure 5. 3 (a) Kinugawa River condition before collapse (May 6th, 2008) and (b) after collapse (September 11th, 2015). The image was orthorectified by Geospatial Information Authority of Japan (GSI). (c) Google Earth image (October 9th, 2015).

The extraction methods were verified by using an aerial photo from GSI as shown in Fig. 5.4(a); it was recorded on September 11th, 2015 by aerial photography during the peak of the flood. The flood area is showed by the blue line; the author manually delineated it by using ArcGIS 10.2.2. Since it has high spatial resolution, the flooded area and non-flooded area can be distinguished clearly. Fig. 5.4(b) was composed by Red Green Blue (RGB) from ALOS-2/PALSAR-2 image. The flooded area was designated as the red color to show the contrast of flooded and non-flooded area. Thus, pre-disaster image filled red band; post-disaster image occupied green band, and the post-disaster image occupied Blue band. We selected the HH polarization for detecting the flood because water is easier to distinguish in this polarization [Manjusree, et al., 2012]. Both of figures in Fig. 5.4 (a) and (b) show a similar pattern of the flood. In order to extract the spatial information as shown in Fig. 5.4(b) for further analysis (e.g., calculating the area, distribution, so on), the red color in Fig. 5.4(b) was extracted by 3 methods (unsupervised, supervised and binary/backscattering threshold).

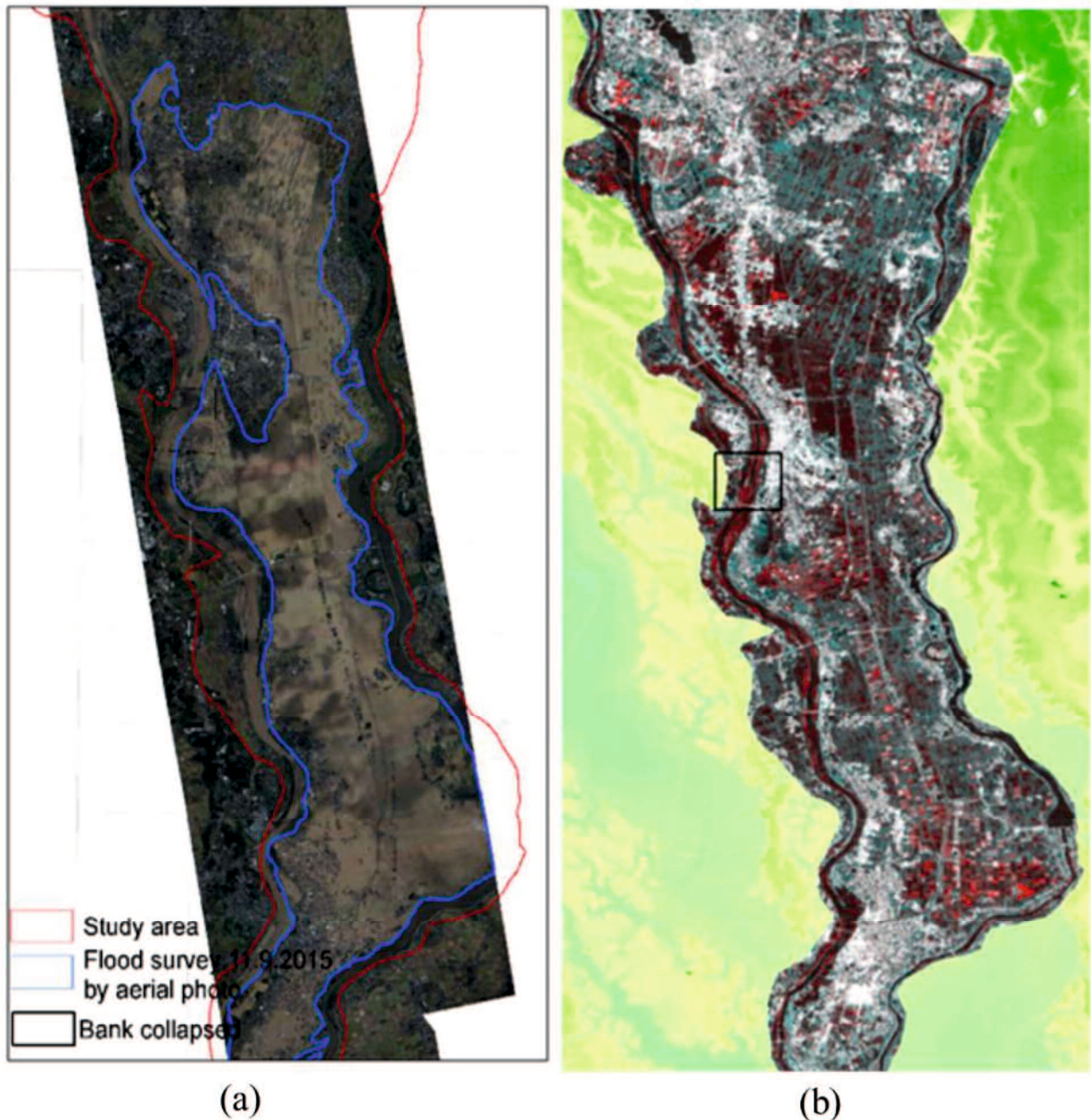


Figure 5. 4 (a) Aerial photography by GSI; (b) Pre-and post-disaster RGB (before-after-after)

5.4.1. Accuracy assessment

Figure 5.5 shows the inundated flood extraction in Joso City by the three applied methods. Figure 5.5(a) shows the unsupervised classification method to extract flood inundation, Fig. 5.5(b) displays extraction of inundation area by the supervised classification method and Fig. 5.5(c) extracted the flooded area by the binarization method. Figures 5.5(a) and 5.5(b) were extracted by classifying the land use of pre- and post-disaster images. The land use was classified into five

classes. The change detection of land use from the pre- and post-disaster was identified as flooded area.

As shown in Fig. 5.5(a) and 5.5(b), unsupervised classification shows more overestimation than supervised classification. The reason unsupervised classification has overestimated results is because many classes of unsupervised classification have similar spectral (Enderle & Weih Jr, 2005). We did not recommend this for classification activity if the user knows the study area well. This classification can be used when the user has no local knowledge of the area (Tempfli, et al., 2009). Supervised classification shows that flooded area is overestimated compared to the field survey (the black line shaded area is the field survey of flood inundation area). The pattern of the flood by supervised classification is un-cohesive as we can see in bottom part of flooded area. The supervised classification is unable to show the flooded area as one unit; the field survey, as illustrated in Fig. 5.4(a), shows that the flood distributes as one polygon. Comparing among the flood extraction methods, binarization or thresholding the backscattering method displayed the flooding as one unit polygon. We found less overestimated area compared to the unsupervised and supervised method, especially in the top of the study area. When using unsupervised and supervised classification, the area that was wet due to the rain was identified as flooded area. Because the image was recording during rain, the soil moisture was very high. Thus, the wet soil has low backscattering as backscattering of water; the binarization could threshold the moisture level of the soil moisture according to the mean value of the water histogram. Threshold process needs the local knowledge of the study area. Thus, we could generate the high accuracy of classification of flooded and non-flooded area. Joso City was inundated due to the bank collapse, and the location of bank collapse can be seen in the black square in Fig. 5.5. Applying unsupervised and supervised classification method did not show patterns of the bank collapse. The black box in Fig. 5.5(c) shows a similar pattern to the field survey of bank collapse in Fig. 5.3. Thus, binarization method was more informative than other methods.

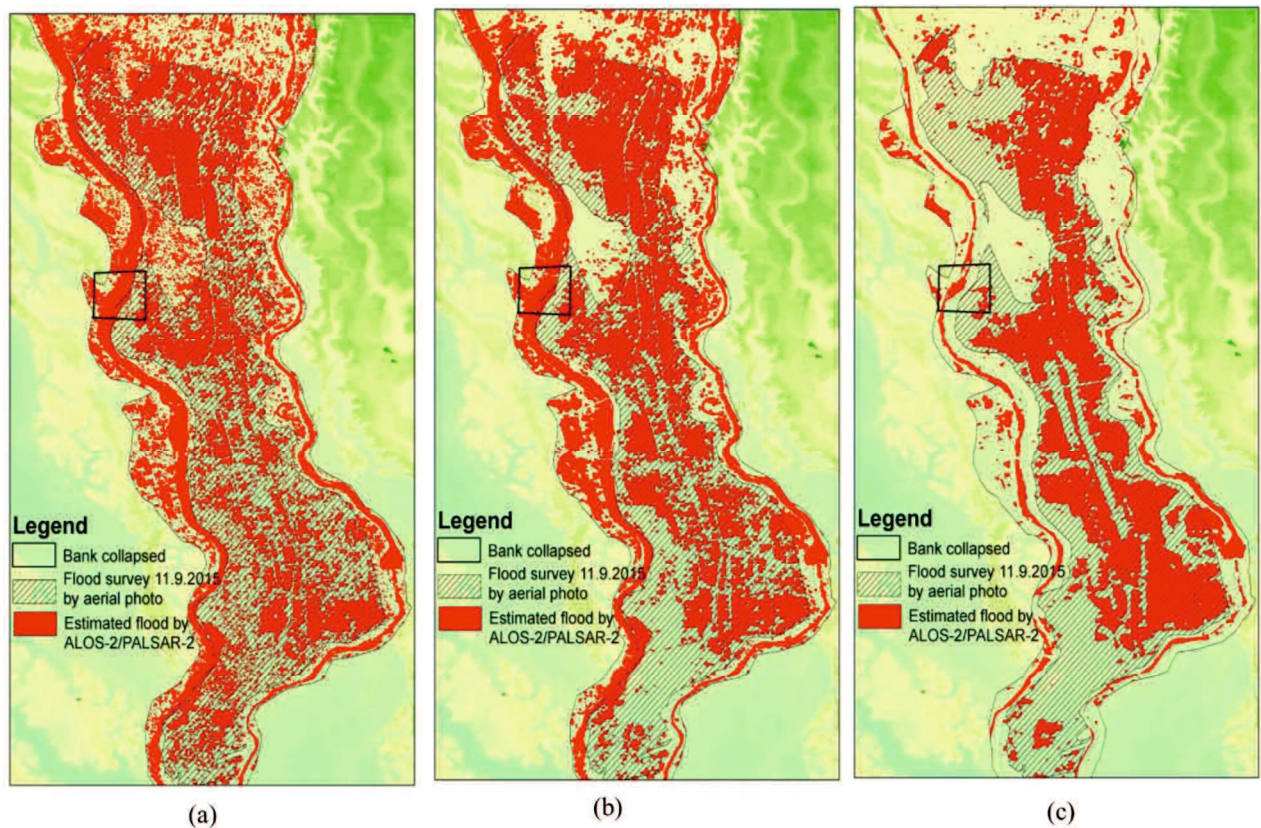


Figure 5. 5 Estimation of flooded area by using methods; (a) Unsupervised classification, (b) Supervised classification and (c) Binary/Backscattering threshold.

We applied two kinds of accuracy assessment: overall accuracy and Kappa coefficient. Kappa coefficient has lower value than overall accuracy because kappa coefficient measures the agreement between the predicting map and reference data (Lillisand, et al., 2004; Danoedoro, 2012). It means that kappa accuracy measures the mistake and correct prediction. Overall accuracy is only measure the correct prediction (i.e. only measuring the diagonal of the matrix). Table 5.3 lists the result of accuracy assessment by statistics.

Table 5. 3 Accuracy assessment of flood extraction approaches

Extraction approaches	Accuracy assessment	
	Overall accuracy	Kappa coefficient
Unsupervised method	74 %	69 %
Supervised method	79 %	72 %
Binary/backscattering threshold	95 %	94 %

According to the statistic accuracy assessment in Table 5.3, Binary/backscattering threshold method shows the highest accuracy in overall accuracy and kappa coefficient comparing

to other methods. We calculated this accuracy after removed the backscattering of building because it has effect double bouncing in SAR image. Hence, flooding in building area was difficult to detect. This study was considered a good accuracy due to the kappa coefficient 94%. A Kappa of 0.8 or above is considered as good accuracy; 0.4 or below is considered poor.

5.4.2. The limitation of using SAR images

By using SAR images, overestimation due to the slant-range distortion, e.g., shadowing, could occur. Shadowing in slant range distortion occurs when the peak of the object, e.g., mountain covers the object's behind [SARMap, 2009; McCandless Jr. & Jackson, 2004]. We utilized the DEM data from GSI to generate the slope map. We checked the flooded area in Joso City by superimposing the extended flood with the slope map (Fig. 5.6(a)) of Joso City. The flooded areas were less than 2%. Thus, we eliminated the flood estimation area which has slope more than 2%. The shadowed area which identified as the inundation area due to the slope were removed when its slope was more than 2%.

Figure 5.6 (b) shows the land use distribution of Joso City before the flood. It shows that along the river was dominated by buildings or settlement and the center area of the study area was dominated by rice field. In Fig. 5.6b, we emphasized the building area by red circle. Figure 5.6 (b) shows high illuminating in ALOS-2/PALSAR-2 due to the double bounce effect in SAR images. Thus, the flood was unable to be detected. Nevertheless, this area was flooded as shown in Fig. 5.6 (d). Another problem in utilizing SAR images was double bouncing of the signal to the sensor [Hong & Wdowinski, 2013]. In this case, the signal from the sensor transmitted to the water and water reflected it back to the sensor. Unfortunately, the reflected signal from water was first reflected to the building before being reflected back to the sensor. Hence, the sensor received the signal of water backscattering as building backscattering. However, the sensor transmitted the signal to the building and the building reflected the signal back to the sensor. Thus, the sensor received signal from building twice, i.e., double bouncing. This condition caused flood surrounding the building to be difficult to detect. It may be possible to detect this area by using different off nadir and polarization type. Different off nadir needs a difference of recording angle. Different polarization is different in transmitted and received signal.

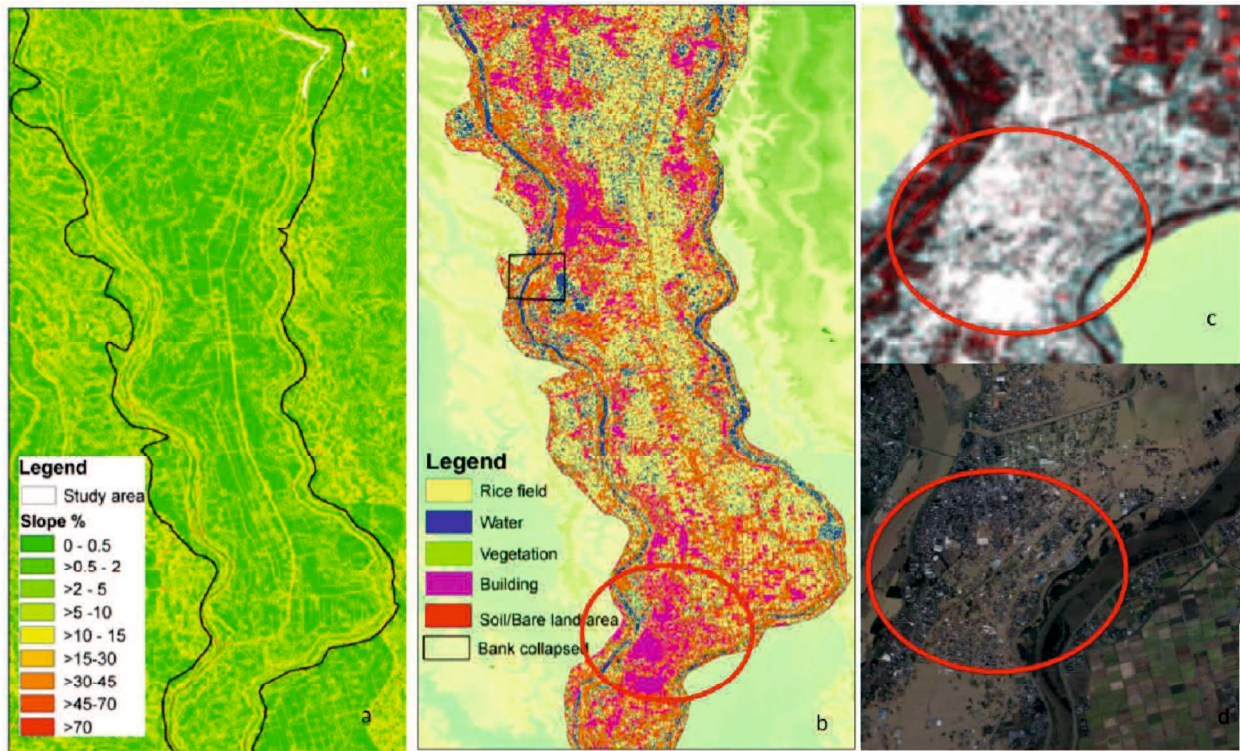


Figure 5. 6 (a) Slope map, (b) Land use classification of pre-disaster image by supervised classification, (c) Building area in Pre-and post-disaster RGB (before-after-after), (d) Building area in Aerial photography

5.4.3. Flood extraction from ALOS/PALSAR in Okazaki City

The different off-nadir angle of image before and after should be considered by using ALOS/PALSAR image in this study. Hence, we extracted the building backscattering from pre- and post-disaster images by Region of Interest (ROI) and corrected the backscattering value of image. Due to the effect of double bouncing of SAR images, the backscattering of building will not be influenced by water. Thus, we extracted building backscattering from both image to correct the backscattering value as shown in Fig. 5.7. The green ellipse shows the different part of backscattering. From the flood extraction by ALOS/PALSAR images, the backscattering of flood was (-7.4) ~ (-9.4) dB.

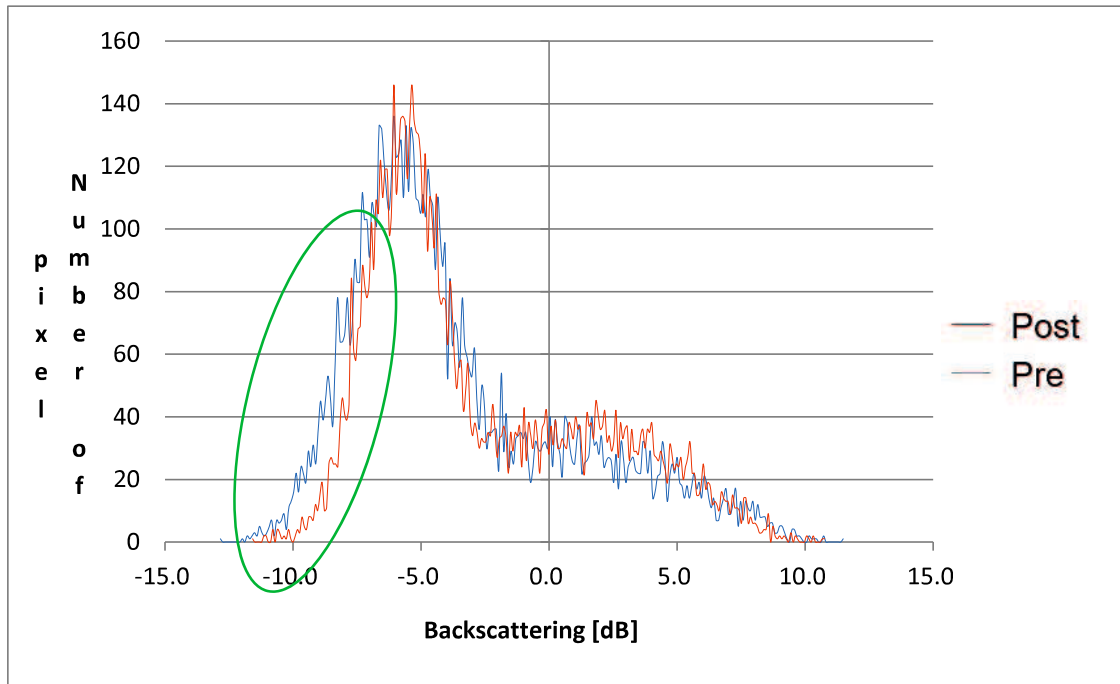


Figure 5. 7 Building histogram of building from Pre- and Post-disaster images

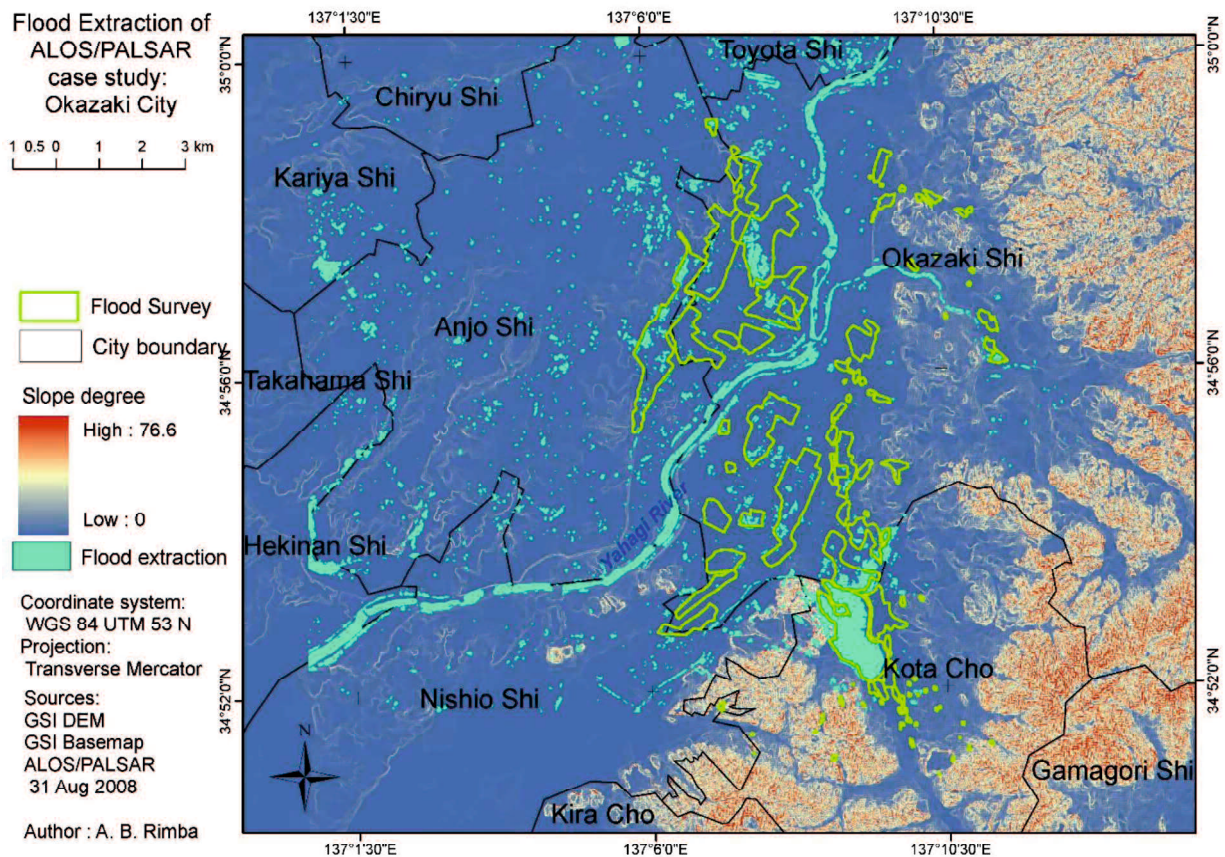


Figure 5. 8 Flood extraction by binarization method from ALOS/PALSAR image in Okazaki City

Figure 5.8 shows the distribution of flooded area in 2008 from ALOS/PALSAR images. The flooded area was extracted by utilizing binarization method as recommended method from this study. The shadowing effect in mountain area was removed by using DEM data. According to the section 5.4.2, the flooded area distributed in the area less than 2% of slope or 1.1 degree (level to near level as listed in Table 3.10).

5.4.4. Flood extraction from ALOS/PALSAR and flood vulnerable area by AHP method in Okazaki City

Figure 5.9 shows the distribution of flood extraction from ALOS/PALSAR during flood in Okazaki City in 2008 and predicted flood vulnerable area by AHP method. This figure used to measure the effectivity of predicted flood vulnerability model by AHP.

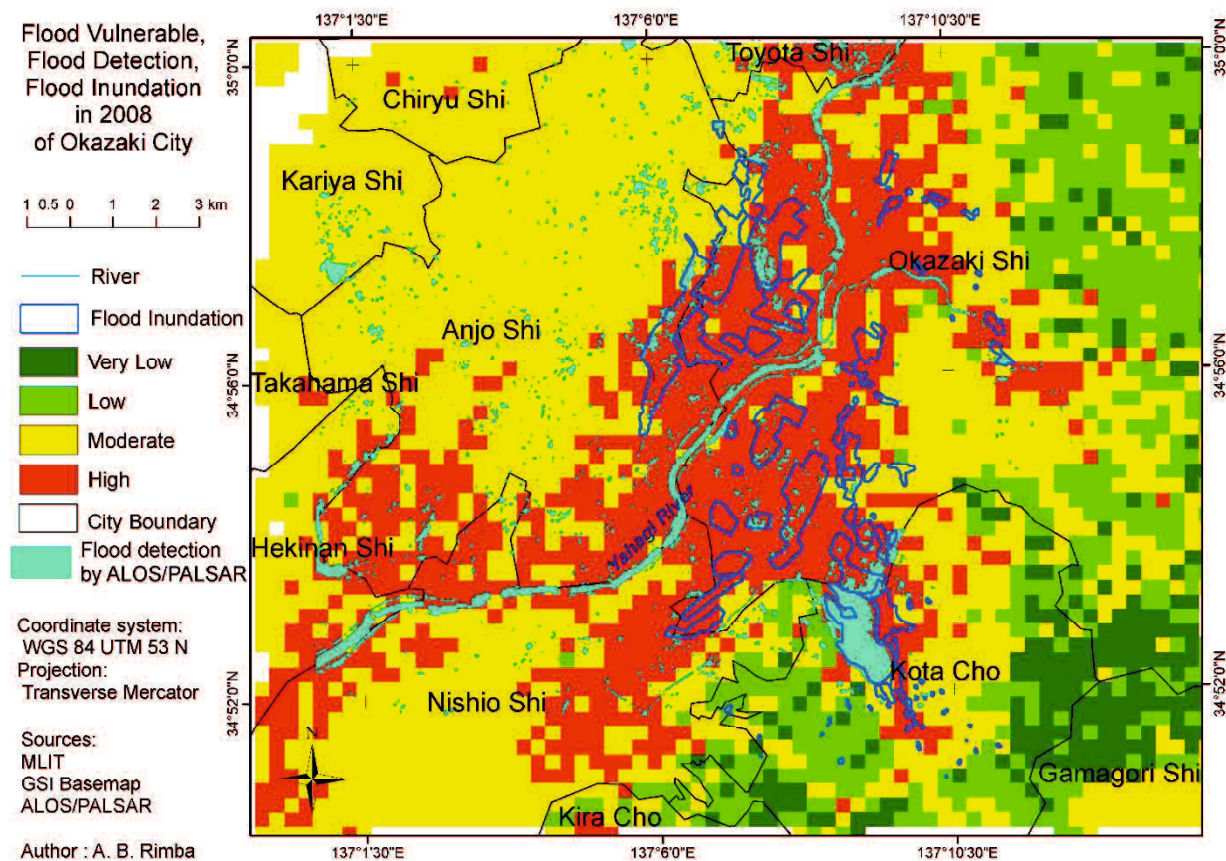


Figure 5. 9 Flood vulnerable area by AHP method and flood extraction method from ALOS/PALSAR during flood in 2008 in Okazaki Prefecture.

We generated the similar pattern of the AHP prediction and extraction from ALOS/PALSAR image. By utilizing Kappa coefficient from flood Okazaki City and Flood

vulnerability prediction, the accuracy was 89%. It was considered as a good accuracy due to kappa coefficient more than 0.8. Comparing the extraction method to field survey, we found 67 % accuracy by Overall accuracy.

5.5. Conclusions

We utilized ALOS-2/PALSAR-2 data in this study to find the fastest and most accurate method to extract the flooded in Joso City. The binarization method was most efficient in time and derived a more informative map from extracting the flood inundation compared to extracting the flood inundation using the land cover change by unsupervised and supervised classifications. Using the binarization method, the flow pattern from the river collapse could be detected. The overall accuracy and Kappa coefficient measured the accuracy assessment. Both of metric assessments show; binary/backscattering threshold (94 % for overall accuracy and 94% for Kappa coefficient) was the highest accuracy comparing to unsupervised classification (74 % for overall accuracy and 69% for Kappa coefficient) and supervised classification (79 % for overall accuracy and 72% for kappa coefficient). Thus, binarization method is suitable for the rapid response of flooded area extraction.

Unsupervised and supervised classifications showed overestimated flooded area. The unsupervised classification was more overestimated comparing to the supervised classification because in the unsupervised classification categorized the pixel according to pixel distances or similarity of pixel characteristic. Hence, the number of similar classes were uncounted that lead the misclassification. We do not recommend this classification system when the user know the study area. An unsupervised classification was fully automatic because it permits the computer to classify the pixel. Supervised and the binarization method need the local knowledge of the area. We could arrange the threshold of the water by using the binarization. Thus, this method was high accuracy comparing two other methods. The binarization method can be applied to other area and other SAR images for flood detection when the user has the local knowledge or the study area.

The best flood extraction method from ALOS-2/PALSAR-2 images was applied to ALOS/PALSAR images to measure effectivity of flood-vulnerable area by AHP model. Before the flood extraction was conducted, the different of off-nadir angle should be considered in the pre-processing process. The value of backscattering have to be corrected. The backscattering of building was utilized to correct because the building is not influenced by flood due to double bounce effect. The author evaluated the accuracy of flood extraction from ALOS/PALSAR to

flood vulnerability from AHP model. The accuracy showed good accuracy i.e., 89% by Kappa coefficient. Comparing the extraction method by binarization to field survey, we found 67 % accuracy by overall accuracy.

Overestimation of the flood inundation area due to shadowing effect in SAR image could be solved by using slope distribution. According to flood distribution found using field survey, the slope of the flooded area was less than 2%. This study utilized the HH polarization to detect the flood. Nevertheless, HH polarization cannot detect flooding in settlement areas. We utilized ALOS-2/PALSAR-2 image with 35.8° off-nadir angle; we will consider other polarization, e.g., VV, HV or VH and smaller or greater off-nadir angle to detect flooding in settlement areas for future work.

CHAPTER 6

CONCLUSIONS

Natural hazards are natural phenomena whose occurrence is almost impossible to reduce. We only can minimize the impact of these events by performing countermeasures such as an initial assessment to map the vulnerable areas, and so forth. The development of remote sensing technology and its applications including Geographical Information System (GIS) application enable the use of satellite imagery for mapping of the distribution of an area damaged by a disaster and to assess vulnerable areas. Satellite images have the advantage of being able to deliver simultaneous images of wide areas.

This study dealt with flood extended area and evaluation of flood vulnerability in which remote sensing approach was applied to solve the research problems. The utilized data in this study are ALOS (PALSAR/AVNIR-2), ALOS-2/PALSAR-2 from JAXA, Sentinel-2 from ESA, DEM data from GSI, AMeDAS meteorological data from JMA and Google Earth data to show the research locations and verify the interpretation.

Chapter 3 discussed the method how to reduce the flood impact by vulnerable flood mapping in Shirakawa watershed in Kumamoto Prefecture and Okazai City in Aichi Prefecture. Assessing the vulnerability area to flood disaster is one of the parameters in creating flood risk map. This study tried to assess the area that vulnerable to flood disaster using integrated approaches of remote sensing, GIS, and spatial multi-criteria evaluation (MCE) through the simply superimposed method and AHP method. The simply superimposed method was refined by AHP approach. By AUC accuracy, the AHP (0.95) was better than Simply superimposed method (0.89).

The parameter of slope, drainage density, rainfall intensity, infiltration rate, and land cover were applied to predict the affected area of flood. The AHP calculation shows that slope was the highest weight (43%) in determining vulnerability area to flood through the spatial-weighted overlay, followed by drainage density (20%), rainfall intensity (17%), infiltration rate (10%) and land cover (10%). This calculation resulted 0.6% in consistency ratio. The slope parameter was the most important parameter because the slope influences the flow direction, runoff and soil infiltration. The result of the flood vulnerability areas shows close enough compared to the reference data of flood event, 0.95 AUC. The highest risk of the land cover to flood was resident area and agriculture area. Those areas were close to the big river. This condition influences the economic condition. By analysis the building distribution and the flood risk area, approximately

110.5 km² total of construction area in the prone area. This method is possible to apply in another area, even though different geography characteristic with this study area. This study contributes an important approach for the effectiveness of disaster mitigation.

Chapter 4 proposed the Double filter method to reduce speckle noise and preserve the edge and object detail on ALOS/PALSAR images and ALOS-2/PALSAR-2 images. Kernel size and type of filter have an important role in the classification process. According to the quantitative assessment (i.e. statistic parameters; SSI, MPI, EEI, MAE, FPI and IDPC) and qualitative assessment (i.e. visual performance) to measure the speckle reduction, edge and fine object detail, we recommended the combination of Local Sigma with Low Pass filter for application in flood detection because Double filter was able to easily separate the edge of flood and non-flooded. Double filtered images show better performance than Single filter images. The Double filtered images combined the advantage of the different images. Hence, we could get the best combination of the filter that can reduce the speckle noise and preserve the edge and object detail. Double filter improved the spatial resolution because the length of impulse response increased by combination Local Sigma filter with Low Pass filter. Applying the Double filter on flooded area has advantages in that it is easy to recognize the flooded area in the shallowly inundated area.

Chapter 5 describes three flood extraction method, e.i., Unsupervised method, supervised method and binarization. We applied to two of flooded area in Japan. The first location is in Joso City, Ibaraki Prefecture that flooded in September 2015. The second location is in Okazaki City, Aichi Prefecture Japan. We was utilized ALOS-2/PALSAR-2 data in this study to find the fastest and most accurate method to extract the flood in Joso City; and also, we applied to ALOS/PALSAR. The binarization method was most efficient in time and derived a more informative map from extracting the flood inundation compared to extracting the flood inundation using the land cover change by unsupervised and supervised classification. Using the binarization method, the flow pattern from the river collapse could be detected. The overall accuracy and kappa coefficient measured the accuracy assessment. Both of metric assessments show; Binary/backscattering threshold (94 % for overall accuracy and 94% for kappa coefficient) was the highest accuracy comparing to unsupervised classification (74 % for Overall accuracy and 69% for Kappa coefficient) and supervised classification (79 % for Overall accuracy and 72% for Kappa coefficient). Thus, binarization method is suitable for the rapid response of flooded area extraction.

Successfully predicting the flood vulnerability in Chapter 3 with high accuracy of AUC and flood extraction by binarization in Chapter 5 with high accuracy of Kappa and Overall accuracy, the study continued to evaluate the effectivity of flood extraction by binarization method

to flood vulnerability by AHP method. The result shows the accuracy was 89 % by Kappa coefficient. Comparing the extraction method by binarization from ALOS/PALSAR to field survey, we found 67 % accuracy by overall accuracy.

In the future works, this study should be developed on:

1. For AHP method, the use of other parameters, including river proximity and the comparison study using other source of elevation data will be analyzed for future work.
2. Evaluating the Double filter for automated extraction of flooded area and apply to other applications, e.g., land classification and other natural disasters, and also, applying the Double filter method to other SAR images, different level and full polarizations are challenging. Thus, it will be analysed for future work.
3. Overestimation of the flood inundation area due to shadowing effect in SAR image could be solved by using slope distribution. According to flood distribution found using field survey, the slope of the flooded area was less than 2%. This study utilized the HH polarization to detect the flood. Nevertheless, HH polarization cannot detect flooding in settlement areas. We utilized ALOS-2/PALSAR-2 image with 35.8° off-nadir angle; we will consider other polarization, e.g., VV, HV or VH and smaller or greater off-nadir angle to detect flooding in settlement areas for future work.

ACKNOWLEDGEMENT

I would like to express my sincere gratitude to my supervisor Prof. Fusanori MIURA and Prof. Norikazu SHIMIZU for the continuous support of my doctoral study, for their patience, motivation, immense knowledge and also critical reading of my dissertation.

I would like to thank my dissertation committee; Prof. Norikazu SHIMIZU, Prof. Fusanori MIURA, Prof. Kesayoshi HADANO, Prof. Koji ASAI, Prof. Hideaki NAKAMURA, Assoc. Prof. Masahiko NAGAI for their constructive opinions and comments.

My sincere thanks also goes to Prof. Tasuku TANAKA, Dr. Eng. Hidenori TANAKA, Associate. Prof. Takahiro OSAWA, Martiwi Diah SETIAWATI, PhD., Dr. Eng. Abu Bakar SAMBAH, Mr. Abd.Rahman AS-SYAKUR, Mr. Tsuyoshi EGUCHI, Mr. Takumi KAJITANI, Miss. Kira ADAMS. and Mr. I Nyoman Sudi PARWATA for their expertise, comments, suggestions and their help to prepare the data and software. Thanks goes to all members for Miura Laboratory, Shimizu Laboratory, Nagai Laboratory, International community and international student community for the togetherness.

I also thank Japan Aerospace and Exploration Agency (JAXA), The European Space Agency (ESA), The Geospatial Information Authority of Japan (GSI), Japan Meteorological Agency (JMA), and Google Earth for providing satellite data; The Ministry of Land, Infrastructure, Transport and Tourism (MLIT) and local government of Okazaki City and Joso city for providing the field survey data.

I heartily dedicate to my parents, brothers and sisters who always pray and support my study.

REFERENCES

- Ilsever, M. & Unsalan, C., 2012. *Pixel-Based Change Detection Methods*. s.l.:SpringerBrifs in Computer Science.
- Adachi, T., 2009. *Flood damage mitigation efforts in Japan*. Tokyo, s.n.
- Adam, S., Wiebe, J., Collins, M. & Pietroniro, A., 2014. Radarsat Flood Mapping in the Peace-Athabasca Delta, Canada. *Canadian Journal Of Remote Sensing*, 7, 24(1), pp. 69-79.
- ADPC & UNDP, 2005. *Integrated flood risk management in Asia*, angkok: Preparedness Center and United Nations Development Programme Asian Disaster.
- Aguarón , J. & Moreno-Jiménez, J., 2000. Stability intervals in the analytic hierarchy process. *European Journal of Operational Research*, Volume 125, p. 114–133.
- Ahmed, B., 2015. Landslide susceptibility mapping using multi-criteria evaluation techniques in Chittagong Metropolitan Area, Bangladesh. *Landslides*, Volume 12, pp. 1077-1095.
- Ahmed, B., 2015. Landslide susceptibility modelling applying user-defined weighting and data-driven statistical techniques in Cox's Bazar Municipality, Bangladesh. *Natural Hazards*, 8, 79(3), pp. 1707-1737.
- Ahmed, B. & Ahmed, R., 2012. Modeling Urban Land Cover Growth Dynamics Using Multi-Temporal Satellite Images: A Case Study of Dhaka, Bangladesh. *ISPRS International Journal of Geo-Information*, 12, 1(1), pp. 3-31.
- Ahmed, B., Ahmed, R. & Zhu, X., 2013. Evaluation of Model Validation Techniques in Land Cover Dynamics. *ISPRS International Journal of Geo-Information*, 2(3), pp. 577-597.
- Aichi Prefecture Government., 2016. *Aichi Prefecture Government (in Japanese)*. [Online]
Available at: <http://www.pref.aichi.jp/soshiki/toukei/kokuchou2015.html>
[Accessed 26 10 2016].
- Alfieri, L. et al., 2014. Advances in pan-European flood hazard mapping. *Hydrological Processes*, 6, 28(13), pp. 4067-4077.
- Al-Khudhairi , D. & Shepherd, I., 1997. *Changes in Land-Use and Land-Cover: A Cause of Flooding? A Literature Review*. s.l.:Institute for Systems, Informatics and Safety .
- ALNAP, 2008. *Flood disasters: Learning from previous relief and recovery operations*, London: ALNAP.
- Alqurashi, A. F. & Kumar, . L., 2013. Investigating the Use of Remote Sensing and GIS Techniques to Detect Land Use and Land Cover Change: A Review. *Advances in Remote Sensing*, 4, pp. 193-204 .
- Amano, Y., 1985. Classification of Cultivated Soils in Japan. *JARQ*, 18(4).

- Anderon, J. R., Hardy, E. E., Roach, J. T. & Witmer, R. E., 1976. *A Land Use And Land Cover Classification System For Use With Remote Sensor Data*. Digital version ed. Washington: United States Government Printing Office.
- Anderson, J. R., Hardy, E. E., Roach, J. T. & Witmer, R. E., 1976. *A land use and land cover classification system for use with remote sensor data*, Washington: United States Government Printing Office.
- Anwar, M. R., 2011. The rainfall-runoff modeling using of the watershed physical characteristic approach. *International Journal of Civil & Environmental Engineering IJCEE-IJENS*, 11(6), pp. 71-75.
- ArcGIS, 2016. *ArcGIS for Desktop*. [Online]
Available at: <http://desktop.arcgis.com/en/arcmap/10.3/manage-data/raster-and-images/ndvi-function.htm>
[Accessed 29 10 2016].
- Argenti, F., Lapini, A. & Bianchi, T., 2013. A tutorial on speckle reduction in Synthetic Aperture Radar images. *The IEEE Geoscience and Remote Sensing Magazine*, 1(3), pp. 6-35.
- Argenti, F., Lapini, A., Bianchi, T. & Alparone, L., 2013. A Tutorial on Speckle Reduction in Synthetic Aperture Radar Images. *IEEE Geoscience and Remote Sensing Magazine*, 1(3), pp. 6-35.
- Arii, M., Okada, Y. & Nishimura, T., 2016. *Flooded Area Extraction from Time-Series ALOS-2 Data*. Hamburg, Germany, s.n.
- Assteerawatt, A. et al., 2016. *Large-scale and High-resolution Flood Risk Model for Japan*. Lyon, s.n.
- Babcock, M. & Mitchell, B., 1980. Impact of Flood Hazard on Residential Property Value in Galt (Cambridge), Ontario. *JAWRA Journal of the American Water Resources Association*, 6, 16(3), pp. 532-537.
- Bahuguna, V., Joshi, S., Deshmukh & Bhalchandra, P., 2013. Assessment of role of GIS for natural disaster management: a critical review. *International journal of Innovative Research in Science, Engineering and Technology*, 2(10).
- Baldassarre, G. D., Schumann, G., Brandimarte, L. & Bates, P., 2011. Timely Low Resolution SAR Imagery To Support Floodplain Modelling: a Case Study Review. *Surveys in Geophysics*, 1, 32(3), p. 255–269.
- Barber, M. et al., 2012. Speckle Noise and Soil Heterogeneities as Error Sources in a Bayesian Soil Moisture Retrieval Scheme for SAR Data. *IEEE Journal of Selected Topics in Applied Earth Observations and Remote Sensing*, 6, 5(3), pp. 942-951.
- Bateman, A., Medina, V. & Velasco, D., 2010. *Soil Infiltration Effect in Flat Areas Floods Simulation*. Barcelona , s.n.
- Bates, P. D., 2012. Integrating remote sensing data with flood inundation models: how far have we got?. *Hydrological Processes*, 7, 26(16), p. 2515–2521.

- Bathrellos, G. D. et al., 2012. Potential suitability for urban planning and industry development using natural hazard maps and geological-geomorphological parameters. *Environmental Earth Sciences*, 66(2), pp. 537-548.
- Bathrellos, G. D. et al., 2013. Assessment of rural community and agricultural development using geomorphological-geological factors and GIS in the Trikala prefecture (Central Greece). *Stochastic Environmental Research and Risk Assessment*, 27(2), pp. 573-588.
- Bathrellos, G. D. et al., 2016. Urban flood hazard assessment in the basin of Athens Metropolitan city, Greece. *Environmental Earth Sciences*, 2.75(319).
- Bathrellos, G. D. et al., 2017. Suitability estimation for urban development using multi-hazard assessment map. *Science of the Total Environment*, Volume 575, pp. 119-134.
- Bazi, Y., Bruzzone, L. & Melgani, F., 2005. An unsupervised approach based on the generalized Gaussian model to automatic change detection in multitemporal SAR images. *IEEE Trans Geosci Remote Sensing*, 43(4), p. 874–887.
- Belward, A. et al., 2007. Mapping severe damage to land cover following the 2004 Indian Ocean tsunami using moderate spatial resolution satellite imagery. *International Journal of Remote Sensing*, 28(13), pp. 2977-2994.
- Birkmann, J., 2005. *Measuring the Unmeasurable. 2nd UNU-EHS Expert Working Group Meeting, Bonn, 12-14*, Bonn: UNU-EHS .
- Birkmann, J. & Wisner, B., 2006. *Measuring the Un-Measurable The Challenge of Vulnerability*. Bonn: UNU Institute for Environment and Human Security (UNU-EHS).
- Bracken, L. J., Cox, . N. J. & Shannon, . J., 2007. The relationship between rainfall inputs and flood generation in south–east Spain. *Hydrological Processes*, 11, Volume 22, pp. 683-696.
- Brivio , P., Colombo , . R., Maggi, M. & Tomasoni, R., 2002. Integration of remote sensing data and GIS for accurate mapping of flooded areas. *International Journal of Remote Sensing* , Volume 23, pp. 429-441.
- Brivio, P. A., Colombo , R., Maggi , M. & Tomasoni, R., 2002. Integration of remote sensing data and GIS for accurate mapping of flooded areas. *International Journal of Remote Sensing*, 23(3), pp. 429-441.
- Brooks, H. E., 2004. Tornado-warning performance in the past and future. *Bulletin of the American Meteorological Society*, 85(6), pp. 837-843.
- Brooks, H. E. et al., 2011. Evaluation of European Storm Forecast Experiment (ESTOFEX) forecasts. *Atmospheric Research*, 100(4), pp. 538-546.
- Brouwer, C., 1990. *Gestion des eaux en irrigation manual de formation No.5 Methodes d'irrigation (in French)*. Rome: Devision de la mise en valeur des terres et des eaux, FAO.
- Bruniquel, J. & Lopes, A., 1997. Multivariate Optimal Speckle Reduction in SAR Imagery. *International Journal of Remote Sensing*, 18(3), pp. 603-627.

- Bryson, N., 1995. A goal programming method for generating priority vectors. *Journal of the Operational Research Society*, Volume 46, pp. 641-648.
- Butt, A., Shabbir, R. & Sheikh, A. S., 2015. Land use change mapping and analysis using Remote Sensing and GIS: A case study of Simly watershed, Islamabad, Pakistan. *The Egyptian Journal of Remote Sensing and Space Science*, 8, 18(2), pp. 251-259.
- Campagnolo, M. & Cerdeira, J., 2007. Contextual classification of remotely sensed images with integer linear programming. *Proceedings of CompIMAGE-Computational Modeling of Objects Represented in Images: Fundamentals, Methods, and Applications Taylor and Francis*, pp. 123-128.
- Campbell, J. B. & Wynne, R. H., 2011. *Introduction to remote sensing fifth edition*. New York(USA): The Guilford Press.
- Canada Center for Remote Sensing, 2016. *Fundamentals of Remote Sensing*, Canada: s.n.
- Central Disaster Prevention Council., 2016. *Evacuation/emergency measures at flood damage 水害時における避難 (Japanese version)*, Tokyo: s.n.
- Chander, G., Markham, B. L. & Helder, D. L., 2009. Summary of current radiometric calibration coefficients for Landsat MSS, TM, ETM+, and EO-1 ALI sensors. *Remote Sensing of Environment*, 113(5), pp. 893-903.
- Chapman, B. et al., 2015. Mapping Regional Inundation with Spaceborne L-Band SAR. *remote sensing*, 4, 7(5), pp. 5440-5470.
- Chow, V. T., Maidment, D. R. & Mays, L. W., 1964. *Applied hydrology*. Online version ed. California: McGraw-Hill International Edition Civil Engineering Series.
- Congalton, R. G., 1991. A review of assessing the accuracy of classifications of remotely sensed data. *Remote Sensing of Environment*, Volume 37, pp. 35-46.
- CRISP, 2001. *Center for Remote Imaging, Sensing and Processing*. [Online] Available at: http://www.crisp.nus.edu.sg/~research/tutorial/sar_int.htm [Accessed 5 9 2016].
- Csaplovics, E., 1998. High resolution space imagery for regional environmental monitoring status quo and future trends. *International Archives of Fotogrammetry and Remote Sensing*, 32(7), pp. 211-216.
- Danoedoro, P., 2012. *Pengantar Penginderaan Jauh (in Indonesia)*. Yogyakarta: Penerbit Andi Yogyakarta.
- Davis, R. S., 2001. Flash Flood Forecast and Detection Methods. In: *Severe Convective Storms*. USA: American Meteorological Society, pp. 481-525.
- De Jong, S., Hornstra, T. & Maas, H., 2001. An integrated spatial and spectral approach to the classification of Mediterranean land cover types: the SSC method. *International Journal of Applied Earth Observation and Geoinformation*, 3(2), pp. 176-183.

- Deledalle, C.-A., Denis, L. & Tupin, F., 2009. Iterative Weighted Maximum Likelihood Denoising with Probabilistic Patch-Based Weights. *IEEE Transaction on Image Processing*, 18(12), pp. 2661-2672.
- Dellepiane, S., Bo, G., Monni, S. & Buck, C., 2000. SAR images and interferometric coherence for flood. *IEEE Proceeding of International Geoscience and Remote Sensing Symposium*, Volume 6, pp. 2608-2610.
- Dellepiane, S. G. & Angiati, E., 2014. Quality assessment of despeckled SAR images. *IEEE Journal of Selected Topics in Applied Earth Observations and Remote Sensing*, 7(2).
- Demek, J., 1972. *Manual of detailed geomorphological mapping*. Prague: Academia, Publishing House of the Czechoslovak Academy of Science.
- Doerr, S., Shakesby, R. & Walsh, R., 2000. Soil water repellency: its causes, characteristics and hydro-geomorphological significance. *Earth-Science Reviews*, 8, 51(1-4), pp. 33-65.
- Dong, Y., Milne, A. K. & Forst, B. C., 2000. *A SAR Speckle Filtering Algorithm Towards Edge Sharpening*. Amsterdam, s.n.
- d'Ozouville, N. et al., 2008. DEM generation using ASAR (ENVISAT) for addressing the lack of freshwater ecosystems management, Santa Cruz Island, Galapagos. *Remote Sensing of Environment*, 112(15), pp. 4131-4147.
- Durand, J. M., Gimonet, B. J. & Perbos, J. R., 1987. SAR Data Filtering for Classification. *IEEE Transactions on Geoscience and Remote Sensing*, 9, 25(5), pp. 629-637.
- Easley, R., Valacich, J. & Venkataramanan, M., 2000. Capturing group preferences in a multicriteria decision. *European Journal of Operational Research*, Volume 125, pp. 73-83.
- Ebert, A. & Kerle, N., 2008. *urban social vulnerability assessment using object-oriented analysis of Remote Sensing and GIS Data..* Beijing, s.n., pp. 1307-1312.
- Edwards, J., Gustafsson, M. & Näslund-Landenmark, B., 2007. *Handbook for Vulnerability Mapping : EU Asia Pro Eco project Disaster Reduction through Awareness, Preparedness and Prevention Mechanisms in Coastal Settlements in Asia Demonstration in Tourism Destinations*. s.l.:Swedish Rescue Services Agency, Janet Edwards, EU and International Affairs Department.
- Egan, J., 1975. *Signal detection theory and ROC analysis, Series in Cognition and Perception*. New York: Academic Press.
- Ekrami, M., Marj, A. F., Barkhordari, J. & Dashtakian, K., 2016. Drought vulnerability mapping using AHP method in arid and semiarid areas: a case study for Taft Township, Yazd Province, Iran. *Environmental Earth Sciences*, 6, 75(1039), pp. 1-13.
- Eliason, E. & A.S, M., 1990. Adaptive box filters for removal of random noise from digital images. *Photogrammetric Engineering and Remote Sensing*, 56(4), pp. 453-458.

- Eliason, E. & McEwen, A., 1990. Adaptive box filter for removal of random noise from digital images. *Photogrammetric Engineering and Remote Sensing*, 56(4), pp. 453-458.
- Enderle, D. I. & Weih Jr, R. C., 2005. Integrating Supervised and Unsupervised Classification Methods to Develop a More Accurate Land Cover Classification. *Journal of the Arkansas Academy of Science*, Volume 59, pp. 65-73.
- ENVI, 2004. *ENVI User's Guide*. [Online]
Available at: http://aviris.gl.fcen.uba.ar/Curso_SR/biblio_sr/ENVI_userguide.pdf
[Accessed 7 January 2015].
- ESA, 2000. [Online]
Available at: <https://earth.esa.int/web/sentinel/user-guides/sentinel-2-msi/resolutions/spatial>
[Accessed 17 12 2016].
- ESRI, 2001. *ArcGIS Spatial Analyst: Advanced GIS Spatial Analysis Using Raster and Vector Data*. New York: ESRI.
- ESRI, 2016. *ESRI Support*. [Online]
Available at: <http://support.esri.com/other-resources/gis-dictionary/term/off-nadir>
[Accessed 6 9 2016].
- EXCIMAP, 2007. *Handbook on good practices for flood mapping in Europe*, The Netherlands: European exchange circle on flood mapping (EXCIMAP).
- Fawcett, T., 2006. An introduction to ROC analysis. *Pattern Recognition Letters*, Volume 27, p. 861–874.
- Fichtner, J., 1986. On deriving priority vectors from matrices of pair-wise comparisons. *Socio-Economic Planning Science*, Volume 20, pp. 341-345.
- Forman, E. & Peniwati, K., 1998. Aggregating individual judgments and priorities with the Analytic Hierarchy Process. *European Journal of Operational Research*, Volume 108, pp. 165-169.
- Foucher, S. & Lopez-Martinez, C., 2014. Analysis, evaluation, and comparison of polarimetric SAR speckle filtering techniques. *IEEE Trans Image Process*, 23(4), p. 1751–1764.
- Frost, V. et al., 1982. A model for Radar Images and Its Application to Adaptive Digital Filtering of Multiplicative Noise. *IEEE Transactions on Pattern Analysis and Machine Intelligence*, 4(2), pp. 157-166.
- Gagnon, L. & Jauan, A., 1997. *Speckle filtering of SAR image-a comparative study between complex-wavelet-based and standard filters*. San Diego, s.n., pp. 80-89.
- Gan, T., Zunic, F., Kuo, C.-C. & Strobl, T., 2012. Flood mapping of Danube River at Romania using single and multi-date ERS2-SAR images. *International Journal of Applied Earth Observation and Geoinformation*, 8, Volume 18, p. 69–81.
- García-Pintado, J. et al., 2013. Scheduling satellite-based SAR acquisition for sequential assimilation of water level observations into flood modelling. *Journal of Hydrology*, 7, Volume 495, pp. 252-266.

- Geokov, 2012. *Geokov Education*. [Online]
Available at: <http://geokov.com/education/slope-gradient-topographic.aspx>
[Accessed 8 11 2016].
- Ghazavi, R., Vali, A. & Eslamian, S., 2010. Impact of Flood Spreading on Infiltration Rate and Soil Properties in an Arid Environment. *Water Resources Management*, 1, 24(11), p. 2781–2793.
- Gillespie, T., Chu, J., Frankenber, E. & Thomas, D., 2007. Assessment and Prediction of Natural Hazards from Satellite Imagery. *Progress in Physical Geography*, 31(5), pp. 459-470.
- Gir, R., Jain, L. & Rai, R., 2015. Speckle Reduction of Synthetic Aperture Radar Images using Median filter and Savitzky-Golay filter. *International Journal of Computer Application*, 113(11), pp. 38-43.
- GISGeography, 2016. *GIS Geography*. [Online]
Available at: <http://gisgeography.com/image-classification-techniques-remote-sensing/>
[Accessed 31 10 2016].
- Giustarini, L. et al., 2014. Accounting for image uncertainty in SAR-based flood mapping. *International Journal of Applied Earth Observation and Geoinformation*, 7, Volume 34, p. 70–77.
- Gonzalez, R. C. & Woods, R. E., 2008. *Digital Image Processing (3rd Edition)*. India: Pearson Education.
- Goodman, J., 1976. Some fundamental properties of speckle. *Journal of the Optical Society of America*, 66(10), pp. 1145-1150.
- Googleearth, 2014. *Google Earth*. [Online]
Available at: <https://www.google.co.jp/maps/@34.0428792,131.2815485,59154m/data=!3m1!1e3>
[Accessed 1 4 2015].
- Greenbaum, N. et al., 1998. A high magnitude storm and flood in a hyperarid catchment, Nahal Zin, Negev Desert, Israel. *Hydrological Processes*, 4, 12(1), pp. 1-23.
- Gregory, K. J. & Walling, D. E., 1968. The variation of drainage density within a catchment. *International Association Science Hydrology Bulletin*, Volume 13, pp. 61-68.
- GSI, 2014. *Geospatial Information Authority of Japan*. [Online]
Available at: <http://www.gsi.go.jp/kiban/index.html>
[Accessed 2 8 2014].
- Guha-Sapir, D., Hoyois, P. & Below, R., 2012. *Annual Disaster Statistical Review 2012 The numbers and trends*, Brussels: Centre for Research on the Epidemiology of Disasters (CRED).
- Guha-Sapir, D., Hoyois, P. & Below, R., 2015. *Annual Disaster Statistical Review 2015; The numbers and trends*, Brussels: s.n.
- Guha-Sapir, D. & Wahlstrom, M., 2015. *The human cost of weather-related disasters 1995-2015*. Belgium: CRED and UNISDR.

- Hagg , W. & Sties, M., 1996. *The Epos Speckle Filter: A Comparison with Some Well-Known Speckle Reduction Techniques*. Vienna, Austria, s.n.
- Halounova, L. & Holubec, V., n.d. *Assessment of Flood with Regards to Land Cover Changes*. Salford Quays, United Kingdom, s.n., p. 2014.
- Hapuarachchi, . H. A. P., Wang, Q. J. & Pagano, T., 2011. A review of advances in flash flood forecasting. *Hydrol. Process.*, p. 2771–2784.
- Hasekiogullari, G. . D. & Ercanoglu, M., 2012. A new approach to use AHP in landslide susceptibility mapping: a case study at Yenice (Karabuk, NW Turkey). *Natural Hazards*, 9, 63(2), pp. 1157-1179.
- Haykin, S., 2001. *Adaptive Filter Theory: 4th (fourth) edition*. New Jersey: Prentice Hall.
- Haynes, R., 1998. *The Canadian system of soil classification Third edition*. Canada: NRC Research Press.
- Hegazy, I. R. & Kaloop, M. R., 2015. Monitoring urban growth and land use change detection with GIS and remote sensing techniques in Daqahlia governorate Egypt. *International Journal of Sustainable Built Environment*, 6, 4(1), pp. 117-124.
- HIPR2, 2004. *Image Processing Learning Resources*. [Online]
Available at: http://homepages.inf.ed.ac.uk/rbf/HIPR2/hipr_top.htm
[Accessed 2 9 2016].
- Honda, K. et al., 2016. *Detecting Disaster Damage from 2015 Typhoon Eta by the Combined Use of Different SAR Satellites*. Prague, Czech Republic, s.n., pp. 79-83.
- Hong, J.-Y. & Bae-Ahn, J., 2015. Change of early summer of precipitation in the Korean Peninsula and Nearby Regions based on RCP simulation. *Journal of Climate*, Volume 28, pp. 3557-3578.
- Hong, S., Jang, . H., Kim, N. & Sohn, . H.-G., 2015. Water Area Extraction Using RADARSAT SAR Imagery Combined with Landsat Imagery and Terrain Information. *Sensors*, 3, Volume 15, pp. 6652-6667.
- Hong, S.-H. & Wdowinski, S., 2013. Double-Bounce Component in Cross-Polarimetric SAR From a New Scattering Target Decomposition. *IEEE Transactions on Geoscience and Remote Sensing*, 6, pp. 1-13.
- Horritt, M., Mason, D. & Luckman, A., 2001. Flood boundary delineation from synthetic aperture radar imagery using a statistical active contour model. *International Journal of Remote Sensing*, Volume 22, pp. 2489-2507.
- Horton, R. E., 1945. Erosional Development of Streams and Their Drainage Basins; Hydrophysical Approach to Quantitative Morphology. *Geological Society of America Bulletin*, Volume 56, pp. 275-370.
- Huang, Y. & Genderen, J., 1996. *Evaluation of Several Speckle Filtering Techniques for ERS-1&2 Imagery*. Vienna, s.n.

- Huisman, O. & de By, R. A., 2001. *Principles of Geographic Information Systems: An introductory textbook*. 1 ed. Enschede: The International Institute for Geo=Information Science and Earth Observation (ITC).
- Hunter, N. M., Bates, P. D., Horritt, M. S. & Wilson, M. D., 2007. Simple spatially-distributed models for predicting flood inundation: A review. *Geomorphology*, 10, 90(3-4), pp. 208-225.
- ICHARM., 2005. *Flood Hazard Mapping Manual in Japan*. Tokyo: Flood Control Division, River Bureau, Ministry of Land, Infrastructure and Transport (MLIT) and International Center for Water Hazard and Risk Management (ICHARM).
- Inglada, J. & Mercier, G., 2007. A new statistical similarity measure for change detection in multitemporal SAR images and its extension to multiscale change analysis. *IEEE Trans Geosci Remote Sensing*, 45(5), p. 1432–1445.
- Institute of Soil Science, A. S., 1981. *Proceedings of Symposium on Paddy Soil*. 1 ed. Beijing: Science Press-Beijing and Springer-Verlag Berlin Heidelberg.
- IPCC, 2007. *Climate Change 2007: Synthesis Report*, Geneva: IPCC.
- IPCC, 2007. *Contribution of Working Groups I, II and III to the Fourth Assessment Report of the Intergovernmental Panel on Climate Change*, Geneva: Intergovernmental Panel on Climate Change.
- Japan Meteorology Agency, 2008. *Natural disaster report in Shikoku, Chugoku, Tokai, Kanto and Tohoku area in Japanese Version*, Tokyo: JMA.
- JAXA, 2003. *Japan Aerospace Exploration Agency*. [Online]
Available at: <https://www.eorc.jaxa.jp/ALOS/en/about/palsar.htm>
[Accessed 7 January 2015].
- JAXA, 2004. *ALOS PALSAR: Technical outline and mission concepts*. Austria, JAXA.
- JAXA, 2016. *Japan Aerospace Exploration Agency (JAXA)*. [Online]
Available at: <http://global.jaxa.jp/projects/sat/alos2/>
[Accessed 12 May 2016].
- Jensen, J., 2000. *Remote Sensing of the Environment: An Earth Resource Perspective*. Minneapolis: Pearson Prentice Hall.
- Jensen, J. R., 2004. *Introductory Digital Image Processing - a Remote Sensing Perspective*. 3rd ed. New Jersey: Prentice Hall.
- JMA, 2016. [Online]
Available at: http://www.jma.go.jp/en/amedas_h/index.html
- Johnson , R., 2000. *GIS Technology for Disasters and Emergency Management*. the United States of America: Environmental Systems Research Institute, Inc. (ESRI).

- Johnson, A., 1991. *A Field Method for Measurement of Infiltration*. 2 ed. Denver: U.S. Geological Survey.
- Joseph, G., 2005. *Fundamentals of remote sensing second edition*. India: Himayatnagar: Universities Press.
- Joso City., 2016. *Verification report on the response to the Kinugawa river flood damage in Joso City, 2015* 平成 27 年常総市鬼怒川水害対応に関する検証報告書 (Japanese version), Joso City: s.n.
- Joso City, 2016. *Joso City*. [Online]
Available at: http://www.city.joso.lg.jp/language/english/general_information/1446170618416.html
[Accessed 26 10 2016].
- Joyce, K. E. et al., 2009. A review of the status of satellite remote sensing and image processing techniques for mapping natural hazards and disasters. *Progress in Physical Geography*, 32(2), p. 183–207.
- Kankaku, Y. et al., 2016. *ALOS-2 operation status*. Beijing, s.n., pp. 3846-3848.
- Kayasthaa , P., Dhital, M. & Smedt, . F. D., 2013. Application of the analytical hierarchy process (AHP) for landslide susceptibility mapping: A case study from the Tinau watershed, west Nepal. *Computers & Geosciences*, 3, Volume 52, p. 398–408.
- Kazakis, N., Kougiass, I. & Patsialis, T., 2015. Assessment of flood hazard areas at a regional scale using an index-based approach and Analytical Hierarchy Process: Application in Rhodope–Evros region, Greece. *Science of The Total Environment*, 12, Volume 538, p. 555–563.
- Kazama , S., Sato, A. & Kawagoe, S., 2009. Evaluating the Cost of Flood Damage Based on Changes in Extreme Rainfall in Japan. *Sustainability Science*, 1.pp. 3-17.
- Kazama , S., Sato, A. & Kawagoe, S., 2010. Evaluating the Cost of Flood Damage Based on Changes in Extreme Rainfall in Japan. In: *Adaptation and Mitigation Strategies for Climate Change*. Online book: Springer, pp. 3-17.
- Kern, J., 2010. *Chapter 14.10 Water Use and Conservation*, California: s.n.
- Konrad, C. P., 2014. *Effects of Urban Development on Floods-USGS*. [Online]
Available at: <http://pubs.usgs.gov/fs/fs07603/>
[Accessed 29 10 2016].
- Kuan, D., Sawchuk, A., Strand, T. & Chavel, P., 1987. Adaptive Restoration of Images with Speckle. *IEEE Transactions on Acoustic, Speech, and Signal Processing*, 35(3), pp. 373-383.
- Kuldeep & Garg, P., 2016. *The Role of Satellite Derived Data from Inundation Mapping Using GIS*. La Grande Motte, s.n., pp. 235-239.
- Kulpa, K. S., Purchla, M. & Malanowski, M., 2004. *Improvement of Resolution in Real-time Unfocused SAR Algorithm*. Ulm,Germany, VERLAG.

- Kumar, G. & Bhatia, P. K., 2014. *A detailed review of feature extraction in image processing systems*. India, Fourth International Conference on Advanced Computing & Communication Technologies IEEE.
- Kyuma, K. & Kawaguchi, K., 1966. Major Soils of Southeast Asia and the Classification of Soils Under Rice Cultivation (Paddy Soils). *Kyoto University Center for Southeast Asian Studies*, 9, 4(2), pp. 290-312.
- Laininen, P. & Hämäläinen, R., 2003. Analysing AHP-matrices by regression. *European Journal of Operational Research*, Volume 148, pp. 514-524.
- Larsen, J. B., 2009. Forestry between land use intensification and sustainable development: Improving landscape functions with forests and trees. *Geografisk Tidsskrift-Danish Journal Of Geography*, 109(2), pp. 191-195.
- Lazzaro, M. D., Zarlenga, A. & Volpi, E., 2014. A new approach to account for the spatial variability of drainage density in rainfall-runoff modeling. *Boletín Geológico y Minero*, 152(3), pp. 301-313.
- Lee, J.-S., 1980. Digital image enhanced and noise filtering by use of local statistics. *IEEE Transaction on Pattern Analysis and Machine Intelligence*, PAMI-2(2), pp. 1651-1681.
- Lee, J.-S. et al., 1994. Speckle filtering of synthetic aperture radar images: A review. *Remote Sensing Reviews*, 8(4), pp. 313-340.
- Li, H., Huang, B. & Huang, X., 2010. A Level Set Filter for Speckle Reduction in SAR Images. *EURASIP Journal on Advances in Signal Processing*, Volume Volume 2010, pp. 1-14.
- Lillisand, T., Keifer, R. & Chipman, 2004. *Remote sensing and image interpretation*. New York: John Wiley and Sons.
- Lopez, A., Nezry, E., Touzi, R. & H, L., 1993. Structure Detection and Statistical Adaptive Speckle Filtering in SAR Images. *International Journal of Remote Sensing*, 14(9), pp. 1735-1758.
- Lopez, A., Touzi, R. & Nezry, E., 1990. Adaptive speckle filters and scene heterogeneity. *IEEE Transaction on Geoscience and Remote Sensing*, 28(6), pp. 992-1000.
- Maity, A., Pattanaik, A., Sagnika, S. & Pani, S., 2015. *A comparative study on approaches to speckle noise reduction in images*. Odisha, India, s.n., pp. 148-155.
- Malvinas, F., Mangkoesubroto, K., Suryadi, K. & Yudhistira, T., 2005. *Development of customer decision model in selecting product concept based on conjoint-analysis-like AHP (CALAHP)*. Honolulu, The International symposium on the Analytic Hierarchy Process.
- Manjusree, P. et al., 2012. Optimization of Threshold Ranges for Rapid Flood Inundation Mapping by Evaluating Backscatter Profiles of High Incidence Angle SAR Images. *International Journal of Disaster Risk Science*, 6, 3(2), pp. 113-122.
- Mansourpour, M., Rajabi, M. & Blais, J., 2006. *Effects and performance of speckle noise reduction filters on active radar and SAR images*. Ankara, Turkey, s.n.

- Manu, L. et al., 2014. Long-term evaluation of Shirakawa river delta due to the extreme events. *Journal of Japan Society of Civil Engineers, Ser. B3 (Ocean Engineering)*, 70(2), pp. I_612-I_617.
- Martinis, S., Kersten, J. & Twele, A., 2015. A fully automated TerraSAR-X based flood service. *ISPRS Journal of Photogrammetry and Remote Sensing*, 6, Volume 104, pp. 203-212.
- Martino, L., Ulivieri, C., Jahjah, M. & Loret, E., 2009. Remote Sensing and GIS Techniques for Natural Disaster Monitoring. In: *Space Technologies for the Benefit of Human Society and Earth*. Netherlands: Springer Netherlands, pp. 331-382.
- Mascarenhas, . N. D. A., 1996. *An Overview of Speckle Noise Filtering in SAR Images*. Buenos Aires-Argentina, s.n.
- Mason, D. et al., 2012. Near real-time flood detection in urban and rural areas using high-resolution synthetic aperture radar images. *IEEE Transactions on Geoscience and Remote Sensing*, 50(8), pp. 3041-3052.
- Mason, D. et al., 2010. Flood detection in urban areas using TerraSAR-X. *IEEE Trans. Geoscience Remote Sensing*, Volume 48, pp. 882-894.
- Mason, I., 1982. A model for assessment of weather forecasts. *Aust. Meteorol. Mag.*, Volume 30, p. 291–303.
- Matgen, P. et al., 2007. Integration of SAR-derived river inundation areas, high-precision topographic data and a river flow model toward near real-time flood management. *International Journal of Applied Earth Observation and Geoinformation*, 8, 9(3), pp. 247-263.
- McAdoo, B., Richardson, N. & Borrero, J., 2007. Inundation Distances and Run-up Measurements from ASTER, QuickBird and SRTM Data, Aceh Coast Indonesia. *International Journal of Remote Sensing*, 28(13-14), p. 2961-2975.
- McCandless Jr., S. W. & Jackson, C. R., 2004. Chapter 1. Principle of Synthetic Aperture Radar. In: *SAR Marine User's Manual*. Washington DC: NOAA/NESDIS, pp. 1-23.
- McCluskey, J., 2001. Water supply, health and vulnerability in floods. *waterlines*, 19(3).
- Meer, P., Park, R.-H. & Cho, K., 1994. Multiresolution Adaptive Image Smoothing. *CVGIP: Graphical Models and Image Processing*, 56(2), pp. 140-148.
- Merz, R. & Blöschl, G., 2008. Flood frequency hydrology:2. Combining data evidence. *Water resources research*, 8, Volume 44, pp. 1-6.
- MLIT, 2013. *Introduction of Urban Land Use Planning System in Japan*, Tokyo: s.n.
- MLIT, 2016. *MLIT*. [Online]
Available at: <http://www.qsr.mlit.go.jp/kumamoto/river/shirakawa/gaiyou.html>
[Accessed 27 10 2016].

- Moglen, G. E., 1998. On the sensitivity of drainage density to climate change. *Water Resources Research*, 4, 34(4), pp. 855-862.
- Nagoya University, 2016. *Laboratory of Meteorology, Hydrospheric Atmospheric Research Center*. [Online] Available at: <http://www.rain.hyarc.nagoya-u.ac.jp/study/2008/2008en.html> [Accessed 6 9 2016].
- Nascetti, A. et al., 2014. Fast terrain modelling for hydrogeological risk mapping and emergency management: the contribution of high-resolution satellite SAR imagery. *Geomatics, Natural Hazards and Risk*, 4, 6(5-7), pp. 554-582.
- Nations, U., 2012. *World Urbanization Prospects - The 2011 Revision*. New York: UN.
- Natsuaki, R. et al., 2016. *Emergency observation and disaster monitoring performed by ALOS-2 PALSAR-2*. Beijing, s.n., pp. 3849-3852.
- Niu, X. & Ban, Y., 2013. Multi-temporal RADARSAT-2 polarimetric SAR data for urban land-cover classification using an object-based support vector machine and a rule-based approach. *International Journal Remote Sensing*, 34(1), pp. 1-26.
- North, H. C. & Wu, Q., 2001. An Edge Preserving Filter for Imagery Corrupted with Multiplicative Noise. *Photogrammetric Engineering & Remote Sensing*, 67(1), pp. 57-64.
- Nyongui, A. N., Tonye, E. & Akono, A., 2002. Evaluation of speckle filtering and texture analysis methods for land cover classification from SAR images. *International Journal of Remote Sensing*, 5, 23(9), pp. 1895-1925.
- Obara, H. et al., 2014. Outline of Comprehensive Soil Classification System of Japan-First Approximation. *JARQ*, 11, Volume 3, pp. 217-226.
- Ogden, F. L., Pradhan, N. R., Downer, C. W. & Zahner, J. A., 2011. Relative importance of impervious area, drainage density, width function, and subsurface storm drainage on flood runoff from an urbanized catchment. *Water Resources Research*, 12.47(12).
- Okazaki City., 2013. [Online] Available at: <http://www.city.okazaki.lg.jp/1300/1301/1313/p017725.html> [Accessed 21 12 2016].
- Okazaki City., 2015. *Creating Master Plan of Okazaki Municipal Water Environment: draft (in Japanese)*, Okazaki: s.n.
- Okazaki City, 2016. *Current status and problems of biodiversity (in Japanese)*, Okazaki city: Okazaki City Government.
- Okazaki City, 2013. *Okazaki City*. [Online] Available at: <http://disapotal.gsi.go.jp/viewer/index.html?code=4> [Accessed 2 9 2016].

- Otsu, N., 1979. A threshold selection method from grey-level histogram. *IEEE Trans. Systems, Man, and Cybernetics*, 9(1), pp. 62-66.
- Otsu, N., 1979. A threshold selection method from grey-level histogram. *IEEE Trans. Systems, Man, and Cybernetics*, 9(1), pp. 62-66.
- Ouma , Y. O. & Ryutaro , T., 2014. Urban Flood Vulnerability and Risk Mapping Using Integrated Multi-Parametric AHP and GIS: Methodological Overview and Case Study Assessment. *Water*, Volume 6, pp. 1515-1545.
- Pallard, B., Castellarin, A. & Montanary, A., 2009. A look at the links between drainage density and flood statistics. *Hydrology and Earth System Science*, 7, Volume 13, pp. 1019-1029.
- Panagiota, M., Jocelyn, C. & Erwan, P., 2011. *State of the Art on Remote Sensing for Vulnerability and Damage Assessment on Urban Context*, France: s.n.
- Patel, V. M., Easley, G. R., Healy Jr, D. M. & Chellappa, R., 2010. Compressed Synthetic Aperture Radar. *EEE Journal of Selected Topics in Signal Processing*, 4, 4(2), pp. 244-254.
- Perrin, J. L. et al., 2001. Rainfall/runoff processes in a small peri-urban catchment in the Andes mountains. The Rumihurcu Quebrada, Quito (Ecuador). *Hydrological Process*, 3, Volume 15, p. 843–854.
- Pierdicca, N., Marco, . C. & Pulvirent, L., 2008. Integrating Physical and Topographic Information Into a Fuzzy Scheme to Map Flooded Area by SAR. 7, Volume 8, pp. 4151-4164.
- Plate, E. J., 2002. Flood risk and flood management. *Journal of Hydrology*, 267(1-2), pp. 2-11.
- Pohl, C. & Genderen , . J. v., 2016. *Remote Sensing Image Fusion: A Practical Guide*. United Kingdom: Taylor & Francis Group CRC Press.
- Poursaber, M. R. & Arika, Y., 2016. Estimation of Tsunami Hazard Vulnerability Factors by Integrating Remote Sensing, GIS and AHP Based Assessment. *Open Access Library Journal*, 4, 3(4), pp. 1-11.
- Pradhan, B., Tehrany, M. S. & Jebur, M. N., 2016. A New Semiautomated Detection Mapping of Flood Extent from TerraSAR-X Satellite Image Using Rule-Based Classification and Taguchi Optimization Techniques. *IEEE Transactions on Geoscience and Remote Sensing*, 4, 57(7), pp. 1-12.
- Proctor, W., 2000. *Towards sustainable forest management—an application of multi-criteria analysis to Australian forest policy*. Vienna, Third International Conference of the European Society for Ecological Economics, May 3-6.
- Pulvirenti, L., Pierdicca, N., Chini, M. & Guerriero, L., 2011. An algorithm for operational flood mapping from Synthetic Aperture Radar (SAR) data using fuzzy logic. *Natural Hazards and Earth System Sciences*, 2, Volume 11, pp. 529-540.
- Qiu, F., Berglund, J. & Thakkard, P., 2004. Speckle noise reduction in SAR imagery using a local adaptive median filter. *GIScience and Remote Sensing*, Volume 41, pp. 244-266.

- Raju , P. R. & Neelima, G., 2012. Image Segmentation by using Histogram Thresholding. *International Journal of Computer Science Engineering and Technology (IJCSET)*, 2(1), pp. 776-779.
- Ramsey III, E. W., Rangoonwala, A. & Bannister, T., 2013. Coastal flood inundation monitoring with Satellite C-band and L-band Synthetic Aperture Radar data. *Journal of the American Water Resources Association*, 49(6), pp. 1239-1260.
- Ran, J. & Nedovic-Budic, Z., 2016. Integrating spatial planning and flood risk management: A new conceptual framework for the spatially integrated policy infrastructure. *Computers, Environment and Urban Systems*, 12, Volume 57, pp. 68-79.
- Raouf, A. & Lichtenegger, J., 18–21 March 1997. *Integrated Use of SAR and Optical Data for*. Florence, Italy, s.n., pp. ESA SP-1204.
- Rawat, J. & Kumar, M., 2015. Monitoring land use/cover change using remote sensing and GIS techniques: A case study of Hawalbagh block, district Almora, Uttarakhand, India. *The Egyptian Journal of Remote Sensing and Space Science*, 6, 18(1), pp. 77-84.
- Richards, J. A., 2009. Scattering from Earth Surface Features. In: *Remote Sensing with Imaging Radar*. Berlin : Springer Berlin Heidelberg, pp. 135-180.
- Rimba, A. B. & Miura, F., 2016. Chapter 8. Predicting Flood-vulnerability of Areas Using Satellite Remote-sensing Images in Kumamoto City, Japan. In: *Geospatial Technology for Water Resource Applications*. Boca Raton: CRC Press Taylor & Francis Group.
- Rimba, A. B. et al., 2016. *The effectivity of Double filter to reduce the speckle and detect flood inundation on ALOS/PALSAR*. Colombo, s.n.
- Rimba, A., Miura, F. & Kajitani, T., 2016. *Extraction Flood Inundation By Utilizing ALOS/PALSAR Image*. Colombo, Sri Lanka, s.n.
- Rosenqvist, A. et al., 2014. Operational performance of the ALOS global systematic acquisition strategy and observation plans for ALOS-2 PALSAR-2. *Remote Sensing of Environment*, 5, Volume 155, pp. 3-12.
- Rozos, D., Bathrellos, G. D. & Skillodimou, H. D., 2011. Comparison of the implementation of rock engineering system and analytic hierarchy process methods, upon landslide susceptibility mapping, using GIS: A case study from the Eastern Achaia County of Peloponnesus, Greece. *Environmental Earth Sciences*, 63(1), pp. 49-63.
- Rufat, S., Tate, E., Burton, C. G. & Maroof, A. S., 2015. Social vulnerability to floods: Review of case studies and implications for measurement. *International Journal of Disaster Risk Reduction* , Volume 14, p. 470–486.
- Saad, A., El Assad, S. & Barba, D., 1996. Speckle filtering in SAR images by contrast modification, comparison with a large class of filters. *Annals of telecommunications - annales des télécommunications*, 51(5-6), pp. 233-244.
- Saaty, T. L., 1977. A scaling method for priorities in hierarchical structures. *Journal of Mathematical Psychology*, 6, 15(3), pp. 234-281.

- Saaty, T. L., 1980. *The analytic hierarchy process*. New York: McGraw-hill.
- Saaty, T. L., 1987. The analytical Hierarchy Process - what it is and how it is used. *Mathematical Modelling*, 9(3-5), pp. 161-176.
- Saaty, T. L., 2003. Decision-making with the AHP: Why is the principal eigenvector necessary?. *European Journal of Operational Research*, 145(1), pp. 85-91.
- Saaty, T. L., 2008. Decision making with the analytic hierarchy process. *International Journal Services Sciences*, 1(1), pp. 83-98.
- Sambah, A. B. & Miura, F., 2014. Integration of Spatial Analysis for Tsunami Inundation and Impact Assessment. *Journal of Geographic Information System*, 1, Volume 6, pp. 11-22.
- Sambah, A. B. & Miura, F., 2014. Remote sensing and spatial multi-criteria analysis for tsunami vulnerability assessment", Disaster Prevention and Management. *Disaster Prevention and Management: An International Journal*, 23(3), pp. 271 - 295.
- Sanyal, J. & Lu, X., 2004. Application of Remote Sensing in Flood Management with Special Reference to Monsoon Asia: A Review. *Natural Hazards*, 11, Volume 33, pp. 283-301.
- SARMap, 2009. *Synthetic Aperture Radar and SARscape; SAR-Guidebook*. Switzerland: SARMap.
- Schanze, J., Zeman, E. & Marsalek, J., 2006. *Flood risk management: hazards, vulnerability and mitigation measures*. s.l.:s.n.
- Schowengerdt, R. A., 1983. *Techniques for Image Processing in Remote Sensing*. New York: Academic Press.
- Schumann, G. J.-P., 2015. Preface: Remote Sensing in Flood Monitoring and Management. *MDPI Remote Sensing*, 7(12), pp. 17013-17015.
- Senthilnath, J. et al., 2013. Integration of speckle de-noising and image segmentation using synthetic aperture radar image for flood extent extraction. *Journal Earth System Science*, 122(3), pp. 5559-572.
- Setiawati, M. D. & Miura, F., 2016. Evaluation of GSMaP Daily Rainfall Satellite Data for Flood Monitoring: Case Study—Kyushu Japan. *Journal of Geoscience and Environment Protection*, 12, Volume 4, pp. 101-117.
- Setiawati, M. D., Miura, F. & Aryastana, P., 2016. Chapter 9. Validation of Hourly GSMaP and Ground Base Estimates of Precipitation for Flood Monitoring in Kumamoto, Japan. In: *Geospatial Technology for Water Resource Applications*. Boca Raton: CRC Press Taylor & Francis Group.
- Shahabi, H. & Hashim, M., 2015. Landslide susceptibility mapping using GIS-based statistical models and Remote sensing data in tropical environment. *Scientific Reports*, 4.5(9899).
- Shamsoddini, A. & Trinder, J., 2010. *Image texture preservation in speckle noise suppression*. Vienna, ISPRS Commission VII Symposium.

- Shapiro, L. G. & Stockman, G. C., 2001. *Computer Vision 1st Edition*. chapter 5 ed. United State of America: Pearson.
- Sheng, A. & Xia, Z. G., 1996. *A comprehensive evaluation of filter for radar speckle suppression*. Lincoln- USA, IEEE Int. Geosci. Remote Sensing Symposium.
- Si Qi, H. & Lei, W., 2002. A Survey of Thresholding Methods for Image Segmentation. *Systems Engineering and Electronics*, 24(6), pp. 91-95.
- Siddayao, G. P., Valdez, S. E. & Fernandez, . P. L., 2014. Analytic Hierarchy Process (AHP) in Spatial Modeling for Floodplain Risk Assessment. *International Journal of Machine Learning and Computing*, 10, 4(5), pp. 450-457.
- Singh , N., Vangani, N. & Sharma, J., 1993. Flash Flood Damage Mapping in Arid Environment Using Satellite Remote Sensing-A Case Study of Pali Region. *Journal of the Indian Society of Remote Sensing*, 2, 21(2), pp. 75-86.
- Singh,, V. P. & Chowdhury, P. K., 1986. Comparing some methods of estimating mean areal rainfall. *the Water Resources Bulletin*, 22(2), p. 275–282.
- Singh, A., 1989. Digital change detection techniques using remotely-sensed data. *International Journal of Remote Sensing*, 5, 10(6), pp. 989-1003.
- Sinha, D. & Dougherty, E. R., 1998. *Introduction to Computer-based Imaging Systems*. Washington: SPIE Optical Engineering Press.
- Smith, J., 2010. *Feedforward Comb Filter*. [Online]
Available at: <http://www.webcitation.org/5pBO6Nubb>
[Accessed 26 11 2016].
- Smith, L., 1997. Satellite remote sensing of river inundation area and discharge: A review. *Hydro Process*, Volume 11, pp. 1427-1439.
- Sohl , T. & Benjamin , S., 2012. Role of remote sensing for land-use and land-cover change modeling. In: *Remote sensing of land use and land cover: principles and applications*. Boca Raton, FL: CRC Press, pp. 225-239.
- Son, N., Chen, C., Chen, C. & Chang, L., 2013. Satellite-based investigation of flood-affected rice cultivation areas in Chao Phraya River Delta, Thailand. *ISPRS Journal of Photogrammetry and Remote Sensing*, 12, Volume 86, pp. 77-88.
- Sumantyo, J. & Amini, J., 2008. A model for removal of speckle noise in SAR images (ALOS PALSAR). *Can. J Remote Sensing*, 34(6), pp. 503-515.
- Swets, J., 1988. Measuring the accuracy of diagnostic systems. *Science* 240, p. 1285–1293.
- Swets, J., Dawes, R. & Monahan, J., 2000. Better decisions through science. *Scientific American*, Volume 283, pp. 82-87.

- Tamari, S. & Guerrero-Meza, V., 2016. Flash Flood Monitoring with an Inclined Lidar Installed at a River Bank: Proof of Concept. *Remote Sensing*, 10, 8(10), p. 834.
- Tanaka, S., 2008. *Local Disaster Management and Hazard Mapping*. Tokyo: International Centre for Water Hazard and Risk Management (ICHARM).
- Tejedor, M., Neris, J. & Jiménez, C., 2013. Soil Properties Controlling Infiltration in Volcanic Soils (Tenerife, Spain). *Soil Science Society of America Journal*, 4, 77(1), pp. 202-212.
- Tempfli, K., Kerle, N., Huurneman, G. C. & Janssen, L. L., 2009. *Principle of Remote Sensing*. Enschede: The International Institute for Geo-Information Science and Earth Observation (ITC).
- Tempfli, K., Kerle, N., Huurneman, G. C. & Janssen, L. L., 2009. *Principles of Remote Sensing : An introductory textbook*. 2 ed. Enschede: ITC.
- Tezuka, S., Takiguchi, H., Kazama, S. & Sarukkalghe, R., 2013. Estimation of the effects of climate change on flood-triggered economic losses in Japan. *International Journal of Disaster Risk Reduction*, Volume 9, pp. 58-67.
- Tockner, K. et al., 2008. Flood plains: critically threatened ecosystems. In: *Aquatic Ecosystems*. s.l.:Cambridge University Press.
- Townsend, P. A. & Walsh, S. J., 1998. Modeling floodplain inundation using an integrated GIS with radar and optical remote sensing. *Geomorphology*, 1, 21(3-4), pp. 295-312.
- Trenberth, K. E., 2005. The Impact of Climate Change and Variability on Heavy Precipitation, Floods, and Droughts. In: *Encyclopedia of Hydrological Sciences*. s.l.: John Wiley & Sons, Ltd..
- Turner, B. L. et al., 2003. A framework for vulnerability analysis in. *roceedings of the National Academy of Sciences of the United States of America*, 100(14), pp. 8074-8079.
- UNDP, 2004. *A global report: Reducing disaster risk-a challenge for development*, New York : United Nations Development Programme Bureau for Crisis Prevention and Recovery.
- UNDRO, 1991. *Mitigation Natural Disaster; Phenomena, Effect and Opinions (a manual for policy makers and planners)*. Geneva: United Nations Disaster Relief Coordinator.
- UN-ISDR, 2004. *Living with Risk: A global review of disaster reduction initiatives*, Geneva: United National-International Strategy for Disaster Reduction.
- UN-ISDR, 2005. *Reducing Disaster Risk: A Challenge for Development*, s.l.: United Nations-Bureau for Crisis Prevention and Recovery.
- Van De Giesen, N., 2001. *Characterization of west African shallow flood plains with L- and C-band radar*. New Mexico, USA, s.n., pp. 365-367.

- Van de Voorde, T. et al., 2004. *Extraction of land use/land cover-related information from very high resolution data in urban and suburban areas*. Rotterdam, Mill Press.
- van Herk, S., Zevenbergen, C., Ashley, R. & Rijke, J., 2011. Learning and Action Alliances for the integration of flood risk management into urban planning: A new framework from empirical evidence from The Netherlands. *Environmental Science and Policy*, 14(5), pp. 543-554.
- Vassileva, M., Nascetti, A., Tonolo, F. G. & Boccardo, P., 2015. *Unsupervised Flood Extent Detection from SAR imagery Applying Shadow Filtering from SAR Simulated Images*. Milan, Italy, s.n., pp. 2707-2710.
- Villagrán De León, J. C., 2006. *Vulnerability: A Concept and Methodological Review*, Bonn: UNU Institute for Environment and Human Security (UNU-EHS).
- Weblio, 2016. *Weblio*. [Online]
Available at:
http://www.weblio.jp/wkpja/content/%E5%B2%A1%E5%B4%8E%E5%B8%82_%E6%A6%82%E8%A6%81#cite_ref-chunichi2016-2-18_4-0
[Accessed 26 10 2016].
- Wei, T. C. & McGuinness, J. L., 1973. *Reciprocal distance squared method, a computer technique for estimating areal precipitation*. Oline version ed. United States: United States. Agricultural Research Service. North Central Region.
- Westen, V. C., 2000. *Remote sensing for natural disaster management*. Amsterdam, s.n.
- Wiesmann, A. et al., 2001. Potential and methodology of satellite based SAR for hazard mapping. *IEEE Proceeding of International Geoscience and Remote sensing Symposium*, Volume 7, pp. 3262-3264.
- Wiesmann, A. et al., 2001. Potential and methodology of satellite based SAR for hazard mapping. *IEEE Proceeding of International Geoscience and Remote sensing Symposium*, Volume 7, pp. 3262-3264.
- Wilby, R. L. & Keenan, R., 2012. Adapting to flood risk under climate change. *Progress in Physical Geography*, 2012(3), pp. 348-378.
- Willmott, C. J. & Matsuura, K., 2005. Advantages of the mean absolute error (MAE) over the root mean square error (RMSE) in assessing average model performance. *Climate Res.*, Volume 30, p. 79–82.
- Wilson, H. & Keich, U., 2016. Accurate pairwise convolutions of non-negative vectors via FFT. *Computational Statistics and Data Analysis*, Volume 101, p. 300–315.
- Wisner, . B., Blaikie , P., Cannon, T. & Davis, I., 2003. *At Risk: Natural Hazards, People's Vulnerability and Disaster*. 2 Edition ed. London: Routledge.
- Wisner, B., Blaikie, P., Cannon, T. & Davis, I., 2003. *At Risk: natural hazards, people's vulnerability and disasters*. 2 ed. London: Routledge.

- Xiao, Q., McPherson, E. G., Simpson, J. R. & Ustin, S. L., 2007. Hydrologic processes at the urban residential scale. *Hydrological Processes*, 7, Volume 21, pp. 2174-2188.
- Xi, R., Wang, Z., Xie, M. & Zhao, X., 2015. A non-local vectorial total variational model for multichannel SAR image speckle suppression. *Chinese Journal of Aeronautics*, 28(3), pp. 770-779.
- Yamazaki, F. & Liu, W., 2016. *Extraction of flooded area due to the 2015 Kanto-Tohoku heavy rainfall in Japan using PALSAR-2 images*. Prague, s.n., pp. 179-183.
- Yan, K., Di Baldassarre, G., Solomatine, D. P. & Schumann, G. J. P., 2015. A review of low-cost 719 space-borne data for flood modelling: topography, flood extent and water level. *Hydrological Processes*, 29(15), pp. 3368-3387.
- Yucel, I., 2015. Assessment of a flash flood event using different precipitation datasets. *Natural Hazards*, 12, 79(3), p. 1889–1911.
- Yulianto, F. et al., 2015. Detecting areas affected by flood using multi-temporal ALOS PALSAR remotely sensed data in Karawang, West Java, Indonesia. *Natural Hazards*, 1, 77(2), pp. 959-985.
- Zhang, D.-w. et al., 2015. Flash flood hazard mapping: A pilot case study in Xiapu River Basin, China. *Water Science and Engineering*, 7, 8(13), pp. 195-204.
- Zhang, W. & Dou, J., 2014. A Fast Thresholding Technique in Image Binarization for Embedded System. *TELKOMNIKA Indonesian Journal of Electrical Engineering*, 12(1), pp. 592-598.
- Zhenghao, S. & Fung, K. B., 1994. *A comparison of digital speckle filters*. Pasadena-California, Institute of Electrical and Electronic Engineering.
- Zhu, A.-X., 1997. Measuring uncertainty in class assignment for natural resource maps under fuzzy logic. *Photogrammetric engineering and remote sensing*, 63(10), pp. 1195-1202.
- Zope, P., Eldho, T. & Jothiprakash, V., 2016. Impacts of land use–land cover change and urbanization on flooding: A case study of Oshiwara River Basin in Mumbai, India. *CATENA*, 10, Volume 145, pp. 142-154.